ISSN 2712-8172

MAGAZINE OF CIVIL ENGINEERING

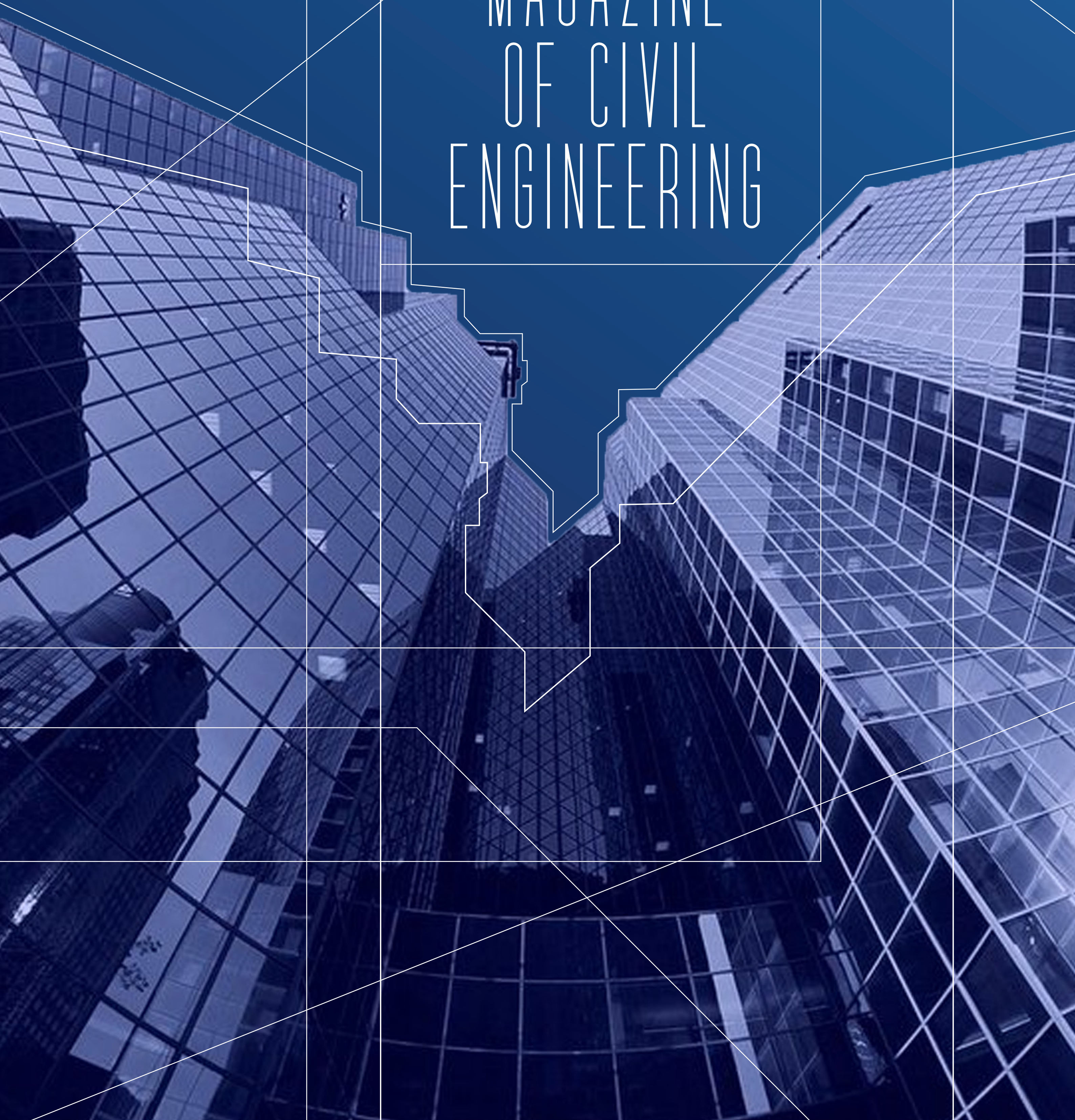

Magazine of Civil Engineering

ISSN 2712-8172

Online peer-reviewed open-access scientific journal in the field of Civil and Construction Engineering

Founder and Publisher: Peter the Great St. Petersburg Polytechnic University

This journal is registered by the Federal Service for Supervision of Communications, Information Technology, and Mass Media (ROSKOMNADZOR) in 2020. Certificate El No. FS77-77906 issued February 19, 2020.

Periodicity: 8 issues per year

Publication in the journal is open and free for all authors and readers.

Indexing: Scopus, Web of Sceince (ESCI, RSCI), DOAJ, Compendex, Google Academia, Index Copernicus, ProQuest, Ulrich's Serials Analysis System, CNKI

Corresponding address: 29 Polytechnicheskaya st., Saint Petersburg, 195251, Russia

Chief science editor:
D.Sc., Galina L. Kozinetc

Deputy chief science editors:
D.Sc., Sergey V. Korniyenko

Executive editor: Ekaterina A. Linnik

Translator, editor: Irina Ye. Lebedeva

Proofreader: Philipp Chrysanthes S. Bastian

DT publishing specialist:
Anastasiya A. Kononova

Contacts:
E-mail: mce@spbstu.ru
Web: http://www.engstroy.spbstu.ru

Date of issue: 10.02.2025

© Peter the Great St. Petersburg Polytechnic University. All rights reserved.
© Coverpicture – Polina A. Ivanova

Editorial board:

T. Awwad, PhD, professor, Damascus University, Syrian Arab Republic
A.I. Belostotsky, D.Sc., professor, StaDyO Research & Engineering Centre, Russia
A.I. Borovkov, PhD, professor, Peter the Great St. Petersburg Polytechnic University, Russia
M. Veljkovic, PhD, professor, Delft University of Technology, The Netherlands
R.D. Garg, PhD, professor, Indian Institute of Technology Roorkee (IIT Roorkee), India
M. Garifullin, PhD, postdoctoral researcher, Tampere University, Finland
T. Gries, Dr.-Ing., professor, RWTH Aachen University, Germany
T.A. Datsyuk, D.Sc., professor, Saint-Petersburg State University of Architecture and Civil Engineering, Russia
V.V. Elistratov, D.Sc., professor, Peter the Great St. Petersburg Polytechnic University, Russia
O.N. Zaitsev, D.Sc., professor, Southwest State University, Russia
T. Kärki, Dr.-Ing., professor, Lappeenranta University of Technology, Russia
G.L. Kozinetc, D.Sc., professor, Peter the Great St. Petersburg Polytechnic University, Russia
D.V. Kozlov, D.Sc., professor, National Research Moscow State Civil Engineering University, Russia
S.V. Korniyenko, D.Sc., professor, Volgograd State Technical University, Russia
Yu.G. Lazarev, D.Sc., professor, Peter the Great St. Petersburg Polytechnic University, Russia
M.M. Muhammadiev, D.Sc., professor, Tashkent State Technical University, Republic of Uzbekistan
H. Pasternak, Dr.-Ing.habil., professor, Brandenburgische Technische Universität, Germany
F. Rögener, Dr.-Ing., professor, Technology Arts Science TH Köln, Germany
V.V. Sergeev, D.Sc., professor, Peter the Great St. Petersburg Polytechnic University, Russia
T.Z. Sultanov, D.Sc., professor, Tashkent Institute of Irrigation and Agricultural Mechanization Engineers, Republic of Uzbekistan
A.M. Sychova, D.Sc., professor, Military Space Academy named after A.F. Mozhaysky, Russia
M.G. Tyagunov, D.Sc., professor, National Research University "Moscow Power Engineering Institute", Russia
M.P. Fedorov, D.Sc., professor, Peter the Great St. Petersburg Polytechnic University, Russia
D. Heck, Dr.-Ing., professor, Graz University of Technology, Austria
P. Cao, D.Sc., professor, Jilin University, China
A.G. Shashkin, D.Sc., PI Georekonstruktsiya, LLC, Russia
B.M. Yazyev, D.Sc., professor, Don State Technical University, Russia

Contents

Magazine of Civil Engineering

ISSN
2712-8172

journal homepage: http://engstroy.spbstu.ru/

Research article

UDC 624.014:621.315.1

DOI: 10.34910/MCE.133.1

Dynamic behavior of power transmission line supports under wind influence

I.M. Garanzha , ***A.V. Tanasoglo*** , ***H.A. Ademola*** , ***M.M. Pisareva***

Moscow State University of Civil Engineering (National Research University), Moscow, Russian Federation

garigo@mail.ru

Keywords: dynamic behavior, wind load, natural frequency, forced oscillation, overhead power line, fast Fourier transform

Abstract. In this article, we give experimental research on the dynamic behavior of steel supports of overhead power lines (OHPL) under the action of wind loads. The methodology and scheme of the experiment were created in two stages on the corner dead-end and intermediate supports of OHPL 220 kV “TPP Zmiev – Zalyutino”. In the first stage, excitation of the support’s oscillations was achieved using wind exposure; in the second stage, there were recorded free oscillations of the system “support – current wires”, which were created by means of handmade resonance. There are presented graphs of stress variations in the structural elements of tower lattice supports under wind action along and across the OHPL. There were experimentally determined basic natural frequencies of steel supports, which are shown on the damping graphs of free oscillations. Analysis of the obtained spectra of longitudinal velocity wind pulsations allowed conclusions about the stationary nature of wind flow. There is a determination of the necessity of the frequency detuning of OHPL support from the natural frequency of 2.2 Hz because external action with the given frequency is possible at the current wire breakage in one of the phases. The first three natural frequencies of oscillations for overhead line support were determined experimentally. Frequencies below 0.75 Hz are associated with the effect of wind on current wires. Analysis of the results made it possible to clarify that the wind at angle of 90° to the overhead line route not only exerts maximum static pressure but is also almost twice as susceptible to the considered “support – wires” system in dynamics. The presented methodology makes it possible to study the dynamic properties and study the response of structures to wind influences not only of overhead line supports but also of wind power installations and antenna supports of radio relays and cellular communications.

Citation: Garanzha, I.M., Tanasoglo, A.V., Ademola, H.A., Pisareva, M.M. Dynamic behavior of power transmission line supports under wind influence. Magazine of Civil Engineering. 2025. 18(1). Article no. 13301. DOI: 10.34910/MCE.133.1

1. *Introduction*

Overhead power lines (OHPL) are characterized by a significant variation not only in structural forms but also in geometric parameters, such as the length of the spans, the difference in the marks of the foundations, various sag arrows, etc. [1–3]. Moreover, as a rule, even on the same line, it is almost impossible to find building structures with overhead line supports with exactly the same static design loads. The spectrum of dynamic impacts is much wider, and the latter not only have a significant impact on the stress-strain state of metal structures, such as towers and masts, but also lead to fatigue damage, which is currently quite difficult to predict due to a significant number of variable factors [4–6].

That is why it is necessary not only to improve the principles of monitoring and observing the behaviour of structures in the wind flow but also to develop simple ways to take into account the dynamic component under the action of climatic and emergency loads, which by their nature are dynamic phenomena.

Improving OHPL supports by increasing their reliability and durability through design using numerical methods, including taking into account the dynamic nature of wind loads on the structure of supports and current-carrying wires is an urgent task today.

The research object is a single-column free-standing lattice support of OHPL.

OHPL is a complex engineering structure, in which flexible elements (wires and cables) work together with rigid supports, and at the same time, the entire network is prestressed and exposed to dynamic phenomena [7].

In [8] is noted that when determining the maximum response of support structures to impulsive impacts attenuation is not as important as for harmonic loads. In this case, the maximum value of the ground reaction is achieved in a very short period of time [9]. The highest values of dynamic coefficients are observed under the action of a “rectangular” pulse [10].

Work [11] sets out the basic principles of dynamic analysis of transition tower supports for OHPL. In this work is noted that is possible to take into account resistance forces when using method of decomposing solutions of oscillatory motion into their own modes of vibration by introducing them into decayed solution. This technique allows one to significantly simplify the solution of equations, however, the presence of dampers and dissimilar materials in design leads to errors in solutions obtained in this way.

Works [12–15] also noted the effectiveness of using numerical integration of the system “support – wires” motion equations under complex form of disturbance.

Solving dynamic problems is usually much more difficult than solving similar problems of static analysis. There is a widely used rule of thumb states that for system with n dynamic degrees of freedom approximately $n/2$ of the first own frequencies and their corresponding own mode shapes can be reliably obtained [16].

The simplest calculation algorithm aimed at using a one-dimensional oscillatory system, such as a cantilever rod, as a construction model is given in [17].

Thus, based on of literary sources analysis, there is a lack of information on the nature of propagation of disturbances from wind loads in time and along the span and have not been studied the shape of pulse and its characteristics in support sections of wires and cables.

Therefore, is necessary not only to revise the existing principles of monitoring and observing the behavior of structures in wind flow but also to develop simple ways to take into account the dynamic component under wind action, ice and emergency loads, which by their nature are dynamic phenomena.

The research purpose is to study the magnitudes and shapes of pulses on anchor and intermediate supports of overhead lines under wind load action taking into account the supporting influence of current-carrying wires and lightning protection cables.

The goal is achieved by solving the following tasks:

1. Experimentally to determine the own vibration frequencies for OHPL supports to further clarify the influence of dynamic characteristics on the supports design models together with current-carrying wires and cables.
2. To determine the main modes of vibration for support structures that describe mechanical properties of “support – wires” system under action of dynamic wind loads.
3. To analyze stresses in structural elements of supports under dynamic influence depending on wind gusts at different speeds.
4. To analyze the influence of wind gust duration on the periods of own vibration frequencies for support structures.

2. Materials and Methods

2.1. Experimental Research Methodology

The purpose of these experimental studies was to study the dynamic properties of tower-type supports in the “support – wires” system and to determine the reaction of these systems to wind impacts.

The anchor-angular support No. 57 (Fig. 1) and intermediate support No. 72 (Fig. 2) belong to the 220 kV OHPL “TPP Zmiev – Zalyutino”. The brand of the anchor-angle support is U-38; the brand of the intermediate support is PBG-4 of the “barrel” type with blind clips.

Figure 1. General view of the anchor-corner support of a 220 kV OHPL.

Figure 2. General view of the intermediate support of a 220 kV OHPL.

The supports are located in rural areas and on arable land in the Donetsk region. In accordance with paragraph 2.5.45 [7, 8], terrain type II. The orientation of the line at this location north-northwest – south-southeast (NNW–SSE). To the south of the experimental site, there was a forest belt at a distance of 0.7 km; from the other sides, at a distance of more than 3 km, there were no significant obstacles causing changes in the wind flow. The terrain of the site has a slight slope of 0.50 in the direction of north-northeast (NNE).

During a full-scale inspection, corrosion wear of the steel structures of the supports was revealed, which for belts and inclined braces was 0.6–0.8 mm, and for horizontal struts located up to the level of the lower traverse, 0.6–1 mm. Corrosion damage to bolted connection packages was also recorded. There was no development of crevice corrosion.

In preparation for the experimental studies, calibration tests of primary converters, in particular strain gauges and thermo-anemometric converters (TAPT), were carried out. After calibration and selection of the experiment location, the sensors were installed on the support structure. Load cells were attached to the belts and braces of the support zone on the belts of the lower traverse. In the cross section, three strain gauges were installed (on the corner feathers and on the rim) parallel to the axis of the corner with an indentation of 10 mm in order to avoid the influence of the edge effect. When the load cells were glued together, the wind speed was recorded. When the wind speed was exceeded by a gust of 2 m/s during the process of load cell labelling and glue polymerization, the load cells were discarded and the process was repeated. The response of the structure was also measured using vibration velocity meters of the VEGIK type installed at the level of the upper traverse in mutually perpendicular directions.

To monitor the incoming air flow at the top of the support so as to exclude shading of the sensors by structural elements, a wind speed meter (thermo-anemometer) and a wind direction meter (rumbometer) were installed. The second thermo-anemometer was installed at a height of 10 m on a horizontal bar made of a corner profile with a length of 750 mm, located at an angle of 45° to the face of the support.

During the experiment, when the wind direction changed in such a way that the angle between the bar of the thermo-anemometer and the incoming flow became less than 90°, the thermo-anemometer was moved to the opposite belt.

As an autonomous power source, a gasoline alternator was used, generated by a voltage of 220 V and a power of 1 kW/h. To reduce the level of noise and interference from the voltage transmitted by the OHPL, the monitoring system, the personal computer, and the generator were grounded.

During the experiment, the system was located in a passenger car. The scheme of the experiment is shown in Fig. 3.

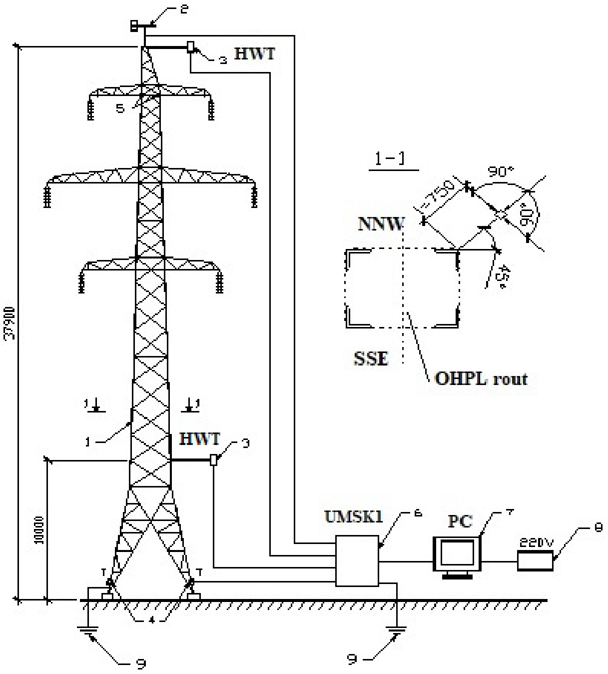

Figure 3. The experimental research scheme: 1 – support PBG-4 type; 2 – rumbometer; 3 – hot-wire transducer (HWT); 4 – strain gauges; 5 – vibration sensor VEGIK; 6 – monitoring system "USMK-1"; 7 – personal computer; 8 – gasoline generator; 9 – ground loop.

The experiment was conducted in two stages. At the first stage, the excitation of vibrations of the structure was achieved with the help of wind; at the second stage, free vibrations of the system were recorded, which were created using manual resonance.

When conducting such studies, it is necessary to control not only the internal parameters of the structure (response) but also external influences, and measurements must be carried out synchronously with a sufficiently high frequency of polling of primary converters and the ability to collect a significant amount of statistical information [8, 9].

3. Results and Discussion

3.1. Experimental Research Results of Support Dynamic Behavior in Wind Flow

The first stage of the experiment was carried out for five days. In total, 57 hours of implementations of the output signals of the primary converters were recorded, of which 16 hours were selected for analysis. The survey of all primary converters was conducted at a frequency of 64 Hz.

In the course of the experiment, two wind directions: north-west (NW) and east-northeast (ENE) – were recorded. According to the results of wind speed measurements at altitudes of 10 m and 37.9 m, the following ratios of average wind flow velocities with an averaging interval of 1 hour were obtained: for the ENE direction, 1.52, and for the NW direction, 1.67. Norms [7] recommend a coefficient of 1.5 in this case. Thus, it can be concluded that the actual measured wind profile corresponds to the normative value.

Fig. 4 shows the characteristic realization of the wind speed in the NW direction. The average velocity with an averaging interval of 1 hour was 2.56 m/s, standard deviation (SD) – 0.788, and turbulence intensity I(t) – 0.307. For the wind in the NNE direction, the average speed was 3.42 m/s, SD – 0.584, I(t) – 0.171.

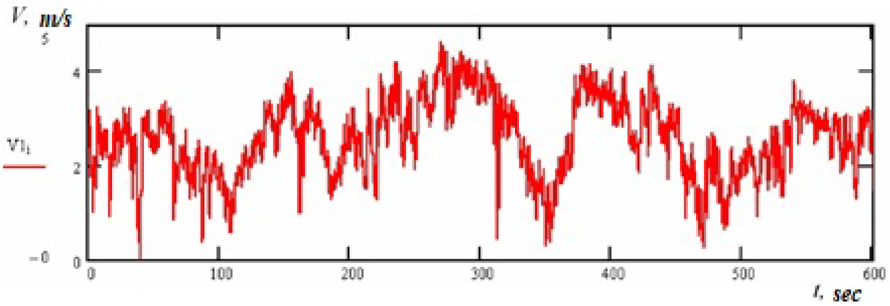

Figure 4. Typical realization of wind speed in the NW direction.

To determine the natural oscillation frequencies of the PBG-4 support, the obtained implementations of the random process were transformed using the fast Fourier transform [10, 11].

The obtained spectra of longitudinal wind velocity pulsations in the NW and ENE directions are shown in Fig. 5. The analysis of spectral densities allows us to conclude that the wind process is stationary, since these spectra correspond to classical representations [12, 13].

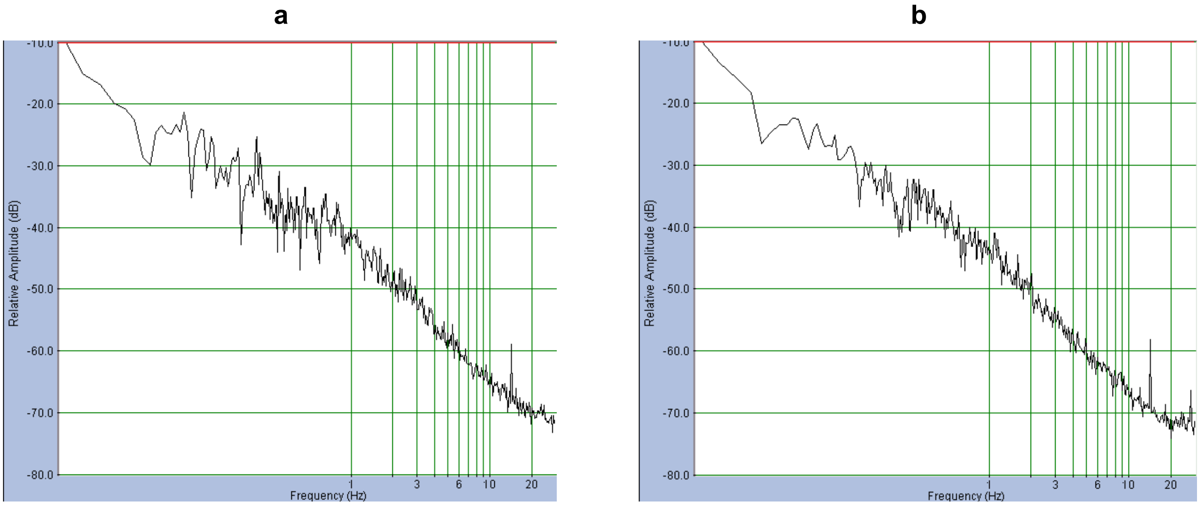

Figure 5. Spectral wind densities: a – NW; b – ENE.

Fig. 6 shows the characteristic implementations of the received signals. Fig. 6a shows graphs of stress changes in windward belts with wind perpendicular to the overhead line; Fig. 6b shows graphs of stress changes in diagonal belts with wind along the overhead line.

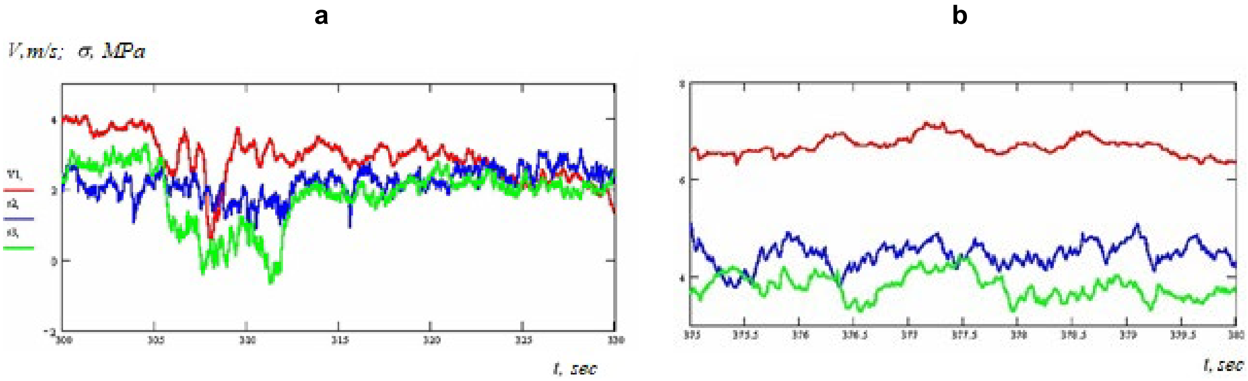

Figure 6. Typical implementations of received signals.

In Fig. 6, the graph ‘Vl’ characterizes the wind speed at an altitude of 10 m above the earth surface; graphs ‘s2’ and ‘s3’ characterize tensions in the belts, MPa.

To remove various noises, a simple coherence function was used [14, 15], showing the coincidence of the signal spectra at different frequencies. A similar function constructed for the windward face belts (Fig. 7) shows almost complete coincidence of the signal spectra. At the frequency bands of 0.85 to 7.5 Hz, the mutual coherence of the two processes exceeds 0.9. This indicates that the main frequencies of natural oscillations are located exactly in this interval. Coherence at lower frequencies also exceeds 0.9; however, this fact is due to the fact that at frequencies less than 0.1 Hz, systems whose first eigenvalues are in the range f ∈ [0,5; 8] Hz perceive the wind load as quasi-static [16].

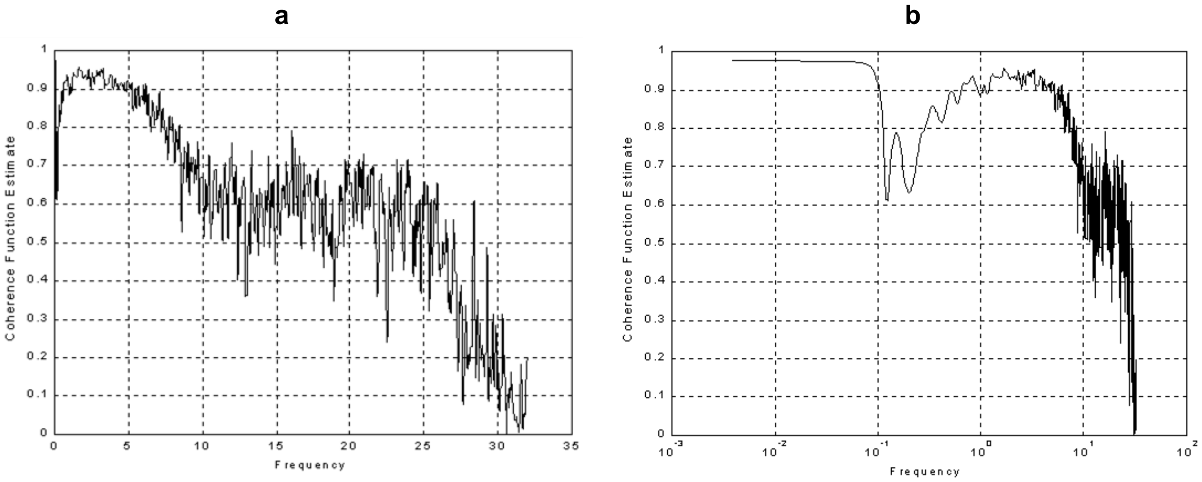

Figure 7. Coherence function of stress realizations in the belts of the windward face: a – linear scale; b – logarithmic scale.

A completely different picture can be obtained for the realizations of stresses in diagonally arranged belts, on which all the natural frequencies of oscillations manifest themselves, and the noise disappears due to some time delay in the reaction of opposite belts to wind action (Fig. 8).

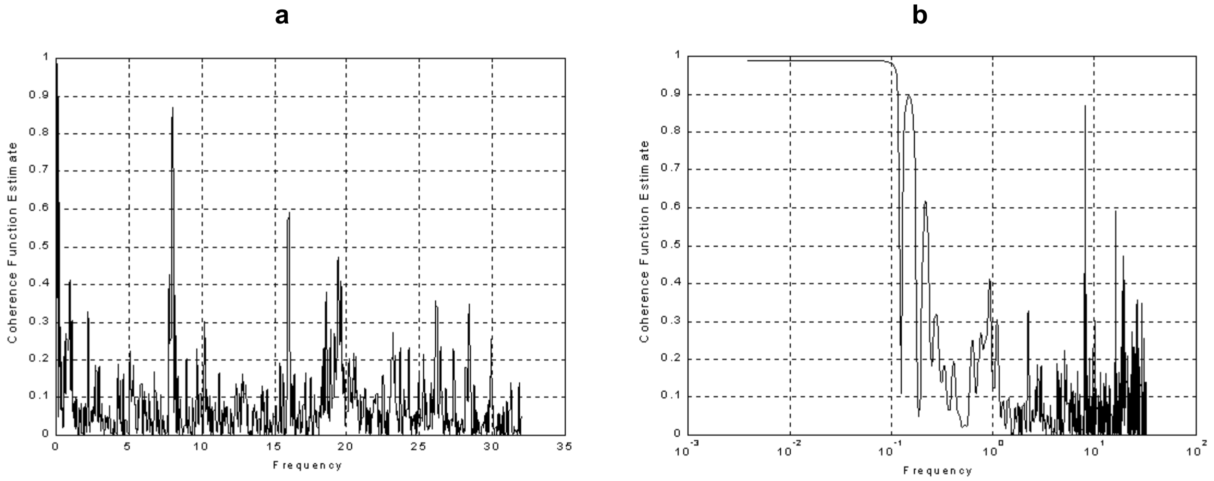

Figure 8. Coherence function of stress realizations in diagonal belts: a – linear scale; b – logarithmic scale.

The analysis of Figs. 5–8 allowed us to establish the natural frequencies of vibrations in the support. The first natural frequency is 1.09 GHz, the second is 2.04 Hz, and the third is 7.98 Hz. Oscillation frequencies below 0.75 Hz on different spectra (Fig. 5) manifest themselves in different ways and are associated with the effect of wind on current-carrying wires.

To compare the spectra of wind speed signals and the response of the structure, graphs of the coherence function for the direction of the wind across the line were constructed (Fig. 9).

In general, the coherence of this process can be characterized as weak [14, 15]. Some peaks have been obtained in the eigen frequency region of the structure, but their magnitude is not significant.

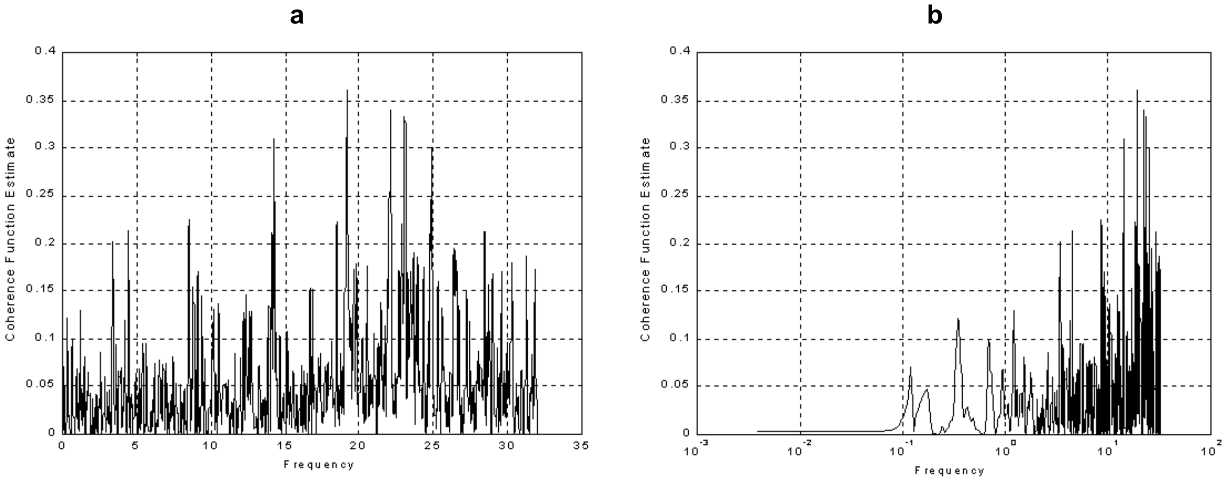

Figure 9. Coherence function of wind speed and structure response when the wind direction is across the line: a – linear scale; b – logarithmic scale.

3.2. Experimental Research Results of Free Oscillations for the “Support – Wire” System

The second stage of the experiment consisted of the study of free oscillations in the “support – wires” system. The excitation of vibrations was carried out by the method of manual resonance. The driving force was applied at the level of attachment of the cable-resistant to the trunk of the anchor-angular support U-38 m No. 57 perpendicular to the line.

A characteristic graph of the damped oscillations of the system for an anchor-angular support is shown in Fig. 10. The type of graph allows us to conclude that there are several frequencies, and in the first third, the vibrations of the support structure with a frequency of about 1 Hz are dominant, and in the rest of the implementation period, the vibrations of the wires with a frequency of 0.2 Hz are predominant. Moreover, the damping of vibrations occurs under the action of dry (Coulomb) friction [15, 18, 19].

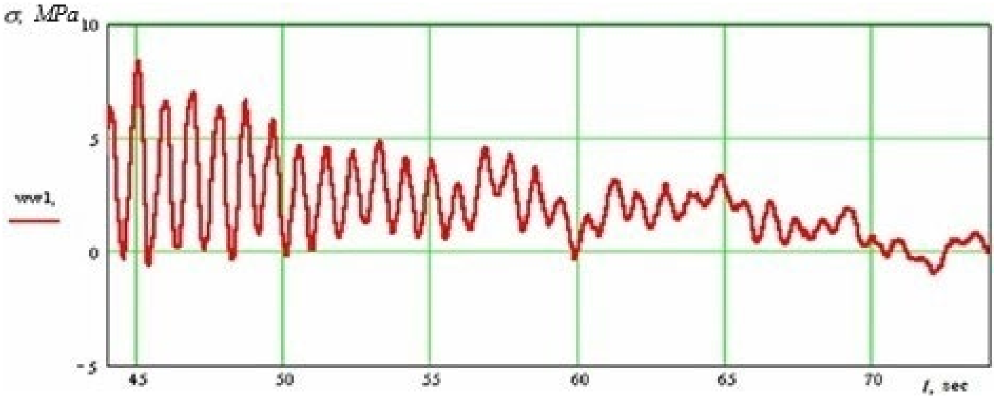

Figure 10. Graph of free damped vibrations for an “anchor support – wires” system.

To determine the average value of the logarithmic decrement of oscillations, the formula [20, 21] is used:

$$\delta = \frac{\ln\left(\frac{A_0}{A_n}\right)}{n}, \tag{1}$$

where A_0 and A_n are the initial and final amplitudes separated by n periods of free, damped oscillations.

For this system, the logarithmic decrement of oscillations obtained in this way is 0/191, with a variance of $4*10^{-4}$.

The coefficient of internal friction of the overhead line support structure is equal to (2) [20, 22, 24]:

$$\xi = \frac{\delta}{\pi} = 0.04. \tag{2}$$

The transformation of signal implementations using fast Fourier transform (FFT) allowed us to construct spectral dependences of the oscillatory process (Fig. 11). The natural frequencies obtained as a result of the first and second stages agree quite well.

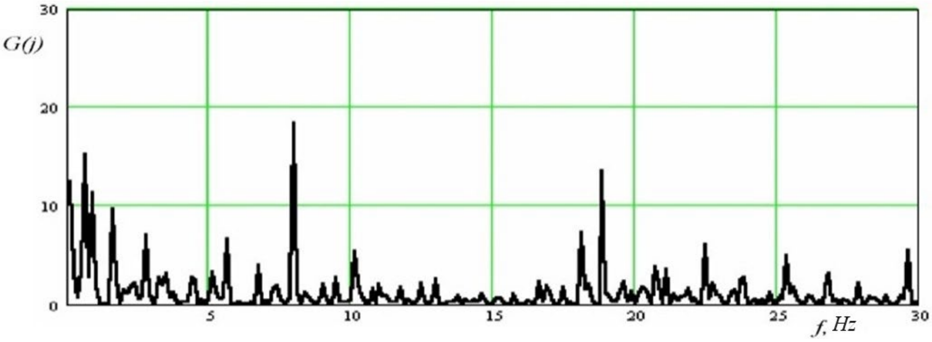

Figure 11. Spectral density of vibrations for an “anchor support – wires” system with freely damped oscillations.

Approbation of this technique was also carried out on the intermediate support PBG-4 No. 72 with blind clamps belonging to the 220 kV OHPL “TPP Zmiev – Zalyutino”.

A characteristic graph of the attenuation of free oscillations is shown in Fig. 12, and the spectral density constructed according to this implementation is shown in Fig. 13, in which the dominant first natural frequency equal to 2.37 Hz is clearly visible. Moreover, this frequency was maintained when the direction of the driving force changed along and perpendicular to the overhead line axis. The logarithmic decrement of vibration damping in this case is 0.049, and the coefficient of internal friction of the structure is 0.016.

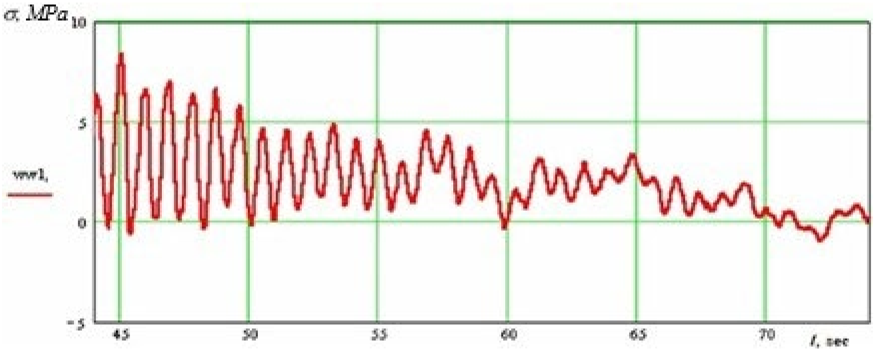

Figure 12. Graph of free damped oscillations for an “intermediate support – wires” system.

The amplitude-frequency characteristics of the system were obtained using the expressions (3) [21–23, 25]:

$$A = \frac{1}{\sqrt{\left(\left(1-\left(\frac{F_p}{F_c}\right)^2\right)+\left(2\cdot\delta\cdot\left(\frac{F_p}{F_c}\right)^2\right)\right)}}, \tag{3}$$

where F_p is the frequency of forced oscillations and F_c is the frequency of natural oscillations.

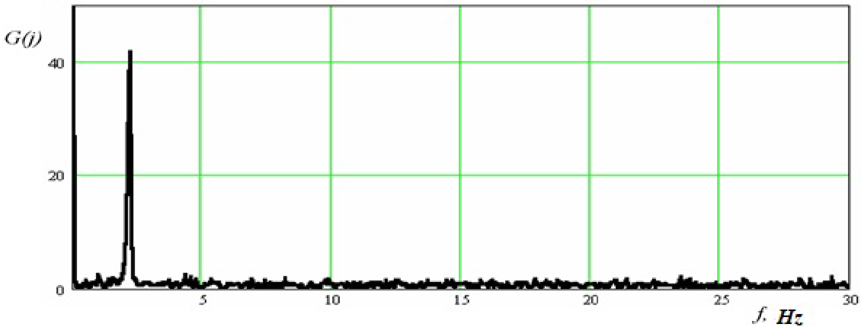

Figure 13. Spectral density of oscillations of an “intermediate support – wires” system with freely damped oscillations.

Thus, if the frequencies of external influence and the natural frequencies of the structure coincide, the dynamic coefficient can be 2.61 for the anchor-angular support U-38 m and 3.99 for the immediate support PBG-4 (Fig. 14).

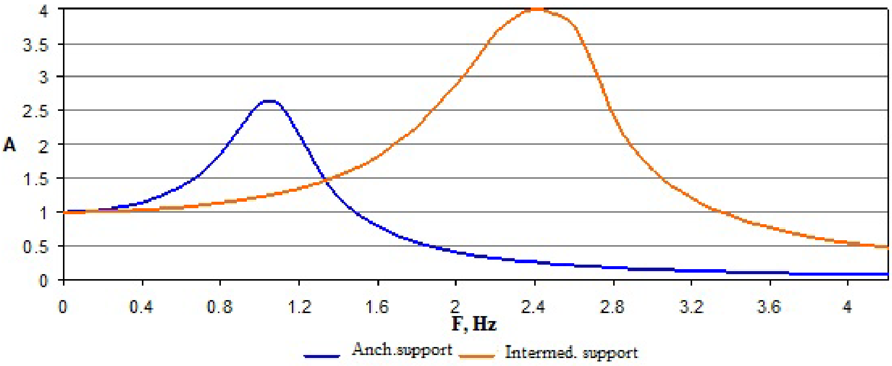

Figure 14. Amplitude-frequency characteristics of supports.

4. Conclusions

1. The first three natural oscillation frequencies of the OHPL support have been experimentally determined. Frequencies below 0.75 Hz are associated with the effect of wind on the current-carrying wires.
2. The analysis of the results made it possible to clarify that the wind at an angle of 90° to the overhead line route exerts not only the maximum static pressure but is also almost twice as susceptible to the considered “support – wires” system in dynamics.
3. As a result of experimental studies, the need for frequency detuning of the support structure from the natural frequency of 2.2 Hz has been established, since an external effect with this frequency is possible when a current-carrying wire breaks in one of the phases.
4. The presented technique makes it possible to study the dynamic properties and investigate the reactions of structures to wind impacts, not only of overhead line poles but also of wind power poles and antenna poles of radio relays and cellular communication.

References

1. Gologorsky, E.G. Spravochnik po stroitel'stvu i rekonstrukcii linij elektroperedachi napryazheniem 0,4–750 kV [Handbook on the construction and reconstruction of power transmission lines with voltage 0.4–750 kV]. Moscow: ENAS, 2017. 560 p.
2. Novoselov, A.A, Pichkurova, N.S. Computational analysis of power transmission line steel structures according to modern regulatory and technical documents. The Siberian Transport University Bulletin. 2022. 4(63). Pp. 86–93. DOI: 10.52170/1815-9265_2022_63_86
3. Korotkevich, M.A. Proektirovanie mekhanicheskoj chasti linij elektroperedachi [Design of mechanical part of electrical power lines]. Minsk: High School, 2019. 577 p.
4. Wadell, B.C. Transmission Line Design. Artech House. Norwood, 1991. 266 p.
5. Pustovgar, A., Tanasoglo, A., Garanzha, I., Shilova, L. Optimal design of lattice metal constructions of overhead power transmission lines. MATEC Web of Conferences. 2016. 86. Article no. 04003. DOI: 10.1051/matecconf/20168604003
6. Uteuliev, B.A., Tarasov, A.G. Life time of overhead transmission line supports. Science Bulletin of the Novosibirsk State Technical University. 2015. 59(2). Pp. 89–97. DOI: 10.17212/1814-1196-2015-2-89-97
7. Kondrateva, O.E., Voronkova, E.M., Loktionov, O.A. Impact assessment of weather and climate events on overhead transmission lines reliability with voltages up to 110–220 kV. 3rd International Youth Conference on Radio Electronics, Electrical and Power Engineering (REEPE). Moscow, 2021. Article no. 9388054. DOI: 10.1109/REEPE51337.2021.9388054
8. Gorokhov, E.V., Kazakevich, M.I., Shapovalov, S.N., Nazim, Ya.V. Aerodinamika elektrosetevyh konstrukcij [Aerodynamics of power transmission lines]. Donetsk: Energy. 2020. 335 p.
9. Taylor, V., Nyame, S., Hughes, W., Koukoula, M., Yang, F., Cerrari, D., Anagnostou, E. Machine learning evaluation of storm-related transmission outage factors and risk. Sustainable Energy, Grids and Networks. 2023. 34. Article no. 101016. DOI: 10.1016/j.segan.2023.101016
10. Coşkun, S.B. Advances in Computational Stability Analysis. InTech. Rijeka, 2019. 132 p. DOI: 10.5772/3085
11. Bazant, Z.P., Celodin, L. Stability of Structures: Elastic, Inelastic, Fracture and Damage Theories. Oxford University Press. New York, 2010. 1011 p. DOI: 10.1142/7828
12. Senkin, N.A. Consideration of progressive collapse in the design of overhead power transmission line supports. Bulletin of Civil Engineers. 2022. 4(93). Pp. 37–46. DOI: 10.23968/1999-5571-2022-19-4-37-46
13. Kondrateva, O.E., Myasnikova, E., Loktionov, O.A. Analysis of the Climatic Factors Influence on the Overhead Transmission Lines Reliability. Environmental and Climate Technologies. 2020. 24(3). Pp. 201–214. DOI: 10.2478/rtuect-2020-0097
14. Diana, G., Bruni, S., Cheli, F., Fossati, F., & Manenti, A. Dynamic analysis of the transmission line crossing “Lago de Maracaibo.” Journal of Wind Engineering and Industrial Aerodynamics. 1998. 74–76. Pp. 977–986. DOI: 10.1016/s0167-6105(98)00089-0

15. Kemp, A.R, Behneke, R.H. Behavior of cross-bracing in latticed towers. Journal of Structural Engineering. 124(4). 2018. Pp. 360–367.
16. Loktionov, O.A., Kondrateva, O.E., Fedotova, E.V. Analysis of prerequisites for changing wind load standards for electric grid facilities. 4th International Youth Conference on Radio Electronics, Electrical and Power Engineering (REEPE). Moscow, 2022. Article no. 9731439. DOI: 10.1109/REEPE53907.2022.9731439
17. Tanasoglo, A., Garanzha, I., Kaledina, O., Swann, W.H. Software package for analysis and design of overhead power transmission line structures. E3S Web of Conferences. 2023. 460(3). Article no. 07008. DOI: 10.1051/e3sconf/202346007008
18. Li, H., Bai, H. High-voltage transmission tower-line system subjected to disaster loads. Progress in Natural Science. 2006. 16(9). Pp. 899–911. DOI: 10.1080/10020070612330087
19. Kadisov, G.M. Dinamika i ustojchivost' sooruzhenij [Dynamics and stability of structures]. Moscow: ASV. 2007. 272 p.
20. Togbenou, K., Li, Y., Chen, N., Liao, H. An efficient simulation method for vertically distributed stochastic wind velocity field based on approximate piecewise wind spectrum. Journal of Wind Engineering and Industrial Aerodynamics. 2016. 151(3). Pp. 48–59. DOI: 10.1016/J.JWEIA.2016.01.005
21. Yoo, C.H., Lee, C. Stability of Structures: Principles and Applications. Elsevier Academic Press. London, 2011. 529 p. DOI: 10.1016/C2010-0-66075-5
22. Hemavathi, G., Bhuvaneswari, P. Transmission Line Fault and Indicating System for Safety Life. Journal of Mechanics of Continua and Mathematical Sciences. 2019. 8(2). Article no. 00063. DOI: 10.26782/jmcms.spl.2019.08.00063
23. Loktionov, O.A., Zabelin, M.A., Belova, E.A. Comparative analysis of evaluation approaches for the climatic factors influence on power grid facilities reliability. 5th International Youth Conference on Radio Electronics, Electrical and Power Engineering (REEPE). Moscow, 2023. Article no. 10086808. DOI: 10.1109/REEPE57272.2023.10086808
24. Loktionov, O.A., Kuznetsov, N.S., Zabelin, M.A., Maksimov, D.O. Assessment Approaches of Climate Factors Influence for Design of Overhead Transmission Lines. 6th International Youth Conference on Radio Electronics, Electrical and Power Engineering (REEPE). Moscow, 2024. Article no. 10479738. DOI: 10.1109/REEPE60449.2024.10479738
25. Dupin, R., Kariniotakis, G., Michiorri, A. Overhead lines Dynamic Line rating based on probabilistic day-ahead forecasting and risk assessment. International Journal of Electrical Power & Energy Systems. 2019. 110. Pp. 565–578. DOI: 10.1016/j.ijepes.2019.03.043

Information about the authors:

***Igor Garanzha**, PhD in Technical Sciences*
ORCID: https://orcid.org/0000-0002-6687-7249
E-mail: garigo@mail.ru

***Anton Tanasoglo**, PhD in Technical Sciences*
ORCID: https://orcid.org/0000-0002-1825-2738
E-mail: a.v.tan@mail.ru

***Habeeb Ademola**,*
ORCID: https://orcid.org/0009-0000-8795-7128
E-mail: ademolahabeeb07@gmail.com

***Milena Pisareva**,*
E-mail: milena.pisareva.02@bk.ru

Received 24.10.2023. Approved after reviewing 03.12.2024. Accepted 09.12.2024.

Magazine of Civil Engineering

journal homepage: http://engstroy.spbstu.ru/

ISSN
2712-8172

Research article

UDC 666.91

DOI: 10.34910/MCE.133.2

Influence of electric current on the mineral matrix of technogenic anhydrite

A.N. Gumeniuk[1], ***A.F. Gordina***[1], ***S.M. Petrynin***[1], ***A.F. Buryanov***[2] ✉, ***V.Y. Skeeba***[3]

[1] *Kalashnikov Izhevsk State Technical University, Izhevsk, Russian Federation*

[2] *Moscow State University of Civil Engineering (MGSU) National Research University, Moscow, Russian Federation*

[3] *Novosibirsk State Technical University, Novosibirsk, Russian Federation*

✉ *rga-service@mail.ru*

Keywords: fluoroanhydrite, modification, carbon fiber, mineral matrix, microstructure, composite materials, electrical properties, electrochemical corrosion, micro heating elements

Abstract. The current conditions for the development of industrial and civil engineering in the regions with a negative average daily temperature require an increase in the economic efficiency of heating systems and reduction of the material consumption for its production and operation. One of the solutions to this problem is electrically conductive concrete. Cost reduction is achieved through the use of binders of anthropogenic origin. The electrically conductive concrete samples with dimensions of 70 × 70 × 70 mm and prototype product with dimensions of 500 × 500 × 50 mm were used for the assessment of the effect of the micro heating elements on the performance and physicochemical properties of mineral matrix. The electrically conductive concrete was based on waste of anthropogenic origin (fluorine-anhydrite) and fine aggregates. The additives in the form of 7 % technical soot suspension and 1 % of carbon fiber were used as micro heating elements. The physical and technical studies were carried out on the 28th day after 3 cycles of heating and cooling of the samples. The obtained results confirm that carbon fiber reduces the specific volume resistance up to 8.5 kOhm·cm. It allows the usage of proposed compositions for the manufacture of large-format heating elements. The experimental operation of large-format heating elements based on the developed compositions made it possible to determine its thermophysical characteristics. The heating of the elements surface from 21.9 to 28.5 °C for 40 minutes were obtained. Thus, the use of the developed prototype as heating elements is possibly provided that the pre-installed electrodes are protected from electrochemical corrosion. The electrochemical corrosion must be established through the use of methods of physicochemical analysis.

Funding: Investigations were performed on the equipment of Core Shared Research Facilities “Center of physical and physical-chemical methods of analysis, investigations of properties and characteristics of surface, nanostructures, materials and products” of Udmurt Federal Research Center of UB RAS

Citation: Gumeniuk, A.N., Gordina, A.F., Petrynin, S.M., Buryanov, A.F., Skeeba, V.Y. Influence of electric current on the mineral matrix of technogenic anhydrite. Magazine of Civil Engineering. 2025. 18(1). Article no. 13302. DOI: 10.34910/MCE.133.2

1. Introduction

Modern trends in the development of electrotechnical concretes, which traditionally consist of aggregates with rationally selected granulometric composition, binder (Portland cement) and modified with carbon-containing components of various morphological structures, are aimed at increasing of economic efficiency and environmental friendliness [1, 2]. The electrically conductive concrete based on Portland cement is the most common type of electrotechnical concrete due to its technological advantages, such as workability, strength, and durability. At the same time, the current intensification in civil engineering, infrastructure development, and urbanization have led to the widespread use of concrete and reinforced concrete on Portland cement and its negative impact on the environment [3, 4]. Production of cement and steel causes a significant CO_2 emission [4]. Environmental monitoring of industrial enterprises of the cement industry shows that every kilogram of produced Portland cement emits about 0.70–0.85 kg of carbon dioxide [4, 5]. The tendency of global industrial production makes it possible to forecast a volume of 5.8 billion tons of cement by 2030 [5, 6].

It has led to the development of research in the field of electrotechnical concretes aimed at solving problems of reducing the environmental burden by recycling of industrial waste in the production of environmentally friendly materials-substitutes for Portland cement [7, 8].

The associated industrial products (gypsum-containing waste), such as products of chemical, forestry, and mining industries, are the potential source of raw materials for the production of electrotechnical concretes. The annual volume of gypsum-containing waste for 2023 is about 100–280 million tons per year [7]. Global volumes of solid gypsum-containing waste are estimated from 7 to 8 billion tons [8]. This type of waste includes phosphogypsum, borogypsum, fluorohydrite, citrogypsum, titanogypsum, and others. One of the common gypsum-containing wastes is fluoranhydrite [4, 5]. This solid sulfate-containing production waste is formed as a by-product in the production of hydrogen fluoride. The technology for producing hydrogen fluoride is based on the interaction of fluorspar with 98 % sulfuric acid according to the reaction:

$$\mathrm{CaF_2 + H_2SO_4 = 2HF + CaSO_4}.$$

The crushed fluorspar is mixed with sulfuric acid, and the resulting mass is fed into rotary kilns. At 160–280 °C, the gas leaving the kiln contains up to 80 % of HF [5, 6]. The product discharged from the kiln contains more than 80 % of $CaSO_4$, 0.5–5.0 % of CaF_2, 10–12 % of H_2SO_4, 1.5–4.0 % of SiO_2, and 0.5–1.5 % of R_2O_3 [6].

In the works of A.A. Ponomarenko and Yu.G. Meshcheryakov [7], the composition of the by-product of the production of HaloPolymer JSC (Perm) after 3–5 years of storage was established to include no less than 20 % of γ-$CaSO_4$; up to 78 % of β-$CaSO_4$; from 1.0 to 1.8 % of CaF_2; from 0.5 to 10.0 % of H_2SO_4; up to 0.2 % of HF.

The water-soluble fluoride and sulfate ions in the composition, as well as suspended matters, have a negative impact on the environment when fluoroanhydrite accumulates in sludge storage facilities and when discharged into water bodies [7, 8].

To reduce the negative impact, several directions for the utilization of sulfate-containing waste have been developed: production of sulfuric acid and lime; of anhydrite binder; of gypsum binder; use as a regulator of the setting time of binders [8, 9].

Today, one of the most common and studied directions is the production of a binder by crushing, subsequent grinding, and milling of coarse-grained fluoroanhydrite stone. The resulting dispersed powder is mixed with a rationally selected solution of water with a hydration catalyst, which can be sodium sulfate, iron sulfate, potassium bisulfate, blast furnace slag, alumina sulfate, and others [10].

In the countries, such as the People’s Republic of China, the United States of America, and the Russian Federation, leading in the volume of accumulation of gypsum-containing waste, this binder has found quite wide application in the building materials industry [9].

Fluoroanhydrite and anhydrite binders are actively used in the production of various materials and products, including cement-free concrete and mortars [9, 10], facing and thermal insulation materials [1, 8].

The research by Russian and Chinese scientists [11] has shown the possibility of using such binders in the production of hollow and cellular blocks. Iron, sodium, and potassium sulfates have been successfully tested as hardening activators.

A sulfate-containing binder, with an optimal selection of a hardening activator, is technologically highly adaptable to modification by introducing extra additives to expand the functional properties of products. Thus, the use of carbon-containing additives made it possible to experimentally test products based on fluoroanhydrite with a relatively low specific resistance [12, 13].

In the last decade, a significant number of research works have been devoted to the formation of electrically conductive properties in mineral matrices by reducing the percolation threshold, which makes it possible to expand the scope of application and create products with a resistive self-heating function [14]. To justify the possibility of producing these products and ensuring the required specific resistance, various models have been proposed that justify the formation of electrically conductive paths in the matrix volume, such as cluster [6], linear [15], and complex [16]. To ensure various forms of electrically conductive paths, the use of additives of various morphology [17] and composition [18] has been proposed. The research results have confirmed the effectiveness of additives based on carbon-containing materials with various morphological features, including finely dispersed industrial soot and carbon fiber [19]. In this case, various types of metal products made of structural or stainless steel, such as reinforcement, plates, pipes, are used to supply electric current to the samples [20].

It is known [21] that the mechanism of electrical conductivity in mineral matrices, such as concrete based on Portland cement or gypsum, is based on ionic conductivity. In ionic conductors, such as electrolytes, ions move under the influence of an electric field. To transfer charge in a mineral matrix, there must be an electrolyte containing charged particles [21] located in pores, voids, in contact zones, and in the matrix [22].

In a mineral matrix based on industrial anhydrite, the presence of electrolyte in the structure depends on the humidity, particle size, their mutual arrangement, and also on the wedging pressure acting in thin layers. Pellicular moisture is several tens of angstroms thick and mainly limits the electrical conductivity of the system [23], moisture in pores and voids is represented by relatively large inclusions isolated from each other and does not make a noticeable contribution to the electrical conductivity of the matrix [23].

In countries with a dry climate, slabs and blocks made of dense mixtures based on gypsum binders are actively used in the construction of walls and partitions [17, 20, 23]. With an average density of 1500–1800 kg/m^3, gypsum concrete products have the required strength properties. Due to a number of reasons, prefabricated gypsum concrete products have not found wide application in housing construction.

The load-bearing capacity of gypsum concrete masonry can be increased by reinforcement: steel mesh, rods [15, 20]. However, steel reinforcement is known to actively corrode when in contact with hydrated gypsum binder [22, 23].

From the data presented in the study [15, 20, 22], it follows that the pH decreases during the hardening of the mineral matrix. The change in pH is observed immediately after the binder is mixed. Also in the works [24, 29], it was established that the presence of sulfates allows the pH to decrease during the first 30 minutes, before the formation of the crystalline structure.

In this regard, during the formation of the mineral matrix in a pre-reinforced product or a product with pre-installed electrodes, an oxide film is formed on the surface of the reinforcement, which is similar to the mechanism of formation of an inhibiting film during the manufacture of reinforced concrete [24, 25]. The subsequent decrease in pH to an acidic environment does not allow the formation of the required thickness of the oxide film on the surface of the reinforcing element [26]. As a result, the presence of bound and free water molecules in the composition of the hydrated sulfate-containing binder determines the emergence of conditions for electrochemical corrosion of iron, a destructive process of metal fracture in liquid conductive media [27, 28].

During the corrosion process in the mineral matrix, under the influence of the corrosion current, the metal dissolves due to electrochemical interaction with the electrolyte. The surface of the metal in the electrolyte is electrochemically heterogeneous, which leads to the formation of microgalvanic corrosion elements [25, 26]. On some areas of the surface, called anodes, the following reaction takes place:

$$\mathrm{Me} \leftrightarrow \mathrm{Men} + + \mathrm{n}\overline{\mathrm{e}}.$$

On other areas called cathodes, the following reactions take place:

- in neutral medium

$$\mathrm{O_2} + \mathrm{2H_2O} + 4\overline{\mathrm{e}} \leftrightarrow \mathrm{4OH^{-}};$$

- in acid medium

$$\mathrm{2H} + + 2\overline{\mathrm{e}} \leftrightarrow \mathrm{H_2} \uparrow .$$

The corroding elements of the circuit, being in an open state, corrode on the anodic and cathodic sections in the forward and reverse directions at the same rate. This is due to the fact that a potential difference arises between the metal and the electrolyte solution, associated with the formation of a double electric layer, i.e. an asymmetric distribution of charged particles at the phase boundary [25, 27].

In turn, the electrode potential of metals, calculated using the Nernst thermodynamic equation, depends on the nature of the electrolyte and the ambient temperature [26, 28]. Studies have shown that the corrosion process of a steel rod occurs actively in both acidic and alkaline electrolytes.

The considered features predetermined the need to assess the effect of electric current on a modified mineral matrix during heating and simulating the operation of a product based on a modified fluoroanhydrite binder.

The purpose of this work is to study the processes occurring in a modified mineral matrix based on fluoroanhydrite when passing electric current through structural reinforcement and to assess the performance of the contact zone “steel reinforcement/mineral matrix” after several heating/cooling cycles.

The results obtained will allow us to assess the possibility of solving the current problem of recycling large-tonnage chemical production waste by offering effective compositions and technical solutions for the production of heating elements.

2. Materials and Methods

Binder. The used fluoroanhydrite was provided by HaloPolymer LLC, Perm, Russia. The chemical composition of the binder is as follows: SiO_2 – 3.5 %; Al_2O_3 – 0.7 %; Fe_2O_3 – 0.95 %; CaO – 37 %; SO_3 – 54.42 %; impurities – 3.43 %. According to X-ray phase analysis, fluoroanhydrite is represented by anhydrite (d = 3.50; 2.85 Aº), gypsum (d = 4.29; 3.81 Aº), and calcium carbonate (d = 3.04 Aº) [7, 8]. In production, ground limestone is used to neutralize the binder, due to which the material has the following potential material composition: $CaSO_4$ – 74.78 %; $CaSO_4{\cdot}2H_2O$ – 13.38 %; $CaCO_3$ – 11.00 %; CaF_2 – 0.82 %; H_2SO_4 – 0.02 % [7].

Hydration catalyst. Based on the analysis of scientific research literature and the results of previous studies, sodium sulfate was selected to be introduced in an amount of 2 % of the mass of the binder in order to activate and intensify the processes of hydration and hardening, as well as to obtain the optimal structure of anhydrite stone [10, 6].

Fine aggregate. To ensure the density of the mineral matrix and homogenization of the fiber in the volume of the material, a fine aggregate in the form of quartz sand with a fineness modulus of 0.7 was introduced.

Monsterfiber carbon fiber. To ensure electrically conductive characteristics, uniform heating of the product, and temperature gradient, carbon fiber was introduced, which is also a reinforcing filler. The modifier is a crushed chopped carbon thread, which is obtained by multi-stage heat treatment of PAN fibers (polyacrylonitrile-based fibers) at temperatures up to 320 °C. Technical characteristics of carbon fiber: tensile strength of fiber not less than 3000 MPa; tensile modulus of elasticity of the fiber not less than 230 GPa; density from 1.68 to 1.80 g/cm^3; fiber stretching test not less than 0.8 %; moisture 0.1 %. The production is certified according to the following standards: ISO 9001, OHSAS 18001, ISO 14001.

Plasticizer (Stahement-2000-M). Uniform distribution of carbon fiber in the structure of the mixture is due to a new generation hyperplasticizer (Group I) based on polycarboxylates. The additive is available in liquid form and complies with EN 934-2:2010. Stahement 2000-M is used to obtain highly mobile, including self-compacting, concrete mixtures, for the production of thin-walled and densely reinforced, vertically molded products, complex-configuration structures with a high degree of factory readiness, monolithic reinforced concrete structures, lightweight concrete, monolithic floors, and roads.

Compositions and methods of testing and research. To study the features of the process of heating products, fluoroanhydrite plates 500 × 500 mm were manufactured. Their compositions are presented in Table 1.

Table 1. Component ratio of compositions.

Compositions	Binder (Fluoroanhydrite), kg	Fine aggregate (Fine sand Russian State Standard GOST 8736, Mk=0.7), kg	Hardening activator (Sodium sulfate, Russian State Standard GOST 4166), %	Carbon fiber (Monsterfiber C), %	Plasticizer (Stahement-2000-M), %	Water-to-Binder Ratio
Control	6.961	1.168	2	–	0.5	0.3
AE-1				0.3		0.3
AE-2				0.4		0.3
AE-3				0.5		0.35
AE-4				0.75		0.4

After gaining strength (28 days), studies were conducted on the physical, mechanical, chemical, and thermal properties of the developed compositions and products.

Mechanical strength. The mechanical compressive strength was determined on samples 70 × 70 × 70 mm at the age of 7, 14, and 28 days on a PGM-100MG4-A hydraulic press with a loading rate of 0.5–0.8 MPa/s.

Specific volume resistance. The specific volume electrical resistance was determined on samples of 70 × 70 × 70 mm. The value was calculated according to the formula:

$$\rho = R \cdot A / L, \ \Omega \cdot \text{cm},$$

where ρ is specific resistance of the sample; R is resistance of the sample, determined by measuring with a two-contact method using an E7-20 immittance meter; L is distance between the probes; A is cross-sectional area of the sample. The scheme used for measuring the specific volume resistance is presented in the paper study [29].

Differential scanning calorimetry. The influence of heating and micro heating modifying elements (carbon fiber) on the phase composition of the studied samples was analyzed by means of DSC analysis. The data were obtained on a TGA/DSC1 device of Mettler-Toledo Vostok CJSC, Switzerland, at the temperature range from 60 to 1100 °C at a temperature increase rate of 30 °C/min in an air atmosphere.

Scanning electron microscopy SEM-EDS. The microstructure of the samples was studied using a Thermo Fisher Scientific Quattro scanning electron microscope, Thermo Fisher Scientific Inc, USA. The samples for SEM-EDS analysis were cubic (an edge of 0.5 cm) and were selected using an angle grinder with a diamond disk. No preliminary preparation of the samples by spraying was performed.

Thermophysical characteristics. The thermophysical properties were assessed based on the research results obtained during the development of electrically conductive concrete [30, 31]. The test method involves generating electrical heat by supplying direct current with U = 120 V and I = 3 A to the electrodes according to the diagram shown in Fig. 1. The electric current was supplied until the maximum surface heating temperature of 30 °C was reached. This temperature threshold is due to the fact that during the exploratory stages of the experiment, heating the products above 35 °C was accompanied by the release of water from the volume of the products.

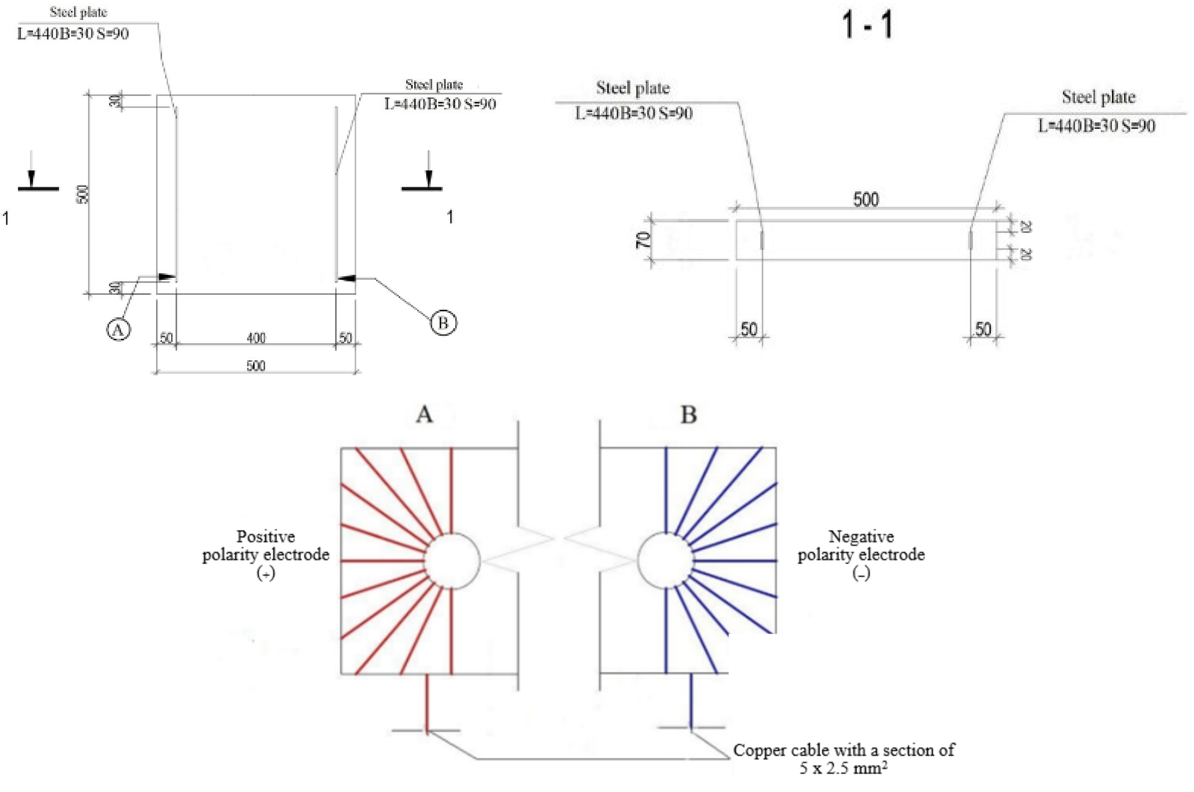

Figure 1. Layout of steel plates in the experimental product (plate).

The change in temperature and its distribution over the surface of the product were recorded using a Guide D192M thermal imaging camera. The intelligent thermal camera of the D series is equipped with a 4-inch high-brightness touch screen, IR resolution of 192 × 144, detector type of 25 µm, temperature range: –20 °C~150 °C, 100 °C~650 °C, 650 °C~1500 °C, accuracy: ±2 °C or ±2 % of readings (at an ambient temperature of 15 to 35 °C and an object's temperature above 0 °C).

3. Results and Discussion

3.1. Analysis of Physical and Technical Properties and Specific Volume Resistance

The analysis of the mechanical strength of the studied compositions shows that the strength of the AE-4 composition in the control test periods is higher than that of the AE-1, 2, 3 compositions by an average of 9.5 %. In turn, on the 28th day of hardening, the strength of the AE-4 composition was 24.2 MPa, which exceeds the strength of the control composition by 7.5 %, the variation coefficient was 7.2 %. After that, the set of properties was determined for the optimal strength of the AE-4 composition.

The results obtained in determining the specific volume electrical resistance of the samples and the change in the parameter during strength gain are shown in Fig. 3. It was found that the specific volume resistance of the control sample corresponds to the parameters given in the literary sources [40, 41] and is 27.1 kOhm·cm on the 28th day. At the same time, the specific volume resistance of the optimal conductive composition with carbon fiber on the 28th day is 8.5 kOhm·cm. This value is 1.5 times lower than that of compositions based on fluoroanhydrite binder modified with a suspension of industrial carbon black, developed and studied in previous works [31–34]. The achieved characteristics are due to the formation of a linear network of conductive elements in the form of uniformly distributed carbon fiber in the volume of the mineral matrix [35–38]. The percolation transition zone is overcome by increasing the breakdown voltage, which allows achieving optimal characteristics in comparison with the results presented in [39–41]. Thus, in [15], for the optimal composition, the specific volume resistance was 13.6 kOhm·cm, and the strength was 35.81 MPa. When gaining strength, an increase in the parameter of specific volume electrical resistance is observed for the control and modified compositions, which is associated with the continued formation of the matrix structure and a decrease in the volume of unbound water [42, 43].

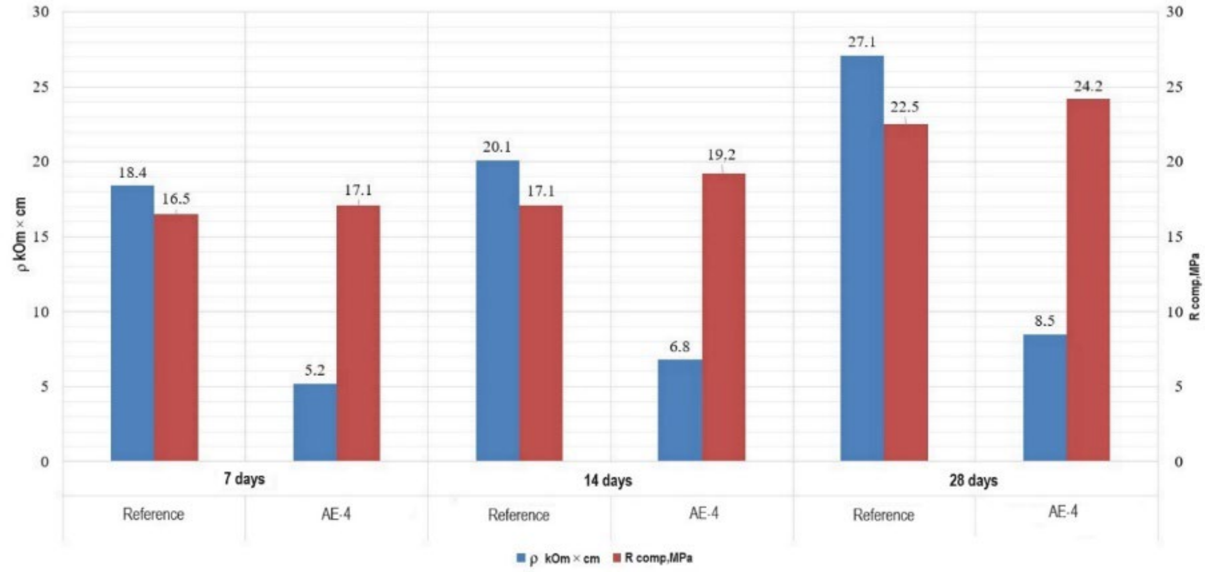

Figure 2. Test results of the control and optimal composition AE-4: mechanical compressive strength, MPa (red); specific volume resistance, kOhm·cm (blue).

Subsequently, the AE-4 composition was used to determine the thermophysical and physicochemical properties and characteristics, as well as to test the heating scheme for the products.

3.2. Study of Thermophysical and Physicochemical Properties

Analysis of data in the field of practical implementation of conductive composite products allows us to determine the parameters of direct current supplied to metal electrodes. Current characteristics varied for current strength I from 0 to 5 A, for voltage U from 0 to 220 V; achieving a uniform temperature gradient over the surface of the product was considered optimal.

The final values ensuring uniform heating were: I = 3A; U = 120V. These characteristics are cost-effective and safe for use in industrial and civil construction. Fig. 3 shows the results of thermophysical tests of a plate with geometric dimensions of 500 × 500 × 50 mm, made of AE-4 composition. The electrodes in the plate were located at a distance of 40 cm from each other, and the dimensions of the electrodes were 44 × 3 cm, installed according to the diagram shown in Fig. 1. Over 40 minutes, the temperature of the product increased uniformly. The maximum temperature of the product after 40 minutes was 31.1 °C, which is 9.2 °C higher than the initial surface temperature. The average power consumption was 660 W/m^2.

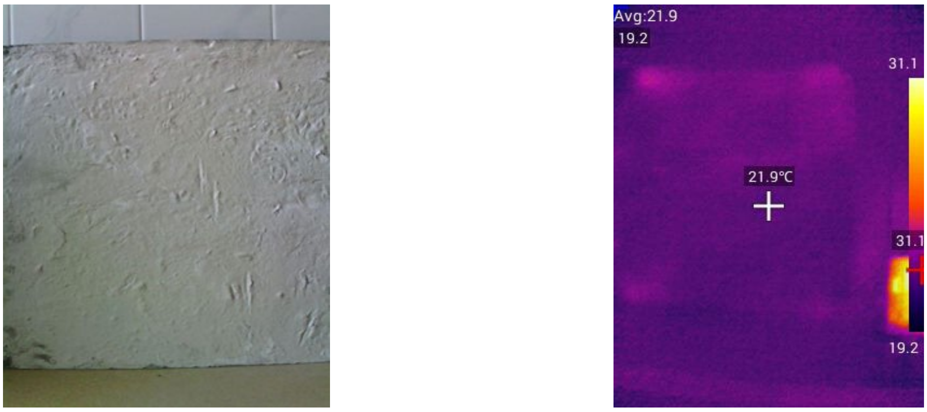

a

b

Emissivity– 0.75;

Ambient temperature T = 19.2 °C;

Average surface temperature of the plate T = 21.9 °C

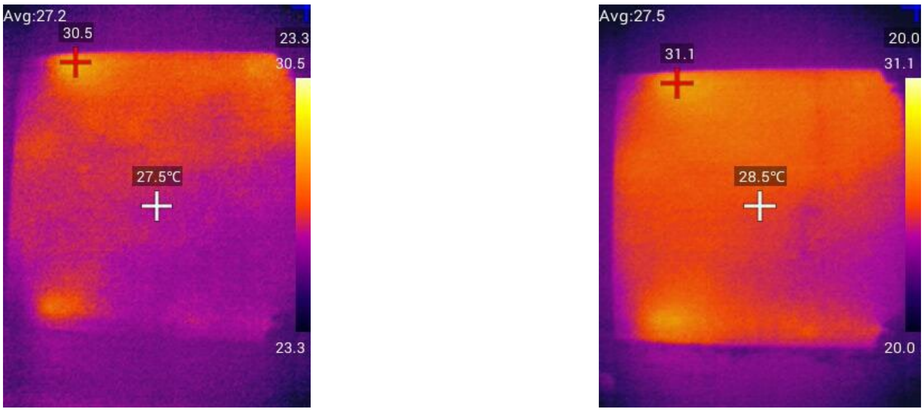

c

d

Emissivity– 0.75;

Ambient temperature T = 23.3 °C;

Average surface temperature of the plate T = 27.5 °C

Emissivity– 0.75;

Ambient temperature T= 20 °C;

Average surface temperature of the plate T = 28.5 °C

Figure 3. Product and thermal imaging camera images obtained during heating at 20-minute intervals: a – general appearance of the product; b – initial surface temperature of the product; c – temperature 20 minutes after the start of heating; d – temperature 40 minutes after the start of heating.

To assess the effect of heating on the structure of the modified matrix based on the AE-4 composition, a microstructure analysis was performed. The samples were taken on the 28th day of hardening, after several cycles of heating the product to the maximum temperature and subsequent cooling, from different zones, depending on the location of the matrix relative to the heated element, according to Fig. 4.

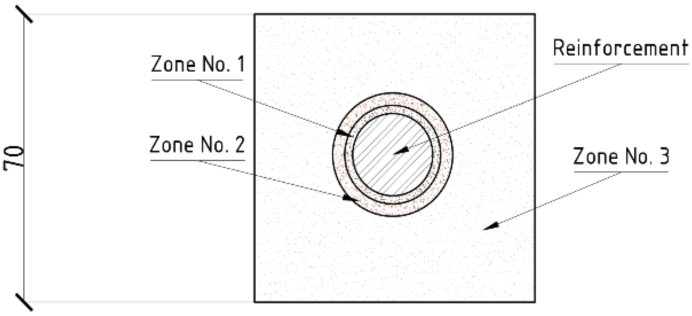

Figure 4. Scheme of sampling for studies of the physical and chemical properties of an electrically conductive composition after several heating/cooling cycles.

The study of the contact zone of the metal and the fluoroanhydrite-based mineral matrix shows a low degree of adhesion (Fig. 5a), which is caused by the formation of lamellar crystals of iron oxide between the mineral matrix and the reinforcement (Figs. 5b and 5d), which are formed in the initial stages of hardening, up to 10 days. In turn, the mineral matrix, including iron oxide, is characterized by a fairly loose structure (Fig. 5c).

Analysis of the microstructure of the mineral matrix, taken from Zone No. 2, remote from direct contact with the metal, shows the presence of poorly soluble iron (III) hydroxide (Figs. 6a and 6b). At the same time, thermal influence on cubic crystalline new formations (Fig. 6c) leads to the deformation of the crystals and the appearance of parallel oriented microcracks, promoting the stratification of hydration products (Fig. 6d).

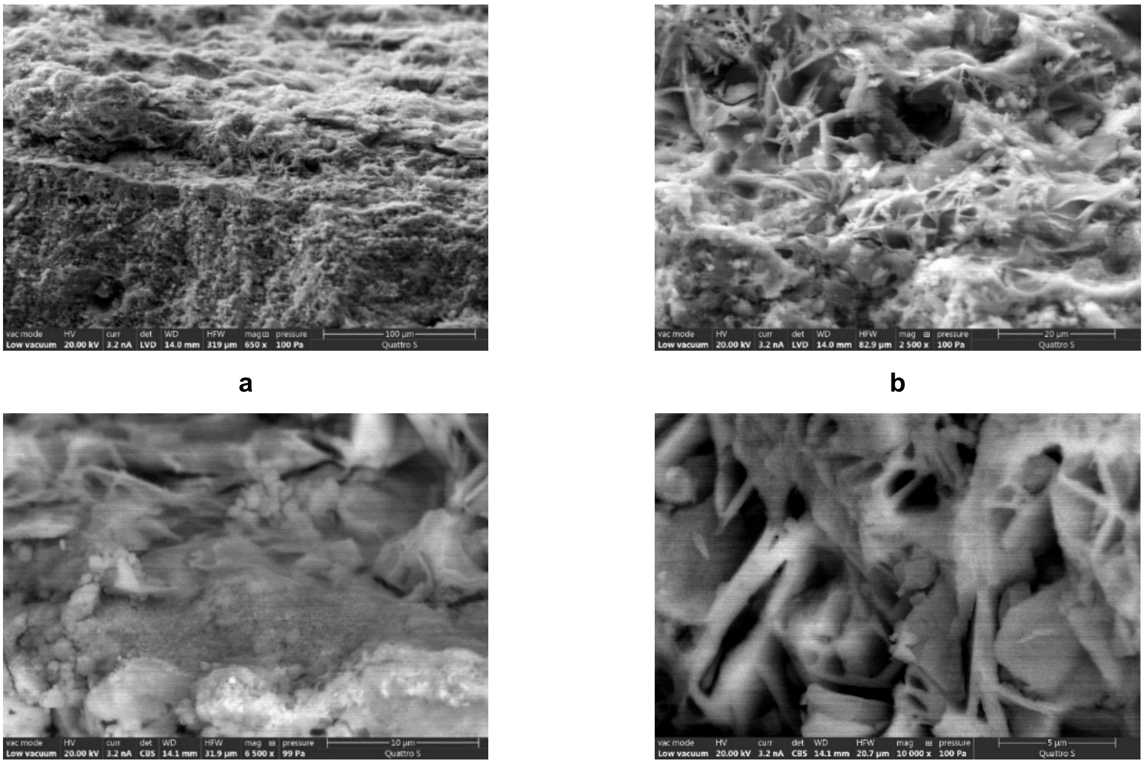

a

b

c

d

Figure 5. SEM of the modified AE-4 sample, sampling Zone No. 1, the area of direct contact of the steel rod (reinforcement) and the mineral matrix at different magnifications: a – 650x; b – 2500x; c – 6500x; d – 10000x.

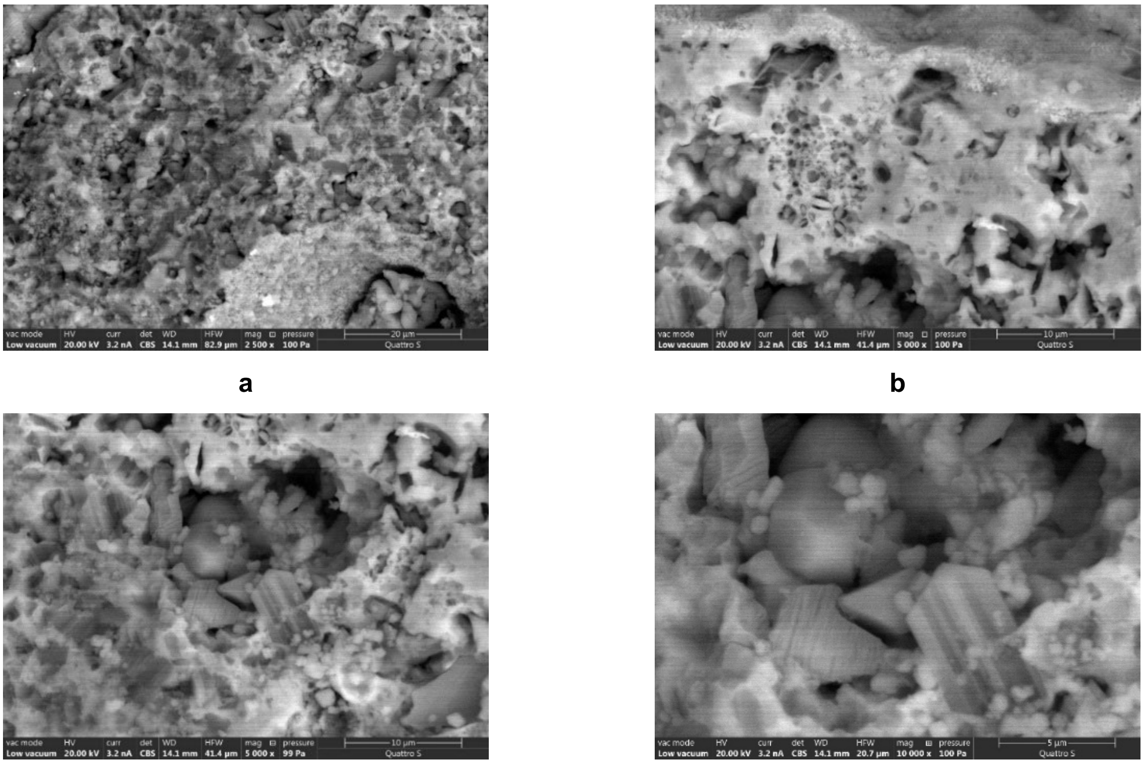

a b

c d

Figure 6.SEM of modified sample AE-4, sampling Zone No. 2, at different magnifications: a – 650x; b, c – 5000x; d – 10000x.

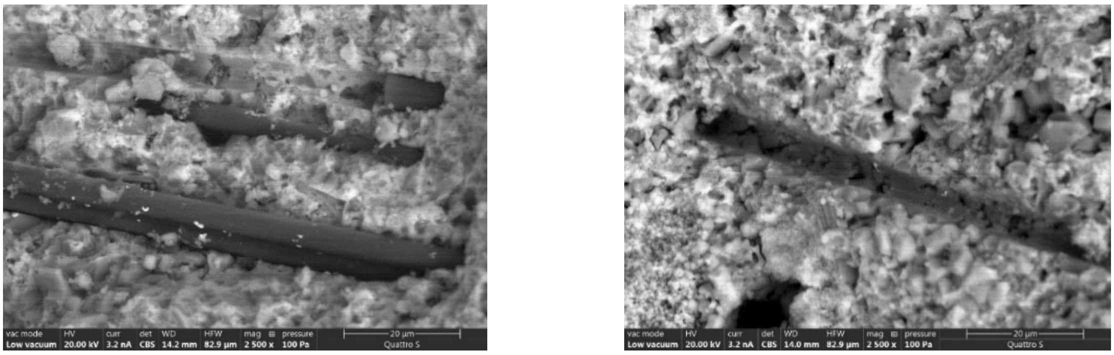

a b

Figure 7.SEM of AE-4modified sample, sampling zone No. 3, at magnifications of 2500x .

Microstructure of the sample taken from Zone No. 3, typical for the modified composition outside the contact zone with the metal element. The presence of carbon fiber uniformly distributed in the volume of the material is noted. The uniformity of distribution is due to the use of a plasticizer and fine filler and the optimality of the composition production (Fig. 7a). At the same time, the absence of chemical interaction in the area of the contact zone of the carbon fiber and the matrix is noted, which is confirmed by the absence of new formations on the surface of the modifier (Figs. 7a and 7b).

To estimate the volume of the matrix structure subject to changes due to heating of the metal reinforcement and to analyze the depth of migration of iron ions into the contact zone of the material around the heating element, the migration of iron ions was analyzed by means of mapping (Fig. 8).

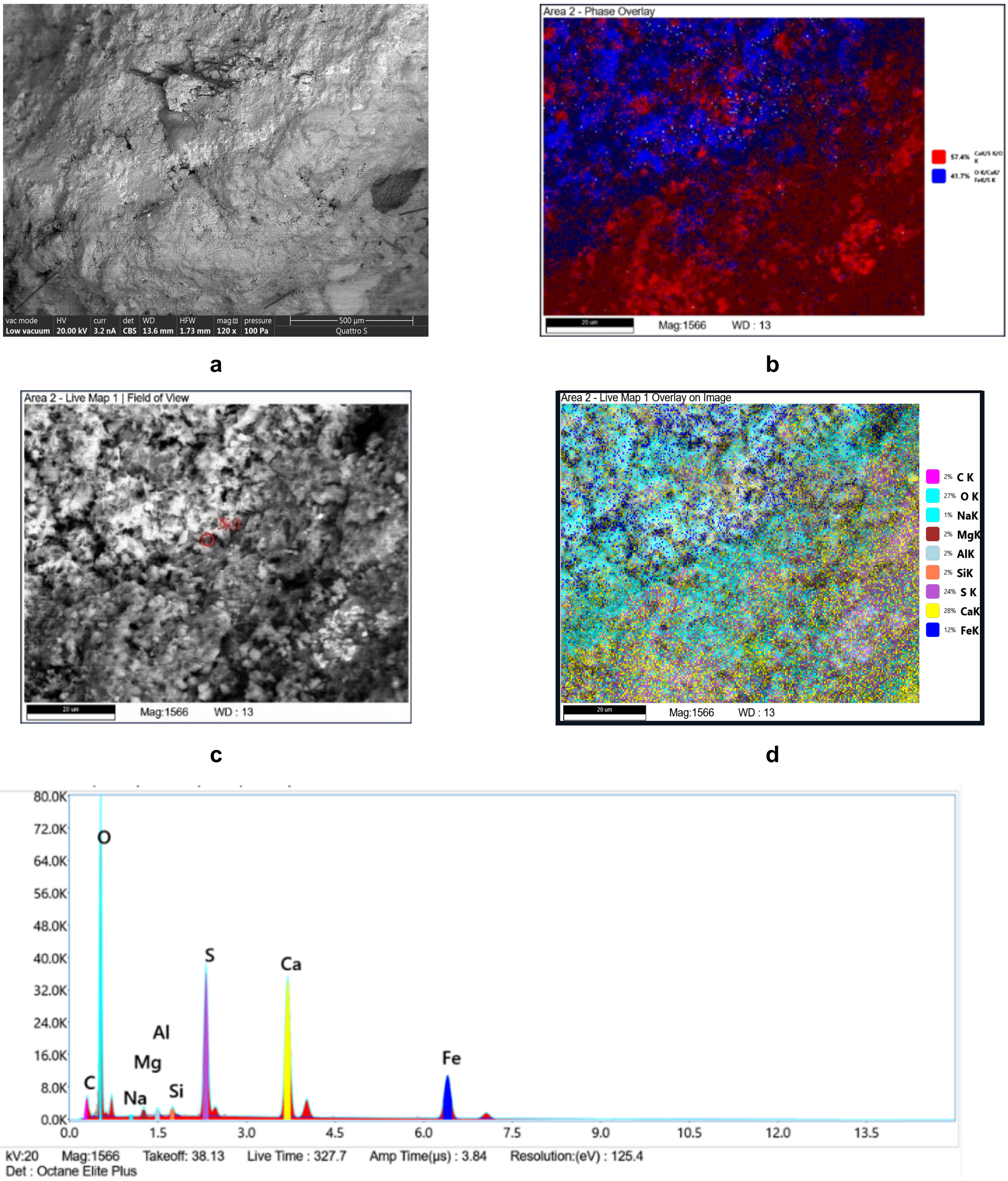

a

b

c

d

e

Figure 8. Iron ion migration analysis, sampling Zone No. 2, after several heating cycles: a – general structure view, boundary of Zones No. 2 and No. 3, at 120x magnification; b – chemical compound mapping (red – CaK/S K/OK, blue – OK/ CaK/ FeK/ SK); c – microstructure of elemental mapping area at higher magnification; d – element mapping of area c; e – quantitative analysis at point 1.

The mapping obtained as a result of energy-dispersive analysis (Figs. 8b, 8d, and 8e) confirmed the active migration of iron ions into the structure of the mineral matrix and the presence of Zones No. 1 and No. 2 with a microstructure different from Zone No. 3, formed due to changes in the conditions of structure formation during heating of the product. This process is caused by electrochemical corrosion of the heating element (reinforcement) due to the presence of a significant amount of bound and free water in the hydrated sulfate-containing binder. In this case, heating determines the emergence of conditions for the accelerated formation of iron-containing compounds, including iron oxides and hydroxides (Figs. 8b, 8d, and 8e).

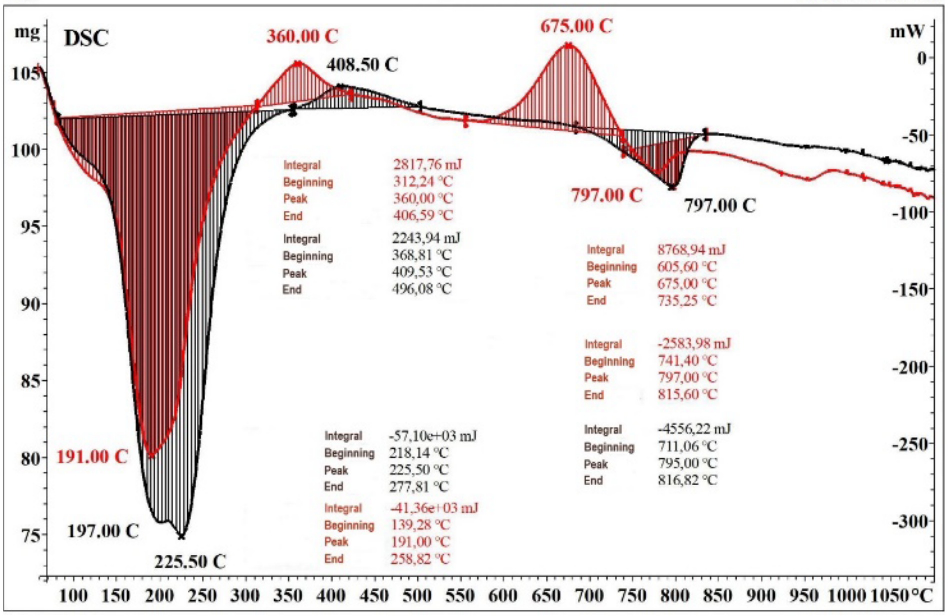

**Figure 9.DSC analysis of samples on the 28th day of hardening,
after several heating/cooling cycles: red – modified composition; black – control composition.**

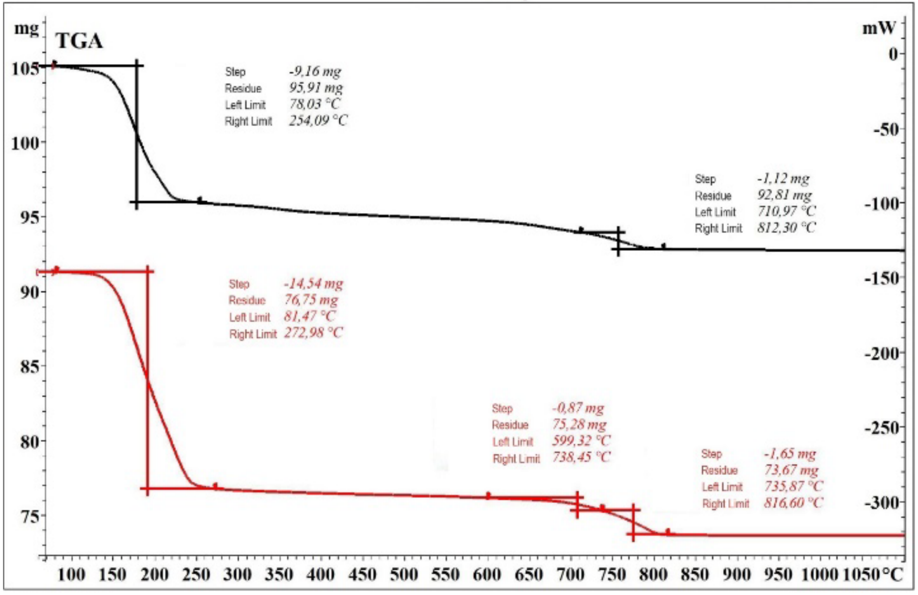

**Figure 10. TG analysis of samples on the 28th day of hardening,
after several heating/cooling cycles: red – modified composition; black – control composition.**

To confirm the insignificant effect of heating the product on the modified matrix located at a distance from the heating elements, DTA/TG analysis was performed on a sample taken from Zone No. 3 after several heating/cooling cycles.

Comparative analysis of differential scanning calorimetry, thermogravimetric analysis of the control and modified samples showed that in the temperature range up to 280 °C, dehydration of crystal hydrate water occurs, characterized by a significant mass loss of 15.9 % for the modified composition and 8.7 % for the control one. In addition, a strong exothermic effect with a maximum at a temperature of 675 °C is observed on the DSC curve for the modified composition. In the studied temperature range, phase transformations of carbon with the release of heat are absent [35], the obtained data probably demonstrate the result of the process of interaction of carbon with oxygen with the formation of carbon monoxide (oxidation and burnout of the additive).

At 408.5 °C in the control composition and 360 °C in the modified composition, calcium sulfate recrystallizes.

The control and modified compositions exhibit an endothermic effect at 797 °C in the control composition and at 777.3 °C in the modified composition, associated with the dissociation of calcium carbonate.

Thus, the analysis of the obtained data allows us to conclude that carbon fiber can be used as micro-heating elements; the additive provides satisfactory physical and mechanical characteristics, thermophysical parameters, while the modification and subsequent heating of the product are not accompanied by physical and chemical changes.

4. Conclusions

Based on the conducted comprehensive analysis of the influence of heating on the microstructure and properties of the mineral matrix based on a binder of anthropogenic origin, the following was found:

1. The introduction of carbon fiber in the amount of 0.75 % of the binder mass, in combination with a hardening activator, provides mechanical strength of 24.2 MPa and specific volume resistance of 8.5 kOhm·cm. The achieved parameters meet the operational requirements for heated products.
2. The optimal electric current values were determined to be U = 120 V, I = 3 A, providing a uniform temperature gradient over the surface of the product and heating the product by 9.2 °C within 40 minutes. The average power consumption was 660 W/m^2.
3. After several heating/cooling cycles, a lack of adhesion was found between the hydrated fluoroanhydrite matrix and the unprotected steel rod (reinforcement) due to accelerated electrochemical corrosion of the heating element.
4. The degree of negative influence of heating on the structure and composition of the modified mineral matrix was determined depending on the distance to the reinforcing element.
5. Migration of iron ions has been established, determining the degree of destruction of the mineral matrix, which can be tracked by the depth of penetration of iron ions and the influence of electrochemical corrosion products.

Thus, based on the proposed compositions, an economically efficient, low-material-intensive system can be developed for heating residential and industrial premises. However, it is necessary to establish the maximum possible number of heating/cooling cycles of products, to offer effective solutions to reduce the degree of influence of electrochemical corrosion on heating elements.

References

1. Litvinova, T.E., Suchkov, D.V. Comprehensive Approach to the Utilisation of Technogenic Waste from the Mineral Resource Complex. Mining Informational and Analytical Bulletin. 2022. 6–1. Pp. 331–48. DOI: 10.25018/0236_1493_2022_61_0_331
2. Alfimova, N., Pirieva, S., Titenko, A. 2021. Utilization of gypsum-bearing wastes in materials of the construction industry and other areas. Construction Materials and Products. 4 (1). Pp. 5–17. DOI: 10.34031/2618-7183-2021-4-1-5-17
3. Alfimova, N.I., Pirieva, S.Yu., Levitskaya, K.M., Kozhukhova, N.I. Optimization of Parameters for the Production of Gypsum Binders Based on Gypsum-Containing Waste. Lecture Notes in Civil Engineering. 2023. 307. Innovations and Technologies in Construction. BUILDINTECH BIT 2022. Pp. 148–154. DOI: 10.1007/978-3-031-20459-3_19
4. Petropavlovskaya, V., Sulman, M.G., Novichenkova, T., Kosivtsov, Y.Y., Zavadko, M., Petropavlovskii, K. Gypsum Composition with a Complex Based on Industrial Waste. Chemical Engineering Transactions. 2021. 88. Pp. 1009–1014. DOI: 10.3303/CET2188168
5. Levickaya, K., Alfimova, N., Nikulin, I., Kozhukhova, N., Buryanov, A. The Use of Phosphogypsum as a Source of Raw Materials for Gypsum-Based Materials. Resources. 2024. 13(5). Article no. 69. DOI: 10.3390/resources13050069
6. Gordina, A.F., Gumenyuk, A.N., Polyanskikh, I.S., Zaripova, R.I. Carbon-Containing Modifier for Fluoranhydrite Binder. Nanotechnologies in Construction. 2022. 14(5). Pp. 381–391. DOI: 10.15828/2075-8545-2022-14-5-381-391
7. Ponomarenko, A.A. Technogenic anhydrite binder for high-strength concrete. Magazine of Civil Engineering. 2021. 107(7). Article no. 10701. DOI: 10.34910/MCE.107.1
8. Alfimova, N.I., Pirieva, S.Yu., Elistratkin, M.Yu., Kozhuhova, N.I., Titenko, A.A. Production methods of binders containing gypsum-bearing wastes: a review. Bulletin of BSTU named after V.G. Shukhov. 2020. 5(11). Pp. 8–23. DOI: 10.34031/2071-7318-2020-5-11-8-23
9. Fedorchuk, Y.M., Tsygankova, T.S. Design methods to reduce the impact of hydrofluoric acid production on the environment. International Journal of Experimental Education. 2014. 1–1. P. 111.
10. Budnikov, P.P., Zorin, S.P. Anhydritovyj Tsement [Anhydrite cement]. Moscow: Promstroyizdat, 1954. 92 p.
11. Yao, G., Cui, T., Jia, Z., Sun, S., Anning, C., Qiu, J., Lyu, X. Effect of Anhydrite on Hydration Properties of Mechanically Activated Muscovite in the Presence of Calcium Oxide. Applied Clay Science. 2020. 196. Article no. 105742. DOI: 10.1016/j.clay.2020.105742
12. Podgorny, D.S., Elistratkin, M.Y., Bondarenko, D.O., Strokova, V.V. Increasing the Radioshielding Properties of Construction Materials in the Microwave Range. Nanotechnologies in Construction. 2024. 16(2). Pp. 100–108. DOI: 10.15828/2075-8545-2024-16-2-100-108
13. Abdullah, A., Mazelan, N., Tadza, M.Y.M., Rahman R.A. The Use of Gypsum and Waste Gypsum for Electrical Grounding Backfill. Lecture Notes in Electrical Engineering. 2021. 666. Pp. 1213–1226. DOI: 10.1007/978-981-15-5281-6_86
14. Zhang, S., Ukrainczyk, N., Zaoui, A., Koenders, E. Electrical Conductivity of Geopolymer-Graphite Composites: Percolation, Mesostructure and Analytical Modeling. Construction and Building Materials. 2024. 411. Article no. 134536. DOI: 10.1016/j.conbuildmat.2023.134536

15. López, F.A., Gázquez, M., Alguacil, F.J., Bolívar, J.P., García-Díaz, I., López-Coto, I. Microencapsulation of Phosphogypsum into a Sulfur Polymer Matrix: Physico-Chemical and Radiological Characterization. Journal of Hazardous Materials. 2011. 192(1). Pp. 234–245. DOI: 10.1016/j.jhazmat.2011.05.010
16. Makul, N. Advanced smart concrete – A review of current progress, benefits and challenges. Journal of Cleaner Production. 2020. 274. Article no. 122899. DOI: 10.1016/j.jclepro.2020.122899
17. Mobili, A., Giosuè, C., Bellezze, T., Revel, G.M., Tittarelli, F. Gasification Char and Used Foundry Sand as Alternative Fillers to Graphene Nanoplatelets for Electrically Conductive Mortars with and without Virgin/Recycled Carbon Fibres. Applied Sciences. 2021. 11(1). Article no. 50. DOI: 10.3390/app11010050
18. Jun, H.-M., Seo, D.-J., Lim, D.-Y., Park, J.-G., Heo, G.-H. Effect of Carbon and Steel Fibers on the Strength Properties and Electrical Conductivity of Fiber-Reinforced Cement Mortar. Applied Sciences. 2023. 13(6). Article no. 3522. DOI: 10.3390/app13063522
19. García-Macíasa, E., Castro-Triguero, R., Ubertini, F. 3D mixed micromechanics-FEM modeling of piezoresistive carbon nanotube smart concrete. Computer Methods in Applied Mechanics and Engineering. 2018. 340. Pp. 396–423. DOI: 10.1016/j.cma.2018.05.037
20. Gordon, A.M., Barrio, M.I.P., Escamilla, A.C. Unveiling the performance of graphene nanofiber additives in gypsum plasters: A solid vs liquid perspective. Journal of Building Engineering. 2024. 87. Article no. 109061. DOI: 10.1016/j.jobe.2024.109061
21. García-Macías, E., D'Alessandro, A., Castro-Triguero, R., Pérez-Mira, D., Ubertini, F. Micromechanics modeling of the electrical conductivity of carbon nanotube cement-matrix composites. Composites Part B: Engineering. 2017. 108. Pp. 451–469. DOI: 10.1016/j.compositesb.2016.10.025
22. Fedorov, V.P. Study of corrosion of reinforcement in gypsum concrete based on high-strength gypsum and methods of its protection: Abstract of thesis for the degree of candidate of technical sciences. Kharkov Engineer-Builder Institute. Kharkov, 1968. 484 p.
23. Kornilova, T.M., Gushcha, E.V., Orehvo, N.K. Corrosion of steel in gypsum concrete. FKS XX: collection of scientific articles. Grodno: Grodno State University, 2012.
24. Tian, Z., Ye, H. Mechanisms underlying the relationship between electrical resistivity and corrosion rate of steel in mortars. Cement and Concrete Research. 2022. 159. Article no. 106867. DOI: 10.1016/j.cemconres.2022.106867
25. Bolzoni, F., Brenna, A., Ormellese, M. Recent advances in the use of inhibitors to prevent chloride-induced corrosion in reinforced concrete. Cement and Concrete Research. 2022. 154. Article no. 106719. DOI: 10.1016/j.cemconres.2022.106719
26. Aguirre-Guerrero, A.M., Robayo-Salazar, R.A., Mejía de Gutiérrez, R. Corrosion resistance of alkali-activated binary reinforced concrete based on natural volcanic pozzolan exposed to chlorides. Journal of Building Engineering. 2021. 33. Article no. 101593. DOI: 10.1016/j.jobe.2020.101593
27. Pan, T., Nguyen, T.A. Shi, X. Assessment of Electrical Injection of Corrosion Inhibitor for Corrosion Protection of Reinforced Concrete. Transportation Research Record. 2008. 2044(1). Pp. 51–60. DOI: 10.3141/2044-06
28. Tuutti, K. Corrosion of steel in concrete. Doctoral Thesis (monograph). Division of Building Material. Swedish Cement and Concrete Research Institute. Stockholm, 1982. 473. p.
29. Dehghanpour, H., Yilmaz, K., Ipek, M. Evaluation of recycled nano carbon black and waste erosion wires in electrically conductive concretes. Construction and Building Materials. 2019. 221. Pp. 109–121. DOI: 10.1016/j.conbuildmat.2019.06.025
30. Liu, X., Qu, M., Nguyen, A.P.T., Dilley, N.R., Yazawa, K. Characteristics of new cement-based thermoelectric composites for low-temperature applications. Construction and Building Materials. 2021. 304. Article no. 124635. DOI: 10.1016/j.conbuildmat.2021.124635
31. Lee, H., Park, S., Kim, D., Chung, W., Heating Performance of Cementitious Composites with Carbon-Based Nanomaterials. 2022. 12. Article no. 716. DOI: 10.3390/cryst12050716
32. Lopanov, A.N., Fanina, E.A., Nesterova, N.V. Differential-Scanning Calorimetry of Graphite and Activated Carbon in Argon. Solid Fuel Chemistry. 2021. 55(2). Pp. 105–109. DOI: 10.3103/S0361521921020051
33. Dudin, M.O., Vatin, N.I., Barabanshchikov, Y.G. Modeling a set of concrete strength in the program ELCUT at warming of monolithic structures by wire. Magazine of Civil Engineering. 2015. 54(2). Pp. 33–45. DOI: 10.5862/MCE.54.4
34. Cherkasova, T.G., Cherkasova, E.V., Tikhomirova, A.V., Gilyazidinova, N.V., Gilyazidinova, N.V., Klyuev, R.V., Karlina, A.I., Skiba, V.Y. Study of Matrix and Rare Elements in Ash and Slag Waste of a Thermal Power Plant Concerning the Possibility of their Extraction. Metallurgist. 2022. 65(11–12). Pp. 1324–1330. DOI: 10.1007/s11015-022-01278-2
35. Rassokhin, A., Ponomarev, A., Shambina, S., Karlina, A. Different types of basalt fibers for disperse reinforcing of fine-grained concrete. Magazine of Civil Engineering. 2022. 109(1). Article no. 10913. DOI: 10.34910/MCE.109.13
36. Bosikov, I.I., Klyuev, R.V., Revazov, V.Ch., Martyushev, N.V. Analysis and evaluation of prospects for high-quality quartz resources in the North Caucasus. Mining Science and Technology (Russia). 2023. 8(4). Pp. 278–289. DOI: 10.17073/2500-0632-2023-10-165
37. Kondratiev, V.V., Karlina, A.I., Guseva, E.A., Konstantinova, M.V., Gorovoy, V.O. Structure of Enriched Ultradisperse Wastes of Silicon Production and Concretes Modified by them. IOP Conference Series: Materials Science and Engineering. 2018. 463(4). Article no. 042064. DOI: 10.1088/1757-899X/463/4/042064
38. Usmanov, R., Mrdak, I., Vatin, N., Murgul, V. Reinforced Soil Beds on Weak Soils. Applied Mechanics and Materials. 2014. 633–634. Pp. 932–935. DOI: 10.4028/www.scientific.net/AMM.633-634.932
39. Wang, X., Wu, Y., Zhu, P., Ning, T. Snow Melting Performance of Graphene Composite Conductive Concrete in Severe Cold Environment. Materials. 2021. 14. Article no. 6715. DOI: 10.3390/ma14216715
40. Farcas, C., Galao, O., Navarro, R., Zornoza, E., Baeza, F.J., Del Moral, B., Pla, R., Garcés, P. Heating and de-icing function in conductive concrete and cement paste with the hybrid addition of carbon nanotubes and graphite products. Smart Materials and Structures. 2021. DOI: 30. Article no. 045010. 10.1088/1361-665X/abe032
41. Kondrat'ev, V.V., Ershov, V.A., Shakhrai, S.G., Ivanov, N.A., Karlina, A.I. Formation and Utilization of Nanostructures Based on Carbon During Primary Aluminum Production. Metallurgist. 2016. 60(7–8). Pp. 877–882. DOI: 10.1007/s11015-016-0380-x
42. Yelemessov, K., Sabirova, L.B., Martyushev, N.V., Malozyomov, B.V., Bakhmagambetova, G.B., Atanova, O.V. Modeling and Model Verification of the Stress-Strain State of Reinforced Polymer Concrete. Materials. 2023. 16(9). Article no. 3494. DOI: 10.3390/ma16093494

43. Amran, M., Onaizi, A.M., Fediuk, R., Vatin N.I., Rashid, R.S.M., Abdelgader, H., Ozbakkaloglu, T. Self-Healing Concrete as a Prospective Construction Material: A Review. Materials. 2022. 15(9). Article no. 3214. DOI: 10.3390/ma15093214

Information about the authors:

***Aleksandr Gumeniuk**, PhD in Technical Sciences*
ORCID: https://orcid.org/0000-0002-2880-8103
E-mail: aleksandrgumenyuk2017@yandex.ru

***Anastasiia Gordina**, PhD in Technical Sciences*
ORCID: https://orcid.org/0000-0001-8118-8866
E-mail: gism56@mail.ru

***Semyon Petrynin**,*
ORCID: https://orcid.org/0009-0009-8950-2907
E-mail: petryninofficial@yandex.ru

***Aleksandr Buryanov**, Doctor of Technical Sciences*
ORCID: https://orcid.org/0000-0002-3331-9443
E-mail: rga-service@mail.ru

***Vadim Skeeba**, PhD in Technical Sciences*
ORCID: https://orcid.org/0000-0002-8242-2295
E-mail: skeeba_vadim@mail.ru

Received 11.07.2024. Approved after reviewing 25.12.2024. Accepted 13.01.2025.

Magazine of Civil Engineering. 2025. 18(1). Article No. 13303

Magazine of Civil Engineering

ISSN
2712-8172

journal homepage: http://engstroy.spbstu.ru/

Research article

UDC 624.03

DOI: 10.34910/MCE.133.3

Dynamic behavior of a reinforced concrete slab of a pedestrian bridge with stiff rebars

A.V. Alekseytsev[1] ✉ ***, K.V. Kvocak***[2] ***, D.S. Popov***[1] ***, M. Al Ali***[2]

[1] Moscow State University of Civil Engineering (National Research University), Moscow, Russian Federation

[2] Technical University in Košice, Košice, Slovak Republic

✉ *aalexw@mail.ru*

Keywords: dynamics, rigid reinforcement, accidental failure, numerical modelling, reinforced concrete slabs, mechanical impact

Abstract. Evaluation of the ultimate bearing capacity of a reinforced concrete slab of a pedestrian bridge with stiff rebars is a relevant issue investigated in the article. Dynamic analysis takes account of low velocities of dynamic loading. A 3D model of a structure is made. A stiff rebar is a U-shaped perforated profile welded to the plate. The focus of the computation methodology is the model verification. Towards this end, mechanical characteristics of materials are experimentally identified; full-size specimens are made and subjected to static load testing. The numerical study focuses on analyzing two sessions of loading by an impactor located in the center of a span. The impactor has symmetrical and nonsymmetrical impact spots. Dynamic loading is proposed to be simulated in several stages. At the final stage, the structure vibrates together with the impactor. The Menétrey–Willam model is chosen to describe the deformation of concrete; the stress-strain state of the structure and stiff rebars is described by a curvilinear diagram that conveys strengthening and shows the actual behavior of the rebars. An implicit integration scheme is employed to identify detailed dependences showing the time-dependent change in the stress-strain state components affecting structural safety. The conclusion is that nonsymmetrical loading is the most substantial dynamic effect, and stiff rebars can greatly increase the survivability of the system subjected to impacts of man-induced origin.

Citation: Alekseytsev, A.V., Kvocak, K.V., Popov, D.S., Al Ali, M. Dynamic behavior of a reinforced concrete slab of a pedestrian bridge with stiff rebars. Magazine of Civil Engineering. 2025. 18(1). Article no. 13303. DOI: 10.34910/MCE.133.3

1. *Introduction*

The present-day socio-economic environment triggers the need to design structures of infrastructure, including elements of engineering structures featuring higher mechanical safety. Safety assurance is vital if a structure is subjected to various man-induced effects such as mechanical impacts, explosions, fires, etc. Concrete, reinforced concrete, steel fiber reinforced concrete and other composite structures are often subjected to such effects [1–5]. The dynamic behavior of load-bearing structures is investigated as a function of the rate of application of dynamic load. In some cases when the dynamics of low velocities is addressed [6, 7], the load is represented as pulses of various forms varying in time. If high velocity dynamics is considered [8–10], dynamic load is applied explicitly, and explicit solvers are used to make the finite element analysis of the problem. The von Mises stress is the fracture criterion for elements made of structural steel; principal stresses, calculated using well-known models of Menétrey–Willam, Drucker–Prager, etc., are the fracture criteria for concrete.

Bridges and bridge structures, subjected to mechanical impacts, are investigated. A computational tool, designed for low-speed dynamics, is employed to analyze various impacts, including those impacts that are triggered by the movement of high-speed trains [11], collisions with heavy machinery [12], impact interaction with ships and barges [13, 14], as well as impacts from rock falling on bridges in mountainous areas [15, 16]. Pedestrian bridges and their structural components can also be subjected to similar impacts. Impacts from a falling body can be effectively analyzed using technologies developed for modeling emergency effects on buildings and structures. First of all, these are the approaches related to elements of pull-down analysis [17–22] and methods of direct integration using implicit integration schemes [23–25].

In most cases, an increase in the safety of structures subjected to dynamic loading means an increase in the consumption of materials or a higher damping capacity of a system. Relevant analytical studies show that such an effect can be achieved by the targeted regulation of natural vibration frequencies of a structure that requires special connections or a change in the stiffness of individual elements of a system [26, 27]. However, such approaches are implemented only for the simplest beam systems made of isotropic materials. Therefore, numerical simulation is the main tool for analyzing the rationality of design solutions.

The modeling of loads, reproducing dynamic impacts on a structure, is also an important and relevant problem [28–32]. When low impact velocities are considered, two techniques can be used: the first one is pulse loading and the second one is a combination of the lumped mass attached to a GAP element, in which the gap value determines the height of the load fall for the case where free falling has gravitational acceleration.

Damping is the key determinant of dynamic analysis results. Dynamic analysis can encompass physical attenuation models and numerical damping used to stabilize the iterative process of computations. Physical attenuation models encompass a well-known Rayleigh scheme, in which a stiffness matrix is used to take into account internal friction forces, and a mass matrix is used to take into account resistance of the medium. The V.N. Sidorov model [33] and the Kelvin–Voigt model are no less effective.

This paper addresses numerical modeling of a pedestrian bridge slab subjected to symmetrical and nonsymmetrical dynamic effects. Pulse load is described by the shape of a complex polygon, reproducing the transfer of kinetic energy of an impactor and subsequent joint oscillation of the system. The ultimate dynamic load is determined. The danger of symmetrical and nonsymmetrical dynamic effects, the nature of fracture, and the ability of stiff reinforcement to take load are identified.

The objective of the work is to evaluate the mechanical safety of slabs used for pedestrian bridge spans under dynamic effects. In order to achieve this goal, the following main tasks were solved:

- creation of the structural solution with the use of rigid reinforcement for the slab structure in the form of metal profiles (stiff rebars);
- experimental study of the slab with stiff rebars, during which the mechanical properties of the materials and the ultimate loads were determined, allowing the design model to be verified;
- numerical modelling of the deformations of the structure under symmetrical and asymmetrical dynamic actions, using the characteristics of the materials and the dimensions of the experimental specimens.

2. Methods and Materials

2.1. Subject of Research and Problem Statement

The purpose of the study is to evaluate the stress-strain state and ultimate load for pedestrian bridge slabs with stiff rebars in the case of dynamic loading. The following research program was implemented to achieve this purpose:

- production of a pedestrian bridge slab and experimental determination of the ultimate static load;
- verification of the finite element model of the subject of research under static loading;
- development of a numerical model of a structure under dynamic loading and its analysis.

The study focuses on the deformation of a slab subjected to symmetrical and nonsymmetrical dynamic loading that can trigger its ultimate state.

The subject of the study is a steel reinforced concrete slab of a pedestrian bridge with a metal profile installed in the tensile zone (Fig. 1a, b). The length of the slab is 6000 mm (the distance between the bridge supports is 5800 mm); the bridge width is 900 mm; the bridge height is 270 mm. The slab has conventional and stiff rebars; they are two steel metal profiles, each has two parts. The bottom part is a solid metal sheet; its thickness is 9.2 mm, and the top part is 8.0 mm thick. It is U-shaped (rotated through an angle of 180 degrees). The lateral surface of profiles has openings with a diameter of 50 mm; they are spaced at intervals of 100 mm. The top and bottom zones of the slab have structural rebars with a diameter of 14 mm.

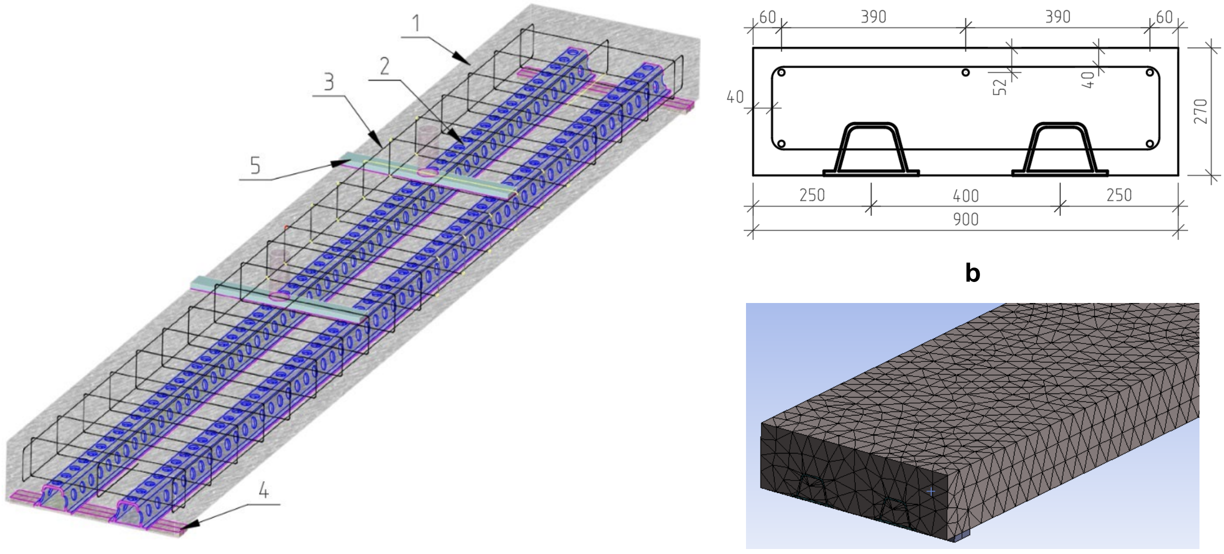

b

a

c

Figure 1. The subject of the study: (a) general view of a pedestrian slab: 1 – concrete, 2 – stiff rebars; 3 – flexible structural rebars, 4 – structure of supports, 5 – point of load transfer; (b) standard cross-section of the slab; (c) finite element model of a slab.

2.2. Numerical Model of the Structure

2.2.1. Description of the finite element model

Ansys software package was used for numerical modeling purposes. Decomposition of the solid body, describing concrete for this model, involves some difficulty due to the presence of stiff rebars in the slab. Attempts to generate a good quality element mesh, using only rectangular 8-node finite elements, were not successful. Therefore, the mesh was generated automatically (Fig. 1c). The size of the finite element was 50 mm. Modeling of stiff rebars and concrete was performed using Solid 186 (20-node finite element) and Solid 187 (10-node tetrahedral finite element).

2.2.2. Models of materials

The behavior of concrete was described using the Menétrey–Willam model [34]. As a rule, the Menétrey–Willam model is better at modeling the behavior of binding aggregates, such as concrete than, for example, the Drucker–Prager model without supplementary modifications [35, 36]. This model is based on the theory of plastic flow.

The model of concrete has three main components:

1. A three-invariant limit surface f_{MW} (Fig. 2), described by equation (1), where s_2 and s_3 are the equation parameters, controlling the shape of the meridional cross-section of the surface and determined from yield strengths in uniaxial tension $\left(R_t\right)$, compression $\left(R_c\right)$ and biaxial compression $\left(R_b\right)$ [37, 38]. The limit surface conveys the strength condition of the material in the Haig–Westergaard principal stress space. This surface has a single singularity point located at the vertex, in the neighborhood of triaxial tension.

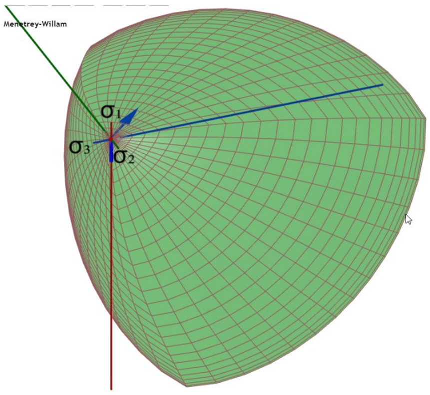

$$f_{MW} = \frac{c_2}{c_3}\left[\sqrt{2\xi} + rp\right] + p^2 - {}^{1}\!/_{c_3}; \tag{1}$$

$$Q_{MW} = \rho^2 + B_g p + C_g \xi; \tag{2}$$

$$B_g = \frac{2\cdot\left(\sqrt{2}\cdot\tan\left(\Psi_b\right)\cdot R_b - R_{bt}\right)}{\sqrt{3}\left(1/\sqrt{2} - \tan\left(\Psi_b\right)\right)}; \tag{3}$$

$$C_g = \frac{B_g}{\sqrt{2}} + 2\cdot\frac{R_{bt}}{\sqrt{3}}. \tag{4}$$

Figure 2. Limit surface of the Menétrey–Willam model and basic expressions used to describe it.

2. Plastic potential surface [35], responsible for the direction of the vector of plastic deformations, described by equations (2)–(4), where Ψ_b is the dilatation angle of concrete in uniaxial compression, which is the quotient of the tensor norm of plastic 3D deformations divided by the deviator norm of plastic deformations; B_g and C_g are parameters characterizing the plastic potential. Values of the dilatation angle, depending on the class of concrete, can be taken from Table 1 [37].

Table 1. Dependence of the dilatation angle on the class of concrete.

Concrete class	B15	B20	B25	B30	B35	B40	B45	B50
ψ_b	4.59	5.68	6.62	7.42	8.24	9.17	9.98	11.13

3. Laws of the limit surface evolution, responsible for strengthening and softening of the material. The model separately conveys evolution laws for compression (see Fig. 3a) and tension (see Fig. 3b).

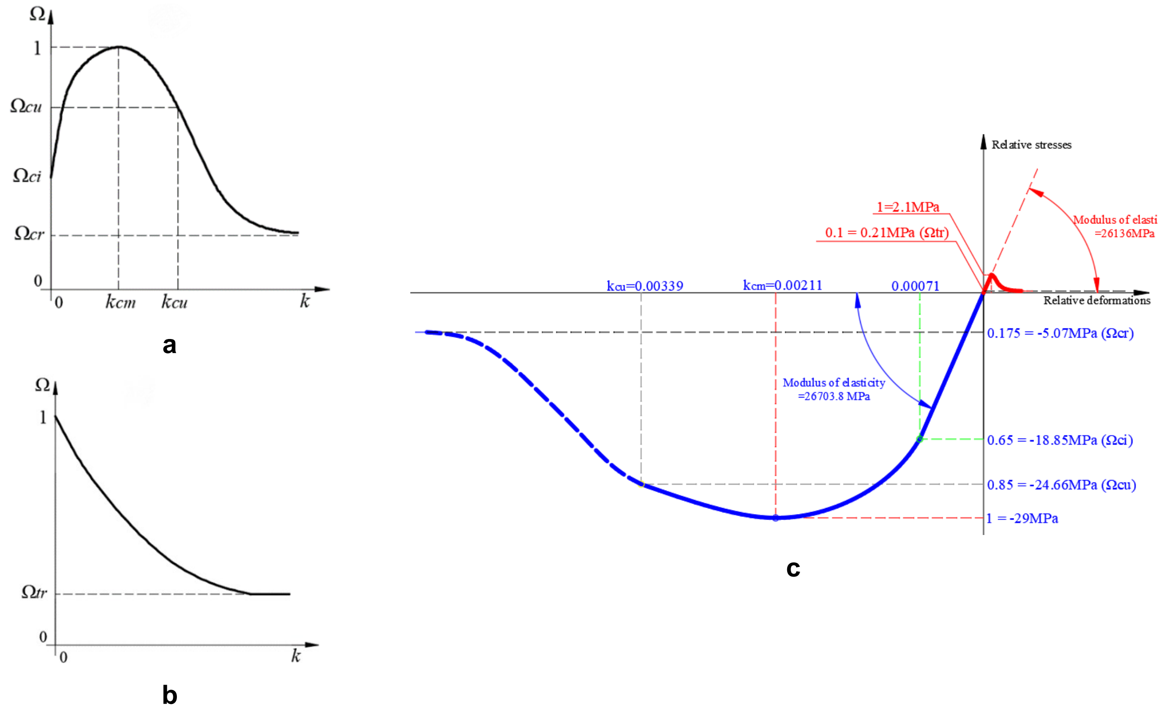

a

b

c

Figure 3. Absolute and relative stress-strain curves.

Exponential softening in compression and tension is used to describe the behavior of concrete in the process of softening. Values of standard stresses and plastic strains at characteristic points are employed for this purpose. Elastic strains, obtained for relative stress $\Omega = 0.65$, are subtracted from total strains, obtained for relative stresses $\Omega = 1.0$ and $\Omega = 0.85$. These elastic strains can be computed according to recommendations provided in applicable regulations, such as Construction Regulations 63.13330.2018. Fig. 3c shows the concrete diagram used in the analysis of a pedestrian bridge slab.

Concrete fracture was taken into account in the analysis. Fracture energy G_F is the parameter characterizing the softening of material under tension [39]. This parameter conveys the amount of energy that must be transmitted to the material to stop the transmission of stresses between the crack edges (to completely break the atomic bonds). Graphically, this value corresponds to the Gft area in Fig. 4. The deformation of stiff rebars was described by a multilinear dependence accompanied by hardening (Fig. 5). Values of strains in the diagrams, conveying the behavior of steel and concrete, are assumed to be plastic in Ansys. The elastic behavior is identified using the value of the modulus of elasticity.

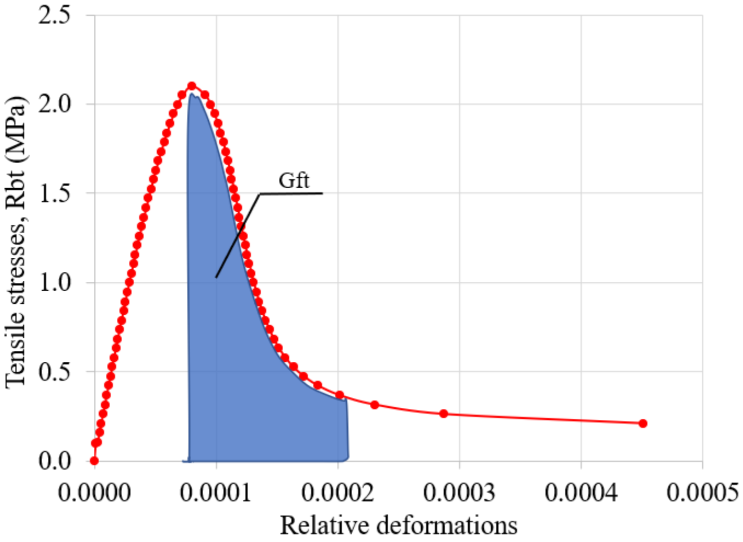

Figure 4. Fracture energy G_F and the tensile curve of concrete.

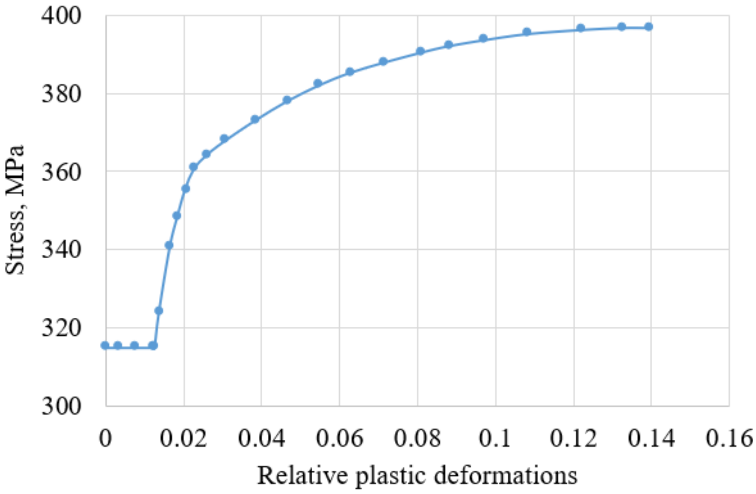

Figure 5. Multilinear diagram of stiff rebar deformation.

Strength characteristics of concrete and steel, used in the numerical computation, were identified in the course of an experimental study [40]. Structural slab reinforcement, made using individual (flexible) bars, was simulated by discrete 3D finite elements REINF264. Hence, there was no need to decompose the finite element mesh in such a way that rebar elements were connected to nodes of 3D elements (simulating concrete). Therefore, a better mesh can be obtained for the models [41, 42]. The behavior of conventional reinforcement steel is described by the bilinear relationship at the yield strength of 400 MPa.

2.2.3. Slab loading and support constraints

The bridge slab model was calculated for the case of the load application to two different zones (Fig. 6), which correspond to the most dangerous points of loading.

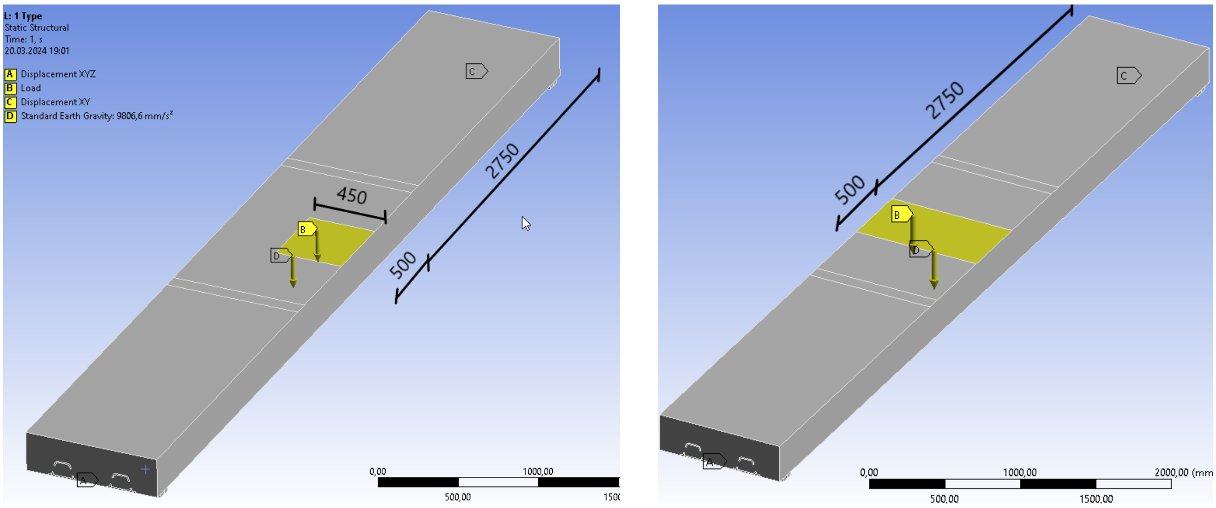

a b

Figure 6. Nonsymmetrical (a) and symmetrical (b) floor slab loading.

The general idea of dynamic load application (Fig. 7a) is as follows:

- application of dead load and stabilization of vibrations (the first stage);
- pulse load increase that simulates the accelerated fall of bodies on the bridge; free fall or other man-induced impact (the second stage);
- maximum pulse value for some period of time (the third stage);
- drop in the pulse load and vibration of the structure together with the impactor (the fourth stage).

Without considering the details of the impact load computation, the maximum value of the pulse load was determined as 90 % of the ultimate value under static loading (determined in the first computation step).

In terms of time, the load was applied to the floor slab in four stages (Fig. 12). Fig. 12 shows the coefficients, by which the load constant is multiplied, meaning that the maximum value of the load is equal to unity in the graph.

The first stage, or the application of dead load, takes 0.5 sec; the second stage, or an increase in dynamic load, takes 0.2 sec; the third stage, or the stabilization of load at the peak value, takes 0.5 sec; the fourth stage, or a reduction in dynamic load to 10 % of the peak value, takes 0.2 sec.

Support components are simulated by separate elements, which are in turn decomposed into two parts: a panel and a line. The panel is hinge-fixed to the slab, and line A has a sliding hinge connection to the panel (Fig. 7b). This way of modeling the boundary conditions better conveys the realistic behavior of supports connected to the slab. It does not trigger any supplementary forces in the support zone and allows for the rotation, preventing the support bending moment.

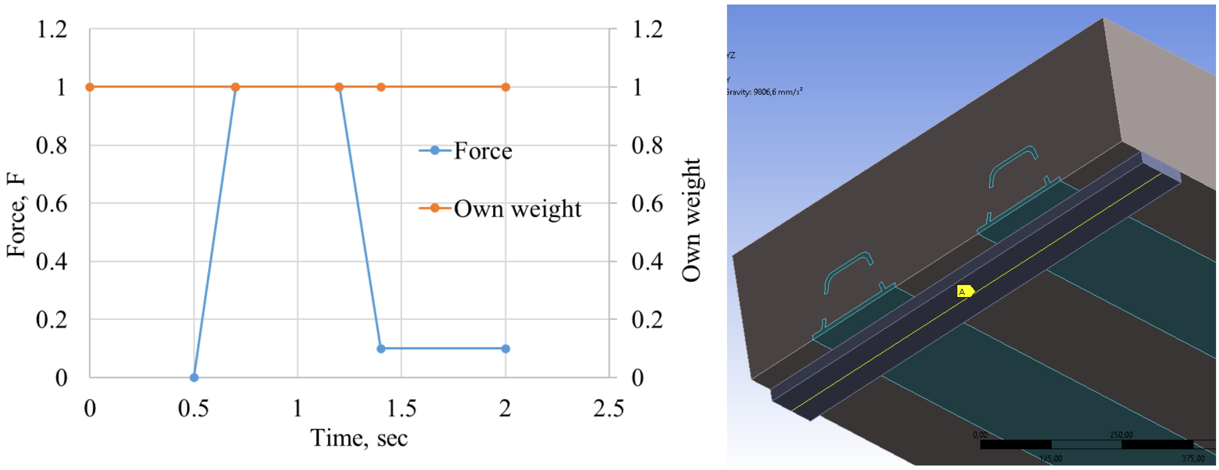

a b

Figure 7. Loading history (a); slab support (b).

2.2.4. Description of the finite element solver

Initially, computations are performed in the Ansys Static Structural module to evaluate the load-bearing capacity of the slab under static loading. At the second stage, modal analysis (Modal analysis module) is performed to find natural frequencies of vibration required to determine the damping properties of the system. At the final stage needed to solve the problem of structural dynamics, the computation is performed in the Transient Structural module, which is based on implicit schemes of integration of the equation of motion, taking into account inertial and damping forces. An important positive property of the Transient Structural module is that this module can be used together with the Static Structural model, meaning that the geometry and all parameters of the material (concrete, rebars, concrete reinforcement, etc.) can be used in computations without changes, except for setting the parameters of dynamic analysis.

The equation of motion used to analyze the dynamic response of structures [34]:

$$F(t) = [M]\{u\}'' + [C]\{u\}' + [K]\{u\}, \tag{1}$$

where $[M]$ is the mass matrix; $[C]$ is the damping matrix; $[K]$ is the stiffness matrix; $F(t)$ is the load; $\{u\}''$ is the nodal acceleration vector; $\{u\}'$ is the nodal velocity vector; $\{u\}$ is the node displacement vector.

At any point in time, these equations can be represented as a set of "static" equilibrium equations that also take into account forces of inertia $[M]\{u\}'$) and forces of damping $\left([C]\{u\}'\right)$. The Transient Structural module uses the Newmark time integration method to solve equations at discrete points in time. Damping is one of the main computation parameters for dynamic loading. Two types of damping, numerical and physical damping, are available in the Ansys software package.

Numerical (artificial) damping is necessary to stabilize problem solving. There are several types of settings for the Newmark α and β parameter method that use the same system of equations:

$$\delta = \frac{1}{2} + \gamma;\ \alpha = \frac{1}{4}(1+\gamma)^2, \tag{2}$$

where γ is the value of numerical damping.

The value of numerical damping is constant depending on the selected type of solver setting, namely: Impact $-\gamma = 0$; High speed dynamics $-\gamma = 0.005$; Moderate speed dynamics $-\gamma = 0.1$; Low speed dynamics $-\gamma = 0.414$.

Rayleigh constants α and β were used to take into account physical damping. These constants, multiplied by the mass matrix $[M]$ and the stiffness matrix $[K]$, are used to compute the damping matrix $[C]$:

$$[C] = \alpha[M] + \beta[K]. \tag{3}$$

In Ansys, two approaches, including "Direct input" and "Damping vs Frequency", can be used to take into account physical damping. In the first approach, Rayleigh alpha and beta coefficients are input directly, meaning that they have specific values. In this computation, the second approach is used, where the natural frequency of vibration (ω) is applied; the damping coefficient (ξ) equals 0.05 for reinforced concrete; the alpha coefficient equals zero (given that the external environment has no effect), and the beta coefficient is automatically determined in the solver using the formula:

$$\beta = \frac{2\xi}{\omega}. \tag{4}$$

The frequency of natural vibrations of the bridge slab was determined in the module "Modal analysis", and it equals 14.3 Hz.

2.3. Experimental Verification of the Numerical Model of the Structure

Computations were made to verify the results obtained using the numerical model. The conditions and characteristics of these computations corresponded to the experimental tests described in detail in [40]. The computation model had the following characteristics of materials obtained during the test: cylinder strength of concrete – 32.17 MPa; yield strength and ultimate tensile strength of stiff steel rebars – 315 MPa and 396 MPa, respectively; yield strength of flexible rebars – 355 MPa.

Fig. 8 shows the graphical dependence between slab deflection and load in the experimental specimen and numerical model.

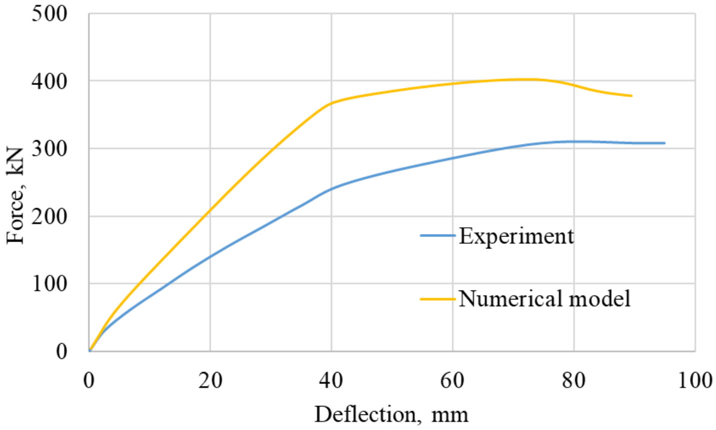

Figure 8. Dependence between deflection and load in experimental and numerical models.

The comparative analysis of (1) load-deflection dependencies for experimental specimens and (2) the results of numerical computation are in good agreement. The discrepancy between deflection values is 3 %; the discrepancy between values of the fracture force does not exceed 24 %. It confirms the proper modeling of strength and stiffness characteristics of materials, types of finite elements, boundary conditions, models simulating the behavior of concrete and rebars, and, as a result, it allows for reliable numerical studies of these models by changing the type and area of application of loads. The general view of experimental specimens and the course of the experiment is shown in Fig. 9.

a **b**

c d

Figure 9. Experimental testing of the pedestrian bridge slab: general view of the testing bench (a), load application scheme (b), reinforcement frame (c), testing the cube and cylinder strength of concrete specimens (d).

The compressive strength of the concrete specimens (Fig. 9d) and the tensile strength of the rebars were experimentally determined earlier. Then pedestrian slab specimens were fabricated. Their reinforcement scheme is shown in Fig. 9c. Slab specimens were mounted on a steel frame (Fig. 9a) and subjected to ultimate static loading using two power generation units (Fig. 9b). Experimentally determined mechanical characteristics of materials and average measured values of 3D dimensions of the specimen were used in the computations.

3. *Results and Discussion*

The ultimate load and deflections under symmetrical and nonsymmetrical loading are determined from the results of numerical computations of models subjected to static and dynamic loading. Under nonsymmetrical loading, the maximum static ultimate load and deflection values are 318.3 kN and 55.8 mm; under dynamic loading, they equal 345.2 kN and 53.41 mm. Under symmetrical loading, the maximum static ultimate load and deflection values are 291.1 kN and 52.1 mm; under dynamic loading – 331.7 kN and 42.8 mm.

Figs. 10a, 10b show the ultimate static load under symmetrical and nonsymmetrical loading. Figs. 10c, 10d show a time change in deflection (f-c) and actual load (N-c). On average, the ultimate value of deflection under nonsymmetrical loading was 30 % higher than under symmetrical loading, and the discrepancy between values of ultimate dynamic load did not exceed 10 %, which translates into a greater danger of nonsymmetrical emergency effects for such structures.

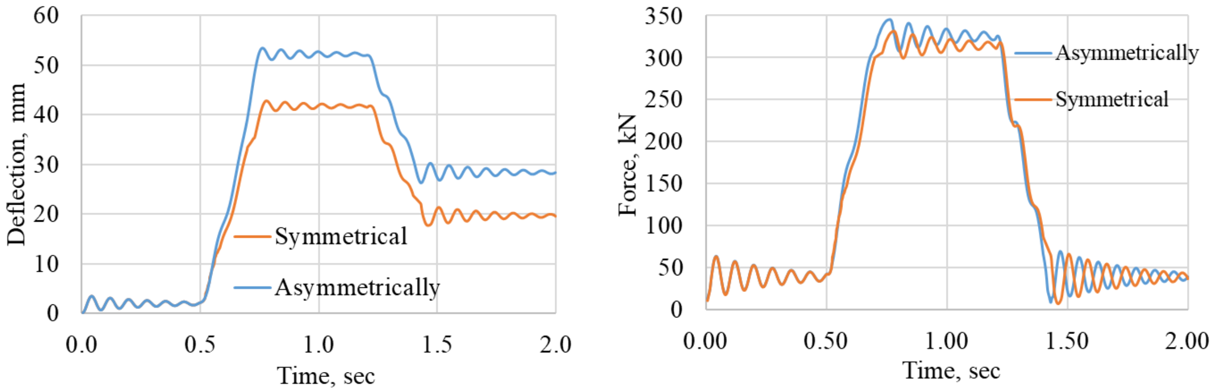

a b

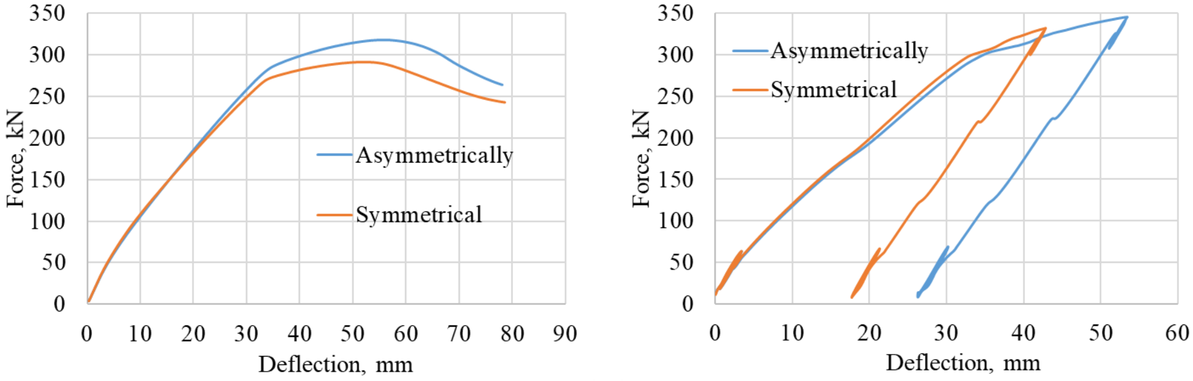

c d

Figure 10. Time change in deflection (a) and load (b);
N-f dependence under static (c) and dynamic (d) loading.

Fig. 11 shows the value of stresses arising in concrete and stiff rebars in the middle of the slab span for a standard cross-section under maximum dynamic loading. For nonsymmetrical loading, stress is 1.28 times the cylinder strength, which can be interpreted as the onset of concrete fracture in the top zone of the slab. For symmetrical loading, stresses do not exceed the cylinder strength. However for symmetrical loading, the bottom part of both stiff rebars, capable of resisting loads, is subjected to great plastic deformations, and is in the hardening zone with a bearing capacity margin of 13 % at the maximum resistance of 390 MPa. In case of nonsymmetrical loading, the behavior of the left stiff rod is elastic, while the right one has a 12 % safety margin for the maximum resistance. It confirms that dynamic nonsymmetrical loading is particularly dangerous in terms of the ultimate limit state of the structure. In addition to standard stresses, used for the preliminary evaluation of the stressed state of concrete and rebars, von Mises equivalent stresses in stiff rebars were computed, and the same about principal stresses $\sigma_1 - \sigma_3$ in concrete. The stress state of slab elements is the same as when only standard stresses are analyzed.

When the time change in standard stresses was analyzed according to Fig. 7a, the following characteristic states were considered:

- load in the course of normal operation (t = 0.5 c);
- an increase in dynamic loading up to the peak value (t = 0.7 c);
- maximum dynamic load (t = 1.2 c);
- the de-loading moment: the onset of vibrations together with the impactor (t = 1.4 c).

The distribution of stresses in the structure, corresponding to these moments in time, is shown in Fig. 12. The analysis of the figure shows that stresses in concrete do not stabilize at the moments of onset and termination of the peak dynamic load; on the contrary, they rise.

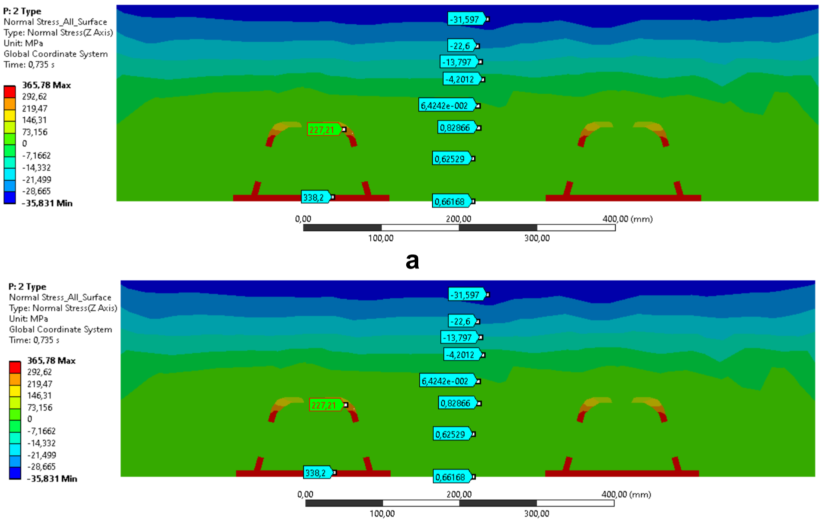

a

b

Figure 11. Stresses in the slab cross-section under symmetrical (a)
and nonsymmetrical loading (b).

Symmetrical loading

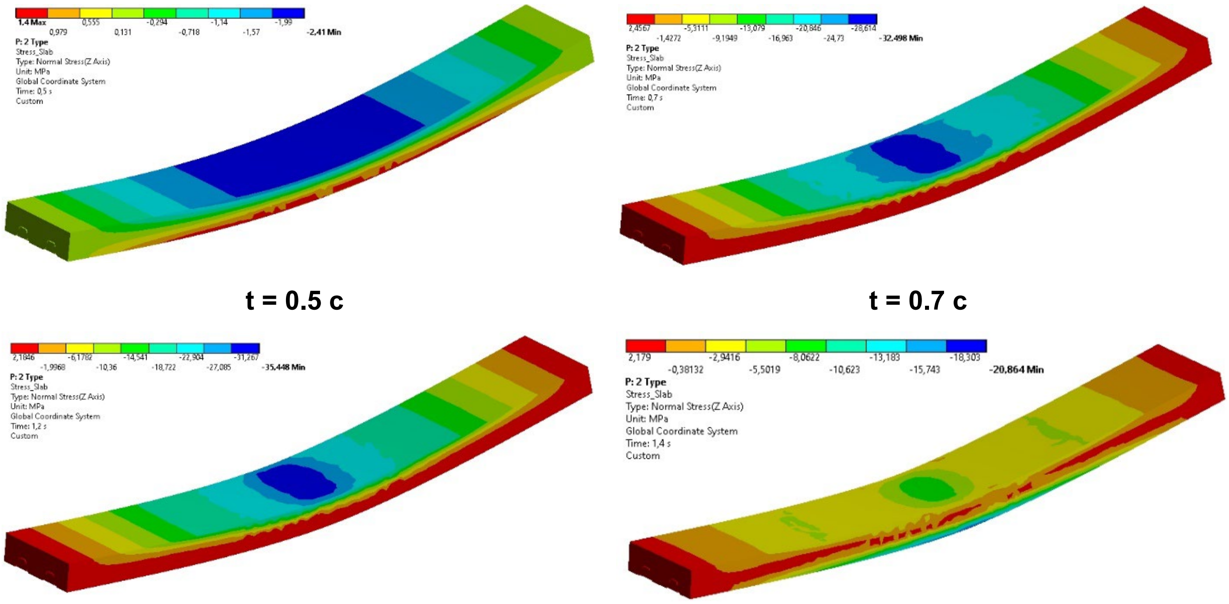

t = 0.5 c **t = 0.7 c**

t = 1.2 c **t = 1.4 c**

Unbalanced load

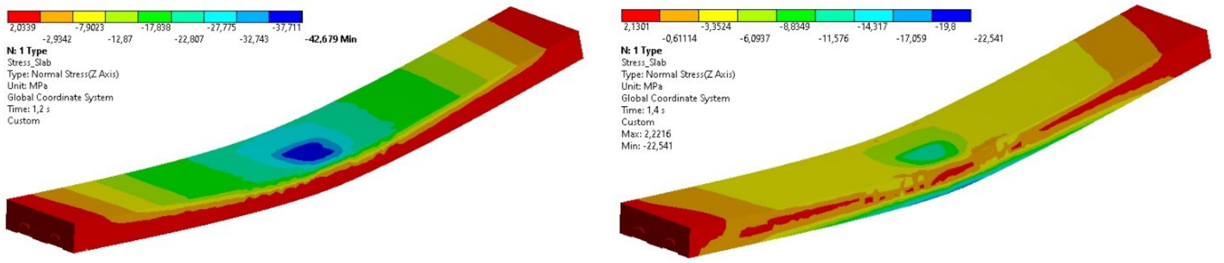

t = 1.2 c **t = 1.4 c**

Figure 12. Time change in stresses in the slab concrete.

This indicates the importance of taking into account the time of application of peak dynamic load: if applied for a period longer than 1.2 – 0.7 = 0.5 s, it may lead to the collapse of the structure. In addition, at the moment of de-loading, tensile stresses, essential for cracking, emerge in the middle of the slab. The bottom zone of the slab is compressed. As a result of the further analysis of joint vibrations, the concrete tensile zone extends to the top part of the slab in the neighborhood of the area of dynamic load application. Hence, a conclusion can be made that the collapse of this structure predominantly follows the concrete fracture pattern.

3.1. Discussion

The use of stiff rebars in bending reinforced concrete elements nearly prevents the complete emergency collapse of structures, meaning that an increase in structural survivability can be discussed. This property was verified by making additional computations of pre-set displacements under static loading. Following the loss of bond with concrete in the bottom zone, the behavior of stiff slab rebars becomes similar to that of a beam, and later it behaves as a cable-stayed mechanism. In this case, its bearing capacity is determined by the bearing capacity of the profile of stiff rebars. Indeed, the slab preserved its bearing capacity, even when it was loaded by pre-set displacements up to 30 cm. Local rules and regulations have a deflection-based criterion of survivability; it equals 1/30 of the span. In the case under consideration, 600/30 = 20 cm, but when the loading of the structure triggered a deflection of 30 cm, the load-bearing capacity of stiff rebars was far from exhaustion. This allows us to suggest expanding and clarifying the survivability criteria for structures with stiff rebars.

The initial value of the dynamic load, needed to identify its limit value, was taken as 90 % of the static load value, but according to the computation results, the maximum value exceeded the static value by 8,5 % under nonsymmetrical loading and by 14 % under symmetrical loading, which may be due to inertial effects and hardening of materials.

The conducted research has promising prospects for comparing the accuracy of concrete models in the simulation of bridge structures. For instance, instead of the model used in [39], the models described in [37, 38] could be applied. Of particular interest is the simulation of the bond between concrete and rigid reinforcement. For this, the assumptions from the review [36] could be used, with the criterion in this work being evaluated based on the cohesion stress in the area of the stiff rebars. Since the surface area of the profile in contact with the concrete is large, no loss of bond between the concrete and reinforcement was observed in the calculations considered. Future studies will explore other profile shapes described in the article [40].

4. Conclusion

1. A numerical modeling method is proposed to simulate the stress-strain state of slabs of pedestrian bridges with stiff rebars. This method encompasses the use of experimentally verified 3D finite element schemes that allow taking into account the actual behavior of these structures.
2. It is identified that nonsymmetrical emergency effects are most dangerous for slabs and lead to structural concrete failure in the area of dynamic loading.
3. Stiff rebars are proven to be highly efficient for the bending elements considered in this article. It is found that stiff rebars prevent the complete fracture of a structure; they can rise the structural resistance to mechanical damage and the general level of mechanical safety of structures.
4. The survivability margin of these reinforced concrete slabs with stiff rebars is up to 50 % in terms of deflection constraints regulated by domestic and foreign standards.

References

1. Mahmoud, K.A. Lateral Deformation Behavior of Eccentrically Loaded Slender RC Columns with Different Levels of Rotational End Restraint at Elevated Temperatures. Journal of Structural Fire Engineering. 2021. 12(1). Pp. 35–64. DOI: 10.1108/JSFE-04-2020-0014
2. Kashani, M.M., Crewe, A.J., Alexander, N.A. Structural Capacity Assessment of Corroded RC Bridge Piers. Proceedings of the Institution of Civil Engineers: Bridge Engineering. 2017. 170(1). Pp. 28–41. DOI: 10.1680/jbren.15.00023
3. Yilmaz, T., Kiraç, N., Anil, Ö. Experimental Investigation of Axially Loaded Reinforced Concrete Square Column Subjected to Lateral Low-Velocity Impact Loading. Structural Concrete. 2019. 20(4). Pp. 1358–1378. DOI: 10.1002/suco.201800276
4. Isaac, O.S., Jagadeesh, G. Impulse Loading of Plates Using a Diverging Shock Tube. Experimental Mechanics. 2020. 60. Pp. 565–569. DOI: 10.1007/s11340-019-00573-5
5. Mai, V.C., Vu, N.Q., Nguyen, V.T., Pham, H. Ultra-High Performance Fiber Reinforced Concrete Panel Subjected to Severe Blast Loading. Defence Science Journal. 2020. 70(60). 603–611. DOI: 10.14429/DSJ.70.15835
6. Alekseytsev, A.V., Sazonova, S.A. Numerical Analysis of the Buried Fiber Concrete Slabs Dynamics under Blast Loads. Magazine of Civil Engineering. 2023. 117(1). Article no. 11703. DOI: 10.34910/MCE.117.3
7. Bregoli, G., Vasdravellis, G., Karavasilis, T.L., Cotsovos, D.M. Static and Dynamic Tests on Steel Joints Equipped with Novel Structural Details for Progressive Collapse Mitigation. Engineering Structures. 2021. 232. Article no. 111829. DOI: 10.1016/J.ENGSTRUCT.2020.111829
8. Li, Z.X., Zhang, X., Shi, Y., Wu, C., Li, J. Finite Element Modeling of FRP Retrofitted RC Column against Blast Loading. Compos Struct 2021. 263. Article no. 113727. DOI: 10.1016/j.compstruct.2021.113727
9. Mishra, N., Netula, O. Behaviour of Reinforced Concrete Framed Structure Subjected to Blast Loading. International Journal of Advanced Research in Engineering and Technology (IJARET). 2021. 12(1). 173–181. DOI: 10.34218/IJARET.12.1.2021.014
10. Zhou, X., Jing, L. Deflection Analysis of Clamped Square Sandwich Panels with Layered-Gradient Foam Cores under Blast Loading. Thin-Walled Structures. 2020. 157. Article no. 107141. DOI: 10.1016/j.tws.2020.107141
11. Siguerdjidjene, H., Dyachenko, L.K. Study of Dynamic Impact of Speed Trains on Bridge Structures. International Journal of Mechanics. 2021. 15. Pp. 30–36. DOI: 10.46300/9104.2021.15.4
12. Zhao, W., Qian, J., Wang, J. Performance of Bridge Structures under Heavy Goods Vehicle Impact. Computers and Concrete. 2018. 22(6). 515–525. DOI: 10.12989/cac.2018.22.6.515
13. Fan, W., Shen, D., Huang, X., Sun, Y. Reinforced Concrete Bridge Structures under Barge Impacts: FE Modeling, Dynamic Behaviors, and UHPFRC-Based Strengthening. Ocean Engineering 2020. 216. Article no. 108116. DOI: 10.1016/j.oceaneng.2020.108116
14. Fu, T., Zhu, Z., Li, Y., Sun, Y., Meng, L. Study on the Time-Dependent Reliability of Corroded Reinforced Concrete Bridge Structures Due to Ship Impact. Advances in Civil Engineering. 2022. 2022. Article no. 8190297. DOI: 10.1155/2022/8190297
15. Zhang, J., Wang, R., Han, W., Bao, H. A Comprehensive Approach for Bridge Performance Evaluation under Rockfall Impact Integrated with Geological Hazard Analysis. Engineering Failure Analysis. 2022. 141. Article no. 106668. DOI: 10.1016/j.engfailanal.2022.106668
16. Liu, Z., Lu, Z., Li, Y., Hu, R., Tu, B. Study on Impact Resistance of Flexible Shed Tunnel for Bridges in Mountainous Areas. Tiedao Xuebao/Journal of the China Railway Society. 2023. 45. DOI: 10.3969/j.issn.1001-8360.2023.03.015
17. Terrenzi, M., Spacone, E., Camata, G. Collapse limit state definition for seismic assessment of code-conforming RC buildings. 2018. International Journal of Advanced Structural Engineering. 10(3). Pp. 325–337. DOI: 10.1007/s40091-018-0200-6
18. Sinković, N.L., Dolšek, M. Fatality risk and its application to the seismic performance assessment of a building. Engineering Structures. 2020. 205. Article no. 110108. DOI: 10.1016/j.engstruct.2019.110108
19. Shokrabadi, M., Burton, H.V. Risk-based assessment of aftershock and mainshock-aftershock seismic performance of reinforced concrete frames. Structural Safety. 2018. 73. Pp. 64–74. DOI: 10.1016/j.strusafe.2018.03.003
20. Sinković, N.L., Brozovič, M., Dolšek, M. Risk-based seismic design for collapse safety. Earthquake Engineering and Structural Dynamics. 2016. 45(9). Pp. 1451–1471. DOI: 10.1002/eqe.2717

21. Thai, D.K., Pham, T.H., Nguyen, D.L. Damage assessment of reinforced concrete columns retrofitted by steel jacket under blast loading. Structural Design of Tall and Special Buildings. 2020. 29(1). Article no. e1676. DOI: 10.1002/tal.1676
22. Alekseytsev, A.V. Mechanical safety of reinforced concrete frames under complex emergency actions. Magazine of Civil Engineering. 2021. 103(3). Article no. 10306. DOI: 10.34910/MCE.103.6
23. Kristoffersen, M., Hauge, K.O., Minoretti, A., Børvik, T. Experimental and numerical studies of tubular concrete structures subjected to blast loading. Engineering Structures. 2021. 233. Article no. 111543. DOI: 10.1016/j.engstruct.2020.111543
24. Maazoun, A., Matthys, S., Belkassem, B., Atoui, O., Lecompte, D. Experimental study of the bond interaction between CFRP and concrete under blast loading. Composite Structures. 2021. 277. Article no. 114608. DOI: 10.1016/j.compstruct.2021.114608
25. Li, Z.X., Zhang, X., Shi, Y., Wu, C., Li, J. Finite element modeling of FRP retrofitted RC column against blast loading. Composite Structures. 2021. 263. Article no. 113727. DOI: 10.1016/j.compstruct.2021.113727
26. Alekseytsev, A.V., Gaile, L., Drukis, P. Optimization of steel beam structures for frame buildings subject to their safety requirements. Magazine of Civil Engineering. 2019. 91(7). Pp. 3–15. DOI: 10.18720/MCE.91.1
27. Kumpyak, O.G., Galyautdinov, Z.R., Kokorin, D.N. AIP Conference Proceedings. 2016. 1698(1). Article no. 070006. DOI: 10.1063/1.4937876
28. Chen, Y., May, I.M. Reinforced concrete members under drop-weight impacts. 2009. Proceedings of the Institution of Civil Engineers: Structures and Buildings. 162(1). Pp. 45–56. DOI: 10.1680/stbu.2009.162.1.45
29. Qasrawi, Y., Heffernan, P.J., Fam, A. Dynamic behaviour of concrete filled FRP tubes subjected to impact loading. Engineering Structures. 2015. 100. Pp. 212–225. DOI: 10.1016/j.engstruct.2015.06.012
30. Ngo, T., Mendis, P. Modelling the dynamic response and failure modes of reinforced concrete structures subjected to blast and impact loading. Structural Engineering and Mechanics. 2009. 32(2). Pp. 269–282. DOI: 10.12989/sem.2009.32.2.269
31. Niroomandi, A., Pampanin, S., Dhakal, R.P., Ashtiani, M.S., De La Torre, C. Rectangular RC walls under bi-directional loading: recent experimental and numerical findings. The Concrete NZ Conference 2018. Hamilton, 2018.
32. Magnusson, J., Hallgren, M., Ansell, A. Shear in concrete structures subjected to dynamic loads. Structural Concrete. 2014. 15(1). Pp. 55–65. DOI: 10.1002/suco.201300040
33. Alekseytsev, A.V. Stability of the RC Column under Horizontal Impacts. Reinforced concrete structures. 2023. 2(2). Pp. 3–12. DOI: 10.22227/2949-1622.2023.2.3-12
34. ANSYS Mechanical APDL Verification Manual. https://www.researchgate.net/profile/Girish-Prajapati-2/post/How-composites-can-be-modeled-in-ANSYS-Using-Solid185/attachment/59d6250379197b8077983549/AS%3A315291291062272%401452182710434/download/ANSYS+Mechanical+APDL+Verification+Manual.pdf
35. Dmitriev, A., Novozhilov, Y., Mikhalyuk, D., Lalin, V. Calibration and Validation of the Menetrey-Willam Constitutive Model for Concrete. Construction of Unique Buildings and Structures. 2020. 88. Article no. 8804. Pp. 84–91. DOI: 10.18720/CUBS.88.4
36. Korsun, V.I., Karpenko, S.N., Makarenko, S.Yu., Nedoresov, A.V. Modern strength criteria for concrete under triaxial stress states. Building and Reconstruction. 2021. 97(5). Pp. 16–30. DOI: 10.33979/2073-7416-2021-97-5-16-30
37. Budarin, A.M., Rempel, G.I., Kamzolkyn, A.A., Alekhin, V.N. Stress-strain concrete model with double independent reinforcement. Vestnik MGSU [Monthly Journal on Construction and Architecture]. 2023. 18(4). Pp. 517–532. DOI: 10.22227/1997-0935.2023.4.517-532
38. fib Model Code for Concrete Structures 2010. International Federation for Structural Concrete, 2013. 434 p. DOI: 10.1002/9783433604090
39. Menétrey, Ph. Numerical analysis of punching failure in reinforced concrete structures. PhD thesis. L'école polytechnique fédérale de Lausanne. Lausanne, 1994. p. 179.
40. Al Ali, M., Kvočák, V., Dubecký, D., Alekseytsev, A. Experimental research on composite deck bridges with encased steel beams. Delta University Scientific Journal. 2023. 6(1). Pp. 31–38. DOI: 10.21608/dusj.2023.291004
41. Alekhin, V., Budarin, A., Pletnev, M., Avdonina, L. MATEC Web of Conferences. 2019. 279(2). Article no. 02005. DOI: 10.1051/matecconf/201927902005
42. Turteltaub, S. Inelastic analysis of structures, Milan Jirásek and Zdeněk P. Bažant, John Wiley & Sons, 2002, ISBN 0-471-98716-6, 758 Pages. Structural and Multidisciplinary Optimization. 2002. 24. Pp. 87–88. DOI: 10.1007/s00158-002-0217-z

Information about the authors:

***Anatoly Alekseytsev**, Doctor of Technical Sciences*
ORCID: https://orcid.org/0000-0002-4765-5819
E-mail: aalexw@mail.ru

***Vincent Kvocak**, Doctor of Engineering*
ORCID: https://orcid.org/0000-0002-5229-638X
E-mail: vincent.kvocak@tuke.sk

***Dmitry Popov**, PhD in Technical Sciences*
ORCID: https://orcid.org/0000-0003-0768-8808
E-mail: popovds89@mail.ru

***Mohamad Al Ali**, PhD in Technical Sciences*
E-mail: mohamad.alali@tuke.sk

Received 29.07.2024. Approved after reviewing 05.01.2025. Accepted 12.01.2025.

Magazine of Civil Engineering

ISSN
2712-8172

journal homepage: http://engstroy.spbstu.ru/

Research article
UDC 624.012.3
DOI: 10.34910/MCE.133.4

Axial capacity and ductility of reinforced concrete columns with strip plate steel and conventional stirrup reinforcements

B.K. Pradipta* ✉ *, M.Y. Bhayusukma, S. As'ad

Sebelas Maret University, Surakarta, Indonesia

✉ *bondankartika@student.uns.ac.id*

Keywords: strip plate steel, axial capacity, transverse reinforcement, compressive strength performance, reinforced concrete column

Abstract. A column is a vertical structural element that transmits loads to the foundation and is required to withstand a variety of loads. The incorporation of reinforcing bars serves to enhance the axial capacity and mitigate the risk of sudden collapse of the column. The potential use of alternative materials for stirrup reinforcement represents a topic of significant interest within the academic community. Prior research has demonstrated that the stirrup reinforcement ratio exerts a significant influence on the strength and ductility of concrete. Specifically, higher ratios have been shown to lead to enhanced performance in both of these attributes. This study examined the behavior of core concrete in reinforced concrete columns with varying types of reinforcing bars, including 3×25 mm, 3×30 mm, 4×25 mm strip plate steel, and 10 mm diameter deformed conventional stirrups. A total of thirteen columns were tested until collapse in order to evaluate a number of factors, including column shortening, peak axial load, column stress, reinforcement and core concrete strain, and a comparison of theoretical and actual confined core concrete compressive strength. The study demonstrated that the incorporation of strip plate stirrups in reinforced concrete columns exerted a marginal influence on the column's axial capacity. The columns reinforced with conventional stirrups exhibited enhanced peak axial load, column stress, and restraint strength, accompanied by a reduction in column shortening. Conversely, the columns with 3×30 mm strip plates demonstrated superior ductility. An elevated stirrup reinforcement ratio was observed to enhance the compressive strength of confined concrete, although a discrepancy was noted between the theoretical calculations and the actual values.

Citation: Pradipta, B.K., Bhayusukma, M.Y., As'ad, S. Axial capacity and ductility of reinforced concrete columns with strip plate steel and conventional stirrup reinforcements. Magazine of Civil Engineering. 2025. 18(1). Article no. 13304. DOI: 10.34910/MCE.133.4

1. Introduction

Concrete is the most prevalent building material in use today. Conventional concrete is composed of coarse aggregate, fine aggregate, water, and cement [1]. These building materials are utilized extensively in the construction of a multitude of infrastructure projects, including buildings, roads, bridges, and underground structures such as foundations and tunnels [2]. Concrete has a high compressive capacity, is relatively inexpensive to maintain, is readily available in raw form, and can be molded into a variety of shapes, making it a versatile and economical material for a range of construction applications [3]. Nevertheless, concrete has a relatively low tensile strength, which necessitates the use of reinforcing steel to enhance its tensile strength performance [4]. The reinforcement system utilizes reinforcing steel, which is capable of withstanding tensile loads on concrete, thereby preventing cracking and enhancing the ductility of the structure [5]. In this context, the two principal types of reinforcing steel are plain and deformed [6]. The combination of the two materials results in the formation of a composite material that is capable of bearing both compressive and tensile loads. This material is known as reinforced concrete [7].

In a frame structure, columns are vertical structural elements that bear the load of the beams and floor slabs above them [8]. A column is a structural element that serves to compress and reinforce a building's framework. It is responsible for transferring the total building load to the foundation, which includes both dead and live loads, as well as earthquake loads [9]. A column, as a vertical structural element, is required to provide resistance to bending, shear, axial, and torsional collapse due to the aforementioned loads [10]. One of the principal causes of collapse in a column is axial loading. The objective of transverse reinforcement is to enhance the axial capacity of the column [11].

The function of the transverse reinforcement is to maintain the axial capacity of the column by ensuring the stability of the core concrete [12]. The installed transverse reinforcement will serve to resist the lateral forces generated by the axial loads received by the core concrete [13]. The role of transverse reinforcement in columns is of paramount importance, given that collapse can occur abruptly and without warning [14]. Prior research has investigated the impact of transverse reinforcement on the axial capacity of reinforced concrete columns subjected to confinement. This has involved the utilisation of diverse configurations and ratios of transverse reinforcement [15].

The cross-sectional area of the transverse reinforcement is intimately associated with the transverse reinforcement ratio, which exerts a profound influence on the ductility of the confined core concrete. In their research, Imran and Antonius demonstrated that an elevated transverse reinforcement ratio gives rise to a heightened ductility strength of the confined concrete. Nevertheless, if the reinforcement ratio is excessively high, the concrete will succumb to collapse before the transverse reinforcement reaches its yield point [15, 16]. In their research, Saatcioglu and Razvi demonstrated that the strength and ductility of confined concrete increase as the reinforcement ratio increases. Columns with low reinforcement ratios exhibited brittle behavior, displaying a pronounced reduction in strength after reaching the peak load. In contrast, columns with higher reinforcement ratios demonstrated the capacity to undergo significant deformation without a notable reduction in strength [17, 18]. Similarly, research conducted by Cusson and Paultre indicates that an increased transverse reinforcement ratio is associated with enhanced confinement efficiency [19].

The research on the performance and influence of transversal reinforcement has become increasingly diverse over time. This has prompted researchers to seek alternative materials that are stronger and more efficient, such as the use of strip plate steel as transversal reinforcement. Previous studies have demonstrated the efficacy of strip plate steel in increasing the shear capacity of wide concrete beams, enhancing the durability of wide concrete beams after the first shear crack, increasing ductility, and facilitating easier management during the construction process [20]. Furthermore, the use of strip plate steel in the transverse reinforcement of concrete can enhance its shear capacity, particularly in the context of beams. Reinforced concrete beams with the incorporation of strip plate steel exhibit enhanced resistance to maximum loads and exhibit greater stiffness compared to their plain concrete counterparts. However, it is observed that the crack pattern in beams with the aforementioned reinforcement tends to produce cracks with larger inclination angles, a more uniform distribution on the side of the beam, and a greater number of cracks compared to plain concrete beams [21].

The objective of this study is to conduct a more thorough investigation into the effect of using strip plate steel as a stirrup reinforcement in columns on the axial capacity of columns and the ductility of columns subjected to concentric axial loads. Strip plate steel is used as an alternative to deformed steel. The utilization of strip plate steel is predicated on the assumption that strip plate steel is more readily manipulable than deformed steel. Additionally, strip plate steel possesses a more substantial cross-sectional area than deformed steel, which allows for more effective confinement of the core concrete. Further research will be conducted on the behavior of reinforced concrete columns using strip plate steel reinforcement. The axial load that can be achieved, the strain that occurs in stirrup reinforcement, longitudinal reinforcement, and core concrete, as well as the amount of shortening that occurs in the column, will be reviewed. This research is expected to corroborate the preceding research hypothesis, namely that the axial capacity of reinforced concrete columns can be enhanced.

2. Materials and Method

This study focused on a particular type of column, characterized by conventional stirrup reinforcement and strip plates. The conventional transverse reinforcement measures 10 mm in diameter, while the strip plate steel has dimensions of 3×25 mm, 3×30 mm, and 4×25 mm. The design of concrete mixtures is guided by the Indonesian Standard SNI 7656:2012. Subsequently, the concrete cylinders were subjected to testing in accordance with the standards set forth in SNI 1974:2011. The steel utilized in this investigation was evaluated for tensile strength in accordance with the standards set forth in SNI 8389:2017. The particular attributes of the concrete and reinforcing steel used are set forth in Tables 1 and 2, respectively.

Table 1. Concrete properties.

	Average Values
Slump	100 mm
Compressive Strength	23.9 MPa

Table 2. Steel reinforcements properties.

Type of Steels	**Cross-Sectional Area (mm^2)**	**Yield Stress (MPa)**	**Ultimate Stress (MPa)**	**Elongation (%)**
D10	57.13	346.20	460.65	10.84
3×25 mm	63.42	366.10	541.58	6.56
3×30 mm	80.96	392.39	543.96	8.78
4×25 mm	84.75	383.86	524.60	9.37

A total of thirteen column specimens were subjected to axial loading until collapse occurred. Column specimens bearing the initials D10 represent reinforced concrete columns using conventional transverse reinforcement, whereas column specimens bearing the initials 3×25, 3×30, and 4×25 represent reinforced concrete columns using strip plate steel transverse reinforcement. The test area was situated between two simple pedestals, with both ends of the columns attached to the compression tester. In all columns, the longitudinal reinforcement comprised four pieces of 6 mm diameter plain reinforcement, which served as a tie for the transverse reinforcement.

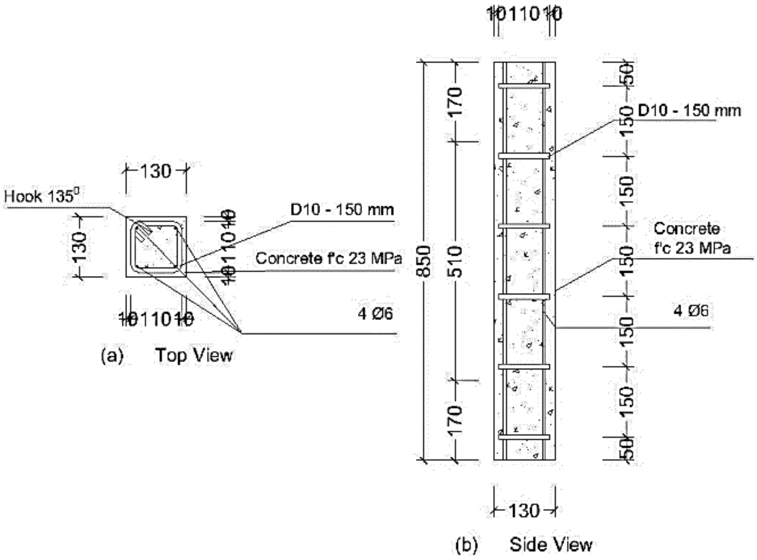

Figure 1. Schematic of conventional stirrup reinforcement installation on columns.

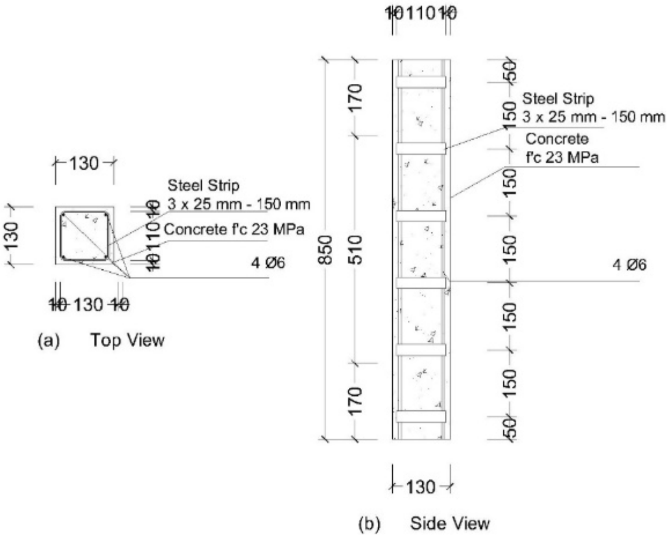

Figure 2. Schematic installation of 3×25 mm strip plate reinforcement on columns.

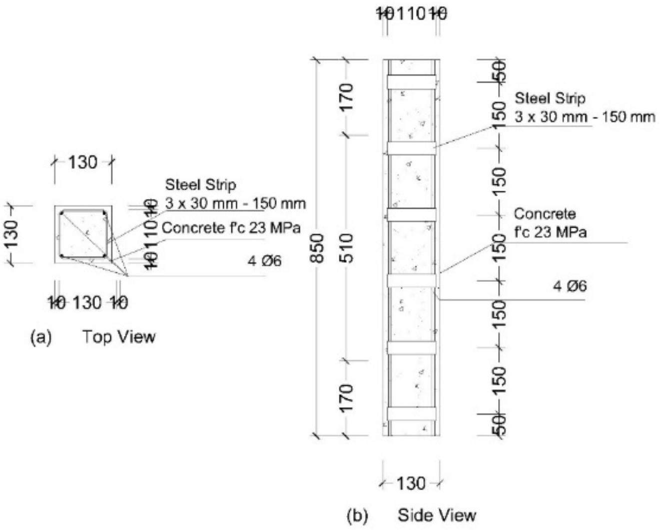

Figure 3. Schematic installation of 3×30 mm strip plate reinforcement on columns.

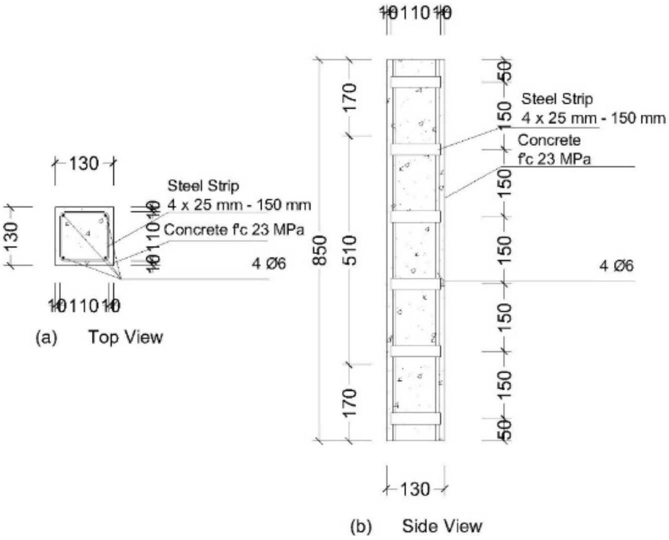

Figure 4. Schematic installation of 4×25 mm strip plate reinforcement on columns.

The experiments were conducted in the structural laboratory of the Civil Engineering Department at Sebelas Maret University. The loading frame is equipped with hydraulic jacks for loading, with a capacity of 500 kN. Furthermore, the hydraulic jack is equipped with a load cell with a capacity of 100,000 pounds (453 kN), which serves to measure the load applied to the column. To quantify the shortening of the specimen, a linear vertical displacement transducer was utilized and installed centrally within the span of the column specimen. The observed shortening of the specimen spanned the range from a load of 0 kN to the peak load tolerated by the column.

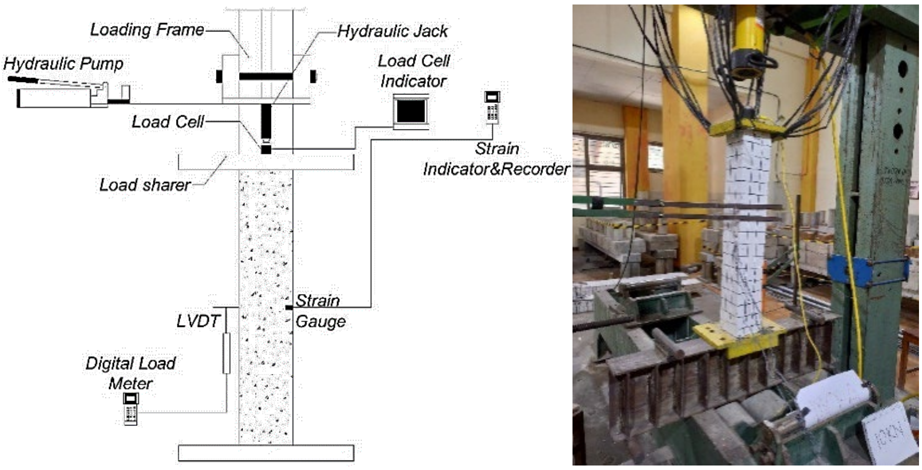

Figure 5. Testing equipment installation scheme and test program setup.

3. Results and Discussion

This test identifies the relationship between the applied axial load and the shortening of the column, as well as the strain occurring in the transverse reinforcement, longitudinal reinforcement, and core concrete. Strain gauges were installed on the stirrup reinforcement, longitudinal reinforcement, and core concrete at the center, with the gauges connected to a strain indicator to obtain the amount of strain at each loading interval. Column shortening was measured using an LVDT attached to the midpoint of the column and connected to a digital load meter. The axial load applied to the column was measured using a load cell connected to a load cell indicator. The objective of this study is to examine the axial load on the column, the strain on stirrup reinforcement, longitudinal reinforcement, and core concrete, and the shortening of the column. Axial load-shortening curves and axial load-strain curves are plotted up to the point of failure, which is indicated by the column reaching its peak load.

Figure 6. Strain indicator, digital load meter, and load cell indicator.

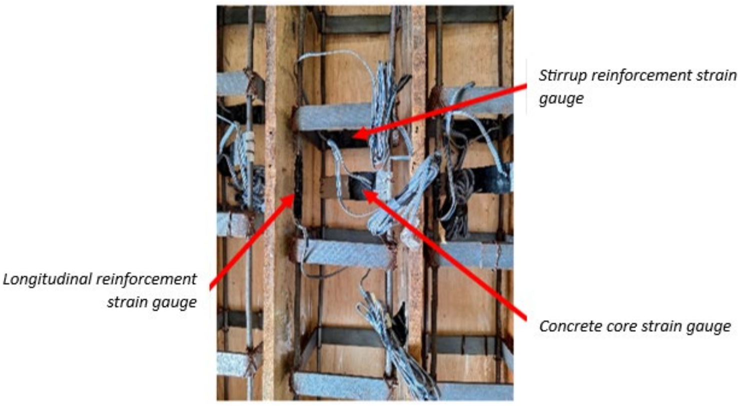

Figure 7. Installation location of strain gauge.

3.1. Column Shortening

The response of reinforced concrete columns with conventional transverse reinforcement and strip plate steel stirrups is linear elastic prior to the formation of the first crack. The shortening of reinforced concrete columns with conventional transversal reinforcement commences at a load of 75 kN, whereas the shortening of reinforced concrete columns with strip plate steel stirrups begins at a load of 45 kN for 3×25 columns, 30 kN for 3×30 columns, and 15 kN for 4×25 columns. As the load increases, the formation of additional cracks causes the shortening curve to become linear. The shortening at maximum axial load in reinforced concrete columns with conventional transversal reinforcement is less than that observed in columns with strip plate steel stirrups. The discrepancies in shortening at maximum axial load are 26.29 % for the 3×25 columns, 78.32 % for the 3×30 columns, and 52.90 % for the 4×25 columns. Columns with conventional reinforcement demonstrate enhanced bearing capacity. It is observed that the shortening of the columns is less pronounced in comparison to columns utilising strip plate stirrups, and they are capable of withstanding greater axial loads before significant shortening occurs. This outcome may be attributed to the fact that conventional stirrups possess a greater cross-sectional thickness in comparison to strip plate stirrups. This allows for a more robust confinement of the concrete core, which ultimately results in the smallest column shortening in comparison to columns with strip plate stirrups, despite the latter exhibiting the lowest tensile strength. However, columns with 3×30 mm strip plate stirrups display greater ductility than other columns. This is demonstrated by the larger shortening of the column in comparison to the other columns, despite the relatively minor differences in load. The relationship between the mean column shortening and the peak axial load at the time of column failure is illustrated in Fig. 8.

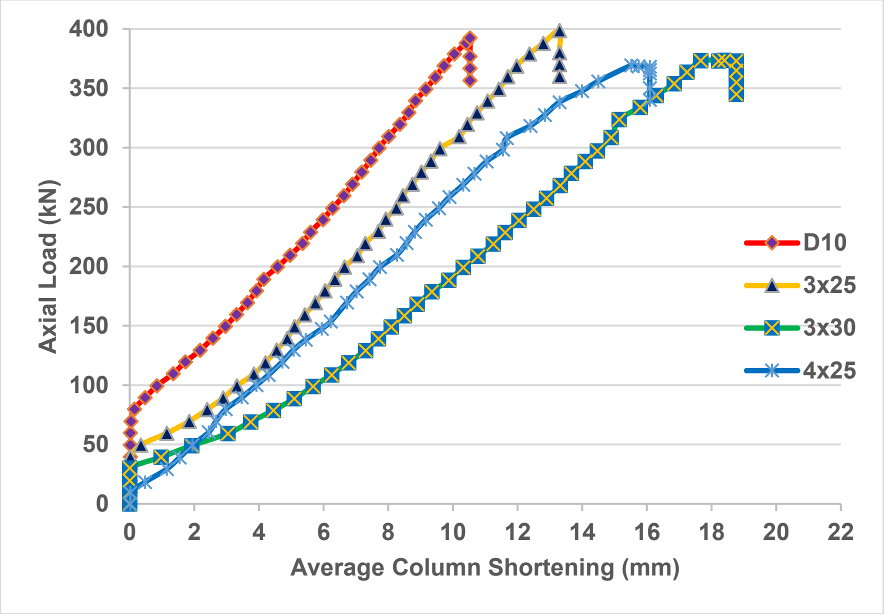

Figure 8. Maximum axial load-shortening curve of column specimen.

3.2. Relationship between Peak Axial Load and Longitudinal Reinforcement Strain

Each column exhibits the same amount of longitudinal reinforcement and the same steel tensile strength. The findings of the research indicate that as the axial load applied to the column increases, there is an accompanying increase in the strain in the longitudinal reinforcement. From the initial to the final stages of loading, the relationship between axial load and longitudinal reinforcement strain is proportional, indicating an increase in longitudinal reinforcement strain for each incremental increase in axial load. The ratio of transversal reinforcement used affects the peak. While there are differences in the strain magnitude occurring in the longitudinal reinforcement, they are not significant. The 3×30 column has the highest strain value in the longitudinal reinforcement compared to the other columns, suggesting that the longitudinal reinforcement in 3×30 mm strip plate columns is more ductile than that observed in columns with alternative stirrup reinforcement. Fig. 9 illustrates the relationship between the average longitudinal reinforcement strain and the peak axial load at the point of column failure.

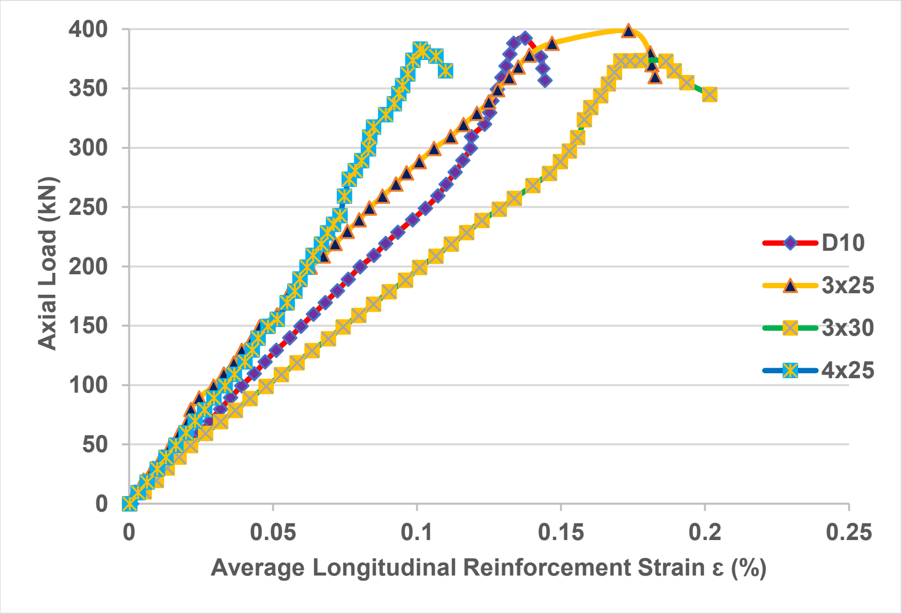

Figure 9. Load-strain curve of longitudinal reinforcement of column specimen.

3.3. Relationship between Peak Axial Load and Transverse Reinforcement Strain

Each column exhibits the same form of transversal reinforcement, yet exhibits differences in tensile strength of steel, cross-sectional area, and transversal reinforcement ratio. The test results demonstrate that the strain in the transverse reinforcement increases in conjunction with the application of an increasing axial load to the column. From the outset to the conclusion of the loading process, the relationship between axial load and the strain in the transversal reinforcement demonstrates a proportional increase in strain for each incremental increase in axial load. The ratio of the transversal reinforcement affects the maximum axial load that can be sustained until the column reaches its failure point. The degree of strain in the transversal reinforcement exhibits variability, but it is not statistically significant. Column D10 shows the higher level of strain in the transversal reinforcement in comparison to the other columns. These findings indicate that the stirrup reinforcement in conventional columns exhibits the greatest confinement strength, the most ductility, and the most effective performance when compared to columns with alternative stirrup reinforcement. The 10 mm diameter deformed stirrups utilized in column D10 are more readily manipulable than alternative forms of transversal reinforcement, as they do not necessitate the use of specialized tools for the bending of steel into stirrup shapes. The relationship between the average transversal reinforcement strain and the peak axial load at the point of column failure is illustrated in Fig. 10.

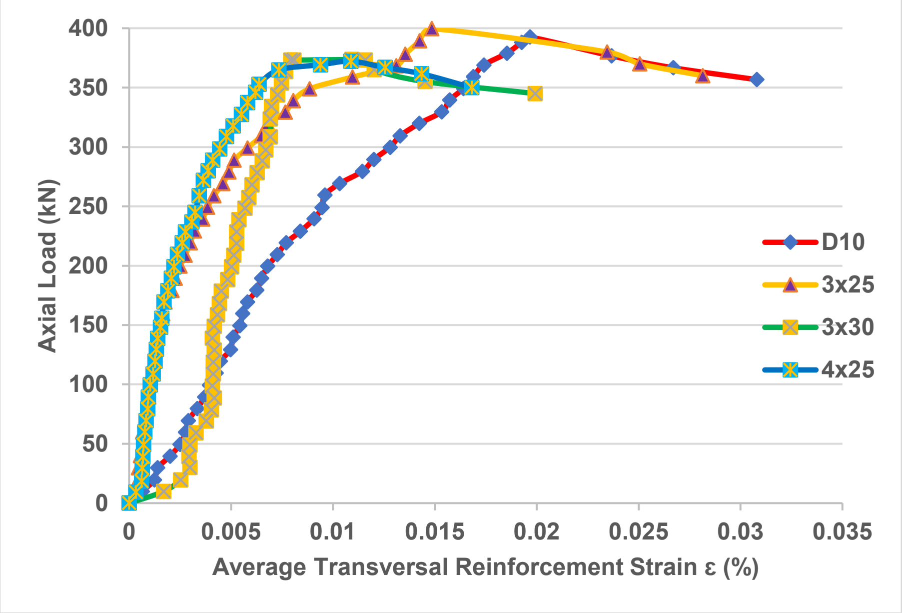

Figure 10. Load-strain curve of trasnsversal reinforcement of column specimen.

3.4. Relationship between Peak Axial Load and Core Concrete Strain

The columns are of identical dimensions with respect to both core concrete and concrete cover, and are constructed using the same concrete mixture. The test results demonstrate that the strain in confined core concrete increases in conjunction with the rise in axial load and stress on the column. From the outset to the conclusion of the loading process, the relationship between the axial load applied to the column and the strain in the confined core concrete demonstrates a proportional increase in core concrete strain for each incremental increase in axial load and concrete stress. The ratio of transverse reinforcement exerts a significant influence on the peak axial load that can be sustained until column failure and the magnitude of concrete stress that occurs in the column. The strain in the core concrete varies among the different column types, but it is not significant. The 3×25 column exhibits the highest strain in the core concrete and peak axial load compared to the other columns. This suggests that the core concrete in columns with 3×25 mm strip plate steel stirrups is more ductile than in columns with alternative stirrups. The relationship between the average strain of confined core concrete and the peak axial load at the point of column failure is illustrated in Fig. 11.

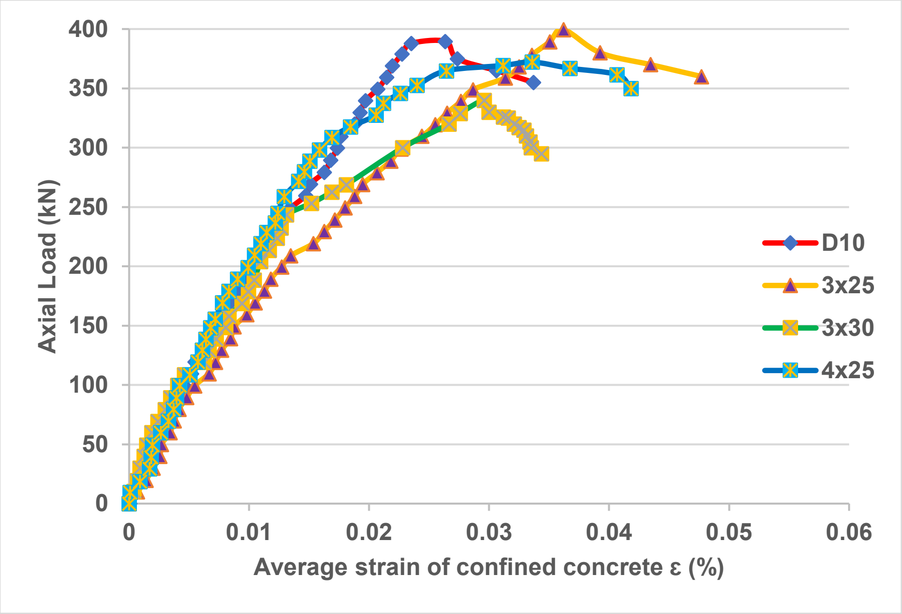

Figure 11. Maximum axial load-strain curve of confined core concrete.

3.5. Actual and Estimated Compressive Strength of Confined Concrete Cores

The estimated confined core concrete compressive strength is expressed in Equation 1. In this study, the equation proposed by Mander et al. is used to estimate the confined core concrete compressive strength observed in column test specimens [22–24]. The predicted results are then compared with the actual confined core concrete compressive strength, as stated in Equation 2.

$$f'_{cc} = f'_{c0}\left(-1.254 + 2.254\sqrt{1+\frac{7.94 f_l}{f'_{c0}}} - 2\frac{f_l}{f'_{c0}}\right); \tag{1}$$

$$f'_{cc\cdot test} = \frac{P}{A}; \tag{2}$$

$$\rho_s = \frac{\sum_{i=1}^{n}\left(A_{sx}\right)_i}{bc_y s} + \frac{\sum_{i=1}^{n}\left(A_{sy}\right)_j}{bc_x s}. \tag{3}$$

Furthermore, the equation proposed by Attard and Setunge is used to estimate the confined concrete compressive strength as demonstrated in Equation 4 [25–27].

$$\frac{f_o}{f'_c} = \left(\frac{f_r}{f_t}\right)^k; \tag{4}$$

$$k = 1.25\left[1 + 0.062\frac{f_r}{f'_c}\right]\left(f'_c\right)^{-0.21}; \tag{5}$$

$$f_t = 0.56\sqrt{f'_c}. \tag{6}$$

Table 3 shows the confined concrete compressive strength of reinforced concrete columns with various types of stirrups. In the calculation of $f'_{cc\cdot cal}$ actual, it is observed that as the dimensions of transversal reinforcement increase, the confined concrete compressive strength also increases. However, the test results indicate that the actual confined concrete compressive strength does not differ significantly. Based on the ratio $f'_{cc\cdot test} / f'_{cc\cdot cal}$ using the equation from Mander et al., it is evident that the actual value is higher than the predicted confined concrete compressive strength. On the other hand, when compared with the estimated value according to the equation from Attard and Setunge, the actual value is lower than the estimated value. The results from both equations indicate that the estimated confined concrete compressive strength values do not accurately represent the actual values due to the differences obtained.

Furthermore, the calculations derived from both equations illustrate the impact of the transversal reinforcement ratio. A larger ratio is associated with an elevated estimated confined concrete compressive strength. Column D10 exhibits a relatively lower transversal reinforcement ratio compared to the 3×25 column by 23.59 %, the 3×30 column by 57.98 %, and the 4×25 column by 66.56 %. This indicates that the ratio of transversal reinforcement to the cross-sectional area of the core concrete has a significant impact on the confined concrete compressive strength that can be achieved.

Table 3. Confined concrete compressive strength column specimens

Test Specimen	$f'_{cc\ test}$ (MPa)	$f'_{cc\ cal\ Mander}$ (MPa)	$f'_{cc\ test}/f'_{cc\ cal}$ *Mander*	$f'_{cc\ cal\ Attard}$ (MPa)	$f'_{cc\ test}/f'_{cc\ cal}$ *Attard*	ρ_s
D10	31.96	24.70	1.29	35.00	0.91	1.27 %
3×25	33.06	25.57	1.29	38.06	0.87	1.58 %
3×30	31.24	26.41	1.18	42.66	0.73	2.01 %
4×25	32.62	26.23	1.24	43.17	0.76	2.12 %

3.6. Crack Pattern

All columns were subjected to concentric axial loads until collapse occurred, which was limited by the capacity of the load cell, which reached 400 kN. All columns exhibited the initial cracking at the top or bottom, with the most prevalent type of cracking being compressive. A compressive crack is a fracture caused by a load exceeding the structural capacity of the material. As the axial load is increased, the cracks lengthen and widen, and the number of cracks caused by compressive axial load increases until the column collapses. The axial load at the first crack and the load at collapse can be seen in Table 4. The columns that have been tested with axial load until collapse can be seen in Figs. 12–16.

Table 4. Axial load at first crack and collapse.

Specimen	Axial load at first crack (kN)	Axial load at collapse (kN)
K	100	370.13
D10 A	230	386.74
D10 B	240	Not Collapsed Yet
D10 C	–	Not Collapsed Yet
3×25 A	300	399.99
3×25 B	220	Not Collapsed Yet
3×25 C	300	Not Collapsed Yet
3×30 A	160	280.00
3×30 B	210	377.96
3×30 C	180	Not Collapsed Yet
4×25 A	80	394.74
4×25 B	230	370.26
4×25 C	290	380.08

Figure 12. Column K after testing under axial load.

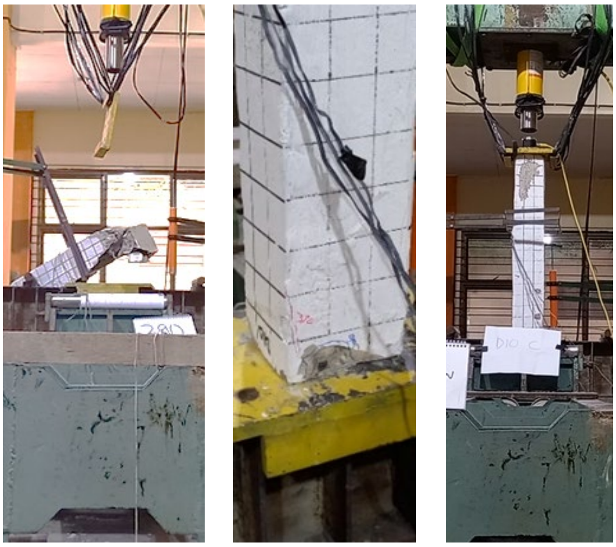

(A) (B) (C)

Figure 13. D10 column after testing under axial load.

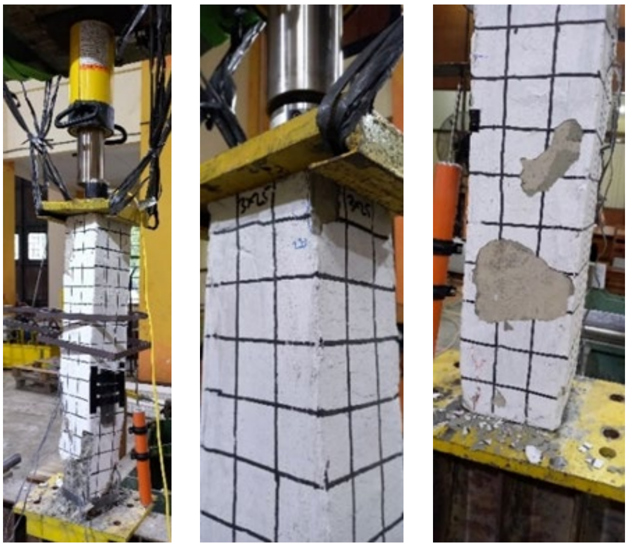

(A) (B) (C)

Figure 14. 3×25 column after testing under axial load.

(A) (B) (C)

Figure 15. 3×30 column after testing under axial load.

(A) (B) (C)

Figure 16. 4×25 column after testing under axial load.

The initial cracks are predominantly observed in the concrete blanket and typically initiate at the support area, both above and below. As the axial load increases, the number and size of the cracks also increase, extending into the core of the column. By the time the ultimate axial load was reached, the majority of the concrete material had cracked, and visible cracks were present in all areas of the column at the support area. Additionally, cracks were observed in the concrete blanket and column core [28–30].

It can be observed that all columns exhibiting the initial signs of deterioration present compressive cracks at either the top or bottom. A compressive crack is defined as a fracture that occurs as a result of a load exceeding the structural capacity of the material in question. In general, the stirrups were unable to confine the core concrete due to the open bond of the stirrups. This ultimately results in the longitudinal reinforcement being unable to maintain the integrity of the core concrete, which subsequently buckles. Therefore, the concrete failed in a collapse. As the load was applied to the test specimen, the cracks exhibited an increase in length and width, accompanied by the formation of additional cracks due to the compressive load until the column reached its failure point. With respect to the number of cracks, columns with strip plate stirrups, particularly those with dimensions of 3×30 mm and 4×25 mm, exhibited a greater number of cracks than columns with conventional stirrups. This is due to the larger dimensions of the stirrup reinforcement, which enables columns with 3×30 mm and 4×25 mm strip plate stirrups to distribute the load more evenly than columns with 3×25 mm deformed and strip plate stirrups. The additional reinforcement provided by the strip plate stirrups on the sides of the column reduces the surface area of the column that is only reinforced with concrete.

Columns without reinforcement demonstrate a proclivity to undergo load transfer when subjected to loading, with the transfer occurring predominantly in the column support area, both above and below. This is substantiated by the vertical cracks that emerge in the column support area. When the cracks commenced to propagate beyond the support area, the column collapsed as a consequence of the absence of reinforcement on the sides of the column.

4. Conclusion

The experimental testing results obtained in the laboratory led to the following conclusions:

1. Conventional columns are typically more robust in terms of load acceptance but may exhibit brittle behavior. It can be observed that the shortening of the column is less pronounced and the peak axial load that can be achieved is greater. This is attributed to the relatively small cross-sectional area of the stirrups. However, columns with 3×30 mm strip plate steel stirrups exhibit enhanced ductility as indicated by the larger column shortening with a peak axial load that is not significantly different from conventional columns.
2. Columns with 3×30 mm strip plate steel stirrups exhibit the greatest longitudinal reinforcement strains, suggesting that the longitudinal reinforcement in the column displays enhanced ductility due to the 3×30 mm strip plate stirrups. The stirrup reinforcement ratio exerts a notable influence on both the peak load that can be attained and the strain on the longitudinal reinforcement, although the observed difference is not substantial.

3. It can be observed that conventional columns experience the greatest strain on the stirrup reinforcement in comparison to other types of columns. Conventional stirrup reinforcement exhibits the greatest confining strength, the greatest ductility, and the most effective performance compared to columns with alternative stirrup reinforcement. With the same shape of stirrup reinforcement, conventional stirrup reinforcement is more readily workable because it does not necessitate the use of specialized tools to bend the reinforcement. The stirrup reinforcement ratio affects the achievable peak load and the strain in the stirrup reinforcement, although the impact is not significantly different.

4. Columns with 3×25 mm strip plate steel stirrups exhibited the highest core concrete strain and peak load compared to the other columns. This suggests that the core concrete of the column is more ductile due to the 3×25 mm strip plate stirrups. The stirrup reinforcement ratio affects the achievable peak load and strain in the core concrete, although the difference is not statistically significant.

5. Columns with larger ratios of stirrup reinforcement exhibit enhanced compressive strength of confined core concrete, a finding that aligns with the theoretical predictions put forth by Mander et al. [22] and Attard and Setunge [25]. However, the observed compressive strength values did not fully align with the predicted values.

6. Columns with strip plate stirrups, particularly those with dimensions of 3x30 mm and 4×25 mm, exhibited a higher incidence of cracking. The larger dimensions of stirrup reinforcement impart greater ductility to the column, enabling more even load distribution. The strip plate stirrups provide supplementary reinforcement at the sides of the column, thereby reducing the surface area of the column reinforced with concrete only.

7. Columns with strip plate stirrup reinforcement can be substituted for columns with conventional reinforcement due to the fact that both types of reinforcement have the capacity to withstand axial loads that tend to be similar. However, it should be noted that strip plate stirrup reinforcement has the advantage of being more ductile than conventional stirrup reinforcement. These columns have been determined to be suitable for use in residential buildings. The test specimens employed in this study exhibited dimensions equivalent to those of standard residential columns. Further investigation is necessary to assess the performance of larger specimens.

The application of strip plate stirrup reinforcement in reinforced concrete columns has a notable impact on the axial capacity of these structures. However, this influence is not particularly pronounced as evidenced by the comparable peak axial loads observed in the tested columns. Furthermore, the strains experienced in the longitudinal reinforcement, stirrups, and confined core concrete exhibit minor discrepancies, yet these differences are not statistically significant. Similarly, the compressive strength of the confined core concrete does not exhibit a considerable variation.

References

1. Nedeljkovic, M., Visser, J., Savija, B., Valcke, S., Schlangen, E. Use of fine recycled concrete aggregates in concrete: A critical review. Journal of Building Engineering. 2021. 38. Article no. 102196. DOI: 10.1016/j.jobe.2021.102196
2. Wangler, T., Roussel, N., Bos, F.P., Salet, T.A.M., Flatt, R.J. Digital Concrete: A Review. Cement and Concrete Research. 2019. 123. Article no. 105780. DOI: 10.1016/j.cemconres.2019.105780
3. Tasevski, D., Ruiz, M.F., Muttoni, A. Compressive Strength and Deformation Capacity of Concrete under Sustained Loading and Low Stress Rates. Journal of Advanced Concrete Technology. 2018. 16(8). Pp. 396–415. DOI: 10.3151/jact.16.396
4. Abbass, W., Khan, M.I., Mourad, S. Evaluation of mechanical properties of steel fiber reinforced concrete with different strengths of concrete. Construction and Building Materials. 2018. 168. Pp. 556–569. DOI: 10.1016/j.conbuildmat.2018.02.164
5. Bastian, M.A., Tambusay, A., Komara, I., Sutrisno, W., Irawan, D., Suprobo, P. Enhancing the Ductility of a Reinforced Concrete Beam using Engineered Cementitious Composite. IOP Conference Series: Earth and Environmental Science. 2019. Article no. 012044. DOI: 10.1088/1755-1315/506/1/012044
6. Markic, T., Amin, A., Kaufmann, W., Pfyl, T. Strength and Deformation Capacity of Tension and Flexural RC Members Containing Steel Fibers. Journal of Structural Engineering. 2020. 146(5). DOI: 10.1061/(ASCE)ST.1943-541X.0002614
7. Ahmad, J., Zhou, Z. Mechanical Properties of Natural as well as Synthetic Fiber Reinforced Concrete: A Review. Construction and Building Materials. 2022. 333. Article no. 127353. DOI: 10.1016/j.conbuildmat.2022.127353
8. Wang, Y., Cai, G., Li, Y., Waldmann, D., Larbi, A.S., Tsavdaridis, K.D. Behavior of Circular Fiber Reinforced Polymer – Steel Confined Concrete Columns Subjected to Reversed Cyclic Loads: Experimental Studies and Finite-Element Analysis. Journal of Structural Engineering. 2019. 145(9). DOI: 10.1061/(ASCE)ST.1943-541X.0002373
9. Azim, I., Yang, J., Javed, M.F., Iqbal, M.F., Mahmood, Z., Wang, F., Liu, Q. Prediction model for compressive arch action capacity of RC frame structures under column removal scenario using gene expression programming. Structures. 2020. 25. Pp. 212–228. DOI: 10.1016/j.istruc.2020.02.028
10. Abdulsalam, M.A., Chaudhary, M.T.A. Progressive collapse of reinforced concrete buildings considering flexure-axial shear interaction in plastic hinges. Cogent Engineering. 2021. 8(1). DOI: 10.1080/23311916.2021.1882115
11. Ding, Y., Zhou, Z., Wei, Y., Huang, Y., Tian, H. Axial compressive behavior of ultra-high performance concrete confined by high strength transverse reinforcements. Construction and Building Materials. 2022. 324. Article no. 126518. DOI: 10.1016/j.conbuildmat.2022.126518

12. Tripathi, M., Dhakal, R. Designing and detailing transverse reinforcement to control bar buckling in rectangular RC walls. Bulletin of the New Zealand Society for Earthquake Engineering. 2021. 54(3). DOI: 10.5459/bnzsee.54.3.228-242
13. Dang, H.V., Lee, K., Han, S.W., Kim, S.J. Experimental assessment of the effects of biaxial bending moment and axial force on reinforced concrete corner columns. Structural Concrete. 2018. 19(4). Pp. 1063–1078. DOI: 10.1002/suco.201700211
14. Dhakal, R.P., Su, J. Design of transverse reinforcement to avoid premature buckling of main bars. Earthquake Engineering Structural Dynamics. 2018. 47(1). Pp. 147–168. DOI: 10.1002/eqe.2944
15. Antonius, A., Imran, I. Experimental Study of Confined Low-, Medium- and High-Strength Concrete Subjected to Concentric Compression. Journal of Engineering and Technological Sciences. 2012. 44(3). Pp. 252–269. DOI: 10.5614/itbj.eng.sci.2012.44.3.4
16. Classen, M., Kalus, M. Punching Shear Response Theory (PSRT) – A two degree of freedom kinematic theory for modeling the entire punching shear vs. deformation response of RC slabs and footings. Engineering Structures. 2023. 291. Article no. 116197. DOI: 10.1016/j.engstruct.2023.116197
17. Saatciouglu, M., Razvi, S.R. Strength and ductility of confined concrete. Journal of structural engineering. 1992. 118(6). Pp. 1590–1607.
18. Saatciouglu, M., Razvi, S.R. High-strength concrete columns with square sections under concentric compression. Journal of Structural Engineering. 1998. 124(12). Pp. 1438–1447.
19. Cusson, D., Paultre, P. High-Strength Concrete Columns Confined by Rectangular Ties. Journal of Structural Engineering. 1994. 120(3). Pp. 783–804. DOI: 10.1061/(ASCE)0733-9445(1994)120:3(783)
20. Al, S.J., Ibrahim, A.M., Agarwal, V.C. Effect Steel Plate of Shear Reinforced Wide Beam Concrete. International Journal of Science and Research (IJSR). 2015. 4(2). Pp. 596–601.
21. Eklou, R.J., Yani, M.B., Saifullah, H.A., Sangadji, S., Kristiawan, S.A. Experimental study: Shear behaviour of reinforced concrete beams using steel plate strips as shear reinforcement. IOP Conference Series: Materials Science and Engineering. 2021. 1144. Article no. 012040. DOI: 10.1088/1757-899X/1144/1/012040
22. Mander, J.B., Priestley, M.J., Park, R. Theoretical Stress-Strain Model for Confined Concrete. Journal of Structural Engineering. 1988. 114(8). Pp. 1804–1826.
23. Ali, M., Abbas, S., Azevedo, A.R.G. de, Marvila, M.T., Khan, M.I., Rafiq, W. Experimental and analytical investigation on the confinement behavior of low strength concrete under axial compression. Structures. 2022. 36. Pp. 303–313. DOI: 10.1016/j.istruc.2021.12.038
24. Chang, W., Hao, M., Zheng, W. Strength and ductility of laterally confined concrete. Structural Concrete. 2021. 22(5). Pp 2967–2991. DOI: 10.1002/suco.202000299
25. Attard, M.M., Setunge, S. Stress-Strain Relationship of Confined and Unconfined Concrete. Materials Journal. 1996. 93(5). Pp. 432–442.
26. Zhao, D., Zhang, J., Lu, L., Liang, H., Ma, Z. The Strength in Axial Compression of Aluminum Alloy Tube Confined Concrete Columns with a Circular Hollow Section: Experimental Results. Buildings. 2022. 12(5). Article no. 699. DOI: 10.3390/buildings12050699
27. Wang, L., Huang, X., Xu, F. Stress–Strain Model of High-Strength Concrete Confined by Lateral Ties under Axial Compression. Buildings. 2023. 13(4). Article no. 870. DOI: 10.3390/buildings13040870
28. Li, Y., Liu, F., Du, T., Pan, Y., Yang, H., Li, Y. Experimental behavior of axially loaded circular high strength concrete-filled high-strength steel tubular stub columns after exposure to fire. Thin-Walled Structures. 2024. 203. Article no. 112189. DOI: https://doi.org/10.1016/j.tws.2024.112189
29. Liu, W.-W., Ouyang, L.-J., Gao, W.-Y., Liang, J., Wang, T.-C., Song, J., Yang, J. Repair of fire-damaged RC square columns with CFRP textile-reinforced ECC matrix. Engineering Structures. 2023. 292. Article no. 116530. DOI: 10.1016/j.engstruct.2023.116530
30. Kanavaris, F., Jedrzejewska, A., Sfikas, I.P., Schlicke, D., Kuperman, S., Smilauer, V., Honorio, T., Fairbairn, E.M.R., Valentim, G., Faria, E.F. de, Azenha, M. Enhanced massivity index based on evidence from case studies: Towards a robust pre-design assessment of early-age thermal cracking risk and practical recommendations. Construction and Building Materials. 2021. 271. Article no. 121570. DOI: 10.1016/j.conbuildmat.2020.121570

Information about the authors:

Bondan Kartika Pradipta*,*
E-mail: bondankartika@student.uns.ac.id

Muhammad Yani Bhayusukma*, PhD*
E-mail: muhammadyani@staff.uns.ac.id

Sholihin As'ad*, PhD*
E-mail: sholihinasad@staff.uns.ac.id

Received 15.08.2024. Approved after reviewing 05.01.2025. Accepted 07.01.2025.

Magazine of Civil Engineering. 2025. 18(1). Article No. 13305

Magazine of Civil Engineering

journal homepage: http://engstroy.spbstu.ru/

ISSN
2712-8172

Research article

UDC 624.074.433

DOI: 10.34910/MCE.133.5

Natural vibrations of buried pipeline section

T.V. Maltseva , ***A.V. Dmitriev*** , ***V.G. Sokolov***

Industrial University of Tyumen, Tyumen, Russian Federation

maltsevatv@tyuiu.ru

Keywords: natural vibration, finite element method, half momentless theory of cylindrical shells, frequency of vibrations, linear-elastic soil

Abstract. To ensure reliable operation of the pipeline, the design takes into account the natural vibration of the structure caused by the uniform flow of the product along the pipeline. A pipeline section in the form of a steel-concrete cylindrical shell placed in the soil condition is considered. The inner part of the pipeline is made of steel, and the exterior is covered with a concrete layer 30–50 mm thick. Determination of natural vibration frequencies for a two-layer cylindrical shell in the soil is clarified using two methods. The first method is analytical, according to which the dependence for the frequency is obtained using the half momentless theory of cylindrical shells. The second is numerical and is based on the finite element method (FEM) with the construction of the computational model in the Lira Sapr environment. Modeling of steel and concrete layers of the composite shell in the software package was carried out by 4-node plates, which are combined into a common structure by means of absolutely rigid bodies (ARB). Two cases of taking into account the soil condition surrounding the shell were considered. In the first case, a soil mass (with dimensions of 5.3×5.3 m) is created by volumetric bodies, while in the second case, the pastel coefficient for the concrete layer is specified. It was found that the second method of setting the soil conditions allowed to reduce the time of data input by 5–6 times with the same results obtained. The discrepancy between the frequencies of natural vibration for the object of study determined by the analytical method and FEM does not exceed 10 %, and for the first 3 frequencies of the spectrum is not more than 6 %, therefore, both methods are applicable. The use of an analytical expression made it possible to obtain results an order of magnitude faster with the pastel coefficient than with the help of numerical soil modeling using volumetric elements.

Funding: The article was prepared with the financial support of the Ministry of Education and Science of Russian Federation the project “Computer modeling of mechanical, temperature and dynamic processes in weak and permafrost soils to ensure the reliability of soil foundations of engineering structures” (No. FEWN-2024-0006)

Citation: Maltseva, T.V., Dmitriev, A.V., Sokolov, V.G. Natural vibrations of buried pipeline section. Magazine of Civil Engineering. 2025. 18(1). Article no. 13305. DOI: 10.34910/MCE.133.5

1. Introduction

Trunk pipelines are laid in different soil conditions, including areas with predicted watering and in waterlogged soils. For stability calculations, the pipeline section is represented as a cylindrical shell placed in the different soil condition. To prevent floating of the pipeline section, balancing measures are carried out for such sections. Steel pipelines are protected by concrete weights, which in the course of works can damage the original geometry of the pipe cross-section and negatively affect the reliable operation of the structure. One of the options to exclude such situations is the use of pipe-concrete products, the inner part of which is made of large-diameter steel pipes (d < 1000 mm) with the parameter $0.015 \le h/R \le 0.05$ and the outer part is formed by a concrete layer 40–100 mm thick. The reliability of such structures must be ensured by vibration resistance design calculations. Natural vibration can arise due to the movement of the pumped product. The sources offer calculation methods using analytical expressions and numerical solutions obtained by the finite element method (FEM) in various software packages. Below is an analysis of these works and the vibration resistance calculation models used in them.

In publications, there is the rod models of pipeline without influence of soil. In [1], the influence of critical values of fluid flow velocities in a pipe on the natural vibration of the pipe section is considered. The pipe in static equilibrium loses stability. Based on the Timoshenko beam theory, equations describing nonlinear vibration near a nontrivial static equilibrium configuration are formulated and the influence of system parameters on the equilibrium configuration, critical velocity, and frequency of natural vibration is shown.

In [2], the effect of fluid velocity on the dynamic characteristics of the pipe was studied using two methods: the derived analytical expressions for the critical flow velocity and natural frequencies of the pipe and the developed FEM. However, the developed FEM cannot reflect the effect of fluid flow on the pipe vibration mode.

In the study [3], the flow characteristics in the pipe are studied using computational fluid dynamics by numerical solution of low velocity compressible flow problems. In all these works, to determine the frequencies of natural vibrations of single-layer pipelines, taking into account the velocity of the flowing fluid, it is proposed to use analytical expressions or numerical solutions obtained for the calculation scheme of the pipeline in the form of a rod without taking into account the influence of the external environment on the pipe. The papers show the influence of static [4] and dynamic [5] ground modes on the vibrations of the underground pipeline. It is revealed that the oscillatory process of the pipeline can be realized at frequencies close to resonance frequencies. At frequencies close to resonance, the values of moments can be large in the pipeline sections, which is the cause of the pipeline stability loss. Pipelines partially resting on the ground based on the rod theory were studied in [6]. This approach does not allow to take into account the section deformation, and it was proposed to use it for the calculation of thick-walled cylindrical shells with parameters $0.07 < h/R < 0.125$.

The application of cylindrical shell theory to the calculation of pipelines made it possible to take into account vibrations in the transverse direction of the pipeline. In [7], the vibrations of an underwater pipeline for the pipe-liquid-soil system were investigated, but the issue of internal pressure acting on the pipeline walls was not considered. In [8, 9], the influence of internal unsteady pressure on the bending vibrations of the pipe was studied for closed cylindrical shells, but the influence of the external environment was not studied. The authors of [10–12] used different shell theories: Sodel, Flügge, Morley–Koiter and Donnell to determine the frequencies of natural vibrations of the pipeline. The result of the solution within the framework of these theories is the determinant for determining the natural frequency of vibrations, which was found in [13] for aluminum shells. In [14, 15], radial vibrations of the shell without taking into account the ground conditions are studied, the solution is obtained using the Vlasov–Novozhilov half momentless theory of cylindrical shells. In [16], analytical dependences for determining the frequencies of natural vibrations of a large-diameter pipeline partially buried in the ground were obtained. In [17], a similar approach is realized for a 2-parameter soil foundation. In [18], the natural frequencies are obtained for a metal-ceramic cylindrical shell placed in an elastic Pasternak base, but the internal pressure from the pumped product is not taken into account. Works [19, 20] are devoted to 3-layer shells, but the functional of the obtained solutions is extremely narrow, as it does not take into account the internal pressure on the wall of the shell, as well as the repulsion of the different soil conditions, preventing the deformation of the walls.

On the basis of the three-dimensional theory of elasticity, a parametric study was carried out, in which the influence of the parameters: shell thickness, mean radius, length and numbers of vibrational modes on the critical velocity of the shell without the influence of the ground was determined [21].

In [22], numerical modeling in ANSIS and, in [23], numerical modeling in ABAQUS were carried out, and the results of numerical modeling were compared with the results obtained from analytical formulas. Not always researchers compare the results of numerical modeling with analytical solutions. For example, in [24], the frequencies of natural vibrations for a subway tunnel are obtained in the MSC Patran Nastran software package, without comparison with analytical solutions, because they are not obtained for the problem under consideration. The issue of the influence of different soil conditions for buried pipelines is poorly studied.

The authors of [25, 26] investigated the free vibrations of cylindrical shells in an elastic inertia-free medium based on the Winkler–Pasternak hypothesis. The frequencies of free oscillations were obtained taking into account the deformation of the cross-section of the closed shell, but without taking into account the ground resistance forces. The influence of damping properties of the ground on the frequency characteristics of the pipeline is not taken into account.

In the problem [27] of static loss of pipeline stability solved by the FEM, the influence of rheological properties of the ground on the pipeline blowout is taken into account. The soil-pipeline interaction is considered using two approaches in [28]: laboratory experiment and numerical modeling using the discrete element method (DEM). The review article [29] analyzes experimental and numerical studies on pipeline deformations under the influence of dynamic processes in soils (seismic activity). Tests on a vibration test bench to estimate the soil resistance force required to move the buried pipeline in the transverse direction are presented. It is found that the drag force decreases at higher vibration amplitude and becomes more appreciable in case of complete liquefaction of sand, indicating its viscous behavior. The application of elasto-viscos-plastic soil models for structural design is shown in [30, 31]. However, these works do not take into account the natural vibrations of the pipeline in the ground caused by product transportation.

The authors of this article did not find any works, in which composite shells are considered in soil. This paper is devoted to partial elimination of the mentioned gaps, i.e., it is proposed to model the free vibrations of a steel-concrete cylindrical shell in an elastic soil medium analytically and numerically. A plane problem of the momentless shell theory is considered, in which the influence of the ground is taken into account through the radial ground repulsion. The ground repulsion varies along the circumference around the shell. The influence of the pumped product is taken into account through the longitudinal force.

The purpose of this paper is to study the influence of the soil on the configuration of the pipeline in its natural vibrations and to compare the natural frequencies of vibration for a closed two-layer cylindrical shell in the ground, obtained using the analytical formula and FEM.

2. Materials and Methods

The first method for determining the frequency of natural vibrations is analytical. The formula for the natural frequencies of vibrations for a two-layer cylindrical shell is obtained by the authors on the basis of the momentless theory of cylindrical shells and for the articulated support of the ends of the pipeline section under consideration. Here is the system of equations.

The equations of equilibrium for the cylindrical shell are written in the form [32]:

$$\begin{gathered}\frac{\partial T_1}{\partial \xi}+\frac{\partial S}{\partial \theta}+RQ_2\tau=-RX_1, \qquad \frac{\partial T_2}{\partial \theta}+\frac{\partial S}{\partial \xi}+\frac{R}{R_2^*}Q_2=-RX_2, \\ \frac{\partial Q_2}{\partial \theta}-\frac{R}{R_2^*}T_2-\frac{R}{R_1^*}T_1=-RX_3, \quad \frac{\partial M_1}{\partial \xi}+\frac{\partial H}{\partial \theta}-RQ_1=0, \quad \frac{\partial M_2}{\partial \theta}-\frac{\partial H}{\partial \xi}-RQ_2=0.\end{gathered} \tag{1}$$

From the formulas of the momentless theory:

$$\left(\frac{\partial \nu}{\partial \theta}+w=0;\ \frac{\partial \nu}{\partial \xi}+\frac{\partial u}{\partial \theta}=0;\ \vartheta_2=\frac{\partial w}{\partial \theta}-\nu\right),$$

the equations (1) take the form:

$$\begin{gathered}\frac{\partial^2 T_1}{\partial \xi^2}+\frac{\partial}{\partial \xi}\left(\tau\frac{\partial M_2}{\partial \theta}\right)-\frac{1}{R^2}\cdot\frac{\partial^3}{\partial \theta^3}\left(R_2^*\frac{\partial M_2}{\partial \theta}\right)-\frac{\partial}{\partial \theta}\left(\frac{1}{R^2}\cdot\frac{\partial M_2}{\partial \theta}\right)+ \\ +\frac{\partial^2}{\partial \theta^2}\left(\frac{R_2^*}{R_1^*}T_1\right)+R\frac{\partial X_1}{\partial \xi}-R\frac{\partial X_2}{\partial \theta}-\frac{\partial^2}{\partial \theta^2}\left(R_2^*X_3\right)=0.\end{gathered} \tag{2}$$

Forces of inertia: in longitudinal direction $X_1=-\dfrac{Rh\rho_0\partial^2 u}{\partial t^2}$, circumferentially $X_2=-Rh\rho_0\partial^2 v/\partial t^2$, radially $X_3=-\dfrac{Rh\rho_0\partial^2 w}{\partial t^2}+p_0-C_{1z}Rw\left(0.5-\alpha_1\cos\theta-\alpha_2\cos 3\theta\right)$. The components of the inertia force were substituted into the expression (2), taking into account the linear relationship between forces and deformations, displacements and deformations, we obtained the linearized differential equation of motion of the shell in displacements:

$$\frac{\partial^3 u}{\partial \xi^3}+\eta h_v^2\frac{\partial^3}{\partial \theta^3}\left(\frac{\partial^2 \vartheta_2}{\partial \theta^2}+\vartheta_2\right)+2\frac{\partial^2}{\partial \theta^2}\left(\frac{\partial^2 w}{\partial \xi^2}\varepsilon_0\right)-\frac{R}{E_0 h}p_0\frac{\partial^3 \vartheta_2}{\partial \theta^3}+\frac{1}{2}\frac{R^2 C_{1z}}{E_0 h}\frac{\partial^2 w}{\partial \theta^2}-$$
$$-\frac{R^2\rho_0}{Eh}\left(\frac{\partial^3 u}{\partial \xi \partial t^2}-\frac{\partial^3 v}{\partial \xi \partial t^2}-\frac{\partial^3 w}{\partial \theta^2 \partial t}\right)-\frac{R^2\alpha_1 C_{1z}}{E_0 h}\left(\frac{\partial^2 w}{\partial \theta^2}\cos\theta-2\frac{\partial w}{\partial \theta}\sin\theta-w\cos\theta\right)- \tag{3}$$
$$-\frac{R^2\alpha_2 C_{1z}}{E_0 h}\left(\frac{\partial^2 w}{\partial \theta^2}\cos 3\theta-\frac{\partial w}{\partial \theta}6\sin 3\theta-9w\cos 3\theta\right)=0.$$

The terms with the multiplier C_{1z} in the equation (3) describe the influence of the soil on the pipeline section. In problems on vibration stability in the framework of shell theory, these additional summands are considered for the first time. The backpressure of the ground medium in the radial direction (see Fig. 1) is described by the expression:

$$q_{gr}=C_{1z}\times R_w\times\left(0.5-\alpha_1\times\cos\theta-\alpha_2\times\cos 3\theta\right).$$

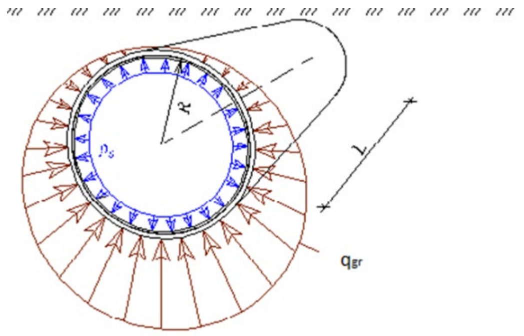

Figure 1. The effect of soil pressure on a pipeline section.

The boundary conditions described the articulated resting of the shell ends:

$$v\left\{\xi=0,\ \xi=\frac{L}{R}=0\right\},\quad \theta_2\left\{\xi=0,\ \xi=\frac{L}{R}=0\right\},$$
$$w\left\{\xi=0,\ \xi=\frac{L}{R}=0\right\},\quad \frac{\partial^2 w}{\partial \xi^2}\left\{\xi=0,\ \xi=\frac{L}{R}=0\right\}. \tag{4}$$

Solving the equations (3) with the conditions (4), obtain the displacements in the form of Fourier series.

Free oscillations of the cylindrical shell are represented by the harmonic law $\varphi(t)$ in the form of:

$$\varphi(t)=\sin\omega_{mn}\times t;\quad \varphi''=-\omega_{mn}^2\times\sin\omega_{mn}\times t, \tag{5}$$

where ω_{mn} is natural frequency.

Expression for determination of natural frequencies for the pipeline:

$$\omega_{mn}=\frac{1}{2\pi}\cdot\sqrt{\frac{\lambda_n^4+\eta\cdot m^4\left(m^2-1\right)\left(m^2-1+\dfrac{p^*}{\eta}\right)+C_{1z}^*\cdot m^4}{\rho_{sh}^*\cdot R_0\cdot h\left(\lambda_n^4 h_v+m^4+m^2\right)}}, \tag{6}$$

here: n is number of half-waves in the longitudinal direction; m is number of half-waves in the circumferential direction; $\lambda_n=\dfrac{n\times\pi\times R_0}{L\times\sqrt{h_v}}$ is length parameter of a two-layer cylindrical shell; L is section length (m); $R_0=R-Z_0$ is shell radius (m); R is radius of the steel layer of the shell (m);

$Z_0 = \dfrac{E_1 h_1^2 - E_2 h_2^2}{2\left(E_1 h_1 + E_2 h_2\right)}$ is distance from the jointing layer to the original surface (m) (Fig. 2); h_1, h_2 is thickness of concrete and steel layer of the shell, respectively (m); $h = h_1 + h_2$ is wall thickness of the two-layer shell (m); E_1 is modulus of elasticity of concrete layer (N/m^2); E_2 is modulus of elasticity of steel layer (N/m^2); $h_v = h/R_0 \sqrt{12\left(1-v^2\right)}$ is relative shell thickness parameter; ν is Poisson's ratio; $\eta = E_v/E_0$ is heterogeneity factor; $E_v = \left(1-v^2\right)\cdot 12D\big/h^3$ is reduced modulus of elasticity (bending) (N/m^2); $D = \dfrac{1}{3\left(1-v^2\right)}\left[E_1\left\{\left(h_1 - Z_0\right)^3 + Z_0^3\right\} + E_2\left\{\left(h_2 - Z_0\right)^3 - Z_0^3\right\}\right]$ is flexural stiffness (Nm); $E_0\left[E_1 h_1 + E_2 h_2\right]/h$ is reduced modulus of elasticity (tensile/compression) (N/m^2); $p^* = p_0\left(R_0\big/E_0 h \cdot h_v^2\right)$ is internal working pressure parameter; p_0 – internal pressure in the two-layer shell (N/m^2); $\rho_{sh}^* = \rho_0\left(R_0\big/E_0 \cdot h \cdot h_v^2\right)$ is shell material density parameter (c^2/m^2); $\rho_0 = \dfrac{1}{g}\left[\left(\gamma_1 h_1 + \gamma_2 h_2\right)/h\right]$ is reduced density of the shell material (N·c^2/m^4); γ_1 is concrete density N/m^3; γ_2 is steel density N/m^3; $C_{1z}^* = R_0^2 C_{1z}\big/E_{gr} h \cdot h_v^2$ is reduced coefficient of soil rigidity (posteli coefficient); $C_{1z} = E_{gr}\big/R_0\left(1+v_{gr}\right)$ is soil stiffness coefficient (N/m^3); E_{gr} is ground elastic modulus (N/m^2).

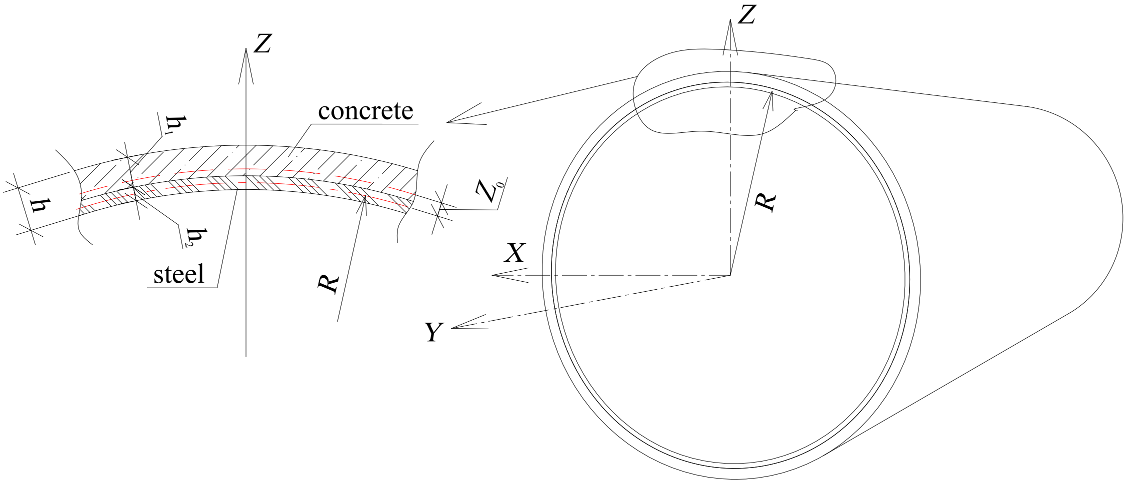

Figure 2. Geometric dimensions of the two-layer shell.

Lira Sapr software was used to calculate the natural vibration frequencies using the second method. Modeling of each layer of the two-layer shell (Fig. 3) was carried out by plates, and to ensure the joint operation of the layers were used to combine the displacements for each corresponding node by staging absolutely rigid bodies (ARB). The linear displacement constraint of the boundary nodes along the Z (X3) and Y (X2) axis was introduced to create a hinge-unstiffened shell end fixation.

Consideration of the soil, in which the shell is placed, was performed in two ways. In the first method, a ground mass of volumetric bodies with a cross-section size of 5.3×5.3 m was created. In the second method, the mass was not created, and the elastic rebound of the soil was taken into account by assigning the pastel coefficient C_{1z} = 473620 N/m^3. As external loads, only the own weight of the shell layers was taken into account (without taking into account the weight of the soil conditions). Determination of natural vibration frequencies was carried out using “Modal Analysis”, which was used to form a matrix of the masses of the structure and the number of vibration forms.

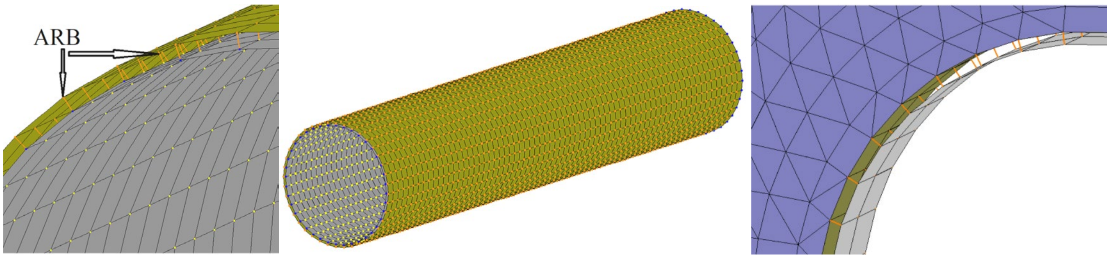

Figure 3. Modeling of a cylindrical shell.

3. Results and Discussion

For numerical implementation, a section of a cylindrical two-layer shell with the radius of the first layer R = 0.71 m and thickness h_1 = 18 mm is considered. The thickness of the second layer is h_2 = 40 mm. The length of the section under consideration is taken as 7, 8 and 9 m. The modulus of elasticity of concrete, modulus of elasticity of steel and density of layers are respectively equal to E_1 = 3.24711·10^{10} N/m^2, E_2 = 2.06·10^{11} N/m^2, γ_1 = 24516.6 N/m^3, γ_2 = 76982.2 N/m^3. Poisson's ratio for steel and concrete of class B30 is taken equal to ν = 0.3. The structure is placed in a ground medium with different ground deformation modulus and parameters: ground density is γ_{gr} = 11770 N/m^3; ground Poisson's ratio is ν_{gr} = 0.49. Internal pressure is assumed to be p_0 = 0 MPa.

The values of natural vibration frequencies for different lengths of pipe sections are summarized in Table 1. The first column shows the values of vibration frequencies using the analytical formula (6), the second column shows numerical solutions of vibration frequencies found using the FEM method when the soil medium array is created, the third column shows the frequencies found using the FEM method when the soil stiffness coefficient is set.

Analysis of the data in Table 1 shows that the difference in the frequency values determined by the FEM with the soil array assignment (column 2) and by assigning the bedding coefficient C_{1z} = 473620 (N/m^3) (column 3) does not exceed 2 %, therefore, in order to reduce the labor input during model creation, it is recommended to use the second method of taking into account different soil conditions using the C_{1z} coefficient. The second method allowed to reduce the time of data processing by the processor by 5–6 times.

Table 1. The results of determining the frequencies of natural oscillations in various ways.

Analytical formula (Hz)	PC Lira Sapr mass (Hz)	PC Lira Sapr ratio C_{1z} (Hz)	Analytical formula (Hz)	PC Lira Sapr mass (Hz)	PC Lira Sapr ratio C_{1z} (Hz)	Analytical formula (Hz)	PC Lira Sapr mass (Hz)	PC Lira Sapr ratio C_{1z} (Hz)
1	**2**	**3**	**1**	**2**	**3**	**1**	**2**	**3**
L=7 m (R/L=1/10)			L=8 m (R/L=1/11)			L=9 m (R/L=1/13)		
ω_{11}=71.52	ω_{11}=69.80	ω_{11}=68.99	ω_{11}=55.16	ω_{11}=57.08	ω_{11}=56.04	ω_{11}=43.86	ω_{11}=48.4	ω_{11}=47.14
ω_{12}=64.23	ω_{12}=69.90	ω_{12}=63.13	ω_{12}=62.53	ω_{12}=68.21	ω_{12}=67.58	ω_{12}=61.61	ω_{12}=67.2	ω_{12}=66.54
ω_{13}=169.4	ω_{13}=164.7	ω_{13}=164.4	ω_{13}=169.3	ω_{13}=164.10	ω_{13}=163.8	ω_{13}=169.2	ω_{13}=163.8	ω_{13}=163.5
ω_{22}=109.2	ω_{22}=109.6	ω_{22}=109.3	ω_{22}=92.18	ω_{22}=95.40	ω_{22}=95.01	ω_{22}=81.62	ω_{22}=86.2	ω_{22}=79.20
ω_{23}=174.3	ω_{23}=174.6	ω_{23}=174.3	ω_{23}=172.1	ω_{23}=170.9	ω_{23}=170.6	ω_{23}=170.9	ω_{23}=168.7	ω_{23}= 168.4
ω_{32}=211.9	ω_{32}=186.5	ω_{32}=186.3	ω_{32}=167.4	ω_{32}=154.8	ω_{32}=154.6	ω_{32}=137.6	ω_{32}=132.3	ω_{32}=132.0
ω_{33}=194.6	ω_{33}=199.7	ω_{33}=199.5	ω_{33}=184.4	ω_{33}=188.2	ω_{33}= 1879	ω_{33}=178.7	ω_{33}= 181.3	ω_{33}= 180.7

Comparison of the results of determining the frequencies of natural vibrations using the expression (6) and FEM shows that the difference for the first 3 frequencies does not exceed 6 %, and for the rest of the results 10 % (Fig. 4).

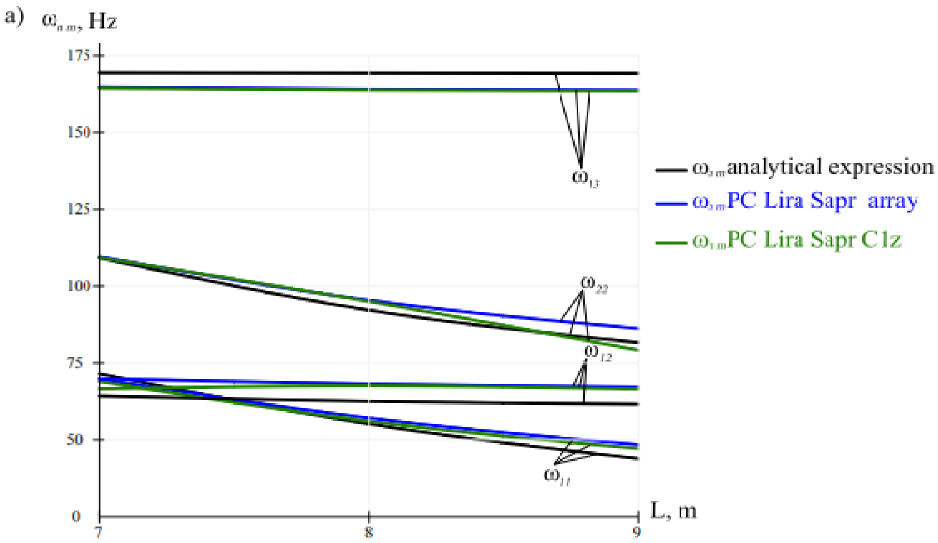

Peat C_{1z} **= 473620 N/m³;** γ_{gr} **= 11770 N/m³;** E_{gr} **= 5·10⁵ N/m²;** ν_{gr} **= 0.49**

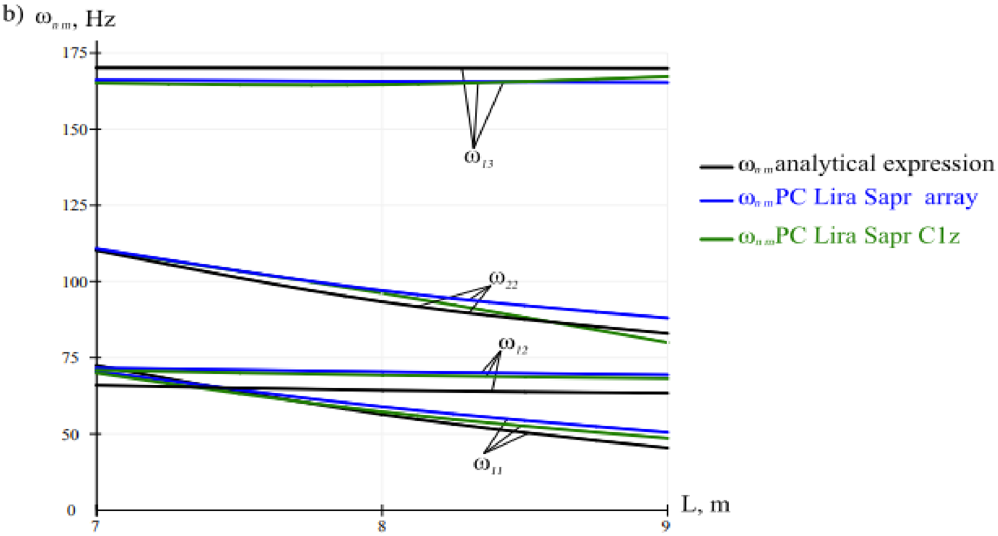

Loose bulk soil C_{1z} **= 3136416 N/m³;** γ_{gr} **= 16660 N/m³;** E_{gr} **= 3·10⁶ N/m²;** ν_{gr} **= 0.35**

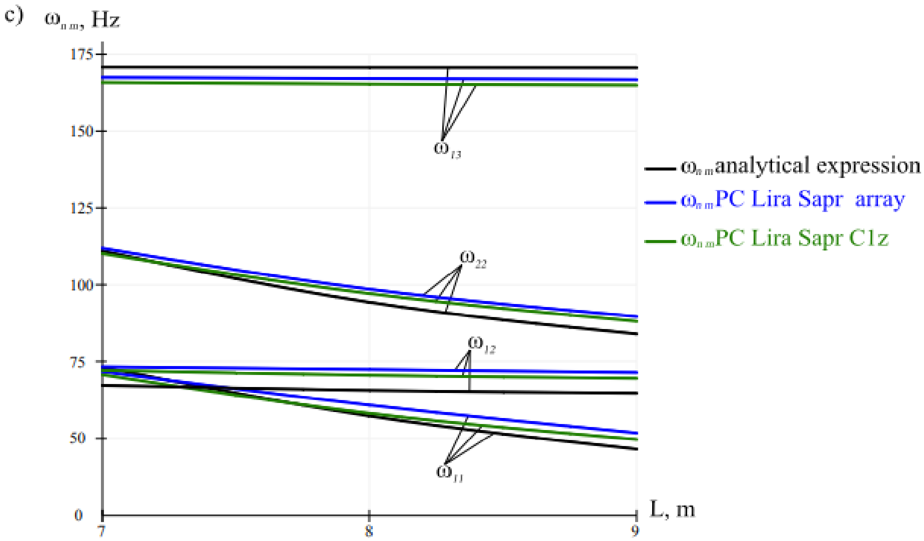

Bulk compacted soil C_{1z} **= 5227360 N/m³;** γ_{gr} **= 17660 N/m³;** E_{gr} **= 5·10⁶ N/m²;** ν_{gr} **= 0.35**

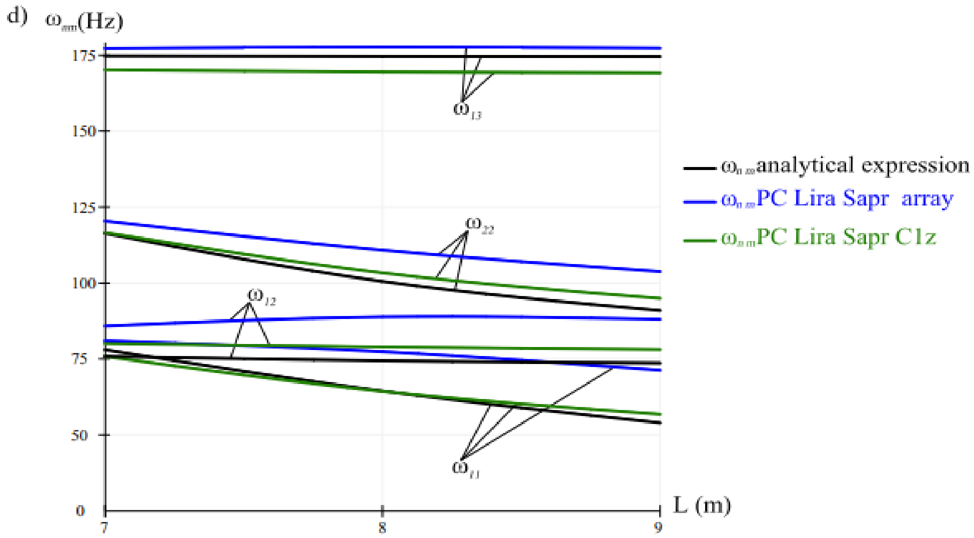

Clay C_{1z} = 19878694 N/m^3; γ_{gr} = 19620 N/m^3; E_{gr} = 2·10^7 N/m^3; ν_{gr} = 0.42

Figure 4. Variation of natural oscillation frequency from the length of the pipeline section.

For the pipe section with length of 7 m, the minimum frequency was ω_{12} (Fig. 4c), the change in cross-section corresponded to the shell form of oscillations. For the pipe sections of lengths 8 and 9 m, the minimum frequencies corresponded to the ω_{11} form (beam without cross-sectional deformation, Fig. 4a). All other vibration shapes were shell-shaped. Increasing the length of the pipe section by 1 m resulted in an average 1.5–3.1 % decrease in natural vibration frequencies (Figs. 4a–d). The increase in the stiffness of the soil led to an increase in the frequency of natural vibrations of the system steel-concrete shell+soil. The stiffness of the system in the cross-section of the pipe increased due to the soil (Figs. 5, 6). For the seven vibration forms, the changes in the pipe configuration taking into account the soil stiffness coefficient are shown in Fig. 5. Taking into account the influence of the soil massif, the first three vibration forms are shown (Fig. 6).

The analytical method has clear advantages over the FEM, since the calculation of frequencies took 10 times less time with almost the same results. Also, using the analytical method, it is possible to take into account the influence of internal working pressure by the parameter p*, while using the FEM, this factor cannot be taken into account, because when modeling this loading, it is taken into account not as a force preventing the deformation of the cross section but as an additional mass taken into account when calculating frequencies, so all the data in Table 1 are obtained with zero internal pressure.

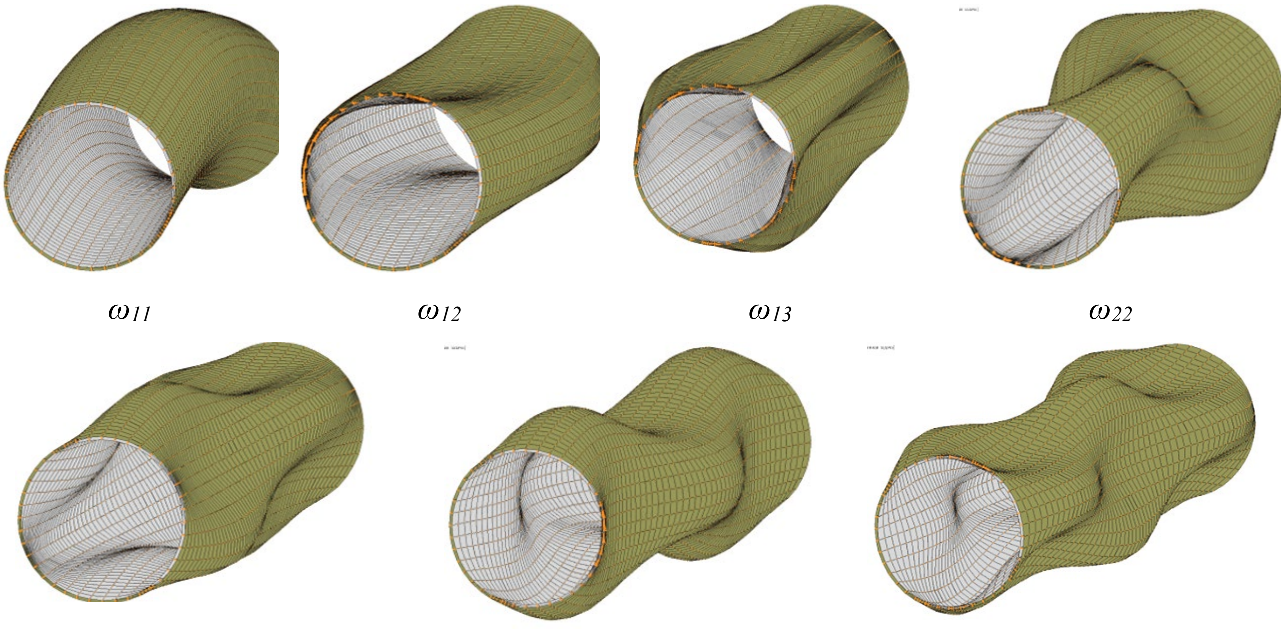

ω_{11} ω_{12} ω_{13} ω_{22}

ω_{23} ω_{32} ω_{33}

Figure 5. Waveforms for the pipeline section under consideration.

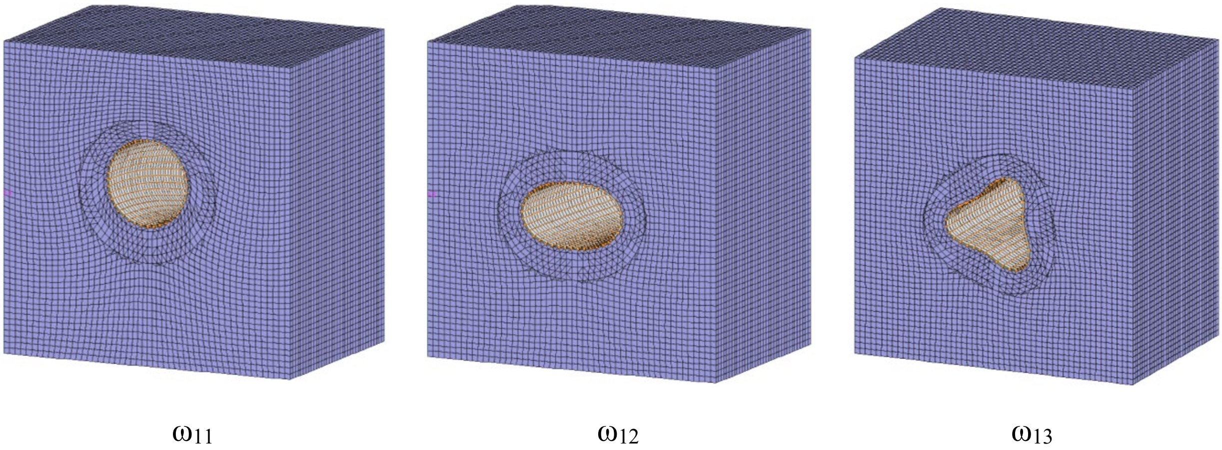
ω_{11} ω_{12} ω_{13}

Figure 6. The waveforms for the pipeline section under consideration at n=1 in the soil mass (the size of the mass is 5.3×5.3 m in cross section).

4. Conclusion

1. The discrepancy between the frequencies of natural vibrations for the object of study determined by the analytical method and FEM does not exceed 10 %, and for the first 3 frequencies of the spectrum does not exceed 6 %, therefore, all the methods are applicable. The use of an analytical expression made it possible to obtain results an order of magnitude faster with the pastel coefficient than with the help of numerical soil modeling using volumetric elements.
2. When calculating the frequencies of natural vibrations by the FEM, the second method of setting ground conditions allows reducing the time of data input by 5–6 times with the same results.
3. Based on the analysis performed, it is recommended to use the analytical expression given in this paper when designing large-diameter pipeline transportation structures for the purpose of maximum productivity.

References

1. Tan, X., Tang, Y.-Qi. Free vibration analysis of Timoshenko pipes with fixed boundary conditions conveying high velocity fluid. Heliyon. 2023. 9(4). Article no. e14716. DOI: 10.1016/j.heliyon.2023.e14716
2. Shui, B., Li, Y., Luo, Y., Luo, F. Free vibration analysis of Timoshenko pipes conveying fluid with gravity and different boundary conditions. Journal of Mechanics. 2023. 39. Pp. 367–384. DOI: 10.1093/jom/ufad031
3. Shao, Y.F., Fan, X., Shu, S. et al. Natural Frequencies, Critical Velocity and Equilibriums of Fixed–Fixed Timoshenko Pipes Conveying Fluid. Journal of Vibration Engineering & Technologies. 2022. 10. Pp. 1623–1635. DOI: 10.1007/s42417-022-00469-0
4. Mardonov, B., An, E., Shojalilov, S., Khakimova, Y., Ismoilova, G. Transverse Vibrations of Underground Pipelines with Different Interaction Laws of Pipe with Surrounding Soils. E3S Web of Conferences. 2021. 264. Article no. 02035. DOI: 10.1051/e3sconf/202126402035
5. Sultanov, K.S., Vatin, N.I. Wave Theory of Seismic Resistance of Underground Pipelines. Applied Sciences (Switzerland). 2021. 11(4). Article no. 1797. DOI: 10.3390/app11041797
6. Xü, W.-H., Xie, W.-D., Gao, X.-F., Ma, Y.-X. Study on vortex-induced vibrations (VIV) of free spanning pipeline considering pipe-soil interaction boundary conditions. Journal of Ship Mechanics. 2018. 51. Pp. 446–453. DOI: 10.3969/j.issn.1007-7294.2018.04.007
7. Leontiev, E.V., Travush V.I. Fluctuations of pipelines of gas-containing liquids under changing bearing conditions. Structural Mechanics of Engineering Constructions and Buildings. 2022. 18(6). Pp. 544–551. DOI: 10.22363/1815-5235-2022-18-6-544-551
8. Yulmukhametov, A.A. Bending vibrations of the pipeline under the influence of the internal added mass. AIP Conference Proceedings. 2020. 2288(1). Article no. 030093. DOI: 10.1063/5.0028885
9. Shakiryanov, M.M., Akhmedyanov, F.V. Nonlinear Oscillations of a Pipeline under the Action of Variable Internal Pressure and Moving Supports. Journal of Machinery Manufacture and Reliability. 2020. 49. Pp. 555–561. DOI: 10.3103/S1052618820070134
10. Farshidianfar, A., Oliazadeh, P. Free Vibration Analysis of Circular Cylindrical Shells: Comparison of Different Shell Theories. International Journal of Mechanics and Applications. 2012. 2(5). Pp. 74–80. DOI: 10.5923/j.mechanics.20120205.04
11. Oliazadeh, P., Farshidianfar, M., Farshidianfar, A. Exact analysis of resonance frequency and mode shapes of isotropic and laminated composite cylindrical shells; Part I: Analytical studies. Journal of Mechanical Science and Technology. 2013. 27. Pp. 3635–3643. DOI: 10.1007/s12206-013-0905-1
12. Lee, H., Kwak, M.K. Free vibration analysis of a circular cylindrical shell using the Rayleigh–Ritz method and comparison of different shell theories. Journal of Sound and Vibration. 2015. 353. Pp. 344–377. DOI: 10.1016/j.jsv.2015.05.028
13. Piacsek, A., Harris, N. Resonance frequencies of a spherical aluminum shell subject to prestress from internal fluid pressure. The Journal of the Acoustical Society of America. 2019. 145(3). Article no. 1881. DOI: 10.1121/1.5101813
14. Kumar, A., Das, S., Wahi, P. Instabilities of thin circular cylindrical shells under radial loading. International Journal of Mechanical Sciences. 2015. 104. Pp. 174–189. DOI: 10.1016/j.ijmecsci.2015.10.003

15. Kumar, A., Das, S., Wahi, P. Effect of radial loads on the natural frequencies of thin-walled circular cylindrical shells. International Journal of Mechanical Sciences. 2017. 122. Pp. 37–52. DOI: 10.1016/j.ijmecsci.2016.12.024
16. Sokolov, V. Razov, I. Free Oscillations of Semi-underground Trunk Thin-Wall Oil Pipelines of Big Diameter. Advances in Intelligent Systems and Computing. 982. International Scientific Conference Energy Management of Municipal Facilities and Sustainable Energy Technologies EMMFT 2018. Springer. Cham, 2020. Pp. 615–627. DOI: 10.1007/978-3-030-19756-8_58
17. Bochkarev, S.A. Natural Vibrations of a Cylindrical Shell with Fluid Partly Resting on a Two-Parameter Elastic Foundation. International Journal of Structural Stability and Dynamics. 2022. 22(6). Article no. 2250071. DOI: 10.1142/S0219455422500717
18. Shahbaztabar, A., Izadi, A., Sadeghian, M., Kazemi M. Free vibration analysis of FGM circular cylindrical shells resting on the Pasternak foundation and partially in contact with stationary fluid. Applied Acoustics. 2019. 153. Pp. 87–101. DOI: 10.1016/j.apacoust.2019.04.012
19. Baghlani, A., Khayat, M., Dehghan, S.M. Free vibration analysis of FGM cylindrical shells surrounded by Pasternak elastic foundation in thermal environment considering fluid-structure interaction. Applied Mathematical Modelling. 2020. 78. Pp. 550–575. DOI: 10.1016/j.apm.2019.10.023
20. Alshabatat, N., Zannon, M. Natural frequencies analysis of functionally graded circular cylindrical shells. Applied and Computational Mechanics. 2021. 15. Pp. 105–122. DOI: 10.24132/acm.2021.654
21. Ebrahimi, Z. Free vibration and stability analysis of a functionally graded cylindrical shell embedded in piezoelectric layers conveying fluid flow. Journal of Vibration and Control. 2022. 29(11–12). Pp. 2515–2527. DOI: 10.1177/10775463221081184
22. Dyachenko, I.A. Mironov, A.A., Sverdlik Yu.M. Comparative analysis of theories and finite element models for calculating free vibrations of cylindrical shells. Transport Systems. 2019. 3(13). Pp. 55–63. DOI: 10.46960/62045_2019_3_55
23. Kumar, A., Das, S., Wahi, P. Instabilities of thin circular cylindrical shells under radial loading. International Journal of Mechanical Sciences. 2015. 104. Pp. 174–189. DOI: 10.1016/j.ijmecsci.2015.10.003
24. Dashevskij, M., Mitroshin, Mondrus, V.V., Sizov. D. Impact of metro induced ground-borne vibration on urban development. Magazine of Civil Engineering. 2021. 6(106). Article no. 10602. DOI: 10.34910/MCE.106.2
25. Bochkarev, S.A. Natural vibrations of cylindrical shell partially resting on elastic foundation. Computational Continuum Mechanics. 2017. 10(4). Pp. 406–415. DOI: 10.7242/1999-6691/2017.10.4.32
26. Kuznetsova, E.L., Leonenko, D.V., Starovoytov, E.I. Natural vibrations of three-layer circular cylindrical shells in an elastic medium. Mechanics of Solids. 2015. 50. Pp. 359–366. DOI: 10.3103/S0025654415030127
27. Mardonov, B., Mirzaev, I., Nishonov, N.A., An, E.V., Kosimov, E.A. Buckling of underground pipelines and appropriate countermeasures against liquefaction-induced uplift of pipes. VI International Scientific Conference “Mechanical Science and Technology Update” 22–23 March 2022. Omsk, 2022. DOI: 10.25206/978-5-8149-3453-6-2022-45-53
28. Calvetti, F. Experimental and Numerical Analysis of Soil–Pipe Interaction. Journal of Geotechnical and Geoenvironmental Engineering. 2004. 130(12). Pp. 1292–1299. DOI: 10.1061/(ASCE)1090-0241(2004)130:12(1292)
29. Castiglia, M., Fierro,T., Santucci de Magistris, F. Pipeline Performances under Earthquake-Induced Soil Liquefaction: State of the Art on Real Observations, Model Tests, and Numerical Simulations, Shock and Vibration. 2020. 2020. Article no. 8874200. DOI: 10.1155/2020/8874200
30. Maltseva, T.V., Nabokov, A.V., Vatin, N. Consolidation of water-saturated viscoelastic subgrade. Magazine of Civil Engineering. 2024. 17(1). Article no. 12502. DOI: 10.34910/MCE.125.2
31. Vasenin, A., Sabri, M.M. Compressible soil thickness and settlement prediction using elastoviscoplastic models: a comprehensive method. Magazine of Civil Engineering. 2024. 17(4). Article no. 12803. DOI: 10.34910/MCE.128.3
32. Sokolov, V.G., Razov, I.O., Lobodenko, E.I., Volynets, S.I. Free Vibrations of a Thin-Walled Two-Layer Pipeline, Taking into Account the Effect of the Longitudinal Compressive Force in a Semi-Underground Laying. Architecture, Construction, Transport. 2022. 2. Pp. 47–57. DOI: 10.31660/2782-232X-2022-2-47-57

Information about the authors:

Tatyana Maltseva*, Doctor of Physics and Mathematics*
ORCID: https://orcid.org/0000-0002-0274-0673
E-mail: maltsevatv@tyuiu.ru

Andrey Dmitriev*, PhD in Technical Sciences*
ORCID: https://orcid.org/0000-0003-3832-5321
E-mail: dmitrievav@tyuiu.ru

Vladimir Sokolov*, Doctor of Technical Sciences*
ORCID: https://orcid.org/0000-0002-3380-0835
E-mail: sokolovvg@tyuiu.ru

Received 18.11.2024. Approved after reviewing 20.01.2025. Accepted 21.01.2025.

Magazine of Civil Engineering. 2025. 18(1). Article No. 13306

Magazine of Civil Engineering

journal homepage: http://engstroy.spbstu.ru/

ISSN
2712-8172

Research article

UDC 699.86

DOI: 10.34910/MCE.133.6

Correlation model for cost and technical characteristics of thermal insulation material used in enclosing structure

K.A. Lukash, E.A. Shurshilin ✉, Y.A. Olekhnovich , A.E. Radaev

Peter the Great St. Petersburg Polytechnic University, St. Petersburg, Russian Federation

✉ *Shurshilinegor@yandex.ru*

Keywords: housing construction object, enclosing structure, mathematical model, correlation, thermal insulation material, specific cost, technical characteristics

Abstract. Research relevance is determined by the need for development of the effective design and organizational-technological solutions at the stage of design or renovation of housing construction objects in the conditions of tightening requirements for the duration, cost, and quality of construction projects being implemented, as well as the limitations of scientific developments used for determination of the characteristics for the above-mentioned solutions in terms of the completeness of the factors under consideration and the objectivity of taking into account the relationships between them. Problem statement: The paper considers a design solution formed in relation to the enclosing structure within housing construction object, which involves the use of thermal insulation material as a separate layer of the structure. It is necessary to form mathematical description of the relationships between the technical and cost characteristics of the thermal insulation material and the energy and economic efficiency indicators of the design solution. Research aim: development of tools to determine the characteristics of design solutions formed in relation to the enclosing structure within housing construction object, based on energy and economic efficiency criteria. Research tasks are the following: review and comparative analysis of scientific developments in the field of determination of characteristics for design solutions formed in relation to enclosing structures within housing construction objects; development of analytical model describing correlation between the specific cost and technical characteristics of thermal insulation material used as a separate layer of the enclosing structure; implementation of the model on a practical example; formation of recommendations for the use of the model during solution of the problems related to determination of characteristics of design solutions for enclosing structures. Results. The analytical model has been developed that describes the linear dependence of the specific cost of thermal insulation material used in the enclosing structure on its technical characteristics. The results of the implementation of the analytical model on a practical example confirmed its high practical significance. Findings. The developed analytical model can be used for predictive calculation of the specific cost of thermal insulation material corresponding to the mineral wool on the basis of the specified values for its technical characteristics. Due to the composition of the factors taken into account, the developed analytical model can be effectively integrated into the structure of tools for determination of the characteristics for design solutions related to enclosing structures within housing construction object on the basis of energy and economic efficiency criteria.

Citation: Lukash, K.A., Shurshilin, E.A., Olekhnovich, Y.A., Radaev, A.E. Correlation model for cost and technical characteristics of thermal insulation material used in enclosing structure. Magazine of Civil Engineering. 2025. 18(1). Article no. 13306. DOI: 10.34910/MCE.133.6

1. *Introduction*

In the modern conditions of the construction industry's upgrowth, characterized by tightening of requirements for the duration, cost, and quality of construction projects, the issues of rational justification of design and organizational-technological solutions (formed at the stage of design or renovation of housing construction objects) with taking into account energy and economic efficiency indicators, gain particular importance. At the same time, the above-mentioned indicators are generally significantly influenced by the characteristics of enclosing structures within construction objects. Nevertheless, the results of the preliminary analysis of scientific developments related to the formation of design solutions for enclosing structures have shown the limitations of the applied tools in terms of objectively taking into account the relationships between the characteristics of design solutions in terms of the technologies and materials used and the corresponding indicators of energy and economic efficiency. At the same time, the problem of mathematical description of the above-mentioned relationships is aggravated by the presence of a wide variety of applied building materials and technologies. The above circumstances determined the feasibility of conduction of the research aimed at the development of tools for determination of the characteristics for design solutions formed in relation to the enclosing structure as part of housing construction object on the basis of energy and economic efficiency criteria.

The object of the research is a design solution formed in relation to the enclosing structure as part of housing construction object, which involves the use of thermal insulation material as a separate layer in the structure.

The subject of the research is the relationship between the characteristics of the thermal insulation material within the enclosing structure and the indicators connected to the energy and economic efficiency of the corresponding design solution.

At the initial stages of the research, the review and comparative analysis of scientific developments in the field of determination of the characteristics for design solutions formed in relation to enclosing structures within construction objects has been conducted. Based on the results of the mentioned-above review and analysis, the following conclusions have been made:

1. Scientific developments related to the subject area under consideration are classified according to the following main features:
   - category of scientific results: methodological developments [1–4]; instrumental developments [5–37];
   - category of instrumental developments: models and methods based on analytical calculation [5–19]; models and methods involving the implementation of optimization procedures [20–37];
   - research area: analysis of the relationships between the characteristics of design solutions for enclosing structures within housing construction objects and the corresponding energy efficiency indicators on the basis of experimental and statistical studies [1–4]; determination of the characteristics related to the temperature and thermal conditions for enclosing structures within housing construction objects [5–12]; determination of energy [13–15] and economic [16–19] efficiency indicators for design solutions connected to enclosing structures within housing construction projects; determination of characteristics for design solutions connected to enclosing structures within housing construction projects on the basis of energy and economic efficiency criteria [20–37];
   - category of computational algorithms used: stochastic swarm intelligence algorithms [20, 25, 29, 35]; stochastic evolutionary algorithms [23, 27, 29–33, 36, 37]; deterministic integer convex optimization algorithms [26].
2. The overwhelming majority of scientific developments have relatively low practical significance due to the following features:
   - significant dependence of the results obtained on the volume and quality of the initial experimental or statistical data [1–4, 24, 28];
   - lack of description for principles related to the developments' application during the procedures of comparative analysis of various design solutions for enclosing structures [5, 6, 8, 10, 12];
   - high labor intensity of the calculation process's implementation due to the need for experimental justification of individual formula components for each alternative variant of conditions related to the technological process of construction [7, 9, 11];
   - lack of consideration of the influence of the building materials' structure characteristics on the calculated values of energy efficiency indicators [12–15];
   - lack of direct consideration of changes over time in the construction object's operational characteristics on the calculated values of economic efficiency indicators [16, 17];
   - lack of consideration of the influence of design solutions' characteristics on the corresponding indicators of economic efficiency [21];

- impossibility of objective assessment of the development's practical significance due to absence of description of its implementation process on practical example, as well as obtained results [22];
- significant reduction of the area of admissible combinations of values for characteristics of the design solution during implementation of sequential analytical calculation [16, 17, 34];
- presence of a large number of binary unknown variables and indirect constraints associated with them, which causes relatively low convergence rate for the computational algorithm [20, 23, 25–27, 29, 31–33, 35–37];
- relatively high labor intensity of the calculation process, implementation due to necessity of creation of artificial neural network, its training and verification of obtained results [27, 29, 30, 33, 36, 37];
- relatively high labor intensity of the calculation process's implementation due to complex structure of mathematical expressions in the absence of appropriate software tools for automation of calculations [34].

Thus, based on the obtained results of the review of scientific developments, the conclusion has been made about insufficiency of the level of scientific elaboration of the issues related to the determination of the characteristics for design solutions formed in relation to enclosing structures within construction. The mentioned-above results also determined the formulation of following research objectives:

1. Development of the analytical model of the correlation between the specific cost and technical characteristics of thermal insulation material used in the enclosing structure.
2. Implementation of the developed model on a practical example.
3. Formulation of recommendations for the use of the developed model during the solution of the problems related to determination of the characteristics for design solutions connected to enclosing structures within housing construction objects.

2. *Materials and Methods*

The main provisions based on which the analytical model has been developed include the following:

1. The object of consideration is thermal insulation material used as a separate layer in the external enclosing structure of a housing construction project.
2. The specific – per unit area of the structure's surface – cost of thermal insulation material is determined by its technical characteristics, for which specific numerical values are known for various options (manufacturers and models) of the material. The recommended composition of technical characteristics determining the specific cost of thermal insulation material is presented in Table 1.
3. There is a functional dependence of the specific cost of thermal insulation material – dependent category – on the values of its technical characteristics (hereinafter referred to as the functional dependence).
4. The functional dependence is linear with respect to the following components (factors): the inversed value of the thermal conductivity coefficient; the ratio of other technical characteristics of the material to the thermal conductivity coefficient. The composition of the analytical model's factors corresponding to the recommended composition of the technical characteristics of the thermal insulation material is presented in Table 1.
5. The analytical model of the functional dependence (hereinafter referred to as the analytical model) is determined by an expression of the form:

$$\tilde{y} = \beta_0 + \sum_{j=1}^{n} \beta_j \cdot \theta_j, \tag{1}$$

where $\tilde{y}$ – predicted value of the unit cost of acquisition of thermal heat-insulating material (value of the dependent category), CU/m^2; n – number of factors taken into account in the analytical model, units; θ_j – factor value with index $j\left(j = 1, 2, \ldots, n\right)$, $MU_{\theta j}$; for more information, see Table 1; β_j – analytical model parameter is the coefficient of proportionality of the value of the dependent category to the value of the factor with the index $j\left(j = 1, 2, \ldots, n\right)$, (CU/(m$^2\cdot$ $MU_{\theta j}$); β_0 – an additional parameter of the analytical model is the constant of the unit cost for the material, CU/m^2.

Table 1. Description of the parameters of the thermal insulation material and the corresponding factors of the analytical model.

Index	Name of the technical characteristic for the thermal insulation material	Measure unit	Symbol	Name of the factor of the analytical model	Measure unit	Designation
1	2	3	4	5	6	7
j	–	$MU_{\chi j}$	χ_j	–	$MU_{\theta j}$	θ_j
1	Thermal conductivity coefficient	$\frac{W}{m \cdot {}^\circ C}$	λ	Inversed value of thermal conductivity coefficient	$\frac{m \cdot {}^\circ C}{W}$	$1/\lambda$
2	Thickness	m	δ	Ratio of the thickness to the thermal conductivity coefficient	$\frac{m^2 \cdot {}^\circ C}{W}$	δ/λ
3	Average density to the thermal conductivity coefficient	$\frac{kg}{m^3}$	ρ	Ratio of average density to the thermal conductivity coefficient	$\frac{kg \cdot {}^\circ C}{m^2 \cdot W}$	ρ/λ
4	Water absorption in 24 hours (by volume)	%	ν	Ratio of the water absorption in 24 hours (by volume) to the thermal conductivity coefficient	$\frac{\% \cdot m \cdot {}^\circ C}{W}$	ν/λ
5	Flammability group index [(1)]	-	φ	Ratio of the flammability group index to the thermal conductivity coefficient	$\frac{m \cdot {}^\circ C}{W}$	φ/λ
6	Vapor permeability coefficient	$\frac{mg}{m \cdot h \cdot Pa}$	μ	Ratio of the vapor permeability coefficient to the thermal conductivity coefficient	$\frac{mg \cdot {}^\circ C}{h \cdot Pa \cdot W}$	μ/λ

Note: (1) The parameter of the thermal heat-insulating material has the following alternative values: 1 – non-flammable material, 2 – flammability group “G3”; 3 – flammability group “G4”.

6. It is advisable to determine the parameters of the analytical model by implementation of the procedure related to the formation of a multifactorial linear regression model on the basis of statistical data containing information about the set of variants (models) of thermal insulation material in terms of the technical characteristics’ values specified in Table 1 (converted into the values of the factors connected to the analytical model), as well as the specific cost of the material; the formation of the mentioned-above statistical data is generally carried out without taking into account the operating conditions of a specific enclosing structure.
7. To assess the adequacy of the analytical model, it is advisable to use the coefficient of determination.

The initial data necessary for the formation of an analytical model include the names, values of technical characteristics and unit cost of thermal insulation material for each variant as part of a preliminary prepared sample, as well as data necessary to assess the adequacy of the formed analytical model.

A detailed description of the initial data used in the processes of forming an analytical model and assessing its adequacy is presented in Table 2.

Table 2. Source data used during the processes related to the formation of the analytical model and assessment of its adequacy.

No.	Name of the source data element	Measure unit	Designation/ Expression
1	2	3	4
1	**Indexes**		
1.1	Index of the thermal insulation material’s technical characteristic (factor of the analytical model) (1)	-	$j = 1, 2, ..., n$
1.2	The value of the index for the technical characteristic of the thermal insulation material (factor of the analytical model) corresponding to the thermal conductivity coefficient	-	$j_\lambda \in \{1, 2, ..., n\}$
1.3	Index of the analytical model’s parameter (1)	-	$k = 0, 1, 2, ..., n$
1.4	Index of the thermal insulation material’s variant (model) (2)	-	$l = 1, 2, ..., g$

No.	Name of the source data element	Measure unit	Designation/ Expression
1	2	3	4
2	**Source data used for the formation of an analytical model**		
2.1	General source data		
2.1.1	Number of parameters of thermal heat-insulating material	units	n
2.1.2	Number of thermal heat-insulating material instances	units	g
2.2	Input data specified for each individual instance of thermal heat-insulating material with an index l ($l = 1, 2, ..., g$)		
2.2.1	Name of the copy of the thermal insulation material	-	-
2.2.2	Actual value of specific cost for the thermal insulation material	CU/m^2	y_l
2.3	Initial data specified for each individual variant of thermal insulation material with an index l ($l = 1, 2, ..., g$) and each individual technical characteristic with index j ($j = 1, 2, ..., n$)		
2.3.1	Thermal insulation material's technical characteristic value	CU/(m$^2 \cdot MU_{\chi j}$)(3)	χ_{lj}
3	**Initial data used for the formed analytical model's adequacy assessment**		
3.1	General source data		
3.1.1	Minimum permissive value of the coefficient of determination	-	R^{2min}

Note: (1) the upper value of the index is determined by the input data element in item 2.1.1 of the table; (2) the upper value of the index is determined by the source data element in item 2.1.2 of the table; (3) the designation "$MU_{\chi j}$" defines the measure unit for the thermal insulation material's technical characteristic with the index j (see Table 1).

Detailed description of the calculated characteristics enumerated during the processes related to the formation of the analytical model and assessment of its adequacy is presented in Table 3.

Table 3. Calculated characteristics calculated as part of the process of forming an analytical model and assessing its adequacy.

No	Name of the calculated characteristic	Measure unit	Expression
1	2	3	4
1	**Calculated characteristics enumerated during the formation of the analytical model**		
1.1	Characteristics calculated for each individual variant of thermal insulation material with index l ($l = 1, 2, ..., g$) and each factor of the analytical model with the index j ($j = 1, 2, ..., n$)		
1.1.1	Factor value	$UM_{\theta j}$ (1)	$\theta_{lj} = \begin{cases} \frac{1}{\chi_{lj}}, \text{if } j = j_\lambda; \\ \frac{\chi_{lj}}{\chi_{lj=j_\lambda}}, \text{ else} \end{cases}$
1.2	General calculated characteristics		
1.2.1	An element of the main matrix of a system of equations located at the intersection of a row with an index r ($r = 0, 1, 2, ..., n$) and a column with an index c ($c = 0, 1, 2, ..., n$)	–	$\mathrm{B}_{rc} = \begin{cases} g, \text{ if } r = 0, c = 0; \\ \sum_{l=1}^{g} \chi_{lj=r}, \text{ if } r \geq 1, c = 0; \\ \sum_{l=1}^{g} \chi_{lj=c}, \text{ if } r = 0, c \geq 0; \\ \sum_{l=1}^{g} \chi_{lj=r} \cdot \chi_{lj=c}, \text{ else} \end{cases}$
1.2.2	Main matrix of the system of equations	–	$\mathrm{B} = \{\mathrm{B}_{rc}\}$

No	Name of the calculated characteristic	Measure unit	Expression
1	2	3	4
1.3	Characteristics calculated for each individual parameter of the analytical model with an index k ($k = 0,1,2,...,n$)		
1.3.1	A member of a partial matrix of a system of equations that is at the intersection of a row with an index r ($r = 0,1,2,...,n$) and a column with an index c ($c = 0,1,2,...,n$)	–	$\mathrm{B}_{rc}^{k} = \begin{cases} \sum\limits_{l=1}^{g} y_l, \text{ if } r = 0, c = k; \\ \sum\limits_{l=1}^{g} y_l \cdot \chi_{lj=k'}, \text{ if } r \geq 1, c = k; \\ \mathrm{B}_{rc}, \text{ else;} \end{cases}$
1.3.2	Partial matrix of a system of equations	–	$\mathrm{B}_k = \left\{ \mathrm{B}_{rc}^{k} \right\}$
1.3.3	Analytical model parameter's value (2)	diff. (3)	$\beta_k = \dfrac{\lvert \mathrm{B}_k \rvert}{\lvert \mathrm{B} \rvert}$
2	**Calculated characteristics enumerated during the assessment of the adequacy for the analytical model**		
2.1	Characteristics calculated for each individual variant of thermal insulation material with index l ($l = 1,2,...,g$)		
2.1.1	Predicted value of the material's the specific cost	CU/m²	$\tilde{y}_l = \beta_{k=0} + \sum\limits_{k=1}^{n} \beta_k \cdot \theta_{lj=k}$
2.2	Aggregated calculated characteristics		
2.2.1	Absolute deviation of the predicted value of the unit value from the actual value minimal	CU/m^2	$\Delta^{\min} = \min\limits_{l} \left\{ \lvert \tilde{y}_l - y_l \rvert \right\}$
2.2.2	average	CU/m^2	$\Delta^{aver} = \dfrac{1}{g} \cdot \sum\limits_{l=1}^{g} \lvert \tilde{y}_l - y_l \rvert$
2.2.3	maximal	CU/m^2	$\Delta^{max} = \max\limits_{l} \left\{ \lvert \tilde{y}_l - y_l \rvert \right\}$
2.2.4	Relative deviation of the predicted value of the unit cost from the actual value minimal	–	$\sigma^{min} = \min\limits_{l} \left\{ \dfrac{\lvert \tilde{y}_l - y_l \rvert}{y_l} \right\}$
2.2.5	average	–	$\sigma^{aver} = \dfrac{1}{g} \cdot \sum\limits_{l=1}^{g} \dfrac{\lvert \tilde{y}_l - y_l \rvert}{y_l}$
2.2.6	maximal	–	$\sigma^{max} = \max\limits_{l} \left\{ \dfrac{\lvert \tilde{y}_l - y_l \rvert}{y_l} \right\}$
2.2.7	Calculated coefficient of determination	–	$R^2 = 1 - \dfrac{\sum\limits_{l=1}^{m} \left(\tilde{y}_l - y_l \right)^2}{\sum\limits_{l=1}^{m} \left(y_l - \dfrac{\sum\limits_{l=1}^{g} y_l}{m} \right)^2}$

Note: (1) the notation "$MU_{\theta j}$" defines the measure unit for the analytical model's factor with an index j (see Table 1); (2) the designation $|...|$ in mathematical expression of the calculated characteristic corresponds to the calculation result for the determinant of the corresponding matrix argument; (3) in the case $k = 0$ the measure unit of the design characteristic corresponds to "CU/m²"; otherwise "CU/(m²· $MU_{\theta\, j=k}$)".

The adequacy of the analytical model is assessed on the basis of a condition determined by the expression:

$$R^2 \geq R^{2\,min}. \tag{2}$$

The description of the components for expression (2) is presented in item 3.1.1 of Table 2 and item 2.2.4 of Table 3.

3. Results and Discussion

The proposed analytical model has been implemented on a practical example to solve the problem related to the formation of the dependence of the specific cost for thermal insulation material based on mineral wool, expanded polystyrene foam and extruded polystyrene foam on the corresponding technical characteristics. The initial data for the implementation of the model included information on 100 material variants available on the Russian building materials market in the period from February 2019 to March 2022 – the values of the specific cost and technical characteristics of the material specified in Table 1, with the exception of the vapor permeability coefficient, for which there was no data in the documentation for the material variants (the effect of the vapor permeability coefficient on the specific cost has been assumed to be negligible). The values of the source data elements are given in columns 1–8 of Table 4. Minimum permissible value of the coefficient of determination $\left(R^{2\,min}\right)$ has been assumed to be 0.9. 1 CU has been taken equal to 1 ruble ($0.011687 as of July 29, 2024)

The results of the model implementation in numerical form are presented in Table 5 (including the calculated values of the model parameters and the coefficient of determination) and in column 9 of Table 4 (predicted values of the unit cost of acquisition of various material samples), in graphical form – in Fig. 1 (deviations of the predicted values of the unit cost from the actual values in the context of individual material samples).

According to the results obtained, the average absolute deviation of the predicted value of the unit cost of a material sample from the actual value $\left(\Delta^{\text{aver}}\right)$ is 17.492 CU/m^2, and the corresponding relative $\left(\sigma^{\text{aver}}\right)$ is about 12.4%, while the estimated value of the coefficient of determination $\left(R^2\right)$ is approximately 0.909, exceeding the above-mentioned minimum permissible value.

It is important to note that the proposed analytical model, in comparison with the predictive models presented in [18, 20], is characterized by a similar or slightly lower adequacy (the determination coefficient R^2 for the model presented in [18] is 0.922, for the basic and modified models described in [20] – 0.903 and 0.927, respectively). However, unlike the above-described developments, the proposed analytical model can be effectively used as a basis for creation and implementation of an optimization model for determination of the technical characteristics for thermal insulation material within enclosing structures as part of a housing construction object, since it ensures the direct calculation of optimal values for the material's technical characteristics directly based on the results of the optimization model's implementation without using additional predictive models, for which certain requirements for adequacy indicators must be ensured.

Thus, based on the results obtained, the conclusion was made about high practical importance of the developed analytical model related to the dependence of the unit cost of thermal heat-insulating material on its technical characteristics.

Table 4. Values of technical and cost characteristics of the samples of heat-insulating material used in the process of implementing the analytical model.

Index	Name of the sample of thermal heat-insulating material	The value of the thermal insulation material's technical characteristic with the index (*j*)					Specific cost	
		1	2	3	4	5	Actual	Predicted
1	2	3	4	5	6	7	8	9
l	-	$\chi_{lj=1}$	$\chi_{lj=2}$	$\chi_{lj=3}$	$\chi_{lj=4}$	$\chi_{lj=5}$	y_l	$\tilde{y}_l$
-	-	$\frac{\text{W}}{(\text{m}\cdot{}^\circ\text{C})}$	m	kg/m³	%	–	$\frac{\text{CU}}{\text{m}^2}$	$\frac{\text{CU}}{\text{m}^2}$
1	ISOVER Warm House Twin, 5490×1220×50 mm	0.041	0.05	11	1	1	55	57.72
2	URSA Geo M-11, 7000×1200×50 mm	0.04	0.05	11	1	1	57	57.05
3	URSA Universal, 1250×600×50 mm	0.036	0.05	16	1	1	58	63.30
4	URSA Geo Light, 6250×1200×50 mm	0.044	0.05	11	1	1	58	59.53
5	USSR Geo P-15, 1250×610×50 mm	0.037	0.05	15	1	1	60	62.06
6	KNAUF ECOROLL, 1000×610×50 mm	0.04	0.05	12	1	1	61	58.72
7	KNAUF ECOROLL Rulon, 6800×610×50 mm	0.039	0.05	10.5	1	1	61	55.50
8	ISOVER Classic Plus, 1200×610×50 mm	0.038	0.05	15	1	1	62	62.65
9	ISOVER Warm House Slab, 1170×610×50 mm	0.038	0.05	13.5	1	1	62	60.01
10	ISOVER Profi, 6000×1220×50 mm	0.04	0.05	14	1	1	63	62.06
11	ROCKWOOL Econom, 1000×600×50 mm	0.039	0.05	26	1	1	63	82.04
12	URSA Terra, 1250×610×50 mm	0.036	0.05	16	1	1	64	63.30
13	KNAUF ECOROLL Slab, 1230×610×50 mm	0.04	0.05	12.5	1	1	65	59.56
14	KNAUF ECOROLL Extra Slab, 1230×1220×50 mm	0.037	0.05	11	1	1	66	54.84
15	KNAUF ECOROLL Thermal Cooker, 1230×610×50 mm	0.04	0.05	12.5	1	1	67	59.56
16	ISOVER Warm Walls Strong, 1000×610×50 mm	0.034	0.05	20.5	1	1	72	70.90
17	ISOVER Frame P37, 1170×610×50 mm	0.037	0.05	15	1	1	76	62.06
18	EKOVER Lite 30, 1000×600×50 mm	0.037	0.05	30	2.5	1	77.8	97.18
19	PAROC eXtra Light, 1200×600×50 mm	0.038	0.05	25	1	1	78	80.22
20	ISOROC UltraLite, 1000×600×50 mm	0.038	0.05	33	1.5	1	83	96.89
21	EKOVER Lite Universal, 1000×600×50 mm	0.037	0.05	28	2.5	1	83.5	93.57
22	ISOVER Classic, 6150×1220×50 mm	0.041	0.05	11	1	1	84	57.72
23	URSA PureOne 37RN, 6250×1200×50 mm	0.037	0.05	15	1	1	84	62.06
24	ISOVER Warm walls, 1170×610×50 mm	0.036	0.05	20	2	1	85	76.23
25	TECHNONICOL Rocklight 1200×600×50 mm	0.04	0.05	35	2	1	85	102.08

Index	Name of the sample of thermal heat-insulating material	The value of the thermal insulation material's technical characteristic with the index (*j*)					Specific cost	
		1	2	3	4	5	Actual	Predicted
1	2	3	4	5	6	7	8	9
26	ECOVER Light 35, 1000×600×50 mm	0.035	0.05	35	2	1	86.15	104.62
27	PENOPLEX Osnova, 1200×600×20 mm	0.03	0.02	30	0.4	3	92	154.62
28	ISOVER Warm House Roll, 7000×1220×50 mm	0.038	0.05	17	1	1	93	66.16
29	ISOROC Isolite L, 1000×600×50 mm	0.038	0.05	50	1	1	94	124.15
30	PAROC eXtra, 600×1200×50 mm	0.036	0.05	30.5	1	1	95	90.19
31	TECHNONICOL GreenGuard Universal, 1200×600×50 mm	0.035	0.05	37.5	1	1	96	103.72
32	KNAUF TeploKnauf Nord 1230×610×50 mm	0.035	0.05	20.7	1	1	97	71.66
33	ROCKWOOL Light Butts Scandic, 800×600×50 mm	0.036	0.05	32	1	1	98	92.98
34	PAROC eXtra Smart, 1200×600×50 mm	0.036	0.05	32	1	1	100	92.98
35	ROCKWOOL Light Butts, 1000×600×50 mm	0.036	0.05	37	1	1	108	102.25
36	PENOPLEX Comfort, 1200×600×20 mm	0.03	0.02	30	0.4	3	110	154.62
37	URSA Geo M-11, 7000×1200×100 mm	0.04	0.1	11	1	1	113	136.83
38	URSA PureOne 34PN, 1250×600×50 mm	0.034	0.05	20	1	1	113	69.92
39	Master Therm PSB-S-15, 1200×1000×50 mm	0.043	0.05	12.5	4	2	115	121.23
40	BASWOOL Standard 60, 1200×600×50 mm	0.038	0.05	60	1	1	116	141.72
41	TECHNONICOL Technoblock Standard 1200×600×50 mm	0.035	0.05	45	1.5	1	117	120.86
42	URSA Geo P-15, 1250×610×100 mm	0.037	0.1	15	1	1	119	148.30
43	ISOVER Warm House Slab, 1170×610×100 mm	0.038	0.1	13.5	1	1	123	143.98
44	URSA Universal, 1250×600×100 mm	0.036	0.1	16	1	1	123	151.93
45	ISOROC Isolight Lux, 1000×600×50 mm	0.038	0.05	60	1.5	1	125	144.34
46	ROCKWOOL Econom, 1000×600×100 mm	0.039	0.1	26	1	1	126	163.86
47	URSA Terra, 1250×610×100 mm	0.036	0.1	16	1	1	126	151.93
48	ISOVER Classic Plus, 1170×610×100 mm	0.037	0.1	15	1	1	128	148.30
49	BASWOOL Standard 70, 1200×600×50 mm	0.038	0.05	70	1	1	129	159.30
50	KNAUF ECOROLL Slab, 1230×610×100 mm	0.04	0.1	12.5	1	1	131	139.33

Index	Name of the sample of thermal heat-insulating material	The value of the thermal insulation material's technical characteristic with the index (*j*)					Specific cost	
		1	2	3	4	5	Actual	Predicted
1	2	3	4	5	6	7	8	9
51	KNAUF ECOROLL Extra Slab, 1230×610×100 mm	0.037	0.1	10.5	1	1	133	140.18
52	ISOVER Profi, 5000×1220×100 mm	0.037	0.1	14	1	1	134	146.50
53	PENOPLEX Basis, 1200×600×30 mm	0.03	0.03	30	0.4	3	138	175.90
54	Master Therm PSB-S-25, 1200×1000×50 mm	0.041	0.05	20.05	3	2	146	130.49
55	ECOVER Lite Station Wagon, 1000×600×100 mm	0.037	0.1	28	2.5	1	152.1	179.81
56	ISOVER Warm walls, 1170×610×100 mm	0.036	0.1	20	1	1	160	159.35
57	PAROC eXtra Light, 1200×600×100 mm	0.038	0.1	25	1	1	162	164.19
58	ISOROC Ultralite L, 1000×600×100 mm	0.038	0.1	33	1.5	1	165	180.86
59	URSA PureOne 37RN, 10000×1200×100 mm	0.037	0.1	15	1	1	166	148.30
60	PENOPLEX Comfort, 1200×600×30 mm	0.03	0.03	30	0.4	3	167.5	175.90
61	ROCKWOOL Cavity Butts, 50 mm	0.035	0.05	45	1	1	169	118.03
62	TECHNONICOL Rocklight 1200×600×100 mm	0.04	0.1	35	2	1	170	181.85
63	TECHNONICOL Technovent Standard, 1200×600×50 mm	0.034	0.05	80	1.5	1	176	190.68
64	PENOPLEX Osnova, 1200×600×40 mm	0.03	0.04	30	0.4	3	184	197.17
65	ISOROC Isolite L, 1000×600×100 mm	0.038	0.1	40	1.5	1	188	193.16
66	TECHNONICOL GreenGuard Universal, 1200×600×100 mm	0.035	0.1	37.5	1	1	191	194.89
67	ROCKWOOL Lite Butts Scandic XL, 1200×600×100 mm	0.036	0.1	37	1	1	192.5	190.89
68	ISOROC IsoLite, 1000×600×100 mm	0.038	0.1	50	1	1	193	208.12
69	EKOVER Lite 45, 1000×600×100 mm	0.035	0.1	45	1.5	1	195.8	212.03
70	ROCKWOOL Lite Butts Scandic, 800×600×100 mm	0.036	0.1	37	1	1	196.5	190.89
71	PAROC eXtra, 600×1200×100 mm	0.04	0.1	30.5	1	1	196.5	169.38
72	PAROC eXtra Smart, 1200×600×100 mm	0.036	0.1	32	1	1	200	181.61
73	BASWOOL Standard 50, 1200×600×100 mm	0.038	0.1	50	1	1	207	208.12
74	ROCKWOOL Venti Butts, 1000×600×50 mm	0.035	0.05	90	1	1	207.5	203.88
75	PENOPLEX Comfort, 1200×600×40 mm	0.03	0.04	30	0.4	3	217	197.17

Index	Name of the sample of thermal heat-insulating material	The value of the thermal insulation material's technical characteristic with the index (*j*)					Specific cost	
		1	2	3	4	5	Actual	Predicted
1	2	3	4	5	6	7	8	9
76	TECHNONICOL Technovent Optima, 1200×600×50 mm	0.036	0.05	90	1.5	1	217	203.32
77	ROCKWOOL Lite Butts, 1000×600×100 mm	0.036	0.1	37	1	1	218	190.89
78	BASWOOL Facade 110, 1200×600×50 mm	0.038	0.05	110	1	1	218	229.59
79	Master Therm PSB-S-15, 1200×1000×100 mm	0.043	0.1	12.5	4	2	229	195.44
80	BASWOOL Standard 60, 1200×600×100 mm	0.038	0.1	60	1	1	231	225.70
81	PENOPLEX Osnova, 1200×600×50 mm	0.03	0.05	30	0.4	3	232	218.44
82	TECHNONICOL Technoblock Standard 1200×600×100 mm	0.035	0.1	45	1.5	1	234	212.03
83	TECHNONICOL Technoroof N Extra 600×1200×50 mm	0.037	0.05	100	1.5	1	234	218.15
84	BASWOOL Facade 120, 1200×600×50 mm	0.038	0.05	120	1	1	236	247.16
85	ECLOSE Ecofacade Standard, 1000×600×50 mm	0.036	0.05	100	1.5	1	238.5	221.87
86	EKOVER Ecofacade Optima, 1000×600×50 mm	0.035	0.05	95	1.5	1	241	216.26
87	BASWOOL Facade 140, 1200×600×50 mm	0.038	0.05	140	1	1	246	282.31
88	ISOROC IsoLite Luxe,1000×600×100 mm	0.038	0.1	60	1.5	1	251	228.31
89	PAROC Linio 15 600×1200×50 mm	0.039	0.05	108	1	1	252	222.44
90	BASWOOL Standard 70, 1200×600×100 mm	0.038	0.1	70	1	1	257	243.27
91	ISOVER Plaster facade, 1200×600×50 mm	0.038	0.05	100	1	1	260	212.02
92	ISOROC Isofas 140, 1000×500×50 mm	0.035	0.05	140	1.5	1	262	302.11
93	PENOPLEX Comfort, 1200×600×50 mm	0.03	0.05	30	0.4	3	263	218.44
94	PENOPLEX Osnova, 1200×600×60 mm	0.03	0.06	30	0.4	3	276	239.72
95	PENOPLEX Comfort, 1200×600×60 mm	0.03	0.06	30	0.4	3	277	239.72
96	TECHNONICOL Technofas Optima, 600×1200×50 mm	0.039	0.05	120	1	1	281	242.99
97	ROCKWOOL Rockfasade, 1000×600×50 mm	0.037	0.05	150	1	1	285.5	305.71
98	ISOROC Isophas 160, 1000×500×50 mm	0.039	0.05	160	1	1	293	311.48
99	ROCKWOOL Butts Facade, 1000×600×50 mm	0.037	0.05	130	1.5	1	318	272.29
100	TECHNONICOL Technoroof Extra 600×1200×40 mm	0.037	0.04	180	1.5	1	340	345.28

Table 5. Values of the calculated characteristics obtained during implementation of the analytical model on a practical example.

No	Name of the calculated characteristic		Measure unit	Designation	Value
1	2		3	4	5
1	The value of the model parameter corresponding to the factor	inversed value of thermal conductivity coefficient	$\beta_{k=1}$	$MU_{\theta\ j=1}$	–7.197
2		ratio of the thickness to the thermal conductivity coefficient	$\beta_{k=2}$	$MU_{\theta\ j=2}$	63.819
3		ratio of average density to the thermal conductivity coefficient	$\beta_{k=3}$	$MU_{\theta\ j=3}$	0.067
4		ratio of the water absorption in 24 hours (by volume) to the thermal conductivity coefficient	$\beta_{k=4}$	$MU_{\theta\ j=4}$	0.198
5		ratio of the flammability group index to the thermal conductivity coefficient	$\beta_{k=5}$	$MU_{\theta\ j=5}$	1.982
6	The constant of the unit cost for the material (additional parameter of the model)		$\beta_{k=0}$	CU/m²	84.318
7	Absolute deviation of the predicted value of the unit value from the actual value	minimal	Δ^{min}	CU/m²	0.052
8		average	Δ^{aver}	CU/m²	17.492
9		maximal	Δ^{max}	CU/m²	62.625
10	Relative deviation of the predicted value of the unit cost from the actual value	minimal	σ^{min}	-	0.001
11		average	σ^{aver}	-	0.124
12		maximal	σ^{max}	-	0.681
13	Calculated coefficient of determination		R^2	-	0.909

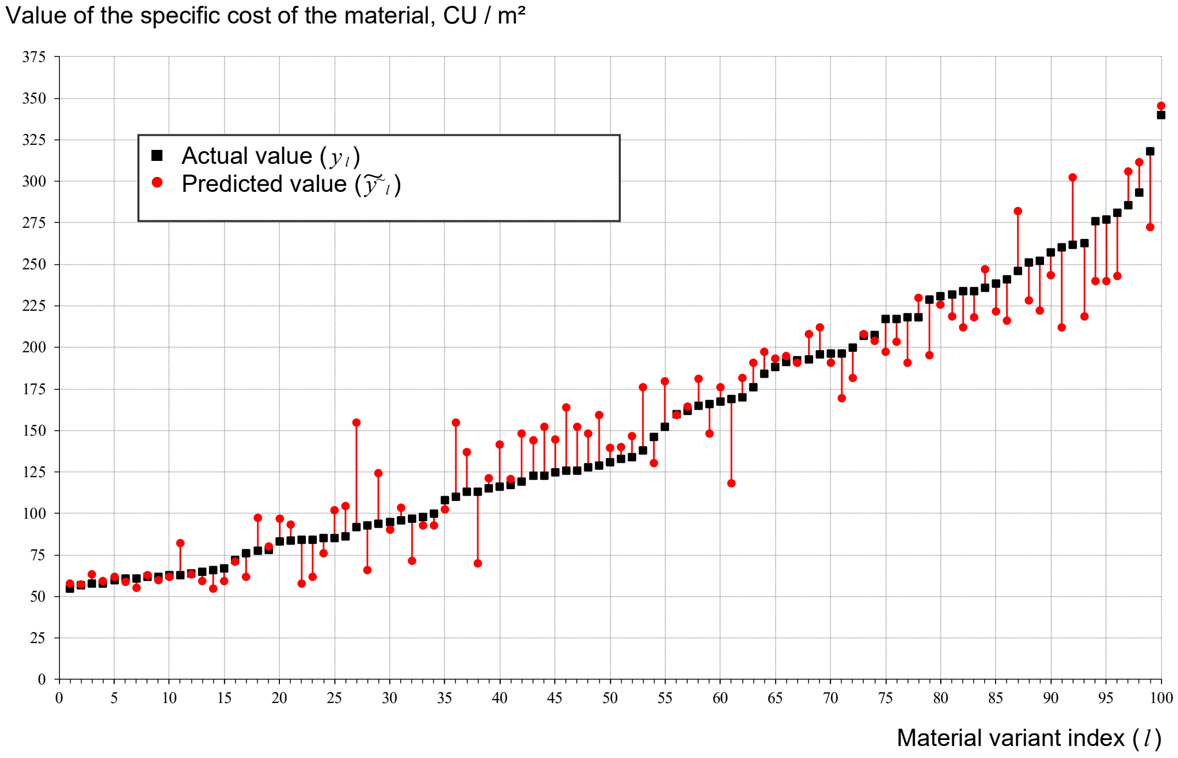

Figure 1. Deviations of the predicted values of the unit cost from the actual values in the context of individual variants of thermal insulation material.

Also, at the final stages of the research, the following recommendations have been formed in relation to the use of the developed analytical model during the solution of the problems related to determination of the characteristics for design solutions connected to enclosing structures within housing construction objects:

1. It is advisable to use the developed analytical model as a component of the mathematical description of energy efficiency indicators for design solutions formed in relation to enclosing structures; in particular, the mathematical expression for the simple payback period for a design solution corresponding to a housing construction object at the renovation stage will have the form

$$T = \frac{\left(\beta_0+\beta_{j=1}\cdot\frac{1}{\lambda}+\beta_{j=2}\cdot\frac{\delta}{\lambda}+\beta_{j=3}\cdot\frac{\rho}{\lambda}+\beta_{j=4}\cdot\frac{\nu}{\lambda}+\beta_{j=5}\cdot\frac{\varphi}{\lambda}+\beta_{j=6}\cdot\frac{\mu}{\lambda}+y_{\text{mnt}}\right)\cdot k_{\text{nrg}}}{\left(\frac{1}{\sum\limits_{s\in S_0}\frac{\delta_s}{\lambda_s}}-\frac{1}{\sum\limits_{s\in S_0}\frac{\delta_s}{\lambda_s}+\frac{\delta}{\lambda}}\right)\cdot c_{\text{he}}\cdot D_{\text{d}}\cdot k_{\text{exp}}} = f\left(\frac{1}{\lambda},\frac{\delta}{\lambda},\frac{\rho}{\lambda},\frac{\nu}{\lambda},\frac{\varphi}{\lambda},\frac{\mu}{\lambda}\right), \tag{3}$$

where T – payback period of the design solution, years; y_{mnt} – specific cost of the thermal insulation material's installation, CU./m^2; k_{nrg} – energy units' conversion factor, W·h/Gcal; s – index of the enclosing structure's layer; S_0 – set of indexes of structural layers that are not related to thermal insulation material; δ_s – thickness of the material related to the layer with index s within the structure, m; λ_s – thermal conductivity coefficient of the material related to the layer with index s within the structure, W/(m·°C); c_{he} – specific cost of thermal energy, CU/Gcal; D_{d} – heating period's temperature-time indicator, °C·day; k_{exp} – conversion factor for time measure units, h/day.; the description of the other components of expression (3) is presented in Table 1.

2. It is advisable to use the factors included in the analytical model as components of the mathematical description of energy efficiency indicators for the mentioned-above design solutions; in particular:
   - the expression for the enclosing structure's thermal resistance will have the form

$$R = \sum_{s\in S_0}\frac{\delta_s}{\lambda_s}+\frac{\delta}{\lambda} = f\left(\frac{\delta}{\lambda}\right), \tag{4}$$

where R – enclosing structure's thermal resistance, m^2·°C/W;

   - the expression for the enclosing structure's vapor permeability resistance (in the case where the thermal insulation material is located between the inner surface of the structure and the corresponding plane of maximum moisture) will have the form

$$R_{\mu} = \sum_{s\in S_{\mu}}\frac{\gamma_s\cdot\delta_s}{\mu_s}+\frac{\gamma\cdot\delta}{\mu} = f\left(\frac{\delta}{\lambda},\frac{\mu}{\lambda}\right), \tag{5}$$

where R_{μ} – enclosing structure's vapor permeability resistance, m²·h·Pa/mg; S_{μ} – set of indexes of structural layers that are not relates to thermal insulation material and located within the space between the inner surface of the structure and the corresponding plane of maximum moisture; γ, γ_s – the share of the thickness of the heat-insulating material and other material related to the layer with the index s in the structure (respectively) within the space between the inner surface of the structure and the corresponding plane of maximum moisture; μ_s – vapor permeability coefficient of the material r to the layer with index s within the structure, mg/(m·h·Pa).

3. The mentioned-above results of the mathematical description of the energy and economic efficiency indicators for design solutions should be used as a basis for creation of the tools for determination of the values for the analytical model factors (see column 4 of Table 1) as characteristics of design solutions formed in relation to enclosing structures within housing construction objects:
   - analytical models – systems of algebraic or transcendental equations – by establishing a correspondence between the calculated and required (specified in the regulatory documentation) values of the energy and economic efficiency indicators for design solutions, taking into account acceptable discrepancies;
   - optimization models – by using individual energy and economic efficiency indicators for design solutions criteria associated with target functions, and the remaining indicators – as criteria associated with constraints with the use of the required (specified in the regulatory documentation) values of the indicators.

It is important to note that the quadratic (relative to the factors of the developed analytical model) structure of expression (3), as well as the structure of expressions (4) and (5), which can be reduced to linear (relative to the factors of the developed analytical model), will ensure the possibility of using standard (available in modern software environments for mathematical modeling) computational algorithms for the implementation of the mentioned-above tools.

4. Conclusions

During the research the following results have been obtained:

1. Review and analysis of scientific developments in the field of determination of the characteristics for design solutions formed in relation to enclosing structures in housing construction objects has been conducted. Based on the results of the of the mentioned-above review and analysis, the conclusion has been made about the limitations of existing tools connected to the taking into account the relationships between the characteristics of design solutions in terms of the technologies and materials used and the corresponding indicators of energy and economic efficiency.
2. An analytical model of the correlation between the specific cost and technical characteristics of thermal insulation material has been developed. The model assumes a linear dependence of the specific (per unit of surface area of the structure) cost of insulation on the inverse value of the thermal conductivity coefficient of the material, as well as on the ratios of the material's other technical characteristics to the mentioned-above coefficient.
3. The developed analytical model has been implemented using a practical example. The results of formation of the model on the basis of a set of thermal insulation material's variants – in particular, the value of the determination coefficient – has shown that the developed tool has high practical significance.
4. Recommendations for the use of the developed analytical model during the solution of the problems related to determination of the characteristics for design solutions connected to enclosing structures within housing construction objects have been formulated.

On the basis of the results obtained during the research, the following conclusions have been made:

1. The developed analytical model can be used for predictive calculation of the specific cost of thermal insulation material based on mineral wool with the use of the specified values of the material's technical characteristics.
2. Due to the composition of the factors taken into account, the developed analytical model can be effectively integrated into the structure of tools for determination of the characteristics for design solutions formed in relation to enclosing structures within housing construction objects on the basis of energy and economic efficiency criteria.

References

1. Musorina, T.A., Gamayunova, O.S., Petrichenko, M.R. Substantiation of design measures to increase energy efficiency of exterior walls. Proceedings of Moscow State University of Civil Engineering. 2017. 12(11(110)). Pp. 1269–1277. DOI: 10.22227/1997-0935.2017.11.1269-1277
2. Gorshkov, A.S. Olshevsky, V.Ya., Gorshkov, R.A. Teploprovodnost' oblitsovochnogo kamennogo sloya iz keramicheskogo pustotelogo kirpicha pri razlichnoy stepeni zapolneniya pustot stroitel'nym rastvorom [Thermal conductivity of the facing stone layer made of hollow ceramic bricks with varying degrees of filling of voids with mortar]. Construction Materials, Equipment, Technologies of the XXI Century. 2018. 9–10(236–237). Pp. 26–33.

3. Gorshkov, A.S., Kabanov, M.S., Yuferov, Yu.V. Analysis of thermal loads and specific consumption of thermal energy in apartment buildings. Thermal Engineering. 2021. 68(8). Pp. 72–80. DOI: 10.1134/S0040363621050052
4. Rahiminejad, M., Khovalyg, D. Numerical and experimental study of the dynamic thermal resistance of ventilated air-spaces behind passive and active façades. Building and Environment. 2022. 225. Article no. 109616. DOI: 10.1016/j.buildenv.2022.109616
5. Statcenko, E.A., Ostrovaia, A.F., Musorina, T.A., Kukolev, M.I., Petritchenko, M.R. The Elementary Mathematical Model of Sustainable Enclosing Structure. Magazine of Civil Engineering. 2016. 8(68). Pp. 86–91. DOI: 10.5862/MCE.68.9
6. Zaborova, D.D., Kukolev, M.I., Musorina, T.A., Petrichenko, M.R. The Simplest Mathematical Model of the Energy Efficiency of Layered Building Envelopes. St. Petersburg State Polytechnic University Journal. 2016. 4(254). Pp. 28–33. DOI: 10.5862/JEST.254.3
7. Gagarin, V.G., Pastushkov, P.P. Changes in the Time of Thermal Conductivity of Gas-Filled Polymer Thermal Insulation Materials. Construction Materials. 2017. 6. Pp. 28–31. DOI: 10.31659/0585-430X-2017-749-6-28-31
8. Zaborova, D.D., Mussorina, M.T., Petritchenko, M.R. Thermal Stability and Thermal Resistance of a Multilayer Wall Construction: Assessment of Parameters. St. Petersburg State Polytechnic University Journal. 2017. 23(1). Pp. 18–26. DOI: 10.18721/JEST.230102
9. Pastushkov, P.P. On the Problems of Determining the Thermal Conductivity of Building Materials. Construction Materials. 2019. 4. Pp. 57–64. DOI: 10.31659/0585-430X-2019-769-4-57-63
10. Musorina, T.A. Konstruktivnoye obespecheniye teplotekhnicheskoy effektivnosti stenovykh ograzhdeniy zdaniy. dissertatsiia kandidata tekhnicheskikh nauk [Structural support of thermal efficiency of building wall enclosures. Cand. tech. sci. diss]. St. Petersburg, 2020. 159 p.
11. Pastushkov, P.P., Gagarin, V.G., Il'in, D.A., Nagaev, I.F., New Results on Research on Changes in Thermal Conductivity over Time of Plates Made of Polyisocyanurate Foam (PIR) of Modern Production. Construction Materials. 2022. 6. Pp. 30–34. DOI: 10.31659/0585-430X-2022-803-6-30-34
12. Sadykov, R.A., Mukhametzyanova, A.K., Filimonova, S.A. Analytical and Numerical Calculations of the Quasi-Steady-State Heat Transfer Mode in the Enclosing Structures of Buildings and Structures. Bulletin of the Kazan State University of Architecture and Civil Engineering. 2022. 1(59). Pp. 90–102. DOI: 10.52409/20731523_2022_1_90
13. Panferov, V.I., Milov, A.E. Calculation of the Average Temperature for Multilayer Wall. Bulletin of the South Ural State University. Series: Construction Engineering and Architecture. 2015. 15(2). Pp. 59–61.
14. Stakhov, A.E., Frolkis, V.A., Kadokova, S.Yu., Andreenko, A.A. Economic and mathematical analysis of thermal protection of building. Bulletin of Civil Engineers. 2019. 4(75). Pp. 107–112. DOI: 10.23968/1999-5571-2018-16-4-107-112
15. Kuts, E.V., Kadokova S.Yu., Andreenko, A.A. Optimization modeling of an energy-saving project. Engineering Journal of Don. 2021. 12(84). Pp. 516–528.
16. Petrov, P.V., Rezanov, E.M., Vedruchenko, V.R., Starikov, A.P. Determination of optimum thickness of thermal isolation of the protecting designs of buildings at capital repairs. Omsk Scientific Bulletin. 2015. 3(143). Pp. 254–258.
17. Petrov, P.V., Sherstobitov, M.S., Rezanov, E.M., Vedruchenko, V.R. The methodology of calculation of effective thermal insulationof external walls of buildings walling during overhaul. Omsk Scientific Bulletin. 2016. 6(150). Pp. 109–113.
18. Belous, A.N., Novikov, B.A., Belous, O.E. Technical-Economic Substantiation of the Facade Heated Insulation System of II-04 Series. Modern Industrial and Civil Construction. 2017. 13(4). Pp. 179–187.
19. Gamaunova, O., Musorina, T. Return on investment in the implementation of energy-efficient solutions for facade insulation. MATEC Web of Conferences. 2018. 251. Article no. 05041. DOI: 10.1051/matecconf/201825105041
20. Delgarm, N., Sajadi, B., Delgarm, S. Multi-objective optimization of building energy performance and indoor thermal comfort: A new method using artificial bee colony (ABC). Energy and Buildings. 2016. 131. Pp. 42–53. DOI: 10.1016/j.enbuild.2016.09.003
21. Stakhov, A.E., Andreenko, A.A. Economic assessment of design solutions for thermal protection of buildings. AVOK: Ventilation, heating, air conditioning, heat supply and building thermal physics. 2018. 4. Pp. 42–47.
22. Alekseytsev, A.V. Poisk ratsional'nykh parametrov stroitel'nykh konstruktsiy na osnove mnogokriterial'noy evolyutsionnoy optimizatsii [Search for rational parameters of building structures based on multi-criteria evolutionary optimization]. Industrial and Civil Engineering. 2019. 7. Pp. 18–22. DOI: 10.33622/0869-7019.2019.07.18-22
23. Rosso, V., Ciancio, V., Dell’Olmo, J., Salata, F. Multi-objective optimization of building retrofit in the Mediterranean climate by means of genetic algorithm application. Energy and Buildings. 2020. 216. Article no. 109945. DOI: 10.1016/j.enbuild.2020.109945
24. Radaev, A.E., Gamayunova, O.S., Bardina G.A. Optimization of energy efficiency design characteristics for construction projects. AlfaBuild. 2021. 5(20). Article no. 2003. DOI: 10.57728/ALF.20.3
25. Yang, J. Wu, H., Xu, X., Huang, G., Cen J., Liang Y. Regional climate effects on the optimal thermal resistance and capacitance of residential building walls. Energy and Buildings. 2021. 244. Article no. 111030. DOI: 10.1016/j.enbuild.2021.111030
26. He, L., Zhang, L. A bi-objective optimization of energy consumption and investment cost for public building envelope design based on the ε-constraint method. Energy and Buildings. 2022. 266. Article no. 112133. DOI: 10.1016/j.enbuild.2022.112133
27. Hosamo, H.H., Tingstveit, M.S., Nielsen, H.K., Svennevig, P.R., Svidt, K. Multiobjective optimization of building energy consumption and thermal comfort based on integrated BIM framework with machine learning-NSGA II. Energy and Buildings. 2022. 277. Article no. 112479. DOI: 10.1016/j.enbuild.2022.112479
28. Radaev, A.E., Gamayunova, O.S., Bardina, G.A. Use of optimization modeling tools to justify the characteristics of an energy efficient structural solution. Construction and Industrial Safety. 2022. 27(79). Pp. 5–25.
29. Liu, Y., Li, T., Xu, W., Wang Q., Huang H., He, B.-J. Building information modelling-enabled multi-objective optimization for energy consumption parametric analysis in green buildings design using hybrid machine learning algorithms. Energy and Buildings. 2023. 300. Article no. 113665. DOI: 10.1016/j.enbuild.2023.113665
30. Yang, H., Xu, Z., Shi, Yu., Tang, W., Liu, C., Yunusa-Kaltungo, A., Cui, H. Multi-objective optimization designs of phase change material-enhanced building using the integration of the Stacking model and NSGA-III algorithm. Journal of Energy Storage. 2023. 68. Article no. 107807. DOI: 10.1016/j.est.2023.107807
31. Ouanes, S., Sriti, L. Regression-based sensitivity analysis and multi-objective optimisation of energy performance and thermal comfort: Building envelope design in hot arid urban context. Building and Environment. 2023. 248. Article no. 111099. DOI: 10.1016/j.buildenv.2023.111099

32. Wong, B.C.L., Wu, Zh., Gan, V.J.L., Chan C.M., Cheng, J.C.P. Parametric building information modelling and optimality criteria methods for automated multi-objective optimisation of structural and energy efficiency. Journal of Building Engineering. 2023. 75. Article no. 107068. DOI: 10.1016/j.jobe.2023.107068
33. Sanchez, V., Gomez-Acebo, T. Building energy performance metamodels for district energy management optimisation platforms. Energy Conversion and Management: X. 2023. 21. Article no. 100512. DOI: 10.1016/j.ecmx.2023.100512
34. Petrov, P.V., Kulagin, V.A., Rezanov E.M., Starikov, A.P. Improvement of Technology of Thermal Insulation of Buildings. Journal of the Siberian Federal University. Series: Engineering and Technologies. 2023. 16(2). Pp. 187–197.
35. Benaddi, F.Z., Boukhattem, L., Tabares-Velasco, P.C. Multi-objective optimization of building envelope components based on economic, environmental, and thermal comfort criteria. Energy and Buildings. 2024. 305. Article no. 113909. DOI: 10.1016/j.enbuild.2024.113909
36. Wu, C., Pan, H., Luo, Zh., Liu, C., Huang, H. Multi-objective optimization of residential building energy consumption, daylighting, and thermal comfort based on BO-XGBoost-NSGA-II. Building and Environment. 2024. 254. Article no. 111386. DOI: 10.1016/j.buildenv.2024.111386
37. Shi, Y., Chen, P. Energy retrofitting of hospital buildings considering climate change: An approach integrating automated machine learning with NSGA-III for multi-objective optimization. Energy and Buildings. 2024. 319. Article no. 114571. DOI: 10.1016/j.enbuild.2024.114571

Information about the authors:

Kseniia Lukash*,*
E-mail: lukashksusha@gmail.com

Egor Shurshilin*,*
E-mail: Shurshilinegor@yandex.ru

Yanis Olekhnovich*,*
ORCID: https://orcid.org/0000-0001-9578-7245
E-mail: oyanis@list.ru

Anton Radaev*, PhD in Technical Sciences*
ORCID: https://orcid.org/0000-0002-0840-6828
E-mail: TW-inc@yandex.ru

Received 14.06.2024. Approved after reviewing 28.11.2024. Accepted 02.12.2024.

Magazine of Civil Engineering

ISSN
2712-8172

journal homepage: http://engstroy.spbstu.ru/

Research article
UDC 67.017
DOI: 10.34910/MCE.133.7

Aluminum surface treatment for shear strength improvement of the laminate composites

D.V. Goncharenko , ***I.A. Kobykhno, E.V. Bobrynina*** ✉ , ***V.K Yadykin***

Peter the Great St. Petersburg Polytechnic University

✉ *bobrynina_ev@spbstu.ru*

Keywords: metal-polymer laminate composite, adhesion, laser surface treatment, etching, anodizing, atomic force microscopy

Abstract. In this paper, the effect of surface treatment on the adhesion between D16AM aluminum alloy and thermoplastic polyurethane is studied. Adhesion between the metal and polymer plays a key role in the formation of the strength properties of the metal-polymer based laminar composites, which are nowadays widely used in load-bearing structures like beams, columns, roofs, pedestrian bridges, etc. The effects of the metal surface treatment, such as chemical etching, electrochemical anodizing, laser treatment, and a combination of the mentioned processing, on the composite's shear strength were examined. The morphology of the metal surface after treatment was studied via scanning electron microscopy and atomic force microscopy. The true value of the adhesive strength was calculated, taking into account the micro- and macro-relief of the surface and its actual surface area determined via atomic force microscopy. A combined method of metal surface treatment to increase adhesion to a polymer is proposed, the method includes chemical or electrochemical etching followed by laser treatment. It was shown that complex treatment of the aluminum surface allows to increase the shear strength of composites by 50 %. It is established that with chemical etching or laser treatment, the value of the true adhesive strength remains virtually unchanged, however, when using the combined method, its significant increase is observed.

Funding: This research is partially funded by the Ministry of Science and Higher Education of the Russian Federation as part of the World-class Research Center program: Advanced Digital Technologies (contract No. 075-15-2022-311 dated 20 April 2022).

Citation: Goncharenko, D.V., Kobykhno, I.A., Bobrynina, E.V., Yadykin, V.K. Aluminum surface treatment for shear strength improvement of the laminate composites. Magazine of Civil Engineering. 2025. 18(1). Article no. 13307. DOI: 10.34910/MCE.133.7

1. Introduction

Metal-polymer based laminar composites (MPLCs), consisting of alternating layers of metal and polymer, belong to the class of lightweight structural materials [1,2]. These materials find applications in load-bearing structures like beams, columns, roofs, multifunctional panels, pedestrian bridges, etc., contributing to improved construction practices and efficiency. Due to combination of light weight, sufficiently high strength, low cost, and easy technological process, MPLCs are widely used in government supported public infrastructure upgrade, thus, it is predicted that the construction composites market will exceed $65 billion by 2025 [3].

Laminar composites consist of continuous two-dimensional panels or sheets aligned for maximum high-strength, their qualities influenced by the constituent materials' characteristics and the geometrical design of the structural elements [1]. The main constituents in MPLCs are layers of metal, usually lightweight ones, for example, aluminum or titanium, and fiber-reinforced polymer. The layered structure of the MPLC provides a significant reduction in the rate of crack growth [4]. When a crack initiates and propagates in one of the layers at the interface, its growth stops until a crack appears in the next layer, and so on. MPLCs dissipate and dampen vibrations via a similar mechanism, and, thus, can be used as damping structural materials [5-7].

The main parameters affecting the properties of MPLCs are the thickness of the layers and their number, the properties of the constituents itself, the quality of pre-preg impregnation, the metal sheet surface condition, and interlayer adhesion. Adhesion between the metal and polymer plays a key role in the formation of the strength properties. It is known [8-10] that adhesion can be increased by increasing the metal layer surface roughness, since this leads both to an increase in the actual metal-polymer contact area and to the engagement of the liquid polymer to the unevenness of the metal surface.

Surface treatment is usually used for metal substrate preparation providing removal of contamination, good wettability, high roughness, mechanical and chemical stability [11,12]. It was shown that a number of factors are important for the adhesion: a stable oxide on the surface is important as this can prevent or minimize the formation of a relatively weakly bound inorganic layer; topography, which favours mechanical keying and provides an increased area over which interfacial interactions can occur is clearly beneficial. There are many methods of metal surface treatment [13]; among chemical ones, the most promising are etching in iron sulfate [14], nitric acid [15], sulfuric acid anodizing [16], and anodizing in a mixture of sulfuric acid with aluminum sulfate. In addition to chemical methods, physical methods are also widely used, the most popular are sandblasting [17,18]. It was found that the chemical treatment resulted in a more wettable and deeper roughness surface than the achieved using a sanded and degreased treatment and the chemical treatment yielded a superior cleaned surface, which in junction with the roughness area, resulted in a superior interfacial contact between the metal and the adhesive-composite material [15,19].

Recently, it was also shown that the laser processing [20-25] offers a fast, easy, and clean operation in metal microstructuring and can be a new strategy to improve joint strength. Laser cleaning enabled to increase dramatically the adhesion between the substrate irrespective of the previous aluminium surface condition [19]. It was shown [20] that laser texturing improved AA7475 surface roughness and wettability and also confirmed that the Al-O-C chemical bond represents the secondary bonding mechanism along the micro-mechanical interlocking. The results presented in the paper [21] have indicated that the laser micropatterning of AISI 430 stainless steel samples have a marked influence on the surface roughness and surface grove morphology, and consequently on joining properties of the materials.

In this paper, the effect of surface treatment of aluminum sheets on the shear strength of the MPLC was investigated. This paper aims to understand how laser treatments affect the mechanical behaviour of joints and the possible improvement achieved by adopting the sequence of laser and chemical treatment steps. Testing the shear strength and studying the surface morphology were conducted.

2. *Methods*

To manufacture the composites, layers of aluminum alloy D16AM of 0.5 mm thick (hereinafter referred to as aluminum) and thermoplastic polyurethane (TPU) film (OOO NPF Vitur) of 0.1 mm thick were used.

The aluminum samples were pre-cleaned with detergents, etched in a 10 % NaOH solution, and then washed with water. The exception was a series of samples processed by laser at different fill factors (D), in which the aluminum samples were only wiped dry, without cleaning agents.

Three types of treatment were carried out: 1) chemical etching in solutions of nitric acid and ferrous sulfate; 2) electrochemical treatment in electrolytes based on sulfuric acid and aluminum sulfate; 3) and laser treatment. The treatment parameters are given in Table 1.

Table 1. Aluminum surface treatment parameters.

№	Treatment type	Designation in the text	Processing details
1	Chemical	HNO_3	HNO_3 – 32 %; T = 20 °C; t = 1 min
2		$Fe_2(SO_4)_3$	$Fe_2(SO_4)_3$ 127 g/l; H_2SO_4 185 ml/l; T = 65 °C; t = 8 min
3	Electrochemical	H_2SO_4	H_2SO_4 200 ml/l; T = 20 °C; t = 20 min;
4		$Al_2(SO_4)_3$	$Al_2(SO_4)_3$ 200 g/l; H_2SO_4 60 ml/l; T = 20 °C; t = 20 min; j = 1.5 A/dm^2
5	Physical	Laser	P = 10 Вт; λ = 1 μm; D = 50 %; t = 5 ns; T = 20 °C; V = 1 m/s

The composites were manufactured by hot pressing. Two plates of size of 80×10 mm were placed in a mold with an overlap of 10 mm. One layer of TPU was placed between the plates. Pressing temperature was 200 °C, time was 20 min.

The shear strength test was performed according to GOST R 57066-2016 on a Zwick//Roell Z050 machine with a constant deformation rate of 1 mm/min. Surface microstructure studies were carried out using a Phenom Pro X scanning electron microscope. Atomic force microscopy (AFM) studies were conducted for a more thorough analysis of the surface relief. Basing on the preliminary study of the optimal scanning parameters, areas of 40x40 μm were analyzed since this provides high data reliability but does not lead to a radical increase in scanning time.

3. Results and Discussion

Fig. 1 shows the microscopic images of the aluminum surfaces after different types of etching. The surface treated in the HNO_3 solution has minimal porosity (Fig. 1a). Maximum porosity was observed after chemical etching in the $Fe_2(SO_4)_3$ (Fig. 1b). The pores' size does not exceed 5 μm. Surfaces treated electrochemically in sulfuric acid and aluminum sulfate electrolytes are almost identical (Figs. 1c, 1d). It should be noted that the pores formed during chemical etching (Figs. 1a, 1b) are shallower than those formed during electrochemical treatment (Figs. 1c, 1d).

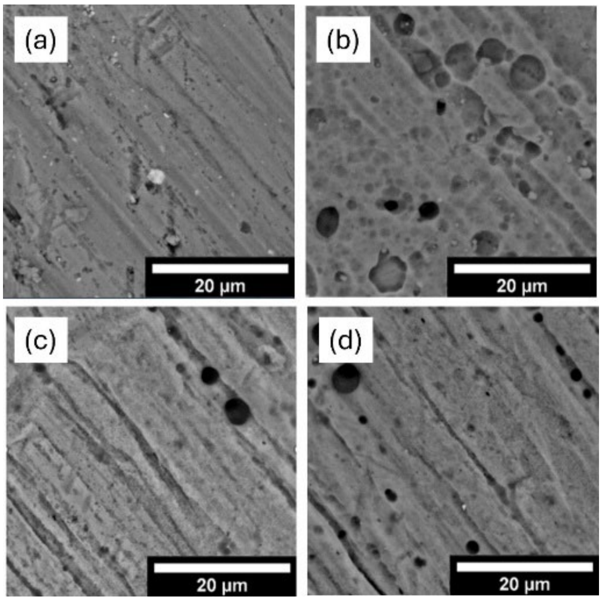

Figure 1. Surface morphology of aluminum depending on the etching: a – HNO_3; b – $Fe_2(SO_4)_3$; c – H_2SO_4; d – $Al_2(SO4)_3$.

The results of shear strength tests depending on the aluminum surface etching type are presented in Fig. 2 (orange bars). The shear strength of the composite generally correlates with the observed porosity of the metal surface. Low roughness of the surfaces treated in HNO_3 solution resulted in a lower strength. Etching in $Fe_2(SO_4)_3$, H_2SO_4, $Al_2(SO_4)_3$ showed fairly close values of shear strength (5±0.5 MPa). However, the shear strength values of the specimens after treatment in $Fe_2(SO_4)_3$ have a much wider spread of values revealing inhomogeneity of the surface condition. This can be explained by the difficulty of maintaining the same concentration of the etchant during the treatment. Since during etching at an elevated temperature (65 °C), there is active evaporation of the components, which changes the ratio of the etchant components. The main advantages of the chemical etching in $Fe_2(SO_4)_3$ are simplicity, high efficiency, and high productivity. The disadvantage of the method is low environmental safety, since the vapors formed during etching are chemically active. The advantages of electrochemical processing are high repeatability, high quality, higher shear strength of the MPLC, and higher environmental friendliness. However, unlike chemical etching, anodizing is a more difficult method to implement, as it requires an adjustable power source and cooling, since the efficiency of the process decreases with increasing temperature.

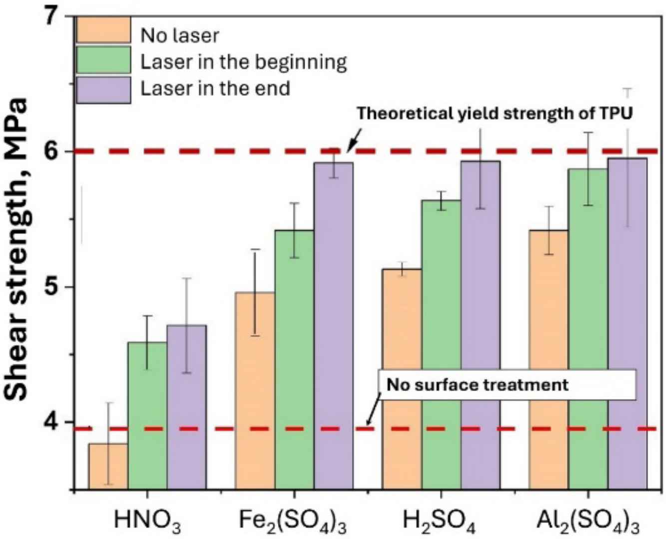

Figure 2. Shear strength of the composites depending on the aluminum surface treatment.

Microphotographs of the aluminum surface in the initial state and after laser treatment with fill factors D = 50 % are shown in Fig. 3. After laser treatment, there is a distinctive structure – craters formed due to the expulsion of molten metal from the heating zone.

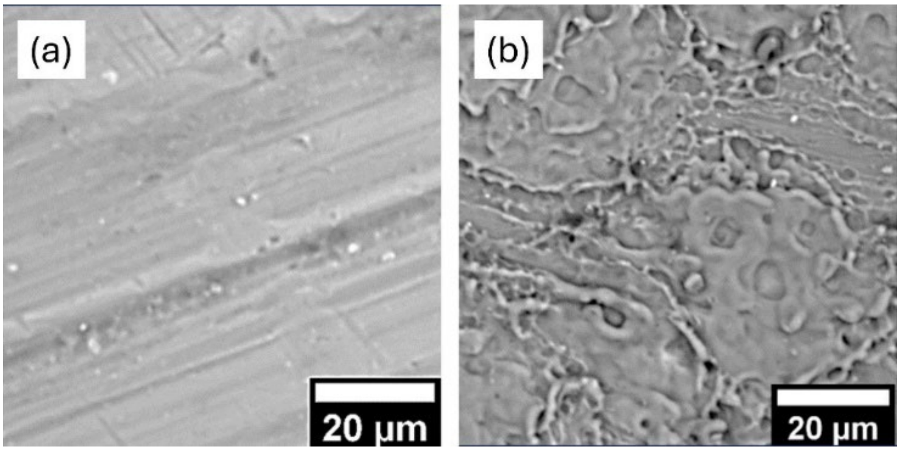

Figure 3. Surface morphology of aluminum:
a – initial state; b – after laser treatment with D = 50 %.

Next, the effect of combination of etching and laser processing and their sequence on the surface condition and shear strength of the composite was studied.

Fig. 2 shows the results of the complex surface treatment on the shear strength of the composite. As seen, laser treatment is effective both before and after chemical or electrochemical treatment. However, a greater effect appears if the laser treatment is carried out after any etching. Thus, changing the order between etching in $Fe_2(SO_4)_3$ and laser treatment allowed to increase the shear strength by 10 %. Regardless of the preliminary treatment, after laser treatment, all samples (except those treated in HNO_3) acquire the same shear strength, because the maximum shear strength of the composite is limited to the yield strength of TPU, which is about 6 MPa.

The effect of laser treatment is most noticeable after etching in $Fe_2(SO_4)_3$. In this case, the increase in shear strength was about 20 %. The morphology of the aluminum surface after different modes of complex treatment is practically identical: the surface is covered with "splash" spots as a result of laser treatment (Fig. 4a). An exception is the treatment mode in which chemical etching in iron sulfate $Fe_2(SO_4)$ was carried out after laser treatment (Fig. 4b). Instead of "splash" spots, the surface has developed porosity, significantly exceeding the porosity acquired after chemical etching of the surface not treated with a laser (Fig. 1b).

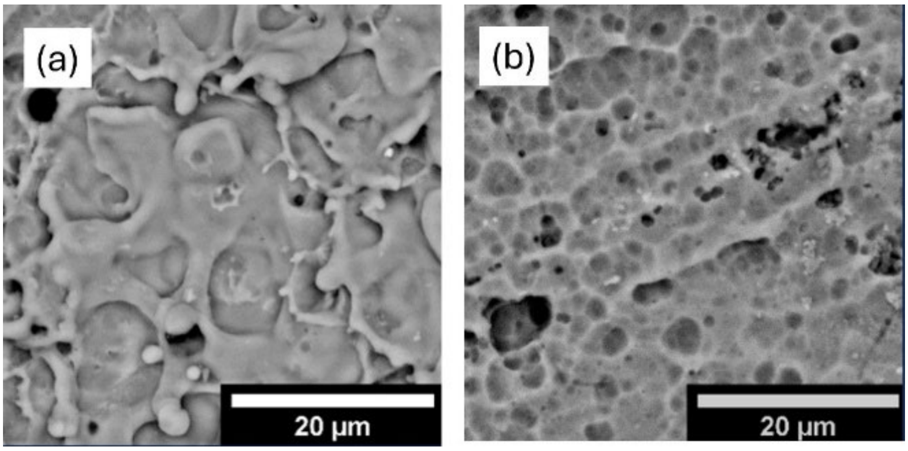

Figure 4. Surface morphology of aluminum depending on the sequency of etching in $Fe_2(SO_4)_3$ and laser processing: a – $Fe_2(SO_4)_3$ →Laser; b – Laser→$Fe_2(SO_4)_3$.

The visually observed surface relief obtained because of various complex treatments does not show a strict correlation with the shear strength of the composite: the samples with visually identical surfaces demonstrate different level of share strength. Based on this, it can be assumed that the difference in strength is due to roughness at the submicron level or the chemical composition of the surface layer (for example, the presence or absence of an oxide film, functional groups, etc.). For a more thorough analysis of the surface relief, surfaces analyses using AFM were carried out. AFM images of the aluminum surface in the initial state and after various processing modes are shown in Fig. 5.

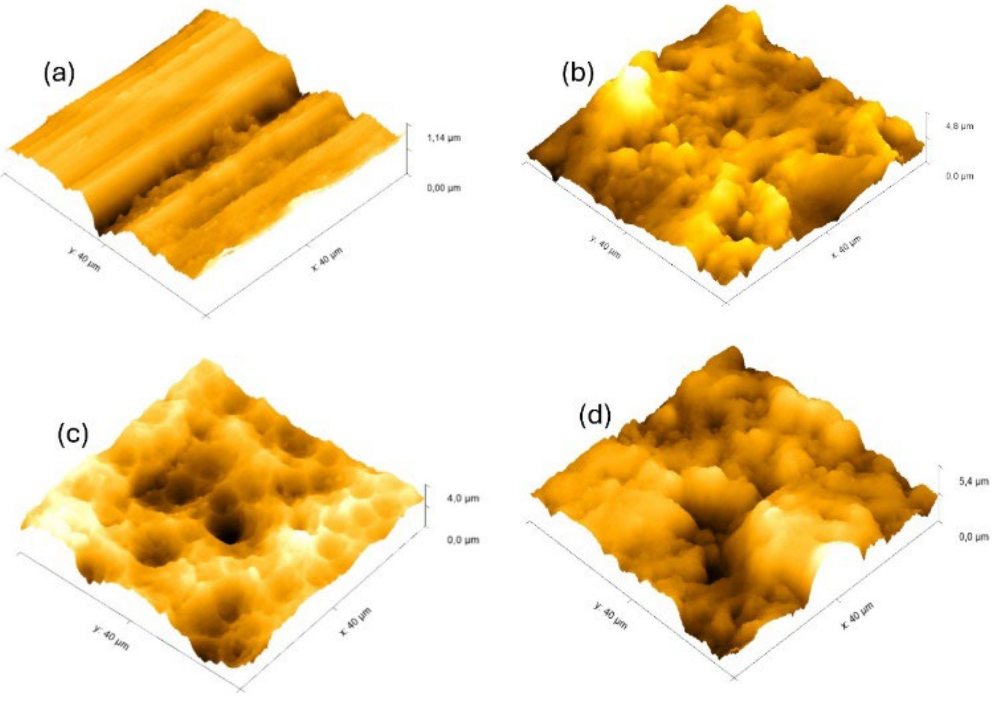

Figure 5. AFM images of the aluminum surface in initial state (a); after laser treatment (b); after complex treatment: laser followed by $Fe_2(SO_4)_3$ (c) and vice versa $Fe_2(SO_4)_3$ followed by laser (d).

Results of AFM measuring of the actual surface area $\left(S_f\right)$ are presented in Table 2. The ratios of the projected surface area $\left(S_0\right)$ to the actual one $\left(S_f\right)$ are presented in the form of a dimensionless normalization coefficient $\left(S_n\right)$:

$$S_n = \frac{S_f}{S_o}. \tag{1}$$

The data obtained show that all types of processing provide an increase in the actual surface area from 14 to 21 %. The maximum increase in the surface area was reached via complex processing –

chemical etching in $Fe_2(SO_4)_3$ followed by laser processing. Next, the true shear strength $\left(\tau_{true}\right)$ was calculated as the ratio of the measured shear strength $\left(\tau_{sh}\right)$ to the normalization coefficient $\left(S_n\right)$:

$$\tau_{true} = \frac{\tau_{sh}}{S_n}. \qquad (2)$$

The calculation results are given in Table 2.

Table 2. Surface characteristics of aluminum and shear strength of the joint depending on the processing method.

Surface treatment	S_0, **μм²**	S_f, **μм²**	S_n	τ_{sh}, **MPa**	τ_{true}, **MPa**	$\frac{\tau_{true}}{\tau_0}$
Without treatment	1600	1660	1.04	3.9	3.7 (τ_0)	–
$Fe_2(SO_4)_3$		1820	1.14	4.7	4.1	**1.10**
Laser		1876	1.17	4.4	3.7	**1.00**
Laser→$Fe_2(SO_4)_3$		1835	1.15	5.4	4.7	**1.27**
$Fe_2(SO_4)_3$→Laser		1933	1.21	5.9	4.9	**1.32**

It was found that when using only one type of processing (etching or laser processing), the ratio of τ_{true} to $\tau_0 \left(\frac{\tau_{true}}{\tau_0}\right)$ has a value close to 1. This suggests that the observed increase in shear strength is associated only with the increase in the actual area of the surfaces being joined. However, when combining two processing methods, a significant increase in true shear strength, more than 25 % $\left(\frac{\tau_{true}}{\tau_0} = 1.27 \div 1.32\right)$, is observed. This allows us to conclude that during the complex processing, a significant change in the chemical composition of the thin surface layer of aluminum occurs, which has a great impact on the adhesive strength of the joint and on the final properties of the composite.

It is already known that the enhancing the adhesion between dissimilar materials represents a key aspect of producing structural hybrid multi-material structures [19]. Additional chemical or laser treatment of the samples surface before hot pressing of metal-polymer composites leads to an increase in shear strength by approximately 25 %. It was shown that the laser treatment of sample surface significantly increase actual surface area of Al-based materials as compare with just chemical treatment of the samples, however, true shear strength remains about the same even with the samples without any treatment, and that means the absence of any additional chemical bonding for the laser treated surface and polymer.

Combined chemical and laser treatment of the sampled provides further increase in shear strength of the material by almost 50 % compared to the original samples without treatment and gives significant increase of true stress as compare with simple single treatment of Al surface.

As a result of the AFM study, it was established that complex treatment of the aluminum surface, including both etching and laser treatment, leads to a significant increase in adhesion to thermoplastic polyurethane, while the mechanism of influence of such treatment consists not only in the increase in the actual surface area but also in its chemical modification. That shows the best results in as compare with modern study of plastic-Al composites (+39 % strength increase with the two-step laser texturing + cleaning treatment), R. Sandeep [20] (+30 % – one step laser treatment).

4. Conclusion

An experimental study of the influence of various methods of surface treatment of aluminum alloys (chemical, electrochemical, and physical) on the adhesive strength of the metal-polymer interface was conducted.

A combined method of metal surface treatment to increase adhesion to a polymer is proposed, the method includes chemical or electrochemical etching followed by laser treatment. It was shown that complex treatment of the aluminum surface allows to increase the shear strength of composites by 50 %. The laser treatment is effective both before and after chemical or electrochemical treatment. However, a greater effect appears if the laser treatment is carried out after etching. Thus, changing the order between etching and laser treatment allowed to increase the shear strength by 10 %. The effect of laser treatment is most noticeable after etching in $Fe_2(SO_4)_3$. In this case, the increase in shear strength was about 20 %.

Based on the study of changes in the morphology of the aluminum surface during treatment, the true value of the adhesive strength is determined, taking into account the micro- and macro-relief of the surface. It is established that with chemical etching or laser treatment, the value of the true adhesive strength remains virtually unchanged (less than 10 %), however, when using the combined method, its significant increase is observed (about 30 %), and that leads to 50 % increase in shear strength.

References

1. Phiri, R., Rangappa, S.M., Siengchin, S., Oladijo, O.P., Ozbakkaloglu, T. Advances in lightweight composite structures and manufacturing technologies: A comprehensive review. Heliyon. 2024. 10(21). Article no. e39661. DOI: 10.1016/j.heliyon.2024.e39661
2. Kadhum, A.M., Faris, S.T., Al-katawy, A.A. Improvement and Properties of Fiber Metal Laminates Used in Aircraft Wing by Using Graphite-Polyester. Diyala Journal of Engineering Sciences. 2019. 12(4). Pp. 92–103. DOI: 10.24237/djes.2019.124010
2. Masterson, J. Construction Composite Materials Market Forecast to Exceed $65 Billion. 2018. [Online]. URL: https://www.constructionexec.com/article/construction-composite-materials-market-forecast-to-exceed-65-billion (reference date: 17.03.2025).
3. Po-Yu Chang, Po-Ching Yeh, Jenn-Ming Yang. Fatigue crack initiation in hybrid boron/glass/aluminum fiber metal laminates, Materials Science and Engineering: A. 2008. 496(1–2). Pp. 273–280. DOI: 10.1016/j.msea.2008.07.041
4. Kobykhno, I., Didenko, A., Honcharenko, D., Vasilyeva, E., Kudryavtsev, V., Tolochko, O. Development thermoplastic elastomer-based fiber-metal laminate for vibration damping application. Materials Today: Proceedings. 2020. 30(3). Pp. 393–397. DOI: 10.1016/j.matpr.2019.12.383
5. Sarlin, E., Liu, Y., Vippola, M., Zogg, M., Ermanni, P., Vuorinen, J., Lepistö, T. Vibration damping properties of steel/rubber/composite hybrid structures. Composite Structures. 2012. 94(11). Pp 3327–3335. DOI: 10.1016/j.compstruct.2012.04.035
6. Chandra, R., Singh, S. P., Gupta, K. Damping studies in fiber-reinforced composites–a review. Composite structures. 1999. 46(1). Pp. 41–51. DOI:10.1016/S0263-8223(99)00041-0
7. Xie, M., Zhan, L., Ma, B., Hui S. Classification of fiber metal laminates (FMLs), adhesion theories and methods for improving interfacial adhesion: A review. Thin-Walled Structures. 2024. Article no. 111744. DOI: 10.1016/j.tws.2024.111744
8. Jiang, N., Lyu, H., Li, Y., Xu, N., Zhang, H., Zhou, N., Zou, X., Zhang, D. Enhanced interfacial adhesion of CF/PEEK-titanium hybrid laminates via rare-earth coordination interaction. Composites Science and Technology. 2023. 239. 110070. DOI: 10.1016/j.compscitech.2023.110070
9. Prolongo, S.G., Ureña, A. Effect of surface pre-treatment on the adhesive strength of epoxy–aluminium joints. International Journal of Adhesion and Adhesives. 2009. 29(1). Pp. 23–31. DOI: 10.1016/j.ijadhadh.2008.01.001
10. Critchlow, G.W., Brewis, D.M. Review of surface pretreatments for aluminium alloys. International Journal of Adhesion and Adhesives. 1996. 16(4). Pp. 255–275. DOI: 10.1016/S0143-7496(96)00014-0
11. Harris, A.F., Beevers, A. The effects of grit-blasting on surface properties for adhesion. International journal of adhesion and adhesives. 1999. 19(6). Pp. 445–452. DOI: 10.1016/S0143-7496(98)00061-X
12. Sinmazçelik, T., Avcu, E., Bora, M.Ö., Çoban, O. A review: Fibre metal laminates, background, bonding types and applied test methods. Materials & Design. 2011. 32(7). Pp. 3671–3685. DOI: 10.1016/j.matdes.2011.03.011
13. Lefebvre, D., Ahn, B., Dillard, D. et al. The effect of surface treatments on interfacial fatigue crack initiation in aluminum/epoxy bonds. International Journal of Fracture. 2002. 114. Pp. 191–202. DOI: 10.1023/A:1015094701018
14. Gonzalez-Canche, N.G., Flores-Johnson, E.A., Cortes, P., Carrillo, J.G. Evaluation of surface treatments on 5052-H32 aluminum alloy for enhancing the interfacial adhesion of thermoplastic-based fiber metal laminates. International Journal of Adhesion and Adhesives. 82. 2018. Pp. 90–99. DOI: 10.1016/j.ijadhadh.2018.01.003
15. Bjørgum, A., Lapique, F., Walmsley, J., Redford, K. Anodising as pre-treatment for structural bonding. International Journal of Adhesion and Adhesives. 2003. 23(5). Pp. 401–412. DOI: 10.1016/S0143-7496(03)00071-X
16. Liu, J., Chaudhury, M., Berry, D., Seebergh, J., Osborne, J., Blohowiak, K. Effect of Surface Morphology on Crack Growth at a Sol-Gel Reinforced Epoxy/Aluminum Interface. Journal of Adhesion. 2006. 82(5). Pp. 487–516. DOI: 10.1080/00218460600713725
17. Ozun, E., Ceylan, R., Özgür Bora, M., Çoban, O., & Kutluk, T. Combined effect of surface pretreatment and nanomaterial reinforcement on the adhesion strength of aluminium joints. International Journal of Adhesion and Adhesives. 2022. 119. 103274. DOI: 10.1016/j.ijadhadh.2022.103274
18. Nassir, N.A., Birch, R.S., Cantwell, W.J., Rico Sierra, D., Edwardson, Dearden, S.P., G., Guan, Z.W. Experimental and numerical characterization of titanium-based fibre metal laminates. Composite Structures. 2020. 245. Article no. 112398. DOI: 10.1016/j.compstruct.2020.112398
19. Sandeep, R., Nagarajan, B.M., Kumar, S.K., Adarsh, S.J., Manoharan, M., Natarajan, A. Strategies to improve joint strength of friction lap welded AA7475/PPS hybrid joint with surface pre-treatment on AA7475. Materials Letters. 2023. 333. Article no. 133561. DOI: 10.1016/j.matlet.2022.133561
20. Moldovan, E.R., Concheso Doria, C., Ocaña Moreno, J.L., Baltes, L.S., Stanciu, E.M., Croitoru, C., Pascu, A., Tierean, M.H. Geometry Characterization of AISI 430 Stainless Steel Microstructuring Using Laser. Archives of Metallurgy and Materials. 2022. 67(2). Pp. 645–652. DOI: 10.24425/amm.2022.137801
21. Kochemirovskaia, S.V., Lebedev, D.V., Fogel, A.A. et al. Properties of Selenium Colloidal Solution Obtained via Laser Ablation and a Subsequent Method for Producing Highly Dispersed CuInSe2. The Journal of The Minerals, Metals & Materials Society. 2021. 73. Pp. 646–654.
22. Trauth, A., Lohr, C., Lallinger, B., Weidenmann, K.A. Interface characterization of hybrid biocompatible fibermetal laminates after laser-based surface treatment. Composite Structures. 2022. 281. 115054. 10.1016/j.compstruct.2021.115054

23. Li, W., Jin, Y., Gu, J., Zeng, Z., Su, X., Xu, J., Guo, B. Critical surface characteristics for coating adhesion and friction behavior of aluminum alloys after laser cleaning. Journal of Materials Processing Technology. 2024. 332. Article no. 118549. DOI: 10.1016/j.jmatprotec.2024.118549.
24. Lambiase, F., Yanala, P. B., Leone, C., & Paoletti, A. Influence of laser texturing strategy on thermomechanical joining of AA7075 aluminum alloy and PEEK. Composite Structures. 2023. 315. 116974. DOI: 10.1016/j.compstruct.2023.116974

Information about the authors:

Dmitry Goncharenko,
ORCID: https://orcid.org/0000-0002-0827-6816
E-mail: honcharenkodmitry@gmail.com

Ilya Kobykhno,
ORCID: https://orcid.org/0000-0002-3873-9316
E-mail: ilya.kobykhno@gmail.com

Elizaveta Bobrynina, *PhD in Technical Sciences*
ORCID: https://orcid.org/0000-0001-5054-3482
E-mail: bobrynina_ev@spbstu.ru

Vladimir Yadykin, *PhD in Economics*
ORCID: https://orcid.org/0000-0003-3603-4635
E-mail: v.yadikin@gmail.com

Received 17.12.2024. Approved after reviewing 28.01.2025. Accepted 28.01.2025.

Magazine of Civil Engineering. 2025. 18(1). Article No. 13308

Magazine of Civil Engineering

ISSN
2712-8172

journal homepage: http://engstroy.spbstu.ru/

Research article

UDC 621.644 : 620.193 : 667.6

DOI: 10.34910/MCE.133.8

Protective coatings of building structures and pipelines for operation in the Arctic

R.I. Sapelkin[1] ✉, ***S.I. Matreninskiy***[2], ***V.Ya. Mishchenko***[3], ***V.A. Tarasov***[4]

[1] Gazprom Invest LLC, Gazprom PJSC, St. Petersburg, Russian Federation

[2] Voronezh State Technical University, Voronezh, Russian Federation

[3] Moscow State University of Civil Engineering (National Research University), Moscow, Russian Federation

[4] Peter the Great St. Petersburg Polytechnic University, St. Petersburg, Russian Federation

✉ *Rom_1976@mail.ru*

Keywords: protective coating, building structures, pipe metal, Arctic, industrial safety, rubber mastic, rubber concrete, recycling, industrial waste, thermal energy, vulcanization, heating wire, induction, temperature-time conditions, physical and mechanical characteristics

Abstract. The article is devoted to the study of the efficiency of using insulating (protective) coatings of building structures and pipeline transport for their reliable and trouble-free operation in extreme conditions of the Arctic zone. Innovative construction and composite materials – rubber concrete and rubber mastic, which have a combination of high physical, mechanical, and operational characteristics, are proposed to be used as protective coatings. A mandatory condition for the structure formation of rubber concrete and rubber mastic with the formation of a durable and corrosion-resistant protective layer is the dosed introduction of thermal energy into the composite material during an experimentally established period of time, which ensures the production of a protective coating with high specified properties. To establish rational technological modes of structure formation of the rubber-containing protective layer, experimental studies were carried out to optimize the temperature and time modes of introducing thermal energy into the composite material of the protective coating. Optimization of the technological modes of forming a protective coating from rubber concrete for reinforced concrete building structures was carried out on a developed and manufactured experimental heat-generating stand with a working element in the form of an uninsulated metal wire. Optimization of technological modes of formation of protective coating from rubber mastic for pipe metal was carried out on an experimental stand using induction heating. It was proposed to use a number of industrial wastes (fly ash, rubber crumb, etc.) as a filler in rubber concrete and in rubber mastic. A comparative analysis of the characteristics of the protective coating of pipe metal based on rubber mastic with the characteristics of the currently widely used multilayer polyethylene coating was carried out. The competitive advantages of rubber-containing protective coating of pipe metal are determined.

Funding: Grant of the Chairman of the Management Board of PJSC Gazprom in accordance with the order of PJSC Gazprom dated 01.09.2022 No. 329.

Acknowledgements: Roman Ivanovich Sapelkin extends his gratitude to the Chairman of the Management Board of PJSC Gazprom, Alexey Borisovich Miller, for providing a Grant from the Chairman of the Management Board of PJSC Gazprom for the preparation of a dissertation for the degree of Doctor of Science at the Voronezh State Technical University.

Citation: Sapelkin, R.I., Matreninskiy, S.I., Mishchenko, V.Ya., Tarasov, V.A. Protective coatings of building structures and pipelines for operation in the Arctic. Magazine of Civil Engineering. 2025. 18(1). Article no. 13308. DOI: 10.34910/MCE.133.8

1. Introduction

The harsh climate and engineering and geological conditions of the Arctic zone place increased demands on the protective characteristics of construction projects operated in this region.

Road surfaces, airfield runways, reinforced concrete emergency dumping areas for fuels and lubricants, sludge beds of treatment facilities, metal tanks and reservoirs, as well as on-site and main gas pipelines are subject to destructive impact.

At the same time, special attention should be paid to protecting steel pipeline transport, widely used for the preparation and transportation of hydrocarbon raw materials, from the negative impact of the environment. First of all, this is due to ensuring industrial safety for people and the unique ecosystem of the Arctic region. The damage from an accident on a main gas pipeline is estimated at hundreds of millions of rubles, associated with both the destruction of pipelines and the costs of their restoration, and with destructive negative man-made impacts on the biosphere of the Arctic zone. Thus, in the conditions of the Arctic region, it is necessary to use protective coatings with the following characteristics: resistance to low temperatures, high physical and mechanical characteristics, a coefficient of thermal linear expansion as close as possible to the coefficient of thermal linear expansion of the protected structure, high adhesion of the coating to the protected surface, high resistance to thermal cycling, low water and air permeability.

A necessary and mandatory factor in the creation of effective protective coatings is the use of Russian-made components, including raw materials, equipment, and technologies required both for the mass production of initial composite materials [1–4] and for technologies for the direct industrial installation of protective coatings for building structures and pipelines in field and factory conditions [5–7].

It should be noted that in the modern scientific community, the greatest relevance is the development of effective polymer composite building materials with high strength and performance characteristics [8–11], as well as improving the applied building materials by optimizing their compositions and introducing nano-components [12–14]. Particular attention is paid to the development of protective coatings for building structures and pipeline transport using polymer composite materials that are resistant to the effects of chemically aggressive environments [15–18], as well as climatic and engineering-geological impacts of the operating environment [19].

In addition, at present, the approach to solving the issue of recycling waste from industrial production and the construction industry, by using it as a filler for concrete, including polymer concrete, is of significant scientific importance, which ensures the sanitation of the surrounding urban and natural environment [20–23].

Thus, the relevance of the study lies in the need to develop effective insulating coatings to protect building structures and pipeline transport from the negative climatic and engineering-geological impacts of the Arctic region with the possibility of using domestic raw materials and recycling a variety of man-made waste. The object of the research work is effective protective coatings of building structures and steel pipeline transport, intended for use in the harsh climatic and engineering-geological conditions of the Arctic region.

Fundamental research work on the creation of rubber concretes and rubber mastics (the “rubber concrete” category) was carried out at the Voronezh State Technical University (VSTU) [18, 24–26]. Rubber concrete is a composite building material obtained by vulcanizing a rubber-concrete mixture.

The filler of the rubber-concrete mixture can make up more than 85 % of its total mass. The filler of the rubber-concrete mixture can make up more than 85 % of its total mass. In this case, it is advisable to use production waste generated during the operation of industrial enterprises [22, 27–29], rubber crumb obtained during the processing of car tires [30], waste from the disposal of electronic products (printed circuit boards, microcircuits, etc.) [31], recycled plastic, etc. as filler. Such a circumstance allows us to solve the global problem of recycling various industrial waste.

The combination of high physical, mechanical, and operational characteristics of rubber concrete creates the necessary prerequisites for its effective use as a protective coating material for construction projects operating in the extremely low temperatures of the Arctic region.

Studies have been conducted to determine the chemical resistance of rubber concrete in relation to various aggressive environments that are widespread in industrial production. Based on the results of the studies, a conclusion has been made that allows us to classify rubber concrete as a chemically resistant material in relation to the aggressive environments studied. Table 1 contains data on the chemical resistance coefficients of rubber concrete.

Table 1. Chemical resistance coefficients of rubber concrete [17].

№	**Names of the studied aggressive environments**	**Values of the chemical resistance coefficient of rubber concrete**
1.	Solutions of organic acids	0.81 – 0.95
2.	Solutions of inorganic acids	0.81 – 0.97
3.	Solutions of alkalis and bases	0.81 – 0.87
4.	Solutions of salts, solvents, petroleum products	0.83 – 0.95
5.	Water	0.995

Rubber concrete has a wide operating temperature range from +80 °C to –80 °C, without deterioration of physical, mechanical, and operational characteristics. At the same time, experimentally established data indicate an increase of up to 25 % in the physical and mechanical characteristics of rubber concrete in the range of negative temperatures from 0 °C to – 80 °C.

Rubber concrete is a frost-resistant, water- and air-impermeable material capable of withstanding up to 500 freeze-thaw cycles without a significant reduction in strength characteristics.

The specified values of the given characteristics of rubber concrete show the feasibility of its use in low-temperature conditions inherent in the Arctic zone. Rubber concrete has been shown to be resistant to thermal-oxidative degradation and ultraviolet radiation, which makes it possible to use the corresponding protective coatings based on it without additional shelter from the influence of sunlight.

The value of the coefficient of linear thermal expansion of rubber concrete is at the level of the coefficient of linear thermal expansion of steel, which allows rubber concrete to be used for external insulation of steel pipes without the risk of its destruction during thermal expansion of steel.

Rubber concrete is a classic dielectric, since its main binding component is synthetic rubber. This circumstance significantly reduces the likelihood of stray currents appearing at the boundary of the rubber concrete-coated pipe metal and the soil, eliminating the possibility of electrochemical corrosion. Table 2 shows the main physical and mechanical characteristics of rubber concrete.

Table 2. Values of physical and mechanical characteristics of rubber concrete [26].

№	**Names of physical and mechanical characteristics of rubber concrete**	**Values of physical and mechanical characteristics of rubber concrete**
1.	Compressive strength, MPa	50…100
2.	Tensile strength, MPa	10…20
3.	Modulus of elasticity, ´10^4 MPa	1.5…3.0
4.	Compressive duration coefficient	0.72…0.76
5.	Poisson’s ratio	0.2…0.3
6.	Heat resistance	100…110
7.	Frost resistance, freeze-thaw cycles	notless than 500
8.	Abrasion, g/cm^2	0.07…0.79
9.	Water absorption by weight, wt. %	0.05

Among the operational characteristics, it is worth noting the high resistance of rubber concrete to abrasion. The minimum value of rubber concrete abrasion – 0.07 g/cm^2 is possible when using corundum as a filler of the composite material.

The structure formation of an effective composite material – rubber concrete, occurs as a result of vulcanization of the rubber component of the material. During heat treatment of the rubber component, the vulcanizing agent – a sulfur-containing substance – forms cross-links between the rubber macromolecules, with the formation of a three-dimensional mesh structure.

Normal structure formation of rubber concrete is possible when creating a given uniform temperature field over the volume of the vulcanizate. The structure formation of rubber concrete occurs as a result of the metered introduction of thermal energy into the rubber mastic over an experimentally established period of time, which significantly complicates the technological process of obtaining reliable protective coatings in the conditions of work directly in the open areas of the Arctic region. Therefore, there is a need to develop a technology for the installation of protective coatings based on rubber concrete using energy-efficient heat-generating devices.

The aim of the study is to develop a technology for the installation of high-strength corrosion-resistant protective coatings for building structures and pipe metal used in the climatic and engineering-geological conditions of the Arctic region using a composite material based on domestic synthetic rubber (low-molecular oligodiene) and using effective methods for introducing thermal energy to ensure the necessary temperature conditions for the structure formation of the coating material.

To achieve the stated goal of the study, the following tasks were solved:

1. New design and technological solutions for devices based on domestic materials, structures, and equipment were developed, implementing various methods for introducing thermal energy into an insulating composite material (low-molecular oligodiene), which ensures high physical, mechanical, and operational properties of the protective coatings of building structures and pipe metal formed in this way.
2. A rational composition of the composite material of the protective coating with a filler made of man-made waste (fly ash, rubber crumb, etc.) was established.
3. A technology for forming protective coatings for building structures and pipe metal has been developed, including the selection of a rational composition of a composite material based on low-molecular oligodiene and the optimization of the modes of introducing thermal energy into the vulcanized coating material.
4. The physical, mechanical, and operational characteristics of protective coatings for building structures and pipe metal using a composite material based on low-molecular oligodiene have been determined.

2. Methods

2.1. Development of Technology for the Installation of Coatings Based on Rubber Concrete for Protection of Building Structures

In order to form protective coatings based on rubber concrete on the surface of reinforced concrete structures, an experimental electric heat-generating device using a heating wire was developed and constructed, and a corresponding technology for the formation of protective coatings of building structures and buildings was developed using this experimental device [5].

The formation of rubber concrete coatings by vulcanizing the rubber component when introducing thermal energy from a heating wire into rubber concrete by passing an electric current through is a complex technological process that begins with the preparation of the surface of the reinforced concrete structure to be protected.

The surface of the reinforced concrete structure is cleaned of any debris, de-dusted, and degreased. The next step is to install the heating wire fastening pins to a height corresponding to the coating thickness on the surface of the protected structure.

Next, steel washers with a thickness of 2.0–2.5 mm are put on the pins of the heating wire fastening, and the heating wire is directly mounted. This heating wire is essentially the working element of the experimental electric heat-generating device, the basic electrical circuit of which is shown in Fig. 1.

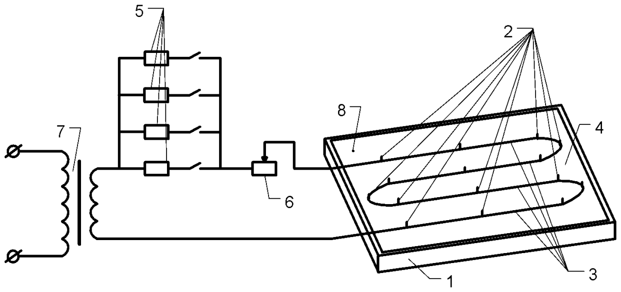

Figure 1. Basic circuit diagram of the experimental electric heat-generating device using a heating wire: 1 – formwork; 2 – heating wire fastening pins; 3 – non-removable heating wire; 4 – surface of the protected reinforced concrete structure; 5 – load resistors; 6 – rheostat; 7 – step-down transformer, 8 – thermocouple.

Steel washers are used to establish the required gap between the heating wire and the surface of the reinforced concrete structure in order to obtain the lowest value of the temperature field dispersion during vulcanization of the coating material by the heating wire. Then, the formwork is mounted and rubber concrete is laid on the surface of the reinforced concrete structure limited by the formwork.

The insulated surface of the reinforced concrete structure is filled with rubber mastic to the height of the mounted pins for fastening the heating wire and covered with polyethylene film in order to reduce heat loss during vulcanization of rubber concrete. The temperature regime is controlled using a thermocouple placed in the vulcanizate and connected to a thermoelectric device.

Vulcanization of the protective coating material based on rubber mastic is carried out in two stages. At the first stage, lasting 55–65 minutes, heat treatment is performed with maintaining the temperature of the coating material in the range from +85 °C to +95 °C. This stage is required to form the initial structural bonds in the protective coating material. The second stage – the main stage of vulcanization of the protective coating material is carried out by maintaining the temperature in the range from +115 °C to +125 °C for 180–200 minutes.

The temperature mode is adjusted using load resistors and a rheostat included in the electrical network. After completion of the main stage of vulcanization of the protective coating material, the power supply to the heating wire is disconnected and the resulting protective coating cools smoothly to the outside air temperature. When observing the above-mentioned experimentally obtained temperature-time technological regimes, the protective coating based on rubber concrete acquires the physical, mechanical, and operational characteristics necessary for the material of the protective coating of building structures.

Fig. 2 shows a full-scale installation of a non-insulated heating wire on a reinforced concrete base, as well as vulcanization of the protective coating material of a reinforced concrete platform by a heating wire connected to the electrical network using the developed experimental device.

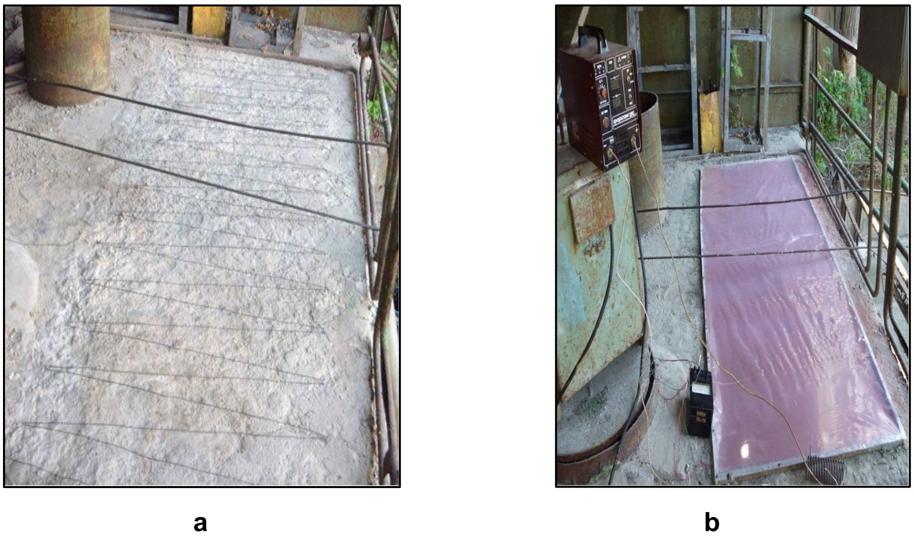

Figure 2. Experimental device for structuring a protective coating based on rubber concrete on the surface of reinforced concrete structures: a – installation of a non-insulated heating wire on a reinforced concrete base; b – vulcanization of the protective coating material by a heating wire connected to the electrical network.

2.2. Development of a Technology for Installing a Protective Coating Based on Rubber Concrete for External Insulation of Pipe Metal

In order to develop the design of a heat-generating device for the effective introduction of thermal energy into the material of the protective composite rubber-containing coating of the pipe metal, a series of exploratory experiments were conducted.

Based on the results of the experiments, it was possible to create a temperature field in the volume of the vulcanizate in the required range from +134 °C to +135 °C with an exit to the temperature mode at a rate of no more than 10 °C/min as a result of induction heating of the steel pipeline [6–7]. The full cycle of structure formation of the rubber mastic on the surface of the steel pipe using induction heating of the pipe metal is about 60–65 minutes.

In order to implement an effective method of introducing thermal energy into rubber mastic, a structural diagram of a pilot experimental device using an induction method of heating pipe metal has been developed. This structural diagram is shown in Fig. 3.

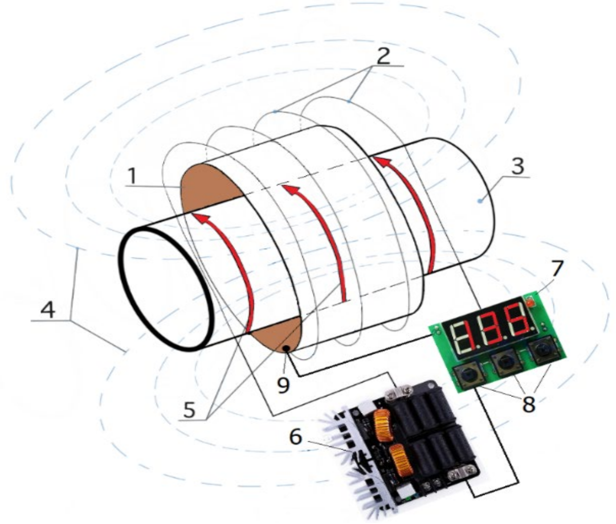

Figure 3. Structural diagram of the electric heat-generating device for vulcanization of rubber mastic on the surface of pipe metal using the induction method: 1 – vulcanizable protective coating of pipe metal; 2 – induction coil; 3 – insulated steel pipe; 4 – magnetic field; 5 – eddy currents in pipe metal; 6 – high-frequency current generator; 7 – thermostat; 8 – temperature setting keys; 9 – thermocouple.

Thus, when using induction heating for heat treatment of a protective layer of rubber mastic on the surface of pipe metal, the heating element itself is the insulated steel pipe as a result of contact with which the heating and vulcanization of the protective coating material occurs. This allows minimizing heat loss and noting the high efficiency of the electric heat-generating device due to the direct contact of the heated material – the protective coating and the heating element – the working body, i.e. the insulated steel pipe heated by the eddy electric currents induced in it.

Maintaining the temperature regime in the required temperature field range of 134–135 °C is carried out using a thermostat built into the electrical circuit of the induction heater. Signals with information about the actual parameters of the vulcanizate temperature field are sent to the thermostat through the connection of the electric wire with a thermocouple placed in the vulcanized material. That is, when the vulcanizate temperature reaches + 135 °C, the induction heating of the pipe metal is temporarily stopped, until the vulcanizate temperature drops to + 134 °C; in this case, the induction heating is automatically turned on again, and thus, a cyclic process of maintaining the temperature regime occurs. The process of structure formation of a protective coating of pipe metal using rubber concrete consists of sequentially performed technological operations:

1. Cleaning the pipe metal from rust and dirt;
2. Application of a protective layer of rubber concrete 2–3 mm thick to the pipe metal;
3. Heat treatment of the protective coating material – rubber concrete – by induction heating, with mandatory provision and control of the temperature regime of vulcanization of rubber mastic.

To ensure the formation of a protective coating based on rubber concrete on the surface of the pipe metal, an experimental setup using induction heating was designed, the appearance of which is shown in Fig. 4.

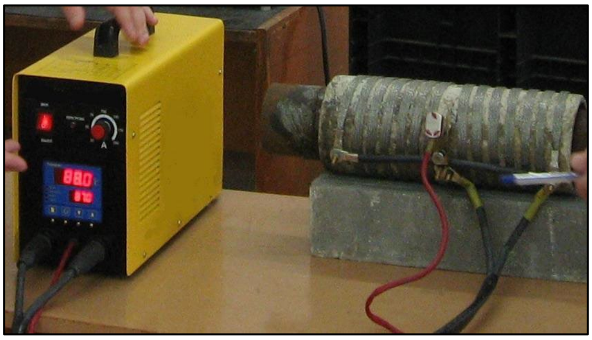

Figure 4. External appearance of the experimental setup for ensuring the formation of a protective coating based on rubber concrete on the surface of the pipe metal using induction heating.

3. Results and Discussion

The combination of high physical, mechanical, and operational characteristics of rubber concrete make it possible to effectively use it as a material for protective coating of construction objects operating in conditions of extremely low temperatures of the Arctic region.

As a result of a series of exploratory experiments, temperature and time modes of rubber concrete vulcanization were determined when installing protective coatings on reinforced concrete building structures using a heating wire as a working element of a heat-generating device. With a protective coating layer thickness of 8–12 mm, heat treatment of rubber concrete should be carried out in two stages to avoid vulcanizate swelling due to increased gas evolution.

The first stage lasting 55–65 minutes is carried out with maintaining the temperature in the range from +85 °C to +95 °C to form initial structural bonds in the vulcanized rubber mastic.

The second main stage of caoutchouc vulcanization lasting 180–200 minutes is carried out maintaining the temperature from +115 °C to +125 °C for the final formation of a protective coating based on vulcanized rubber mastic. Exceeding the temperature of +125 °C leads to increased gas formation, and as a consequence, swelling and destruction of the protective coating material. Also, in order to avoid swelling of the material, the rate of temperature increase during transient processes should not exceed 1 °C/min.

Fig. 5 shows a graph of experimentally established temperature-time modes of rubber concrete vulcanization when using it to create effective protective coatings for building structures.

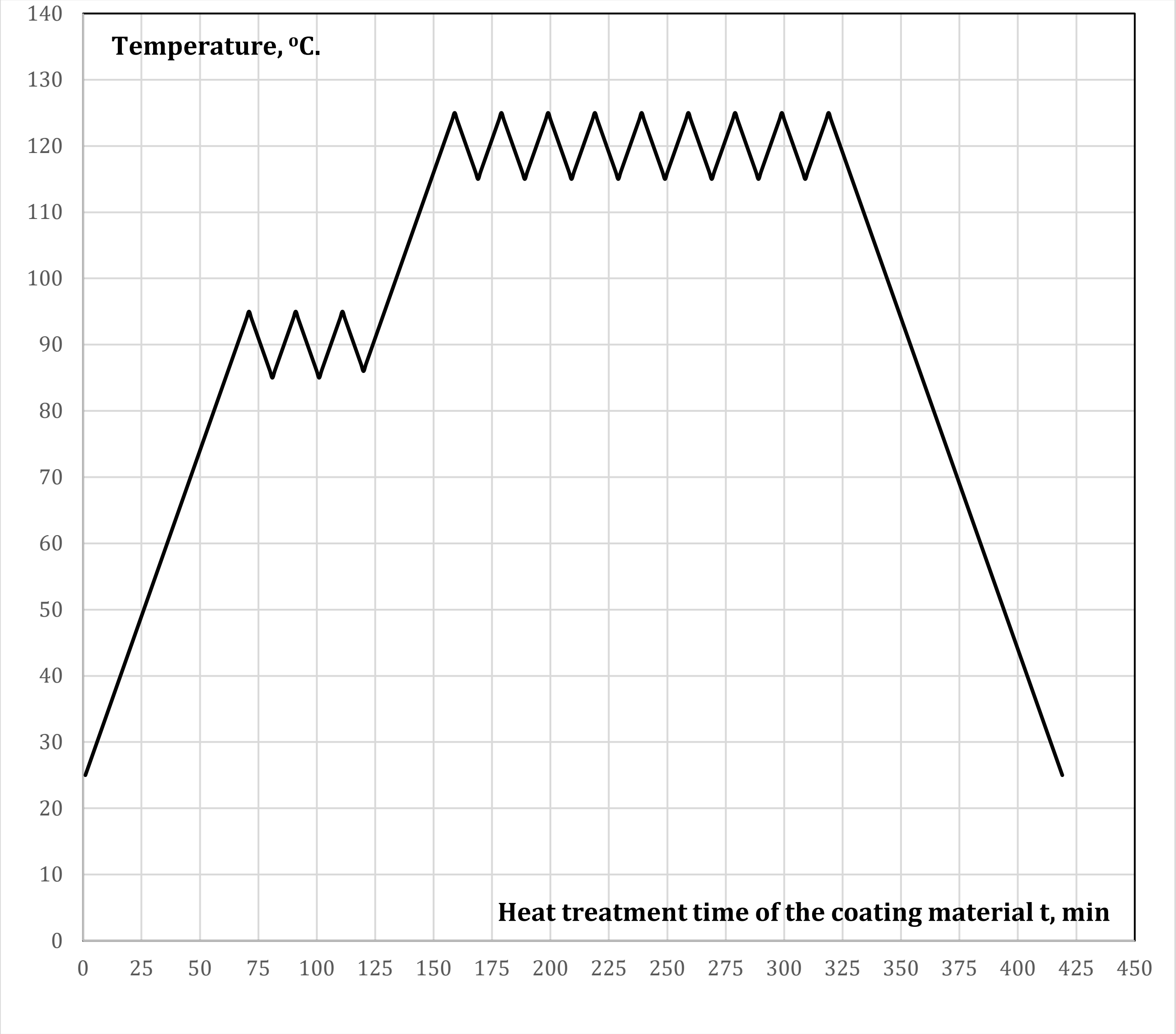

Figure 5. Graph of experimentally established temperature-time modes of rubber concrete vulcanization when using it to create protective coatings for building structures and constructions.

As a result of a series of exploratory experiments, the temperature and time modes of rubber concrete vulcanization were determined when a protective coating of pipe metal was installed on its basis using induction heating. With a protective coating layer thickness of pipe metal up to 1 mm, the heat treatment of rubber concrete can be carried out in one stage lasting 20–25 minutes with the temperature maintained at up to 135 °C. Exceeding the temperature of 135 °C leads to combustion and destruction of the material. At the same time, in order to avoid swelling and destruction of the material, the rate of temperature increase during transient processes should not exceed 10 °C/min.

Fig. 6 shows a graph of the experimentally established temperature and time modes of rubber concrete vulcanization when a protective coating of pipe metal is installed on its basis.

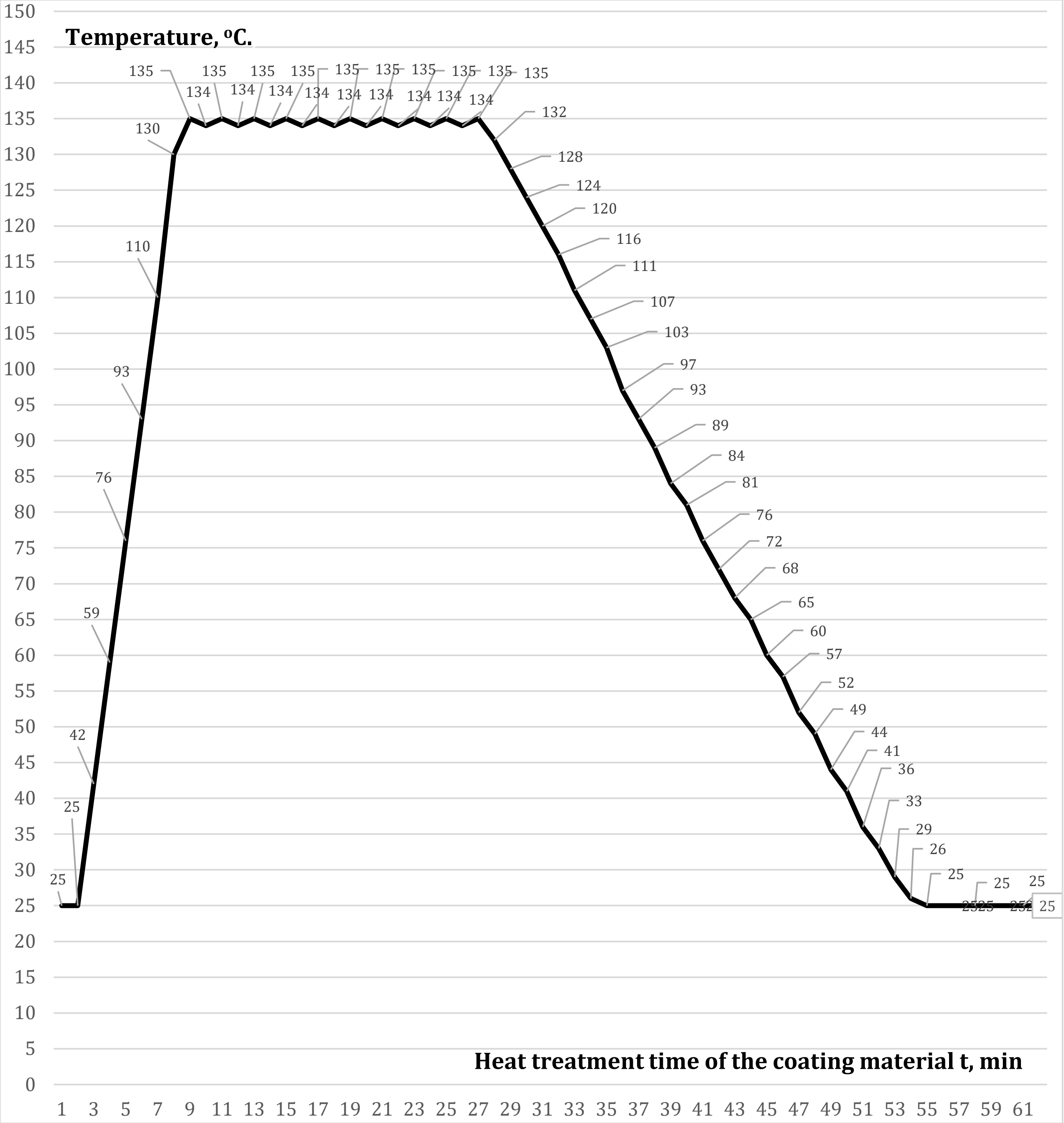

Figure 6. Graph of the experimentally established temperature and time modes of rubber concrete vulcanization when a protective coating of pipe metal is installed on its basis.

Experimental studies were conducted on the obtained samples to determine the characteristics of the protective coating of pipe metal based on rubber concrete. Table 3 presents a comparative analysis of the characteristics of the protective coating of pipe metal based on rubber concrete and the characteristics of the currently widely used multilayer polyethylene coating.

Table 3. Comparison of the characteristics of the protective coating based on rubber concrete with the characteristics of the multilayer polyethylene coating.

№	Characteristic of the protective coating of the pipe metal	Multilayer polyethylene coating	Rubbe rconcrete based coating
1.	Adhesion of the protective coating under shear, N/cm^2	70	100
2.	Water resistance, % reduction in adhesion strength to the steel surface	5-12	5
3.	Operating temperature range, °C	– 20…+60	– 80…+80
4.	Cost, USD/m^2 (according to the manufacturer's website https: www.tk-rapid.ru. as of 02/26/2025)	32.0	11.5

A comparative analysis of the data presented in Tables 2, 3 allows us to conclude that the coating of the pipe metal based on rubber concrete has advantages in higher physical and mechanical characteristics compared to the characteristics of the widely used multilayer polyethylene coating. In addition, the protective coating of metal pipes based on rubber concrete is more than 2.5 times cheaper than a multilayer polyethylene coating.

It has been experimentally established that rubber concrete used as a protective coating material has higher strength characteristics compared to polymer concretes based on polyester and epoxy resins [32]. It has also been experimentally determined that the physical, mechanical, and operational characteristics of rubber concrete are at the level of, or exceed similar characteristics of polymer concretes based on furan, furan-epoxy, urea, and acrylic resins [8–10]. Table 4 presents a comparison of the strength characteristics of rubber concrete with the strength characteristics of currently used polymer concretes obtained on the basis of various types of polymer resins.

Table 4. Comparison of the strength characteristics of rubber concrete with the strength characteristics of the used polymer concretes obtained on the basis of various types of polymer resins.

№	Type of polymer concrete by binder type	Compressive strength, MPa	Tensile strength, MPa	Bending strength, MPa
1.	Rubber concrete	60…110	8…20	19…30
2.	Polymer concrete based on polyester resin	41…68	10…12	12…19
3.	Polymer concrete based on epoxy resin	71…98	14…19	21…22
4.	Polymer concrete based on acrylic resin	70…90	10…13	30…33
5.	Polymer concrete based on furan resin	70…90	5…8	–
6.	Polymer concrete based on furan-epoxy resin	90…110	9…11	–
7.	Polymer concrete based on urea resin	40…70	3…7	–

At the same time, coatings based on rubber concrete can be filled with production waste by more than 85 % by weight, which is the highest indicator among the available results of scientific research in the field of developing "green concrete" [28–31].

Also, during experimental studies to determine the adhesion of a protective coating based on rubber concrete, it was noted that the destruction of samples occurs mainly along the coating material, without its peeling off from the metal surface. This circumstance indicates the high adhesive strength of coatings based on rubber concrete. The appearance of the destroyed sample when determining the adhesion of a protective coating based on rubber concrete is shown in Fig. 7.

Figure 7. The appearance of the destroyed sample when determining the adhesion of a protective coating based on rubber concrete.

4. Conclusions

1. A technology for the installation of protective coatings for reinforced concrete structures using a material based on rubber concrete has been developed for the effective protection of building structures in the climatic conditions of the Arctic region.

2. An experimental stand was constructed to study technological regimes for the formation of an effective protective layer of pipe metal using induction heating and the ability to automatically adjust and maintain the required temperature regime for the formation of the rubber-containing composite material of the protective layer.

3. A comparative analysis of the experimentally obtained characteristics of the protective coating of pipe metal based on rubber mastic with the characteristics of the currently widely used multilayer polyethylene coating has been carried out. The advantage of quantitative indicators of the characteristics of the protective coating of pipe metal based on Cautone compared to the characteristics of the multilayer polyethylene coating is given in Table 3.

4. The use of high-strength corrosion-resistant coatings based on rubber concrete is advisable for the protection of building structures and pipeline transport operating in the harsh climatic and engineering-geological conditions of the Arctic regions.

5. The use of protective coatings based on rubber concrete allows solving the problem of recycling various industrial wastes, as a result of their use as a filler for rubber-concrete mixtures, making up more than 85 % of its total mass.

References

1. Potapov, Y.B., Pinaev, S.A., Arakelyan, A.A., Barabash, A.D. Polymer-Cement Material for Corrosion Protection of Reinforced Concrete Elements. Materials Science Forum. 2016. 871. Pp. 104–109. DOI: 10.4028/www.scientific.net/MSF.871.104
2. Borisov, Yu.M., Polikutin, A.E., Nguen Phan Duy. The Stress-strain state of normal sections of double-layered, rubcon-concrete bending elements of building structures. Russian Journal of Building Construction and Architecture. 2011. 2. Pp. 6–13.
3. Potapov, Y., Polikutin, A., Panfilov, D., Okunev, M. Comparative analysis of strength and crack resistance of normal sections of bent elements of T-sections, made of rubber concrete, cauton reinforcement and concrete. MATEC Web of Conferences. 2016. 73. Article no. 04018. DOI: 10.1051/matecconf/20167304018
4. Borisov, Y.M., Polikutin, A.E. Strength of inclined sections of bendable reinforcing elements. Beton i zhelezobeton [Concrete and Reinforced Concrete]. 2004. 1(526). Pp. 15–23.
5. Surovtsev, I.S., Borisov, Yu.M., Matreninsky, S.I., Sapelkin, R.I. Improvement of technology of application of high-strength corrosion-resistant protective coatings on the basis of low-molecular oligodiene. Scientific Herald of the Voronezh State University of Architecture and Civil Engineering. Construction and Architecture. 2011. 3. Pp. 42–55.
6. Sapelkin, R.I., Matreninsky, S.I., Mishchenko, V.Ya. Effective Protective Coating of Pipe Metal with High-Strength Corrosion-Resistant Material Based on Low-Molecular Oligodiene. Russian Journal of Building Construction and Architecture. 2023. 4(60). Pp. 53–65. DOI: 10.36622/VSTU.2023.60.4.005
7. Sapelkin, R.I., Matreninsky, S.I., Mishchenko, V.Ya. Development of a mathematical model of the temperature field in the material of the protective coating of pipe metal based on low molecular weight oligodiene during its heat treatment. Russian Journal of Building Construction and Architecture. 2024. 1(61). Pp. 58–68. DOI: 10.36622/VSTU.2024.61.1.005
8. Figovsky, O., Beilin, D. Advanced Polymer Concretes and Compounds. 1st edn. CRC Press. Boca Raton, 2013. 267 p. DOI: 10.1201/b16237
9. Figovsky, O. New polymeric matrix for durable concrete. Cement Combinations for Durable Concrete. Thomas Telford Publishing, 2005. Pp. 269–276. DOI: 10.1680/ccfdc.34013.0029
10. Figovsky, O., Beilin, D., Blank, N., Potapov, J., Chernyshev, V. Development of polymer concrete with polybutadiene matrix. Cement and Concrete Composites. 1996. 18(6). Pp. 437–444. DOI: 10.1016/S0958-9465(96)00036-4
11. Polikutin, A., Potapov, Y., Levchenko, A., Perekal'skiy, O. The Stress-Strain State of Normal Sections Rubcon Bending Elements with Mixed Reinforcement. Advances in Intelligent Systems and Computing. 2019. 983. International Scientific Conference Energy Management of Municipal Facilities and Sustainable Energy Technologies EMMFT 2018. Pp. 586–599. DOI: 10.1007/978-3-030-19868-8_56

12. Rybakov, V., Seliverstov, A., Usanova, K. Steel profile corrosion resistance in contact with monolithic foam concrete. E3S Web of Conferences. 2023. 365. Article no. 02001. DOI: 10.1051/e3sconf/202336502001
13. Rybakov, V., Seliverstov, A., Petrov, D., Smignov, A., Volkova, A. Strength characteristics of foam concrete samples with various additives. MATEC Web of Conferences. 2018. 245. Article no. 03015. DOI: 10.1051/matecconf/201824503015
14. Jos, V., Rybakov, V., Sviridenko, V., Brailova, T. Quality Indicators of Nanomodified Cements and Relevant Products. Lecture Notes in Civil Engineering. 2021. 150. Proceedings of EECE 2020. Pp. 35–46. DOI: 10.1007/978-3-030-72404-7_4
15. Gorninski, J.P., Dal Molin, D.C., Kazmierczak, C.S. Comparative assessment of isophtalic and orthophtalic polyester polymer concrete: Different costs, similar mechanical properties and durability. Construction and Building Materials. 2007. 21(3). Pp. 546–555. DOI: 10.1016/j.conbuildmat.2005.09.003
16. Ahmed, H.Q., Jaf, D.K., Yaseen, S.A. Flexural Capacity and Behaviour of Geopolymer Concrete Beams Reinforced with Glass Fibre-Reinforced Polymer Bars. International Journal of Concrete Structures and Materials. 2020. 14(1). Article no. 14. DOI: 10.1186/s40069-019-0389-1
17. Potapov, Yu.B., Chmykhov, V.A., Borisov, Yu.M. Resistance of a polymer concrete based on polybutadiene binder to organic and inorganic acids. Scientific Israel – Technological Advantages. 2013. 15(4). Pp. 7–10.
18. Potapov, Yu.B. Rubcon – a new class of corrosion-resistant building materials. Building materials of the XXI century. 2000. 9. Pp. 9–10.
19. Potapov, Yu.B., Borisov, Yu.M. Wear-Resistant Coatings On The Basis Of Oligodienes. Russian Journal of Building Construction and Architecture. 2010. 1. Pp. 38–44.
20. Kar, A., Ray, I., Halabe, U.B., Unnikrishnan, A., Dawson-Andoh, B. Characterizations and Quantitative Estimation of Alkali-Activated Binder Paste from Microstructures. International Journal of Concrete Structures and Materials. 2014. 8. Pp. 213–228. DOI: 10.1007/s40069-014-0069-0
21. Mehta, K. Reducing the Environmental Impact of Concrete. Concrete international. 2001. 23. Pp. 61–66.
22. Radhakrishna, Venu Madhava, T., Manjunath, G.S., Venugopal, K. Phenomenological Model to Re-proportion the Ambient Cured Geopolymer Compressed Blocks. International Journal of Concrete Structures and Materials. 2013. 7. Pp. 193–202. DOI: 10.1007/s40069-013-0048-x
23. Harilal, M., George, R.P., Philip, J., Albert, S.K. Binary blended fly ash concrete with improved chemical resistance in natural and industrial environments. Environmental Science and Pollution Research. 2021. 28. Pp. 28107–28132. DOI: 10.1007/s11356-021-12453-4
24. Borisov, Yu.M., Shvyryov, B.A., Goshev, S.A. Strenght and perfomance of rubber concretes. Scientific Herald of the Voronezh State University of Architecture and Civil Engineering. Construction and Architecture. 2010. 4. Pp. 23–31.
25. Levchenko, A.V., Polikutin, A.E. Rubber concrete beams under the action of transverse bending. Magazineof Civil Engineering. 2022. 113(5). Article no. 11301. DOI: 10.34910/MCE.113.1
26. Polikutin, A.E., Panfilov, D.V., Oforkaja, T.O. Finite element analysis of reinforced rubber concrete T- beams using experimental results. Russian Journal of Building Construction and Architecture. 2023. 4(60). Pp. 19–26. DOI: 10.36622/VSTU.2023.60.4.002
27. Lokuge, W., Aravinthan, T. Effect of fly ash on the behaviour of polymer concrete with different types of resin. Materials and Design. 2013. 51. Pp. 175–181. DOI: 10.1016/j.matdes.2013.03.078
28. Dr. Ahmad Fuzail, Hashmi, M.S. Khan, M. Bilal, M. Shariq, A. Baqi. Green Concrete: An Eco-Friendly Alternative to the OPC Concrete. Construction 2022. 2(2). Pp. 93–103. DOI: 10.15282/construction.v2i2.8710
29. Al-Hamrani, M., Kucukvar, W., Alnahhal, E., Mahdi, Onat, N.C. Green Concrete for a Circular Economy: A Review on Sustainability, Durability, and Structural Properties. Materials. 2021. 14(2). Pp. 351–387. DOI: 10.3390/ma14020351
30. Assaggaf, R.A., Al-Dulaijan, S.U., Maslehuddin, M., Al- Amoudi, O.S.B., Ahmad, S., Ibrahim, M. Effect of different treatments of crumb rubber on the durability characteristics of rubberized concrete. Construction and Building Materials. 2022. 318. Article no. 126030. DOI: 10.1016/j.conbuildmat.2021.126030
31. Arivalagan, S. Experimental study on the properties of green concrete by replacement of E-plastic waste as aggregate. Procedia Computer Science. 2020. 172. Pp. 985–990. DOI: 10.1016/j.procs.2020.05.145
32. Bedi, R., Chandra, R., Singh, S.P. Reviewing some properties of polymer concrete. Indian Concrete Journal. 2014. 88(8). Pp. 47–68.

Information about the authors:

Roman Sapelkin*, PhD in Technical Sciences*
ORCID: https://orcid.org/0000-0003-0169-3323
E-mail: Rom_1976@mail.ru

Sergei Matreninskiy*, PhD in Technical Sciences*
ORCID: https://orcid.org/0000-0001-5708-1786
E-mail: gso09@yandex.ru

Valery Mishchenko*, Doctor of Technical Sciences*
ORCID: https://orcid.org/0000-0003-2385-5426
E-mail: oseun@yandex.ru

Vladimir Tarasov*, PhD in Technical Sciences*
ORCID: https://orcid.org/0000-0002-1030-8370
E-mail: vtarasov1000@yandex.ru

Received 27.12.2024. Approved after reviewing 28.01.2025. Accepted 28.01.2025.

Magazine of Civil Engineering. 2025. 18(1). Article No. 13309

Magazine of Civil Engineering

journal homepage: http://engstroy.spbstu.ru/

ISSN
2712-8172

Research article

UDC 699.842

DOI: 10.34910/MCE.133.9

Dynamic and statically equivalent approaches for analysis of the turbine foundations under the emergency load

M.S. Abu-Khasan[1], ***A.E. Babsky***[2], ***I.I. Oleinikov***[2], ***I.M. Oleinikova***[2], ***V. Tarasov***[3] ✉

[1] *Petersburg State Transport University, St. Petersburg, Russian Federation*

[2] *JSC "Atomenergoproekt", St-Petersburg Branch, St. Petersburg, Russian Federation*

[3] *Peter the Great St. Petersburg Polytechnic University, St. Petersburg, Russian Federation*

✉ *vtarasov1000@yandex.ru*

Keywords: turbine foundation, vibration-insulated turbine foundation, dynamic analysis, emergency unbalance, short circuit on the generator

Abstract. The article presents the results of the research of the emergency loads effect on reinforced concrete turbine foundations of different types. Computational experiments were performed in a specialized finite element analysis program NX/NASTRAN. Calculations of the high-power turbine foundations of frame, wall, and vibration-insulated structures have been carried out. Emergency loads associated with a short circuit and a loss of synchronization (generator failure) were taken into account in the calculations by equivalent static and dynamic approaches. The comparison was carried out according to the calculated values of displacements and forces, in the elements of the computational model, where extreme values of forces were expected from the design experience. The results of the comparative analysis indicate that the use of a widespread statically equivalent approach often leads to a multiple overestimation of forces and displacements, in comparison with using of dynamic approach. Therefore, strength and dynamic analysis of high-power turbine foundations under emergency loads, it is necessary to apply a dynamic approach. A statically equivalent approach can be used for analysis of foundations for turbine units of relatively low power.

Citation: Abu-Khasan, M.S., Babsky, A.E., Oleinikov, I.I., Oleinikova, I.M., Tarasov, V. Dynamic and statically equivalent approaches for analysis of the turbine foundations under the emergency load. Magazine of Civil Engineering. 2025. 18(1). Article no. 13309. DOI: 10.34910/MCE.133.9

1. Introduction

The turbine unit foundation is a special structure that integrates parts of the turbine and generator into a single system and used for taking static and dynamic loads and their transfer through the foundation plate to the ground base [1].

The object of the research is classic and vibration-isolated turbine unit foundations under the emergency loads, the subject of the research is the methods for calculating turbine unit foundations under emergency loads.

Plenty of previous research works of authors and other scientists, engineers, and researchers were devoted to the analysis of the behavior of vibration-insulated foundations of high power under the seismic impact [2–9].

In particular, researches [2, 4] present methods for accurately accounting for viscous dampers and vibration-isolating elements used in vibration-isolated turbo-generator foundations. Researches [3, 5, 8, 9] confirm the necessity of performing dynamic analysis for seismic calculations and demonstrate the effectiveness usage of seismic isolation.

Research related to the analysis of the dynamic behavior of special building structures has been covered by wide range of works [10–22].

Article [10] investigates the influence of the scale factor on the dynamic response of framed foundations, while article [11] investigates the impact of framed foundation geometry on the dynamic response during high-speed turbomachinery operation.

Research [12] demonstrates the importance of accurately accounting for equipment masses in the dynamic analysis model. Papers [13–15, 17–18] expand various aspects of soil-structure interaction in dynamic analyses of turbine foundation systems. Papers [19–22] demonstrates modern approaches to finite element seismic calculations.

Steam turbine units are the main electrical generating equipment of thermal and nuclear power plants, and uninterrupted power supply to all spheres of life depends on their reliable operation. In the event of an emergency on the turbine units, it is the reliability of the building structure of the turbine unit foundation, which serves as its main support, that determines the severity of the consequences for all equipment and building structures of the engine room.

The correctness of detailing and consideration in the strength analysis of turbine units foundations emergency loads on the generator, which are dynamic vibration loads by their nature, is a primary issue for the computational justification of the reliability of foundation building structures.

Correct accounting of emergency loads on a turbine unit is relevant in the strength analysis and design of all types of turbine units foundations of any capacity. Since the energy industry and its technologies are actively developing [23–32], it is necessary to improve the calculation methods of special building structures – turbine units foundations.

The purpose of the research is to compare the results of dynamic and statically equivalent approaches in the calculation of turbine unit foundations under the action of short-circuit loads on the generator. The research objectives include:

- Performing computational experiments related to the use of dynamic and statically equivalent approaches for accounting of emergency loads from turbo-generators on various types of foundations;
- Performing a comparative analysis of the computational experiment results by comparing two types of calculation approaches: static and dynamic, for different types of turbine unit foundations;
- Evaluating the influence of the structural features of turbine unit foundations on the calculation results.

2. Methods

The main research method is making computational experiments.

During implementing the chosen method, a certified calculation complex NASTRAN was used that implements finite element method [33–37]. The reliability and validity of the results confirmed due to the use of rigorous mathematical statements and hypotheses in the formulation and solution of problems adopted in the mechanics of deformable solids, structural mechanics, and dynamics of structures, as well as the use of modern proven numerical methods implemented by certified calculation complexes.

The methods of static analysis, harmonic analysis based on the decomposition of oscillation forms, and direct integration of equations of motion were used. Due to the large number of time integration steps and degrees of freedom in the finite element model, the number of elements and nodes for comparison results was limited to nodes and elements in which maximum values of displacements and forces were expected.

The analyses were performed using dynamic and equivalent static approaches (using the dynamic coefficient recommended by the standards or the equipment manufacturer). Graphs, diagrams, and graphical schemes were used to interpret the results, the data were summarized in comparative tables.

The results of calculated displacements, forces, and bending moments were used as the main parameters for the comparison. As a result, the coefficients of proportionality between the analysis results for two types of approaches are derived.

One of the common types of emergency loads is considered: a short circuit (two or three-phase) or a loss of synchronization, that are, an accident on the turbine generator.

The results of dynamic analysis obtained for five real types of turboset foundations were calculated and compared in the research. The main characteristics of turbosets and foundations are shown in Table 1.

Table 1. General characteristics of the turboset foundations.

№	**Turbine type**	**Foundation type**	**Vibration isolation**	**Operating frequency, rpm**	**Power, MW**	**Foundation mass, t**	**Turbine unit mass, t**
1	Type-1	Wall	no	1500	1000	22700	5060
2	Type-2	Frame	yes	1500	1250	6270	3540
3	Type-3	Frame	yes	3000	1200	4407	3817
4	Type-4	Frame with columns	no	3000	1000	19082	6190
5	Type-5	Frame	yes	1500	1250	6805	4760

There are two options for steam turbine installations of high power. The installations with an operating frequency of 3000 rpm (the same as the frequency of the 50 Hz in the electrical network) are called “high-speed”. Such turbines and generators have a lower mass and a two-pole generator. Installations with an operating frequency of 1500 rpm (25 Hz is a half of the frequency in the electrical network) are called “low-speed”. These turbines and generators have a large mass and a four-pole generator.

The design scheme of the wall foundation for a “low-speed” (1500 rpm) turbine unit is shown in Fig. 1. The model consists of a massive lower slab, walls, columns, and an upper structure of transverse crossbars (extensions on the walls) and longitudinal massive beams. This scheme is typical for the middle of the 20th century and is currently the only alternative to vibration-insulated turbine units foundations for the “low-speed” machines.

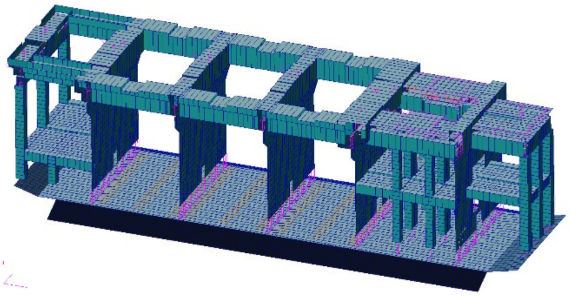

Figure 1. Finite element model of the wall foundation of the turbine unit Type-1 (1500 rpm).

The design scheme of a vibration-insulated frame foundation for the low-speed (1500 rpm) Type-1 turbine unit, manufactured in Russia, is shown in Fig. 2. The model consists of transverse crossbars and longitudinal beams of rectangular or close to rectangular cross-sections. The foundation is supported by vibration isolators, which are blocks that combine packages of cylindrical coaxial (one into the other) springs, some of the blocks are integrated with viscous dampers. The height of the reinforced concrete crossbars bearing the main load is up to 4.4 m. The structures are made of B30 grade concrete.

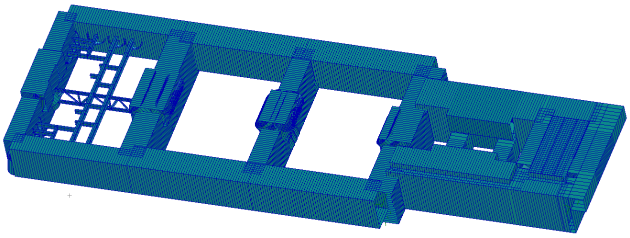

Figure 2. Finite element model of the vibration-insulated part of the foundation of the turbine unit Type-2 (1500 rpm).

The design scheme of a vibration-insulated frame foundation for the Type-3 “high-speed” turbine unit (3000 rpm) is shown in Fig. 3. The model consists of transverse crossbars, and longitudinal beams of rectangular or close to rectangular cross-sections. Similar to the Type-2 foundation, it is supported by vibration isolators (spring/spring-damping supports). The maximum calculated load-bearing capacity of the vibration isolators used in normal operation reaches 1600 kN (2000 kN in an extreme situation). The height of reinforced concrete crossbars bearing the main load is up to 4.24 m. The structures are made of B30 grade concrete.

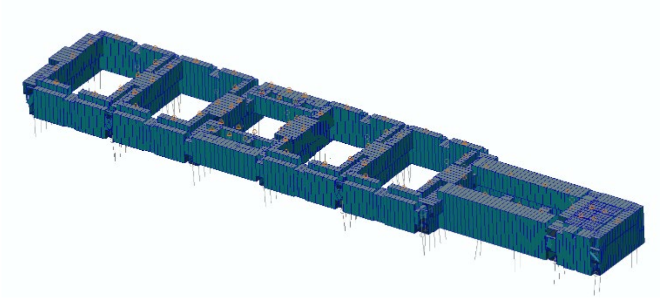

Figure 3. Finite element model of the vibration-insulated part of the foundation of the turbine unit Type-3 (3000 rpm).

The design scheme of the classic frame foundation for the Type-4 "high-speed" (3000 rpm) turbine unit is shown in Fig. 4. The foundation consists of a massive lower slab of trapezoidal cross-section, columns, and an upper frame structure of transverse crossbars and longitudinal beams. Such a topological scheme has been standard for several decades for units with a capacity from 10 to 1000 MW.

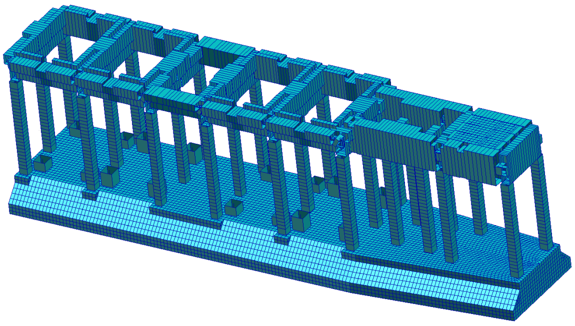

Figure 4. A finite element model of the classic frame foundation Type-4 for a turbine unit (3000 rpm).

The design scheme of the Type-5 vibration-insulated frame foundation for the "low-speed" (1500 rpm) turbine unit, produced in France, is shown in Fig. 5. The model consists of transverse crossbars and longitudinal beams of rectangular or close to rectangular cross-sections. Volumetric (8-node) end elements were used in the simulation to increase the accuracy of calculations. The number of degrees of freedom are 1200,000. Due to the huge mass of the structure, the foundation is supported by unique vibration isolators with high load-bearing capacity. The rated load-bearing capacity of the vibration isolators of this series can reach 4600 kN. The height of the crossbars made of reinforced concrete of B50 grade, bearing the main load, is 5.3 m.

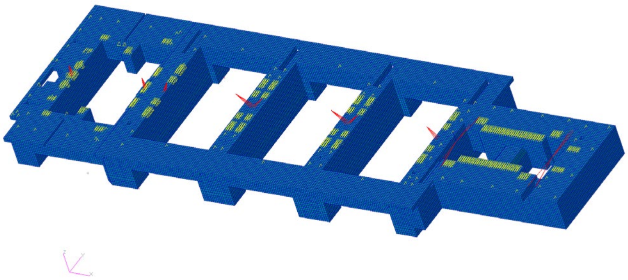

Figure 5. Finite element model of vibration-insulated foundation Type-5 for a turbine unit (1500 rpm), France.

3. Results and Discussions

The following is a reference view of the intermediate results:

- nodes for issuing the results of calculated forces and displacements for the vibration isolators (Fig. 6);
- diagrams of bending moments in the foundation elements during a short circuit (Fig. 7);

- a selection of elements for determining forces (Fig. 8);
- a graph of the vertical displacement of one of the nodes due to the dynamic loads (Fig. 9).

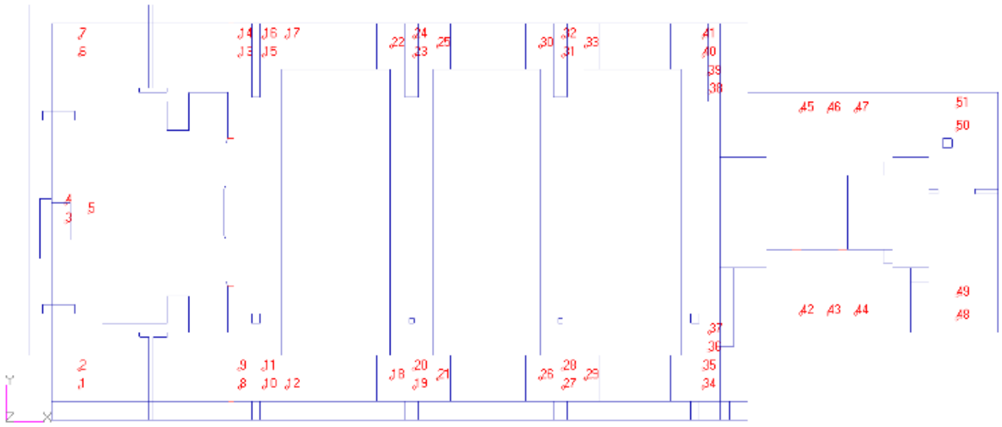

Figure 6. Nodes for issuing the results of calculated forces in vibration isolators and their deformations.

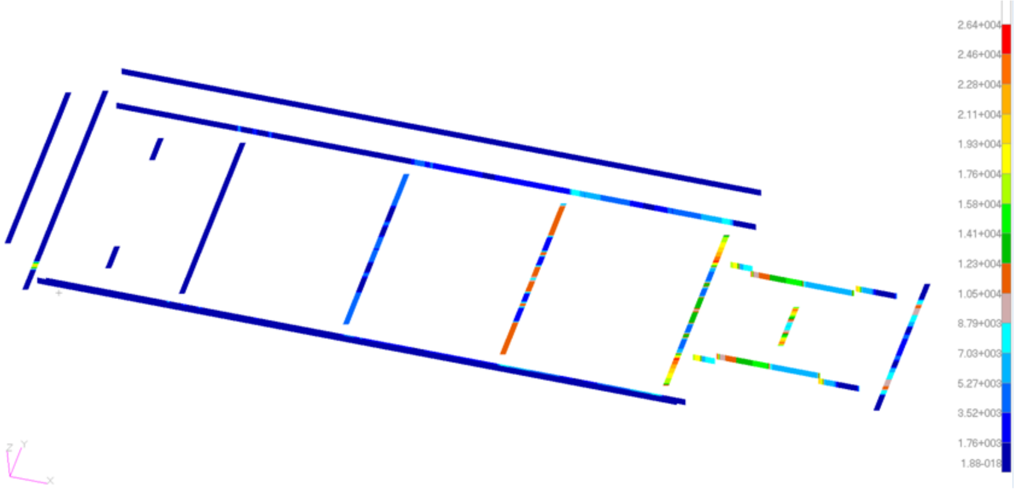

Figure 7. Bending moment diagram in foundation elements during a short circuit of vibration-insulated foundation Type-5.

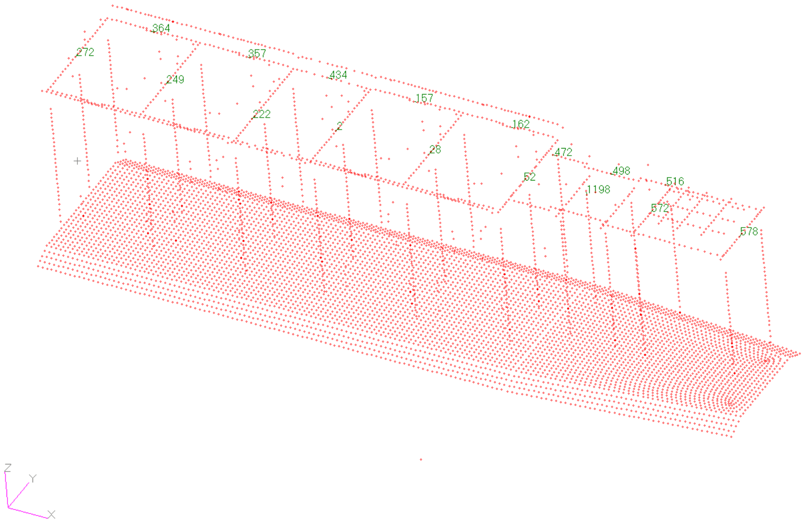

Figure 8. Elements for the internal forces calculation.

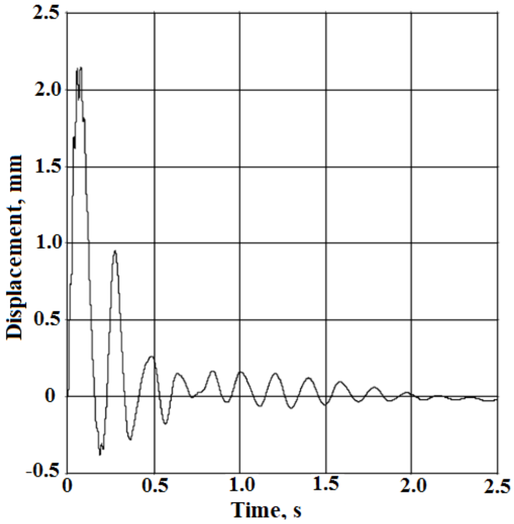

Figure 9. Function of the vertical displacement of the node number 43 of vibration-insulated foundation Type-5 due to a dynamic load.

Table 2 shows the results of displacements and forces due to a short-circuit on the turbine generator, obtained by two types of approaches: dynamic and statically equivalent for a Type-1 wall foundation for the “low-speed” turbine unit (1500 rpm). The coefficients of proportionality between the two types of approaches are derived.

Table 2. The results of the calculation of the wall foundation for the “low-speed” turbine unit Type-1.

Displacements						
No of node	Dynamic analysis		Static analysis		The ratio of a statically equivalent solution to a dynamic solution	
	Uy, mm	Uz, mm	Uy, mm	Uz, mm	K_{Uy}, relative units	K_{Uz}, relative units
7575	0.116	–0.053	2.600	0.002	22.41	0.03
7633	–0.165	–0.293	3.200	2.400	19.45	8.19
7671	–0.171	0.218	3.000	1.400	17.53	6.42
7715	–0.140	0.154	3.300	1.200	23.66	7.80
7826	–0.129	–0.100	3.600	0.200	27.82	2.01
7990	–0.033	0.031	0.400	0.200	12.21	6.44
8015	–0.031	0.036	0.800	0.400	25.46	11.16
8040	–0.066	0.054	1.500	0.800	22.82	14.89
8041	0.043	0.029	0.074	–0.001	1.72	0.03
8071	–0.050	0.032	0.200	–0.200	3.96	6.27
8130	–0.123	–0.068	1.800	0.800	14.61	11.83

Forces (bending and torques of beams and crossbars)						
No of element	Dynamic analysis		Static analysis		The ratio of a statically equivalent solution to a dynamic solution	
	Mz, kNm	Mk, kNm	Mz, kNm	Mk, kNm	K_{My}, relative units	K_{Mk}, relative units
2429	236	–7	677	3	2.9	0.4
2453	200	–10	841	24	4.2	2.4
7291	–106	–24	167	25	1.6	1.0
7340	390	223	1603	46	4.1	0.2
7428	–923	1263	1251	1468	1.4	1.2
18237	152	64	26	20	0.2	0.3
18283	629	70	522	518	0.8	7.4
18301	–529	63	234	287	0.4	4.5
18318	–1328	86	281	611	0.2	7.1

A statically equivalent approach using load data from the turbine supplier results in an overestimation of displacements from 2 to 12 times for the vertical direction and from 1.5 to 28 times for the transverse direction.

At the statically equivalent approach, the values of the bending moments Mz in the characteristic elements are 2–4 times higher than at the dynamic approach. It is impossible to draw an unambiguous conclusion for the Mk torque. A more detailed analysis with a large number of items in the sample is required.

Table 3 shows the results of calculating the displacements and forces from a short circuit on the turbine generator, obtained using two approaches: dynamic and statically equivalent for the Type-2 vibration-insulated frame foundation for the “low-speed” turbine unit. The coefficients of proportionality between the two types of the approaches are derived.

Table 3. Results for a Type-2 vibration-insulated frame foundation for the “low-speed” turbine unit (1500 rpm).

Displacements						
No of node	Dynamic analysis		Static analysis		The ratio of a statically equivalent solution to a dynamic solution	
	Uy, mm	Uz, mm	Uy, mm	Uy, mm	Uz, mm	Uy, mm
2092	–0.158	0.393	0.408	4.150	2.582	10.560
2131	0.240	0.610	0.188	2.030	0.783	3.328
2142	0.173	0.477	0.209	8.220	1.208	17.233
2166	0.246	0.712	–0.291	14.100	1.183	19.803
2232	0.559	0.673	–0.259	11.200	0.463	16.642
2244	0.632	0.802	–0.237	11.800	0.375	14.713
2258	0.420	0.565	–0.388	11.800	0.924	20.885
2268	0.447	0.782	–0.007	11.500	0.016	14.706

Forces (bending and torques of beams and crossbars)						
No of element	Dynamic analysis		Static analysis		The ratio of a statically equivalent solution to a dynamic solution	
	Mz, kNm	Mk, kNm	Mz, kNm	Mk, kNm	K_{My}, relative units	K_{Mk}, relative units
71	731	858	2495	1846	3.4	2.2
248	–10905	–6059	26233	14237	2.4	2.3
260	–2659	–6070	13159	14059	4.9	2.3
453	6430	15134	2761	6795	0.4	0.4
481	–13116	7326	51402	21581	3.9	2.9
504	–21150	–18655	6069	29354	0.3	1.6
660	–5210	–549	794	487	0.2	0.9
668	–13636	6105	2055	597	0.2	0.1
770	1698	1542	5911	7020	3.5	4.6
839	2015	–783	3017	7093	1.5	9.1

A statically equivalent approach using the data from the turbogenerator supplier for a short circuit and using dynamic coefficients (k = 2) gives an overestimation of displacements from 3 to 21 times for the vertical direction and from 0.01 to 2.6 times for the transverse direction. The increased values for the transverse direction are associated with a significant (5-fold) difference in the horizontal stiffness of the vibration isolators compared to the vertical one.

At the statically equivalent approach, the values of bending moments Mz over the defining sections are significantly higher than at the dynamic approach. However, due to the mismatch of the maxima in the diagrams across the entire structural element (beam/crossbar), a research is necessary, including all the final elements inside the structural element.

Table 4 shows the results of displacements and forces due to a short-circuit on the turbine generator, obtained by two types of approaches: dynamic and statically equivalent for a vibration-insulated frame foundation for a “high-speed” (3000 rpm) turbine unit. The coefficients of proportionality between the two types of approaches are derived.

Table 4. Results for a Type-3 vibration-insulated frame foundation for a "high-speed" turbine unit (3000 rpm).

Displacements						
No of node	**Dynamic analysis**		**Static analysis**		**The ratio of a statically equivalent solution to a dynamic solution**	
	Uy, **mm**	Uz, **mm**	Uy, **mm**	Uy, **mm**	Uz, **mm**	Uy, **mm**
459	–0.99	–1.19	0.83	6.93	0.8	5.8
453	–0.79	–0.83	0.79	7.01	1.0	8.4
980	–0.55	–0.66	1.59	6.93	2.9	10.4
985	–0.43	–0.53	2.10	5.95	4.9	11.2
450	0.39	0.63	2.40	6.72	6.1	10.7
435	0.31	–0.27	1.82	3.16	5.9	11.9
466	0.21	–0.18	1.25	1.17	6.0	6.4
778	0.19	–0.10	0.99	0.46	5.2	4.5
770	0.07	–0.12	0.53	0.18	7.7	1.6
768	0.18	–0.15	0.10	0.07	0.5	0.4
Forces (bending and torques of beams and crossbars)						
No of element	**Dynamic analysis**		**Static analysis**		**The ratio of a statically equivalent solution to a dynamic solution**	
	Mz, **kNm**	Mk, **kNm**	Mz, **kNm**	Mk, **kNm**	K_{My}, **relative units**	K_{Mk}, **relative units**
783	1007	–1456	3301	5732	3.3	3.9
772	4569	–1329	14821	5097	3.2	3.8
183	–1509	–1462	1300	4869	0.9	3.3
78	1610	594	6499	1535	4.0	2.6
82	426	612	2230	1771	5.2	2.9
57	–558	605	1592	2307	2.9	3.8
28	–3467	320	880	1077	0.3	3.4
442	–175	190	179	254	1.0	1.3
454	–168	163	121	154	0.7	0.9
478	90	103	78	70	0.9	0.7

A statically equivalent approach using dynamic coefficients (k = 2) for a short circuit in the generator shows at least a 4–12 fold increase in displacement compared to the dynamic calculation in the load application area. In the part of the foundation furthest from the impact, the static forces are less than the dynamic ones, which is associated with a faster "attenuation" of static forces compared to the dynamic ones.

The forces in the rods according to the results of the dynamic calculation are generally significantly less than those obtained from the results of the static calculation. However, there is reversed situation in some elements.

Table 5 shows the results of displacements and forces due to a short-circuit on the turbine generator, obtained by two types of approaches: dynamic and statically equivalent for the classic Type-4 frame foundation for a "high-speed" (3000 rpm) turbine unit. The coefficients of proportionality between the two types of approaches are derived.

Table 5. Results for a Type-4 classic frame foundation for a "high-speed" turbine unit (3000 rpm).

Displacements						
No of node	**Dynamic analysis**		**Static analysis**		**The ratio of a statically equivalent solution to a dynamic solution**	
	U_y, **mm**	U_z, **mm**	U_y, **mm**	U_y, **mm**	U_z, **mm**	U_y, **mm**
478	–0.50	–0.37	4.44	1.22000	8.91	3.325
455	–0.46	–0.29	4.23	1.12000	9.17	3.848
501	–0.49	–0.34	4.60	1.25000	9.38	3.705
431	–0.49	–0.21	4.64	0.00075	9.53	0.004
128	–0.45	–0.19	4.18	0.00019	9.28	0.001
129	–0.45	–0.12	3.93	0.00017	8.78	0.001
130	–0.44	–0.10	3.59	0.00003	8.24	0.000
328	–0.42	–0.06	3.34	0.00005	7.88	0.001
326	–0.42	0.04	3.08	0.00003	7.36	0.001
327	–0.41	0.09	2.81	0.00012	6.84	0.001

Forces (bending and torques of beams and crossbars)						
No of element	**Dynamic analysis**		**Static analysis**		**The ratio of a statically equivalent solution to a dynamic solution**	
	M_z, **kNm**	M_k, **kNm**	M_z, **kNm**	M_k, **kNm**	K_{My}, **relative units**	K_{Mk}, **relative units**
498	–1635	–641	4894	392	–2.99	–0.6
516	402	641	363	512	0.90	0.8
472	381	521	315	191	0.83	0.4
1198	–254	–1	8	70	–0.03	–50.3
162	–373	43	212	69	–0.57	1.6
157	218	–27	96	35	0.44	–1.3
434	88	14	31	21	0.35	1.5
357	–139	18	23	14	–0.17	0.8
364	–117	–12	19	9	–0.16	–0.8
272	60	–52	14	16	0.23	–0.3
249	–85	127	3	37	–0.04	0.3
222	–141	–78	3	80	–0.02	–1.0
28	–137	–174	4	144	–0.03	–0.8
52	515	–409	209	807	0.41	–2.0
572	–503	145	30	228	–0.06	1.6
578	108	74	30	111	0.28	1.5
2	210	–102	6	51	0.03	–0.5

At the static approach, the transverse and vertical displacements in the load application area are greater than the dynamic ones. Away from the load, small (almost zero) values of static and dynamic displacements do not correlate with each other.

The forces in such a rigid foundation with a large number of columns are small themselves and there is no clear connection.

Table 6 shows the results of displacements and forces due to short-circuit on the turbine generator, obtained by two types of approaches: dynamic and statically equivalent for a Type-5 vibration-insulated frame foundation for a "slow-speed" turbine unit (1500 rpm) of French production. The coefficients of proportionality between the two types of approaches are derived.

Table 6. Results for a Type-5 vibration-insulated frame foundation for a "low-speed" turbine unit (1500 rpm) of French production.

Displacements

No of node	U_z, mm				The ratio of a statically equivalent solution to a dynamic solution	
	Loss of synchronization	Two-phase short circuit	Three-phase short circuit	Static analysis	Maximum	Minimal
1	0.96	0.35	0.39	0.27	0.8	0.3
10	0.61	0.18	0.20	0.47	2.6	0.8
19	1.13	0.35	0.37	1.48	4.2	1.3
27	1.99	0.59	0.60	4.49	7.6	2.3
34	3.14	0.90	0.93	9.8	10.9	3.1
43	2.15	0.83	0.82	7.69	9.4	3.6
48	2.28	0.71	0.75	8.18	11.5	3.6

Forces in spring vibration isolators

No of node	P_z, kN				The ratio of a statically equivalent solution to a dynamic solution	
	Loss of synchronization	Two-phase short circuit	Three-phase short circuit	Static analysis	Maximum	Minimal
1	81.4	30.1	33.4	–23	0.7	0.3
10	66.4	19.7	–21.7	–51	2.6	0.8
19	123.6	38.4	40.6	–162	4.2	1.3
27	217.1	64.1	65.3	–490	7.6	2.3
34	266.6	76.6	79.3	–833	10.9	3.1
43	199.9	77.5	76.1	–715	9.4	3.6
48	193.5	60.4	64.1	–696	11.5	3.6

A statically equivalent approach using dynamic coefficients (k = 2) for accidents in the electrical circuits of the generator shows at least a threefold excess in the area of application of loads. The maximum difference is more than 11 times. In the part of the foundation farthest from the impact, the forces are significantly less, and the static ones decrease much faster than the dynamic ones. In connection with the above, the force values in the part of the foundation farthest from the generator, obtained by the static method, may be less than the dynamic ones.

The forces in the spring supports are distributed similarly to the forces in the foundation elements. The force values for vibration isolators near the generator, obtained from the results of dynamic calculation, are significantly less than those obtained from the results of static calculation.

The analyzed literature [2–18] presents researches of the dynamic behavior of turbine foundation structures under vibration and seismic loads, emphasizing the influence of geometry, soil type, and scale factors. All researchers performed dynamic calculations. No comparable publications on similar calculations were found in open access. Therefore, a quantitative or qualitative comparison of the research results with similar results of other authors is not possible.

4. Conclusion

The simulations, analyses, and calculations performed are based on modern theoretical and numerical methods. The theoretical methods were based on the scientific principles of dynamic analysis. The computational studies were carried out using a modern, verified and one of the most powerful software systems. The results obtained during the research can be summarized in the form of the following main conclusions:

1. Emergency loads are crucial in strength analysis of reinforced concrete structures of turbine units foundations and the selection of vibration-insulating elements.
2. An equivalent static approach to load-bearing capacity testing is unacceptable. The dynamic approach gives the values of the criteria parameters several times/tens of times less than at the static solution, and is the only recommended one. Analysis of various types of foundations have shown that, according to the estimates of the maximum forces from a short circuit on the generator,

in reinforced concrete structures, the dynamic approach gives on average of 3–15 times lower values of forces compared with the statically equivalent approach based on the dynamic coefficient.

3. The research results have been implemented in the practice of designing and calculating modern high-power turbine unit foundations for nuclear power plants of Russian design.

At the next stages of the research, an additional analysis are required to clarify the determining forces within the structural element. These calculations should take into account the mismatches of the cross-sections, where the maxima for static and dynamic calculations are reached.

References

1. Korenev, B.G., Smirnov, A.F. Dynamic Calculation of Special Engineering Structures and Constructures. Designer's Guide. Moscow: Stroyizdat, 1986. 461 p.
2. Kostarev, V.V. Bercovsky, A.M., Kireev, O.B., Vasiliev, P.S. Application of mathematical model for high viscous damper to dynamic analysis of NPP pipings. SMIRT-12 conference seminar no. 16 on upgrading of existing NPPs with 440 and 1000 MW VVER type pressurized water reactors for severe external loading conditions. Vienna, 1993. Pp. 726–731.
3. Tarasov, V.A., Lalin, V.V., Radaev, A.E., Mentishinov, A. Methodology for calculation and design of earthquake-resistant vibroisolated turbine foundations. Magazine of Civil Engineering. 2021. 102(2). Article no. 10205. DOI: 10.34910/MCE.102.5
4. Kostarev, V.V., Vasilyev, P.S., Nawrotzki, P. A new approach in seismic base isolation and dynamic control of structures. Transactions of the NZSEE Annual Technical Conference and 15th World Conference on Seismic Isolation, Energy Dissipation and Active Vibration Control of Structures. Auckland, 2017.
5. Babsky, A.E., Tarasov, V.A. Seismic stability of vibration-insulated turbine foundations. Earthquake Engineering. Constructions Safety. 2021. 5. Pp. 36–49. DOI: 10.37153/2618-9283-2021-5-36-49
6. Babsky, A.E., Lalin, V.V., Oleinikov, I.I., Tarasov, V.A. Seismic stability of vibrationinsulated turbine foundations depending on the frequency composition of seismic impact. Structural Mechanics of Engineering Constructions and Buildings. 2021. 17(1). Pp. 30–41. DOI: 10.22363/1815-5235-2021-17-1-30-41
7. Tarasov, V.A. Double Seismic Insulation System of Turbine Unit Foundation. Construction of Unique Buildings and Structures. 2020. 91. Article no. 9101. DOI: 10.18720/CUBS.91.1
8. Kostarev, V., Kultsep, A., Vasilyev, P. Analysis, Testing and Application of the 3D BCS Base Control Isolation System with 3D Viscodampers. Lecture Notes in Civil Engineering. 2024. 533. Seismic Isolation, Energy Dissipation and Active Vibration Control of Structures. WCSI 2023. Pp. 240–251. DOI: 10.1007/978-3-031-66888-3_20
9. Kultsep, A. Effectiveness of Different Types of Seismic Isolation Estimated by Numerical Comparative Study. Lecture Notes in Civil Engineering. 2024. 533. Seismic Isolation, Energy Dissipation and Active Vibration Control of Structures. WCSI 2023. Pp. 394–399. DOI: 10.1007/978-3-031-66888-3_31
10. Ahmed, A., Fattah, M., Mohsen, M. Effect of scale factor on the dynamic response of frame foundations. Open Engineering. 2024. 14(1). Article no. 20240065. DOI: 10.1515/eng-2024-0065
11. Ahmed, A., Fattah, M., Mohsen, M. Effect of Frame Foundation Geometry on the Dynamic Response of High-Speed Turbo Machine Foundations. Heliyon. 2024. 11(1). Article no. 1e41050. DOI: 10.1016/j.heliyon.2024.e41050
12. Ahmed, A., Fattah, M., Mohsen, M. A Static and Dynamic Analysis of A High-Speed Turbo Machine Foundation. Engineering and Technology Journal. 2023. 41(11). Pp. 1390–1402. DOI: 10.30684/etj.2023.142820.1547
13. Fattah, M.Y., Al-Mosawi, M.J., Al-Ameri, A.F.I. Dynamic Response of Saturated Soil – Foundation System Acted upon by Vibration. Journal of Earthquake Engineering. 2016. 21(7). Pp. 1158–1188. DOI: 10.1080/13632469.2016.1210060
14. Fattah, M., Al-Mosawi, M., Al-Americ, A. Stresses and pore water pressure induced by machine foundation on saturated sand. Ocean Engineering. 2017. 146. Pp. 268–281. DOI: 10.1016/j.oceaneng.2017.09.055
15. Tripathy, S., Desai, A.K. Analysis of seismically induced vibrations in turbo machinery foundation for different soil conditions: case study. Journal of Vibroengineering. 2017. 19(6). Pp. 4356–4364. DOI: 10.21595/jve.2017.17436
16. Bhattacharya, S., Ramanjaneyulu, K., Rao, A. Analysis and Design of Tabletop Foundation for Turbine Generators. Lecture Notes in Civil Engineering. 11. Recent Advances in Structural Engineering. Volume 1. Pp. 3–17. DOI: 10.1007/978-981-13-0362-3_1
17. Abdulrasool, A., Fattah, M., Salim, N. Displacements and stresses induced by vibrations of machine foundation on clay soil of different degrees of saturation. Case Studies in Construction Materials. 2022. 17. Article no. e01327. DOI: 10.1016/j.cscm.2022.e01327
18. Rajkumar, K., Ayothiraman, R., Matsagar, V. Effects of Soil-Structure Interaction on Torsionally Coupled Base Isolated Machine Foundation under Earthquake Load. Shock and Vibration. 2021. Article no. 6686646. DOI: 10.1155/2021/6686646
19. Rybakov, V., Nazmeeva, T., Zhang, Y., Rayimova, I. Seismic Performance of the Buckling-Restrained Brace Outrigger. AIP Conference Proceedings. 2023. 2612(1). Article no. 040001. DOI: 10.1063/5.0113969
20. Rybakov, V., Lalin, V., Pecherskikh, M., Saburov, D. Accounting for Rotational Inertia in Calculating Structures for Seismic Impact. AIP Conference Proceedings. 2023. 2612(1). Article 040034. DOI: 10.1063/5.0113989
21. Rybakov, V., Dyakov, S., Sovetnikov D., Azarov, A., Ivanov, S. Finite elements apparatus in thin-walled rods dynamics problems. MATEC Web of Conferences. 2018. 245. Article no. 08007. DOI: 10.1051/matecconf/201824508007
22. Rybakov, V., Jos, V., Raimova, I., Kudryavtsev, K. Modal analysis of frameless arches made of thin-walled steel profiles. IOP Conference Series: Materials Science and Engineering. 2020. 883(1). Article no. 012197. DOI: 10.1088/1757-899X/883/1/012197
23. Hebda, W., Mišík, M. In Search of Energy Security: Nuclear Energy Development in the Visegrad Group Countries. Energies. 2024. 17(21). Article no. 5390. DOI: 10.3390/en17215390
24. Khan, B., Ali, S., Malik, S., Kumar, P., Srivastava, S., Georgieff, D., Gupta, R. Nuclear Energy, Environmental Protection and Sustainable Development. 2024.
25. Breeze, P. Steam Turbines and Generators. Coal-Fired Generation. Academic Press, 2015. Pp. 33–39. DOI: 10.1016/B978-0-12-804006-5.00010-1

26. Jaenudin, J., Sandi, M., Hendriko, H. Development of a Simulator for Steam Turbine Generator Protection System Based on a Distributed Control System. Journal Européen des Systèmes Automatisés. 2024. 57(5). Pp. 1329–1336. DOI: 10.18280/jesa.570508
27. Zabihian, F. Power Generation. Kirk-Othmer Encyclopedia of Chemical Technology. John Wiley & Sons, 2023. Pp. 1–30. DOI: 10.1002/0471238961.1615230503151212.a01.pub2
28. Witarto, W., Wang, S., Yang, C., Nie, Xin N., Mo, Y., Chang, K., Tang, Y., Kassawara, R. Seismic isolation of small modular reactors using metamaterials. AIP Advances. 2018. 8(4). Article no. 045307. DOI: 10.1063/1.5020161
29. Eem, S., Choi, I. Seismic Response Analysis of Nuclear Power Plant Structures and Equipment due to the Pohang Earthquake. Journal of the Earthquake Engineering Society of Korea. 2018. 22. Pp. 113–119. DOI: 10.5000/EESK.2018.22.3.113
30. Ali, A., Hayah, N., Kim, D., Cho, S. Design response spectra-compliant real and synthetic GMS for seismic analysis of seismically isolated nuclear reactor containment building. Nuclear Engineering and Technology. 2017. 49(4). Pp. 825–837. DOI: 10.1016/j.net.2017.02.006
31. Zhu, X., Lin, G., Pan, R., Li, J. Design and analysis of isolation effectiveness for three-dimensional base-seismic isolation of nuclear island building. Nuclear Engineering and Technology. 2021. 54(1). Pp. 374–385. DOI: 10.1016/j.net.2021.07.018
32. Chen, W., Zhang, Y., Wang, D., Wu, C. Investigation on damage development of AP1000 nuclear power plant in strong ground motions with numerical simulation. Nuclear Engineering and Technology. 2019. 51(6). Pp. 1669–1680. DOI: 10.1016/j.net.2019.04.018
33. Goncharov, P.S. NX NASTRAN for a mechanical engineering designer. Siemens PLM Software. Moscow: DMK Press, 2010. 504 p.
34. Alekseytsev, A., Antonov, M. Analysis of the Ultimate Loading on Concrete Beams in FEMAP NX Nastran. Lecture Notes in Civil Engineering. 2022. 197. Advances in Construction and Development. CDLC 2020. Pp. 13–20. DOI: 10.1007/978-981-16-6593-6_2
35. Kuzhakhmetova, E.R. Modeling of a piled foundation in a Femap with NX Nastran. Structural Mechanics of Engineering Constructions and Buildings. 2020. 16(4). Pp. 250–260. DOI: 10.22363/1815-5235-2020-16-4-250-260
36. Gagliardi, G., Kulkarni, M., Marulo, F. Enhancement of NX NASTRAN Flutter Prediction Capabilities and Use of Experimental Parameters in Aeroelastic Calculations. Proceedings of the ASME Aerospace Structures, Structural Dynamics, and Materials Conference. San Diego, 2023. Article no. V001T02A001. DOI: 10.1115/SSDM2023-106747
37. Kumar, D., Carlson, D., Kumar, J., Cao, J., Engelmann, B. Nonlinear frequency response analysis using MSC Nastran. International Journal for Numerical Methods in Engineering. 2024. 125(24). Article no. e7588. DOI: 10.1002/nme.7588

Information about the authors:

***Mahmud Abu-Khasan**, Doctor of Technical Sciences*
ORCID: https://orcid.org/0000-0002-6782-2514
E-mail: abukhasan@pgups.ru

***Aleksandr Babsky**,*
ORCID: https://orcid.org/0000-0002-8297-1630
E-mail: aebabskiy@spbaep.ru

***Ilya Oleinikov**,*
ORCID: https://orcid.org/0000-0002-6473-5669
E-mail: oleinikov.i.i@gmail.com

***Irina Oleinikova**,*
E-mail: zuenko_irina@mail.ru

***Vladimir Tarasov**, PhD in Technical Sciences*
ORCID: https://orcid.org/0000-0002-1030-8370
E-mail: vtarasov1000@yandex.ru

Received 25.12.2024. Approved after reviewing 28.01.2025. Accepted 02.02.2025.